Designing Into 3D for Quadruped Orthotics

by

Amanda Jo Sterling

A dissertation submitted to the Graduate Faculty of
Auburn University
in partial fulfillment of the
requirements for the Degree of
Doctor of Philosophy

Auburn, Alabama
August 6, 2022

Keywords: Equine Keratin, Mechanical Properties, Tubule Density, Orthotics Design, Additive Manufacturing, Therapeutic Horseshoe

Approved by

Jeffrey C. Suhling, Chair, Quina Distinguished Professor of Mechanical Engineering
Julie Gard Schnuelle, Professor of Clinical Sciences (Large Animal/Food Animal)
Kyle Schulze, Assistant Professor of Mechanical Engineering
Michael Zabala, Assistant Professor of Mechanical Engineering

Abstract

The goal of this research is to leverage local equine keratin material properties and their correlation to hoof tubule density (TD), hydration state (biological and environmental), temperature (biological and environmental), and activity (related to strain rate) in order to design custom horseshoes and/or orthotics that accommodate animal- and hoof-specific conditions. A farrier may analyze castoff hoof trimmings inherent to the shoeing process to obtain an approximate TD distribution profile of the hoof capsule. The TD distribution profile paired with the local environment temperature and humidity can be used to reasonably predict the stiffness of the hoof capsule wall. The hoof capsule wall geometry can either be obtained via a three-dimensional exterior scan, an x-ray, manual measurements, or a combination of all three, and a computer aided design (CAD) model can be constructed. From there, a horseshoe can be modeled and functionally graded to match the changing stiffness of the hoof capsule perimeter. If the hoof has conformation issues or injury, this process can be leveraged for a more detailed and powerful solution. An orthotic can then be designed to assist in correcting and healing a myriad of hoof issues, including but not limited to correcting skeletal alignment, keratin capsule growth/reshaping, promoting specific heel expansions/frog engagement, and improving the digital cushion. A CAD model of the equine digit may be constructed and used to simulate a handful of shoeing scenarios to determine the best shoeing practices for a specific animal. In this dissertation, the stages of this procedure were defined and tested to prove the concept.

The local equine keratin tensile properties were systematically examined under a variety of conditions, which were comprised of combinations of hydration, strain rate,

tubule orientation, and temperature. Emphasis was placed upon observing the change in the modulus of elasticity under these circumstances. Thin specimens were fabricated on the micro-scale dimensions to better isolate the different tensile properties of the three hoof wall regions, the Stratum Externum (SE), Stratum Medium (SM), and Stratum Internum (SI). The stiffness of local equine keratin was correlated to the TD of the keratin. Specimens were tested at multiple strain rates (10^{-2}, 10^{-3}, 10^{-4}), but only within the elastic region to facilitate multiple measurements of the elastic modulus (E) for 0-100% relative humidity (%RH). The E of proximodistal specimens ranged from 0.25-18.3GPa for hydration levels ~0-100%RH, demonstrating an exponential decline of stiffness as hydration increased. For example, proximodistal specimens with $19 \leq TD \leq 22$ saw $1.02 \leq E \leq 8.26$GPa with trends: $y=5.361(1-0.022)^x$ ($10^4 s^{-1}$, *s.e.*=0.2803, $r^2=0.9721$), $y=6.610(1-0.019)^x$ ($10^3 s^{-1}$, *s.e.*=0.2419, $r^2=0.9803$), $y=9.886(1-0.020)^x$ ($10^2 s^{-1}$, *s.e.*=0.5776, $r^2=0.9588$). Comparable specimens of similar TD all demonstrated increased stress responses for faster strain rates. The same trend applied to mediolateral specimens, but with lower elastic moduli (0.23-3.25GPa) and significantly less variation. TD, activity, E and %RH significantly impact hoof wall keratin performance. Results highlight the impact of environment on hoof-wall keratin and the importance of TD assessments for comparative hoof wall studies and non-invasive hoof assessments in the field.

Bulk wall keratin specimens were tension tested at a strain rate of 10^{-3} s^{-1} and a variety of hydration conditions. The bulk wall specimens saw stiffnesses ranging from 175.0-829.2 MPa. These experimental results were compared with simulated results obtained via finite element analysis (FEA). The bulk specimens were modeled, and local keratin material properties associated with the TD profiles were assigned to the specimen

model thickness layers. This method of predicting equine hoof keratin properties based on TD, %RH, and temperature is demonstrably successful for applications robust enough to withstand a +10/-16% envelope with regards to stiffness, and a +/-10% envelope for a general stress response.

A CAD model of the equine digit was constructed and used to simulate a handful of scenarios: a barefoot uniform hoof, a uniform hoof with a keg shoe, and a barefoot hoof with multi-toned keratin. Resulting stresses and displacements in the control scenario (keg shoe) were comparable to the literature. This approach to modeling the hoof appears to be an accessible method with the ability to customize this model to match the specific hoof wall properties of monotoned and multitoned keratin as predicted by the TD distribution.

Additively manufactured ABS was analyzed to obtain various mechanical properties of different infill patterns, density settings, and layer orientation to match the typical material behavior of a barefoot equine hoof. Additionally, Formahoof Advanced Polymer was analyzed in order to obtain the mechanical properties needed to simulate gluing a horseshoe onto the hoof as an alternative to nails. A simulated equine digit with an ABS shoe glued to the hoof perimeter demonstrated a reduction and smoothening of the stress distribution in the outer capsule wall as compared to the keg shoe simulation. This overall process was pursued to field trials, where a 3D printed ABS orthotic was designed and tested on a horse. Improved movements and skeletal alignment was observed in the animal post shoeing. This procedure has proven to be effective and a worthy research path to pursue further.

Acknowledgments

Graduate students embody a special brand of madness. To pursue such a winding path with dogged persistence, there is no better word ascribed than “obsession”. Without a guide, one is too easily lost. For this reason among many, I must express my deepest appreciation to my advisor Dr. Jeffrey C. Suhling for his guidance, shelter, and unending support throughout my PhD study at Auburn University. Through him I have learned the true meaning of excellence and integrity, and with him, found my way out of the woods.

Many thanks are owed to my advisory committee members, Dr. Kyle Schulze, Dr. Julie Gard, and Dr. Michael Zabala, for their valuable insight and encouragement. Dr. Debra Taylor, while not a member on paper, was the driving force of this project. Without her brilliance, this research would have been dead in the water.

Pia Laporte and Dr. Ray Wilhite of the Auburn University College of Veterinary Medicine were instrumental for ethical material sourcing and anatomical expertise. Interdisciplinary cooperation is the future of engineering!

Special thanks are extended to my friends and partners-in-crime in the ME3D Laboratory. They never cease to inspire me and remind me of my purpose in the world.

This dissertation would not exist without Ms. Elizabeth Campbell, and without her, my life and future would be very different. I am forever grateful to her friendship and the life lesson I have learned from her incredible strength.

Finally, to my mother and father, I extend my most ardent gratitude. I owe you everything I am, and everything born of that. From the deepest pit of my heart, I love and thank you.

Table of Contents

List of Figures

List of Tables

CHAPTER 1

INTRODUCTION

1.1 The Problem with Hooves

The economic worth of the horse industry worldwide has been estimated to be over 300 billion dollars with the US equine industry estimated to be worth 101 billion dollars [1]. There are over 9.2 million horses in the US [1], with an estimation of 3.91 million horses used for recreational purposes, 2.72 million for showing, and 1.75 million horses are utilized for other activities including farm work, rodeo, polo, police work etc., and 840 thousand are used for racing [1].

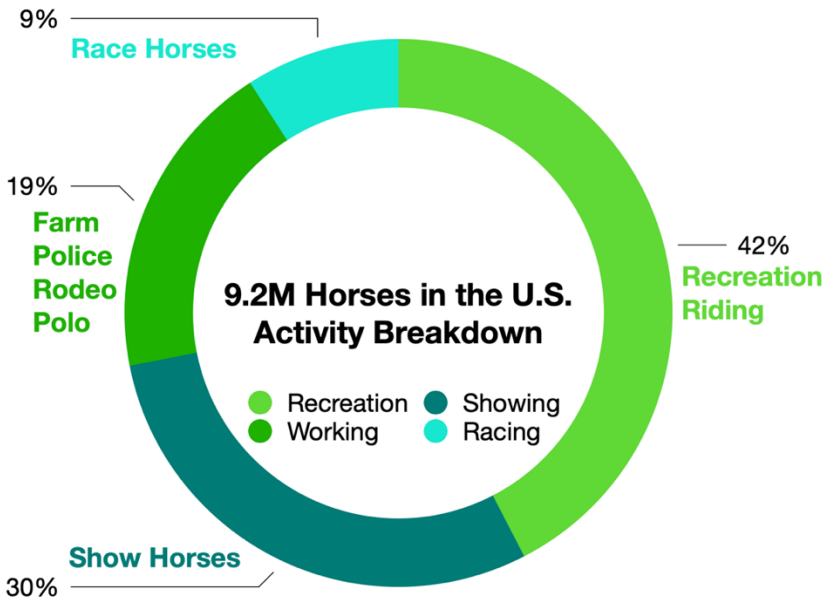

Figure 1.1 Approximate Equine Activity (2017)

The equine racing, showing and recreational industry is said to yearly bring in 10.6 billion dollars, 10.8 billion and 11.8 billion dollars, respectively [1]. Obviously, the equine industry is a significant fraction of the US gross domestic product.

Equine quadrupeds are widely kept, worked, and valued throughout the world, and great investments are made to keep them healthy. Prevention of disease results in increased

economic and animal welfare benefits. Lameness is one of the most prevalent disease states of the equine industry [2]. Some of the most detrimental ailments are problems with the foot, more specifically, the hoof, which can quickly put a horse out of commission. Problems with the hoof wall can lead to lameness and eventually euthanasia if the animal is unable to bear weight in a normal fashion. Lameness most often originates in the foot resulting in alterations in gait and excessive strain on muscles, tendons and ligaments [3]. Lameness in the foot is often due to chronic foot pathology [3]. Chronic foot pathology is very common and was seen in all working horses examined in a 2009 study by Broster et al [3].

One of the most common ailments horses and other quadrupeds are prone to is referred to as a "dropped arch". This foot injury can have significant negative impact on an animal's mobility, milk production, reproduction, and overall health and quality of life —an expensive problem for an expensive animal! Maintenance of appropriate hoof health is key to prevent lameness.

A common misconception is that the equine hoof is one solid block. In actuality, the hoof is a hollow cone-like structure that encapsulates a network of blood vessels, bones, tendons, ligaments, and muscles.

Figure 1.2 A Degloved Equine Hoof

The hoof wall is made of keratin, which is the same class of material that makes up human fingernails. Like fingernails, the hoof is always growing, and can be affected by humidity, temperature, rough terrain, and much more. In fact, most horse hooves will grow 6-9 mm per month [4]! Consistent care and maintenance is necessary to keep the hooves in healthy form.

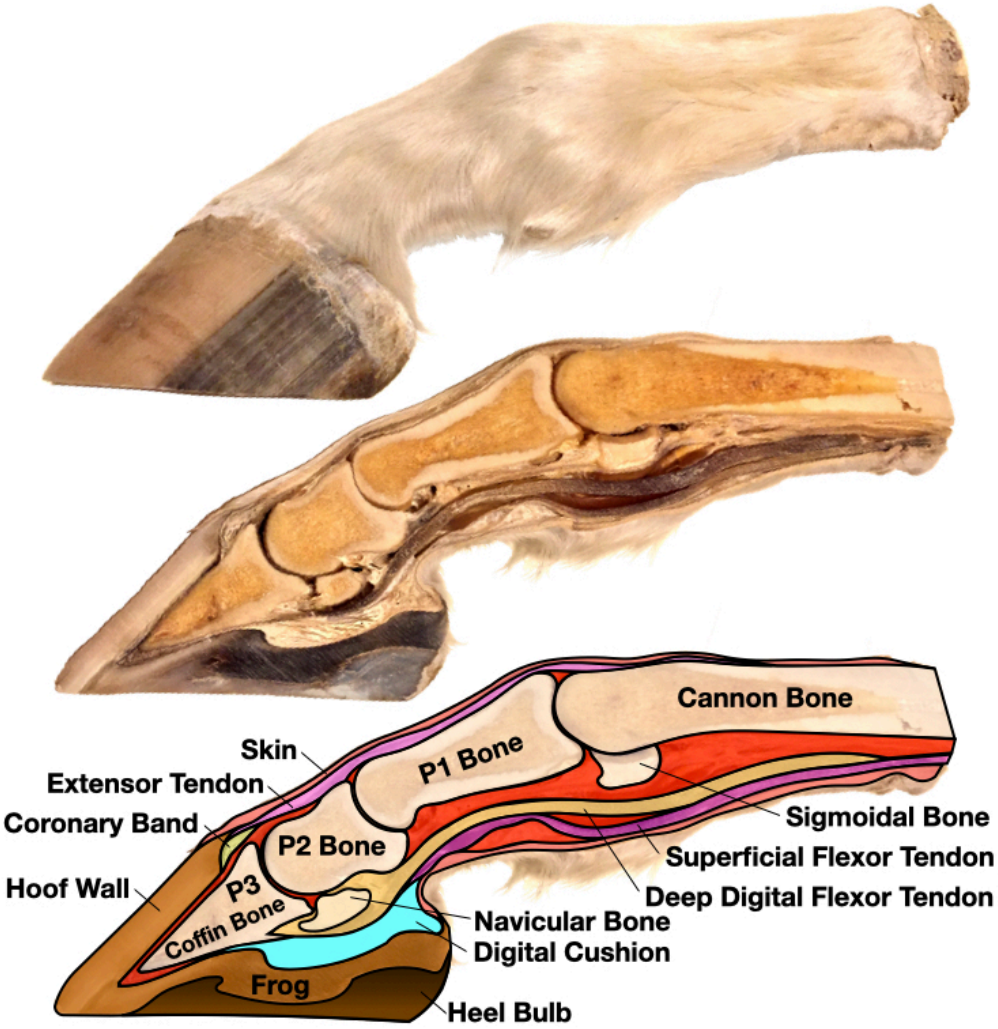

Figure 1.3 A Preserved Equine Hoof

Healthy hooves exhibit traits such as a straight hoof wall to where the coffin bone profile runs parallel, as shown in the x-ray displayed in Figure 1.4. Furthermore, a straight

skeletal alignment and good blood flow throughout the hoof is also desirable. Finally, a strong digital cushion dampens the impact of the horse's step. The equine foot is a sophisticated piece of biology, so what makes this resilient structure degrade? As with any living creature, there are many things that can go wrong, but a primary cause of a dropped arch is the well-known steel horseshoe.

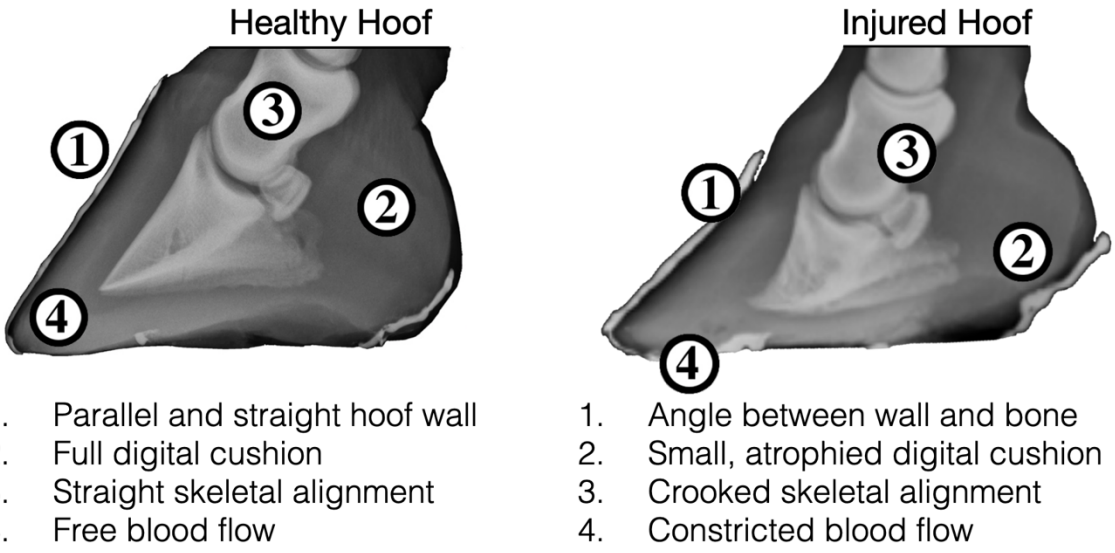

Figure 1.4 Equine Hoof X-Rays Courtesy of the Auburn University College of Veterinary Medicine

The traditional u-shaped horseshoe is nailed to the perimeter of the hoof wall and is intended to protect the hoof from rough terrain, elevated activity, and/or additional carried weight. However, this classic shoe causes perimeter loading, where all of the animal's weight is distributed along the hoof edge, allowing the hoof arch underside to sink down into the empty space directly underneath. Since the metal shoe does not allow the hoof perimeter to flex outward, the arch "drops" lower than usual, which in turn forces greater elongation of the deep digital tendon running under the hoof arch, pulling the heel down towards the ground. This series of events can lead to many damaging traits of an

injured hoof, as shown in Figure 1.4. The dropped arch can compact the coffin bone and misalign the skeletal structure. The additional downward pressure onto the arch can restrict the flow of blood, which can lead to an atrophied digital cushion. Once the digital cushion has been degraded, the horse's step becomes more jarring and damaging. Health degrades further from there.

Signs of damage can eventually be detected by the naked eye. The hoof wall can become visibly bulged due to the continuous downward sinking of the arch through the shoe center. The heel can visibly shift lower to the ground (termed an "underrun heel") due to the continuous pull of an overextended deep digital cushion. Even an elongated toe can occur from the shearing motion of a shoe left on too long while the hoof continued to grow. In fact, the most frequently seen abnormal hoof conformation is an underrun heel, which is often accompanied by a long toe [5]. Such deformation can promote chronic bruising within the palmar/plantar region of the hoof [4] and other musculoskeletal injuries.

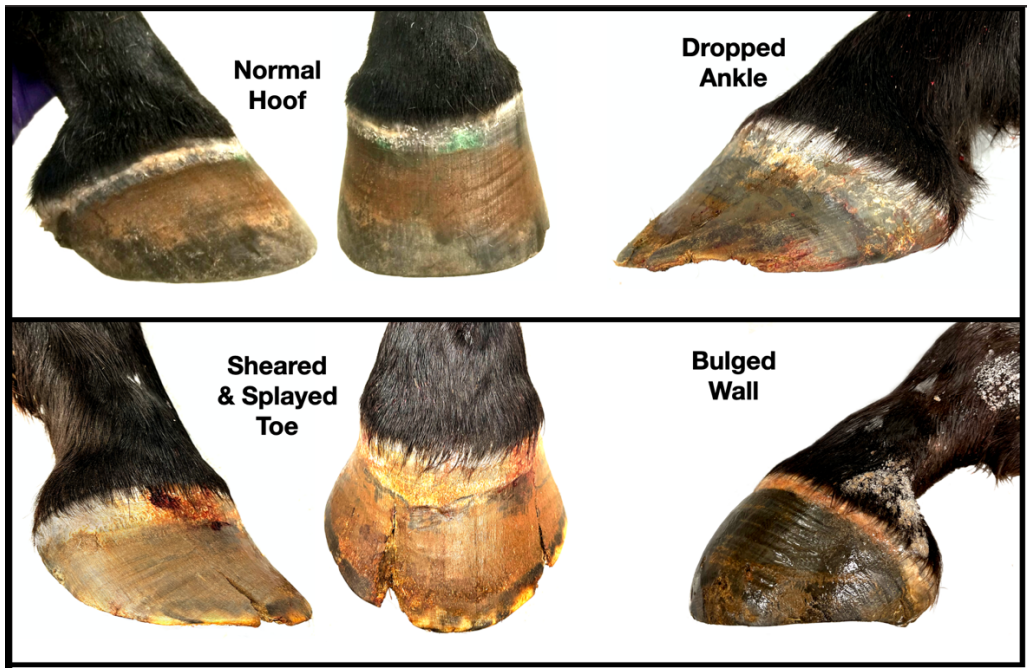

Figure 1.5 Examples of Equine Hoof Capsule Deformation

Treatment to fix hoof wall abnormalities is expensive, complicated, and often cannot be accomplished, hence, the best solution is prevention. To attempt either, one must first understand the mechanical properties of the hoof wall keratin. Only then can new shoeing solutions be designed to sufficiently match those properties. The primary objective of this research is to develop a quadruped orthotic that will help prevent dropped arches and other such issues. Additionally, a therapeutic orthotic or systematic approach that can aid in rehabilitating dropped arches in horses could be developed from the standard, preventative solution. A secondary objective is to develop a design and production process that can be applied to other types of quadrupeds, such as cattle and dairy cows.

1.2 Battleplans and Milestones

The first step in solving any problem, especially one as complicated as this, is to determine the metrics of success. Since the problem with traditional horseshoes is that the steel is much stiffer than the equine hoof wall itself, then it stands to reason that a better shoe would match the properties and/or behavior of the hoof itself. To reach this goal, the first step is to determine the appropriate mechanical properties of equine keratin material.

A series of tension tests will be conducted on hoof samples from a wide selection of horses. This will reveal the equine keratin material stiffness under a variety of conditions:

- various hydration levels
- various temperatures
- various strain rates
- different material orientations
- different hoof pigmentations

Once these values are known, the next step is to identify an appropriate material that is effectively close to the key equine keratin properties, and which is also convenient to manufacturer. Once the new shoe material is identified, develop the structure of the new orthotic.

To begin designing an orthotic, a Computer Aided Design (CAD) model of the hoof capsule will be developed, which will include assigned material properties obtained from the equine keratin tension tests. A series of orthotics can be modeled and tested all without spending fabrication resources in the initial stages by leveraging Finite Element Analysis (FEA). Once a promising design concept has been identified, it should be developed further to take manufacturing methods into consideration. For example, subtractive manufacturing methods can be inexpensive, but limit what forms can be produced. Additive manufacturing can, at times, be more costly, but has the benefit of expanding the solution space so more complex designs can be reasonably configured. There are pros and cons to all manufacturing methods, and they should all be taken into account during the decision-making process.

Once the best choice has been identified, a prototype will be fabricated and tested for efficacy during a clinical trial. The orthotics design can then be analyzed in the field and improved upon. Iterating through this cycle, a new shoe can be developed to not only prevent dropped arches, but also lead to new rehabilitative tools and techniques.

To summarize, the research milestones are as follows:

(1) Investigate the local material stiffness of equine keratin.
    (a) Characterize local keratin stiffness with respect to hydration.
    (b) Characterize local keratin stiffness with respect to temperature.

(c) Characterize local keratin stiffness with respect to orientation.

(d) Characterize local keratin stiffness with respect to strain rate.

(e) Determine the effect, if any, of pigmentation on local keratin stiffness.

(f) Conduct tension tests on bulk equine keratin samples to characterize the "bulk" stiffness of the hoof wall at various hydration levels.

(2) Validate the local keratin stiffness experimental results by creating a CAD model of the bulk wall equine keratin specimens and applying the local keratin stiffness properties throughout the layers. FEA will then apply the same loading conditions of the bulk wall tension tests. If the FEA predictions match the results of the bulk wall tension tests, then the local keratin properties can be used to effectively predict the hoof capsule behavior under loading.

(3) Create a CAD model of the entire hoof capsule that includes custom local keratin material properties.

(4) Choose a material that reasonably matches the properties of equine keratin and design an orthotic that can support and protect the hoof capsule.

(5) Use FEA to analyze and further develop the orthotic design for manufacturing and other life-cycle considerations (such as wear and friction).

(6) Fabricate a prototype of the new shoe and test its efficacy through qualitative analysis in a clinical trial.

1.3 Organization of the Dissertation

This dissertation mainly focuses on investigating the mechanical behavior of equine keratin and developing a horseshoe that prevents some of the common foot problems

originating from traditional horseshoes. The process and results of this endeavor are presented in the following chapters:

Chapter 1: Introduction to the economic value of horses, the problem with traditional horseshoes, and the plan for developing a solution.

Chapter 2: Literature review of horse hoof biology, the mechanical properties of equine keratin, environmental effects, keratin pigmentation, hide glue, and a qualitative assessment of different kinds of horseshoes and farrier practices.

Chapter 3: Description of the various experimental procedures, sample preparation, tubule density (TD) analysis method, data processing and quantitative analysis.

Chapter 4: Characterization of local uniaxial tensile properties of equine keratin with respect to TD, hydration, temperature, strain rate, and material orientation.

Chapter 5: Characterization of bulk uniaxial tensile properties of equine keratin with respect to TD distribution, hydration, and temperature.

Chapter 6: Study the TD distribution of the hoof wall, and its link to keratin pigmentation.

Chapter 7: Study to establish a link between local and bulk keratin stiffness by utilizing FEA.

Chapter 8: Method for modeling the equine digit with simplified internal biology and conducting FEA.

Chapter 9: Presentation of design approach and considerations for developing a new and improved horseshoe.

Chapter 10: Clinical trial exploring the efficacy of the new horseshoe/orthotics.

Chapter 11: Summary of results, conclusive remarks, and recommendations for future research opportunities.

CHAPTER 2

LITERATURE REVIEW

2.1 An Introduction to the Equine Hoof and the Forces at Work

An equine hoof is protected by a keratinous truncated cone-like wall that encapsulates and suspends the "foot bones" (i.e. coffin bone, navicular bone, P2, etc.), tendons, ligaments, and soft tissues from the high impact of a horse's step. When static or dynamic loading is applied to the horse hoof, a healthy hoof capsule possesses a resilient and forgiving geometry and will elastically deform under the applied forces.

A horse's step can be broken down into the following general stages: Concussion, Braking, Stance, Breakover, and Swing. The concussion stage is the first moment of impact when a horse's hoof meets the ground. The hoof is slightly angled forward so the toe touches down first at an angle of ~1º. The loading in this stage is low compared to other phases, but the loading rate is very high. After the first impact is made, the hoof briefly slides along the ground at an angle of ~2º until it comes to a stop (sometimes referred to as braking). Once the hoof is stationary with respect to the ground location, the horse may then transfer the rest of its weight onto the leg. The loading rate diminishes during this phase as the load magnitude becomes great (up to twice the horse's weight). At this point, the horse will shift forward over the leg and transition into the breakover phase, where the heel lifts off the ground and the weight is lifted off the hoof. As the hoof finishes rotating over the toe, it will finally lift off the ground and swing forward to take the next

step. [6] [7] A pictorial representation of the phases of a horse's step is presented in Figure 2.1.

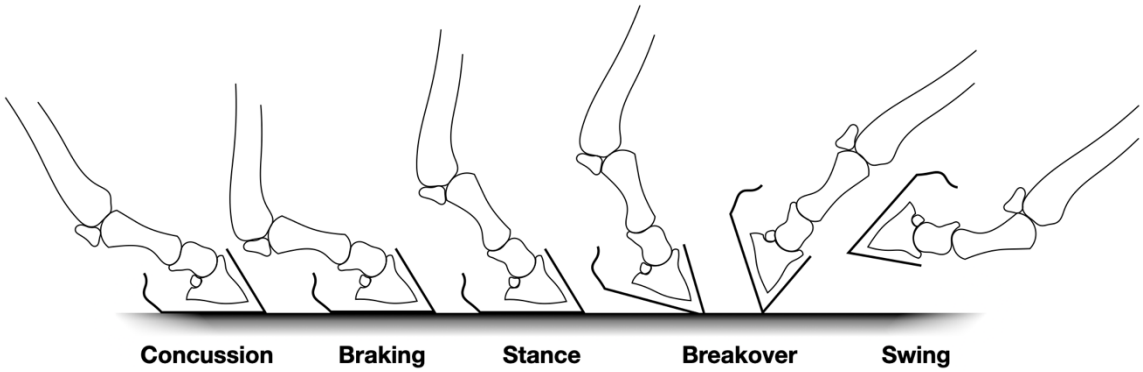

Figure 2.1 Approximate Representation of the Stages of a Horse's Step

When static or dynamic loading is applied, the hoof capsule undergoes a complex elastic deformation and subsequent return to the natural shape. The capsule geometry serves the critical function of distributing the loading throughout the hoof contact areas and dampening the initial impact, which can be quite considerable [8]. As the loading of the horse's weight becomes elevated during the stance phase, the load will press down upon the sole of the hoof and cause is to descend towards the ground. The heels will commonly expand as well, especially in hooves where the frog makes contact with the ground. This combination of deformation in the hoof capsule serves to dampen the impact of the step—the faster the horse's velocity, the more exaggerated the heel expansion becomes [9]. The dampening deformation of the hoof capsule is driven by capsule geometry and loading. For example, horses with upright heels, small frogs, prominent bars, and narrow heels may experience less heel expansion than others [10]. The typical loading on a standing hoof is approximately that of the animal's own body weight, a trotting hoof can reach 8000 N, and a golloping hoof can experience 9000 N on one hoof alone [11]. A healthy hoof capsule

that flexes well is critical to the animal, especially since the loading on the hoof can reach ~2.4 times the horse's body weight at the peak of stance phase during a gallop [12] [6]! While the keratin hoof capsule spends most of its life cycle in compression [13], failures will primarily occur due to tension in the unique geometry. Therefore, the ability to maintain tensile properties of hoof keratin material under various conditions is essential to hoof health and, ultimately, horse health.

The hoof wall is made of epidermal cells filled with α-keratin (fiber-reinforced protein-based molecular composite), and it is mainly composed of three regions: the Stratum Internum (SI), the Stratum Medium (SM), and the Stratum Externum (SE). The SI is credited with the role of transferring the ground reaction forces to the skeletal system [14] [15] and connects the hoof wall to the bones via collagen fibers. The Stratum Medium has been called one of the most fracture-resistant biomaterials in the world [14]. The SM resists crack propagation [11] [16] [17] [14] [18], which inhibits cracks from splitting the hoof inwards and/or upwards towards the living tissue. Finally, the SE forms a thin layer on the outside of the hoof wall [19]. The SE seems to serve as a moderator of hydration, preventing the hoof from drying out [14]. The direction of growth runs from the coronary band to the toe tip, and the overall fibrous direction follows the general toe-to-ground angle all the way around the circumference. Major deviation from this angle may be indicative of hoof issues. Working in tandem, the regions of the hoof wall provide an elegant and effective defense that can withstand incredible loading pressures typical to an active horse. This study aims to characterize the tensile properties of the various stratums of the hoof wall and observe how the properties change with depth.

Due to the necessary flex of the hoof structure, the keratin must remain supple enough to avoid damage. This is accomplished by keeping the hoof wall at a nominal level of hydration. The primary transport of the fluids supplied throughout the hoof wall are through hollow tubules that run along the proximodistal direction (axis defined in Figure 2.2). These tubules have an approximate diameter of 200 µm [20] and are surrounded by an inter-tubular material, which is oriented tangentially along the circumference of the hoof capsule [13]. It is interesting to note that the SE region does not host any tubules but is comprised entirely of the inter-tubular matrix material [21].

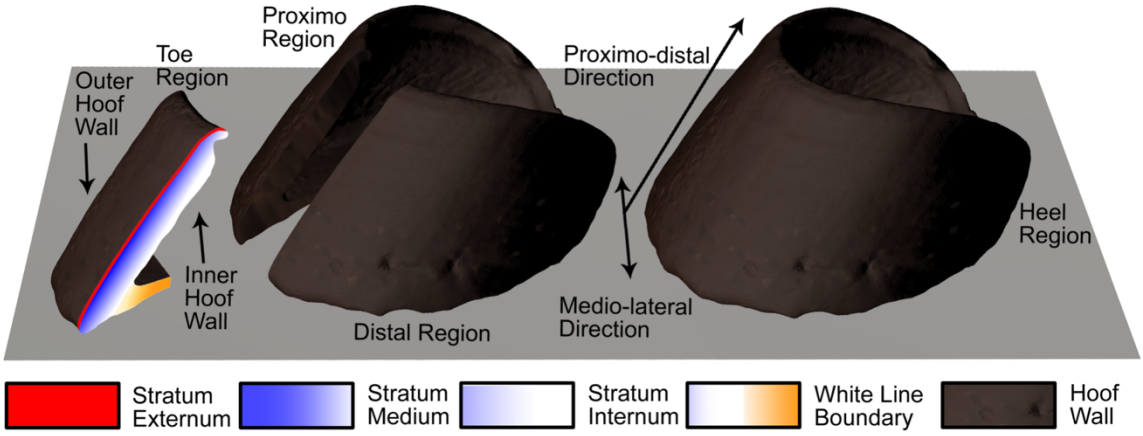

Figure 2.2 Regions of the Equine Hoof Capsule

TD varies throughout the hoof wall thickness, where the highest density is located in the outer area of the SM as it merges into the SE. The TD steadily decreases in density through the SM toward the SI, where keratin merges into papillae and dermis materials [22] [23] [24] [25] [18] [26]. Simply put, the TD is highest near the hoof surface (barring the purely inter-tubular material SE) and decreases through the SM to a minimum in the SI as the wall approaches the internal soft tissue. The tubule density gradient appears to be a mechanism aiding smooth energy transfer, from the rigid (high tubule density) outer wall to the more plastic (low tubule density) inner wall, and ultimately to the distal phalanx [27].

The gradient in tubule density mirrors the gradient in water content across the hoof wall and together these factors represent an optimum design for equine hoof wall. In one study, the average elastic modulus for equine hoof wall ranged from approximately 0.460-1.049 GPa, where the outer wall locations accounted for the higher end of the spectrum and the lower values were derived from the inner hoof wall [28]. This could be due to the presence of more moisture naturally held in the inner hoof wall (where the tubules are surrounded by enlarged medullae and have greater exposure to internal tissue fluids), and the lack of tubules (and thus, moisture) in the SE, despite all samples being tested at similar ambient laboratory conditions.

2.2 Mechanical Properties of Equine Keratin

The tensile properties of equine hoof keratin are reportedly viscoelastic, which implies a strain-rate dependency [17]. Throughout its life, a horse will participate in a myriad of activities with different movement speeds [13] (standing, running, jumping, etc.) and may be expected to carry additional weight (riders, equipment, cargo, etc.). These factors increase the loading and strain rate upon the hoof wall. Hence, it is imperative to understand the tensile properties of the hoof under different strain rates.

Some strain-rate tensile properties of the SM were quantified by Kasapi and Gosline, whose study tested bulk sections of fully hydrated hoof wall. As the strain rate increased, so did the initial elastic modulus (E_i) ranging from 0.28-0.85 GPa ($1.6x10^{-3}$-70 s^{-1} strain rates) [17].

The mechanical properties of keratinous materials, including horse hoof, are also impacted by hydration [16] [29] [28] [30]. The stiffness of horse hoof keratin has been shown to be inversely related to the material's hydration level [30]. The hoof wall is

subjected to various hydration conditions, both biologically and environmentally. Since the hoof wall is avascular, fluids diffuse through a basal membrane that is flush against the vascular dermis, hydrating the keratin cells via biological means [16]. In fact, there are two fluid gradients (high to low hydration level) present in the hoof wall: a) from the proximal region (top of the hoof where the hard keratin meets the flesh of the upper limb, including the coronary band) to the distal region (where the hoof meets the ground plane), and b) from the inner hoof (near the SI) to the outer hoof wall (SE) [31]. Fluid is primarily lost through the external surface of the hoof wall, which is why a healthy SE is so important. It logically follows that a damaged SE may accelerate dehydration of the hoof wall to the point of vulnerability. Increases in hydration of the hoof wall keratin can result from exposure to the surrounding environment such as a horse standing in water or traveling in rain. Variations between horse breed, hooves, and environmental conditions may produce different hydration states in different hoof walls, meaning the stiffness and other mechanical properties of one specific hoof may differ from another. In a study by Bertram and Gosline, the hydration levels of SM horse hoof keratin specimens were adjusted from 100% relative humidity (RH) to 0% RH, which caused the elastic modulus E to increase from 0.41 GPa to 14.6 GPa [16].

Tensile properties of equine hoof keratin have been reported to be viscoelastic in nature, and thus demonstrate a mechanical strain-rate dependency [17]. This is significant, as the loading introduced during a horse's step is rarely static. The loading upon the hoof wall can increase due to different horse activities related to movement speed [13], jumping, lifestyle, and potential cargo. Additionally, the terrain is not always flat and even, and rocky surfaces can produce a wide variation of localized stress concentrations and strain

rates through the hoof wall that exceed the standard loading [17]. Kasapi and Gosline also quantified some strain-rate tensile properties of the SM section of the hoof wall, having been tested in the bulk (entire thickness) and in a fully hydrated condition. The initial elastic modulus E_i increased with a rising strain rate, ranging from 0.28-0.85 GPa ($1.6x10^{-3}$-70 s^{-1} strain rates) [17]. There were various studies conducted on equine hoof keratin that reported values for elastic moduli at different hydrations levels [17] [11] [16] [28] [32] [33] [34]. Bertram and Gosline saw the elastic modulus E of SM horse hoof keratin increase from 0.41 GPa to 14.6 GPa when the hydration levels were adjusted from 100% relative humidity (RH) to 0% RH7. Most studies have been performed in ambient conditions even though horses populate a myriad of environments.

Another significant factor to consider is the tubule structures (approximate diameter of 200 μm [20]) that run proximodistally through the hoof wall, which serve as the primary fluid transport system. These tubules have been the subject of several studies to explore their functional contribution and structure [35] [36], not to mention their mechanical behavior [37] [20] [23] [18] [21].

The TD varies from the outer region of the hoof wall (where the SM merges into the SE), at which the highest TD occurs, through the SM toward the SE, where the TD steadily decreases until the structures merge into papillae and dermis materials [22] [23] [24] [25] [18] [26]. Studies have shown that the mechanical properties of equine keratin alter based on where in the hoof wall the sample was taken [28]. This study aims to contribute novel data regarding the tensile properties of different hoof wall regions with varying TDs.

Because of the presence of these tubules embedded in the interstitial matrix, the α-keratin structure is proposed as both nano-scale and macro-scale fiber-reinforced composite [14] [20] [24] [38] [26]. However, due to the geometry and structure of the keratin hoof capsule, orthogonality with respect to the tubules is not necessarily orthogonal with respect to the inter-tubule material. This directional correlation may change depending on the location within the hoof capsule. The mechanical response may be anisotropic, and the loading direction with respect to the tubules and interstitial fiber growth could have great impact on the material behavior [28] [13]. This study intends to contribute in-depth data comparing the elastic moduli of equine keratin in orthogonal directions with respect to tubule placement under a range of hydration conditions and TDs.

While many studies conducted on equine hoof keratin have contributed values of the elastic moduli E for different hydrations levels [11] [16] [28] [32] [17] [33] [34], there seems to be sparse data density and study-to-study variation when it comes to the correlation between the elastic modulus and intermediate hydration levels, and no data reporting different elastic moduli via hydration in the same sample. While most reported tensile properties of equine keratin are reported for an in vivo hydration level anywhere from 20%-40% [28] tested in ambient laboratory temperatures, it is useful to understand the tensile properties at other hydration conditions. Many factors affect the hydration level in the hoof, such as extreme environments, hoof care techniques such as rasping, and the natural RH gradients in the hoof capsule (~75% in the SM, ~100% in the SI, ~25% near the distal margin, etc [13]). This study intends to fill this gap in the literature by quantifying the stiffness of equine keratin for the full range of hydration.

Similar to human fingernails, the keratin hoof wall is sensitive to both hydration and temperature. Understanding the effects of temperature on equine keratin is also of interest, as horses are known to occupy terrains ranging from snow and ice to abrasive sands and desert heat. Kellon pointed out that desert sand can even be as much as 4.5 ºC hotter than the ambient temperature, and can result in dry cracked hooves, especially if the common practice of rasping is employed [39]. Hence, the examination of tensile properties of hoof keratin material under various temperature conditions is of highest importance for preventing damage to the hoof wall and developing appropriate therapeutic regimens to strengthen the hoof wall. There is a need for additional information on anatomic differences in equine keratin that have an effect on elastic modulus and how the environment alters the elastic modulus. The study herein provides a model for evaluation of the equine keratin from different horses to standardize comparisons and contribute to gaps in the literature.

2.3 Keratin Pigmentation

There is an old wives' tale which supposes that hooves with lighter pigmentation are softer and more prone to foot problems. In fact, farriers came up with an advisory rhyme:

"One white foot, buy him;

Two white feet, try him;

Three white feet, deny him;

Four white feet and a white nose—

Take off his hide and feed him to the crows." [40]

While horses are not actually put down and "fed to the crows" over the matter, it is still a hotly debated topic in the farrier world and is one that has polarized the community for decades. Some scientists have been tracking the pigmentation during their studies [41] [33] [28] in an effort to prove or disprove the rule of thumb, but no correlation has yet been made for equine hoof keratin to any definitive effect.

Some farriers believe the notion arises from the increased visibility of damage in lighter pigmented hooves, making any issues more readily apparent than those occurring in keratin with darker pigmentation. Another theory is one of correlation as opposed to causation, where the old wives' tale came about due to weaker hooves occurring in certain breeds which simply have an unrelated tendency towards lighter pigmentation. The farriers on this side of the fence generally believe that the hoof strength or lack thereof comes down more to capsule shape than pigmentation. [40]

However, there is also a belief that hoof keratin with darker pigmentation tend to be harder, which can withstand the wear and tear of motion better than the lighter pigmented counterparts. However, environmental factors muddy the issue, as a darker hoof in drier climates may in fact cause the "harder" keratin to lose resiliency. [40] This may be one of the primary factors as to why the community is so split on the issue, as the temperature and humidity certainly impact the hoof wall strength in a noticeable way—this may be why different farriers from different regions have such varying opinions based upon their unique experiences.

Despite the opposition, there is still a strong belief that pigmentation can, in fact, affect hoof strength. There is supporting evidence in nature to this effect. For example, lighter pigmented keratin in bird feathers is well known to wear away quicker than black

feathers of the same area [42]. Melanin in the feathers prevents wear, and the effect is significant enough for feather coloration to be considered an ecological function in nature. Albino birds, for example, can lose their wingspan to wear up to 4% more than birds with pigmented feathers, and lose 12% more of their wing surface area. This loss means that albino birds must work harder to maintain their flight (4-9% additional power requirement), which is enough of a disadvantage to fall victim to predation. [43] [44]

In the case of bird beak keratin, the granular fillers of melanin-rich keratin not only increases the resistance to abrasion but is also thicker than non-melanic keratin. Keratin hardness has been seen to increase by 39% due to the granules in melanin-rich keratin. [45] European Starlings with dark bills, for example, will more easily maintain their bill shape due to better abrasion resistance, which benefits them over those with pale bills when it comes to foraging activities. [46] There is a decreased likelihood of scratched or fractured feathers when melanin is present. [45] Furthermore, black feathers have a greater resistant to degradation from bacteria than white feathers due to the embedded melanin granules. [47]

Due to the keratin pigmentation demonstrating benefits for other animals in nature is one of the reasons so many farriers are reluctant to assert that there is no relationship between hoof health and keratin pigmentation. Personal experience and observations are also an obvious, powerful driver to their take on the matter—a number of farriers can be quoted that white hooves tend to be softer and have a greater risk of damage if care is not taken to round them off during shoeing preparations. [40] Another interesting point is a potential prevalence of white hooves on the same animal. An interview by the American Farriers Journal reported an interesting statement by farrier Ed Boyd:

> "It does seem like if I run into a horse with very soft hooves then all four hooves are light. And, if I run into a horse with hooves like iron, then all four hooves are dark. I haven't seen a difference in light and dark hooves mixed on the same horse." [40]

Another farrier observed that while horses with white hooves, or paired white hooves fore- or hindlegs, did not have noticeable strength difference than darker hooves. However, in horses with three dark hooves and one white hoof, the white hoof would be weaker than the other darker hooves. [40]

The passionate debate of experience versus science rages on, where field observations clash with the findings of the few studies that have tracked equine keratin pigmentation. The only indicated different between pigmented and non-pigmented hooves is the melanin granules residing in the keratin. In an effort to account for both field observation and opposing scientific findings, a theory was proposed that the melanin granules may hinder crack propagation, making pigmented hooves more resilient against defects. [40] This study intends to track the pigmentation of the equine hoof samples and contribute more data to the body of knowledge in an effort to further the ongoing debate.

2.4 A Brief History of Hide Glue

An ancient yet oft-overlooked technology is animal glue. Hide glue is one such example, which can be extracted from animal skin, bone, connective tissues, and other slaughtering byproducts with relative ease. Submerging the raw materials in hot water will denature and solubilize the collagen, a process called gelatinization [48]. The extracted colloids are made of complex proteins, the defining elements being chondrin (contributing adhesive strength) and gluten (providing the gel strength) [49].

The historical significance is staggering. Ancient humans were limited to fabricating single component tools (products derived from one thing) until the advent of Hide Glue, which allowed for the creation of elaborate tools with superior mechanical properties [50]. The introduction of natural adhesives is an important milestone in the evolution of manufacturing technology—marked by the development of "hafting", the attachment of stone tools to handles [51] [52]. This development opened the door for interchangeable part design, the impact of which is still felt today in modern component-based technologies [53].

The discovery of artifacts containing animal glue in caves near the Dead Sea mark the earliest known use of the natural adhesive occurring over 8000 years ago [49]. Animal collagen glue was used in Egypt 4000 years ago [49], and it was an ingredient in Egyptian plaster (around 3000 BC). It has even been found on some Egyptian sarcophaguses! In Deir el-Bahari, an ingot of pure hide glue, specifically, was found that dated back around 2000 BC [54].

As society advanced, so the uses of hide glue, expanding beyond stone tools into bookbinding, furniture making, and general product manufacturing as simple as paintbrushes. Hide glue was produced by the artisans themselves in small batch quantities for many centuries, until the first commercial animal glue plant was opened in Holland, circa 1690 [55] [56]. The animal glue industry advanced to England in the early 1700s and steadily spread throughout the rest of the world [55]. 1808 marked the first commercial production of hide glue in the United States [55], though they were the quickest to adopt modern adhesives later in history. The use of animal glue continued well after the WWII in England and across Europe [49]. Today, however, the primary use of animal glue is to

restore antiques, conserve museum pieces, restore antiquarian art and books, and to restore and/or manufacture musical instruments [49].

Society evolved, and the hide glue manufacturing process was refined in small ways. The raw materials are first conditioned with calcium hydroxide (lime), and the pH value is adjusted via dilute mineral acid and water. Heat is applied to initiate the cooking process, and the solution of water and protein is extracted. The solution is then filtered in order to retrieve the protein, which is then dried and ground up into its final, marketable form. Glue viscosity and gel strength (fluidity, stiffness of gel formation, respectively) are tested and the glue is graded on a scale spanning 50 to 512. The lower the animal glue grade, the slower it is to dry and the more flexible it is. Different grades of glues allow artisans to select a version that best suits their needs. [49]

Right up until the advent of synthetic glues, hide glue was widely the adhesive of choice because of its unusual properties. The bond formed by protein glues are both chemical (molecular) and mechanical. Perhaps the most lauded characteristic of hide glue is its ability to reactivate, allowing the components to be repositioned and re-bonded even after the initial drying. By moderating the heat and moisture of the glue, it can change back and forth from its liquid and solid state. Hide glue is "reversable" in this way, and one of the few adhesives with this valuable quality. [49]

While hide glue is used significantly less often since the advent of synthetic glues, it is still relevant and, at times, a preferred option. There are even companies that currently manufacture protein glues (still referred to as "animal glues") out of recycled pharmaceutical gelatin. The market is there due to many favorable properties that synthetic glues do not offer, qualities that are briefly addressed in Table 2.1. The reversibility and

reactivation ability are obvious benefits that fall firmly in the animal glue corner, making this glue a favored option of high-end/bespoke furniture makers. Synthetic glues form a mechanical bond only, as opposed to hide glue which also forms a molecular bond, and synthetic glues often lacks resistance against shear forces. Synthetic glues can be very toxic and sometimes have limited shelf lives, as opposed to Hide glue's unlimited shelf life when in its dried, granulated form. These are only a few examples, and synthetic glues are often preferred due to wide availability and ergonomic applicators.

Table 2.1 Comparison of Qualities Between Hide Glue and Most Modern Adhesives

Glue Quality	Hide Glue	Most Modern Glues
Glue Readily Sourced	~	✓
Reversibility	✓	X
Glued Parts Easily Repaired	✓	X
Creates a Mechanical Bond	✓	✓
Creates a Molecular Bond	✓	X
Workable Surface Finish	✓	~
Resistance to Sheer Forces	✓	X
Can Bond To Itself (Additive)	✓	X
Toxicity	X	✓
Long Shelf Life	✓	~
Ready "Out of the Box"	X	✓
Even Set	✓	~
Singlehanded Application	X	✓

✓	Glue has specified quality.
X	Glue does not have specified quality.
~	Quality partially applies or is a special case.

Historically, expired horses were taken to knackers, where the body was dismantled and distributed to various industries, including sending the hooves to be made into glue. This gave rise to the colloquialism "taking the horse to the glue factory", which is in reference to putting down a lame and/or suffering horse. This author would like to stress that no horse should be killed for such exclusive purposes. Any such biological material

should only be sourced ethically. However, the hoof is a constantly growing body part, just like human fingernails—and like fingernails, the hoof is routinely trimmed. The keratin pieces trimmed from the hoof, and the keratin powder that is cast off via rasping, are ethical sources of material from which hide glue can be made. One never knows when the friendly neighborhood antiquarian book mender might need a pot of historically accurate adhesive!

2.5 Farrier Practices and Shoeing the Hoof

Scholars can date the invention of the horseshoe all the way back to 400 BC. Manufacturing could be as simple as woven plants, as in Ancient Asia, or more complex combinations of plants, rawhide, and leather straps, as made by the Romans. The horseshoe was certainly born of necessity in an increasingly expanding world, as superior hoof protection could affect the key industries civilizations rely on: trade, farm production, transportation, and warfare. [57]

Since then, shoeing technology has progressed to the traditional "lucky" steel shoe people most commonly recognize today, which is secured to the hoof via nails. Still, the horseshoe as we know it today is ever evolving in a constant effort to improve hoof protection and horse performance. After all, inappropriate hoof preparation and shoe selection have long been considered the primary cause of foot pathology [58] [59]. Wise hoof modification (trimming, rasping, etc.) and a well-fit shoe is integral to a sound step and strong performance [60] [61] [41]. In fact, it is becoming widely accepted that appropriate hoof trimming and shoeing could not only enhance animal performance, but also reduce musculoskeletal disease—as concluded by a cohort study involving 95 thoroughbreds [62].

There are three general stages to shoeing a horse: hoof preparation, shoeing, and final adjustments.

2.5.1 Preparing the Hoof for Shoeing

The elements of hoof preparation include analysis and possible adjustments to the hoof angle [4], hoof length [4], mediolateral hoof orientation [4], sole/frog/bar thickness [4], wall contour and ground surface [63], and sole/frog/bar hydration level.

The hoof angle refers to the solar angulation of the hoof capsule as measured at the toe, and the healthy form is the dorsal wall in parallel alignment with the pastern as demonstrated in Figure 2.3. When trimming the hoof, this healthy dorsal hoof angle should be the aim [63] [64] [65]; most horses achieve parallelism when the forehooves are trimmed at 50°-54° and hind hooves at 53°-57° [63]. A major benefit of the hoof and pastern regions becoming well aligned is that the forces at the toe, medial heel, and lateral heel are at their lowest [66]. This is opposed to misalignment, which increases the forces in those areas. When the angle of the hoof is steeper than the pastern, the hoof angle is too high and is referred to as "broken forward" [60] [4]. When the hoof angle is too aslope for the pastern, it is too low and is called "broken backward" [60] [4]. There is an inverse relationship between the hoof angle and the tension in the deep digital flexor tendon. That is to say, the lower the hoof angle, the higher the maxima tension in the deep digital flexor tendon becomes in walking horses [67] [68], and vice versa [67] [68] [69]. The opposite relationship exists between the hoof angle and superficial digital flexor tendon, however, this change only becomes significant when the animal reaches trotting speed [68] [69]. While broken forward and broken backward hooves do not seem to greatly impact the length of the horse's stride when walking, trotting, and cantering, a high hoof angle does

appear to quicken the breakover and a low hoof angle slows breakover [70]. These affects should be carefully considered by the farrier when choosing how to prepare the hoof for shoeing, particularly when alterations are made with the intent to rehabilitate.

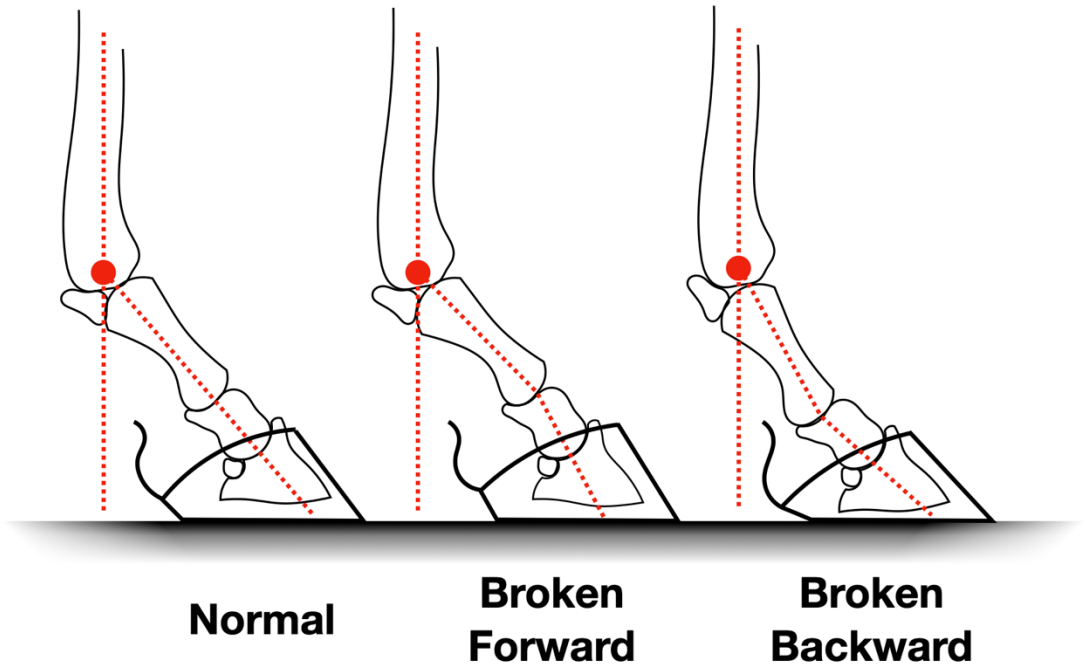

Figure 2.3 Dorsal Hoof Alignment

Hoof length is most commonly measured from the tip of the toe to the coronary rim at the most proximal region of the wall [4], and impacts the kinematics of the hoof [66]. Logically, a longer hoof length effectively creates a longer lever arm over which the hoof must pivot and breakover during a step. Therefore, the maximum height of the hoof flight during a step is increased because the horse must lift its foot higher to step forward [66]. The vertical velocity of the hoof also increases, and the breakover is slowed [66]. However, shifting the breakover back by removing too much toe during trimming can weaken the structural integrity of the hoof wall, and lead to further bending at the toe and damaging the quarters [71]. One can imagine that the altered kinematics would be of interest for

show horses and professional breeders, not to mention the restrictions placed upon maximum allowable hoof length for some competitions and organizations [72]. Beyond trimming, a horseshoe and padding also act as extensions of the hoof, which must also be considered. The general rule of thumb relates toe length to horse weight, where a horse weighing 800-900 pounds should have a toe length of 3.0 inches, 950-1050 pounds to 3.25 inches, and 1150-12-50 to 3.5 inches [4]. While these numbers work for most breeds, there are exceptions. Since lengthening the hoof is analogous to a longer lever arm, the distal limb experiences an increase in applied torque as well as elevated pressure on the navicular bursa from the deep digital flexor tendon during the animal's step. As the hoof is constantly growing, the hoof length must be routinely maintained. If the hoof length is left too long, the horse may develop a tendency to stumble, acquire an awkward gait, become injured [63] [5], and potentially cause lameness [60].

The next adjustments to be considered prior to shoeing is the mediolateral hoof orientation, which, in ideal form, means the lengths and angles of the medial and lateral hoof walls are relatively equal. The goal is to achieve "roll" symmetry in order to maintain good mediolateral balance of the foot. The most common technique utilized to achieve this end is to trim and prepare the ground surface of the hoof capsule to be perpendicular to the cannon bone and phalanges axes [4] [63]. An alternative technique is to trim and prepare the hoof capsule in such a way that enables the ground surface of the hoof to land "flat-footed", or at least on both the medial and lateral heels simultaneously [4]. This is an important preparation to consider, as trimming the hoof to achieve simultaneous landing of the heels is a useful therapeutic supplement when the source of lameness is located within the digit [4]. This is also a traditional treatment for horses with lameness associated

with poor mediolateral balance (i.e. lateral distorted hooves [58] [73], sheered heels [4], chronic heel soreness [4], navicular syndrome [74], and chronic metacarpophalangeal synovitis [75]).

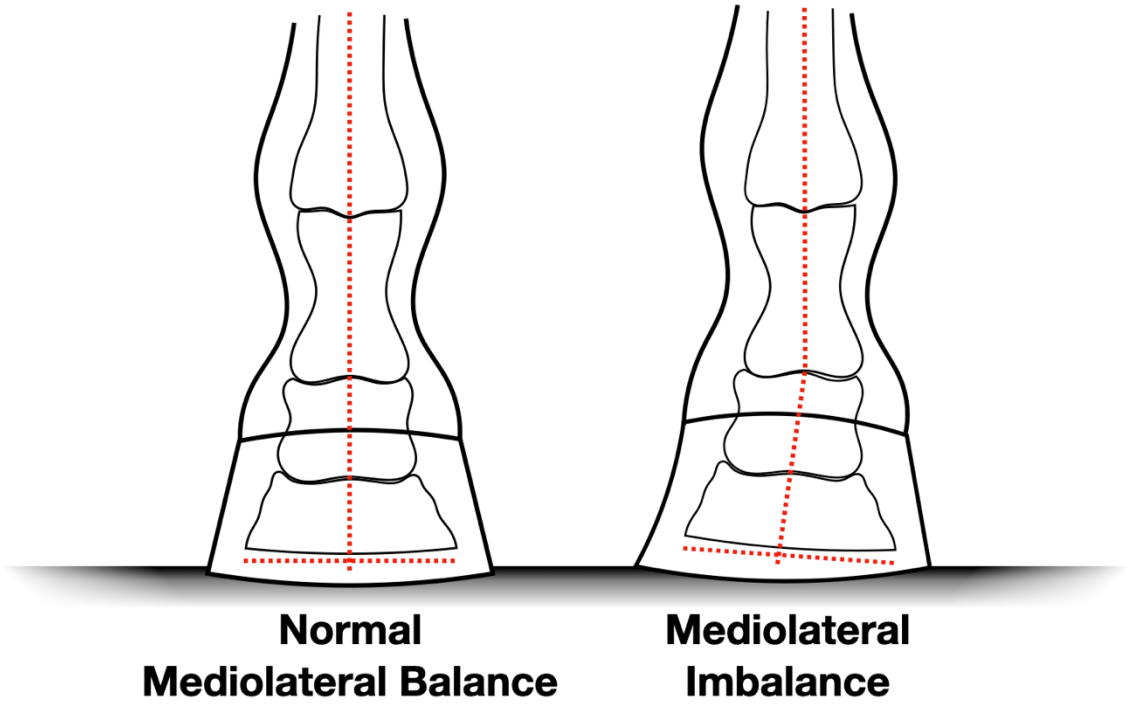

Figure 2.4 Mediolateral View of the Equine Hoof

The underside of the hoof, or "solar surface", consists of the ground surface perimeter of the wall, the sole, the frog, and the bars. During a horse's stance and step, the sole descends under the animal's weight and the heels expand abaxially [4]. Sole thickness and hoof width largely drive how far the sole will descend and how widely the heels will expand when the horse puts weight on the hoof [73] [58]. Sole descent and heel expansion reactions are correlated, and restricting the heel expansion is detrimental to the horse [76]. Shoeing the hoof in a way that restricts the natural heel expansion, as some traditional horseshoes do, reduces soundness. The frog itself is limited in how much weight it can soundly withstand, but it is thought that regular pressure to the frog via ground contact will

stimulate frog growth and heel expansion [63]. In fact, an unshod horse will purposely wear away the outer sole material as it ages and dehydrates, and the frog is molted semi-annually [63]. However, the correlation between frog pressure and heel expansion seems somewhat inconsistent between different horses [77]. This implies that the hoof capsule geometry is a significant driver of the heel expansion response [4], and how the frog would best interact with a horseshoe should be determined on an individual basis. Trimming the superfluous material from the frog and bars, and thinning the concave sole are normal practices to prepare the hoof for shoeing, though how much material is removed and whether or not the frog should rest on the ground plane is adjusted per animal [4]. Finally, the bars seem to act as structural struts for the concave solar surface (possibly even inhibiting heel contraction), and so excess trimming is generally discouraged [63].

The circumferential shape of the conical hoof capsule partially drives the overall measured hoof size and structural stability of the hoof wall [4]. In fact, horses with a small foot-to-body-weight comparison are potentially more prone to navicular syndrome [78]. The ground surface is the region of the hoof wall that contacts the ground when the horse puts weight on the foot, and it drives the spatial relationship between the weight-bearing surface and the rest of the limb [4]. The center of the hoof is identified by the "normal center of equipoise", which is defined as "…the termination of an angle of incidence passing distally through the axes of the phalanges" [4]. To achieve a balanced hoof, the distance from the center to any circumferential point must be equal [59]. Trimming and shoeing decisions are driven by hoof position, which in turn impacts the direction of hoof growth [4]. Since strength is derived from the tubule formation in the hoof wall, bulged/flared walls where the tubule orientation is curved become compromised and

experience a reduced capacity to resist compression [4]. Shifts in the load distribution due to structural changes may lead to weakened or collapsed hoof walls [4]. As the hoof wall continues to distort and lose parallelism, the palmar ground support is diminished and the foot becomes biomechanically predisposed to injury [4]. A wise choice in shoe can extend the ground surface and, thus, compensate for poorly shaped hooves [4].

On a final note regarding hoof preparation, drying the hoof is a practice of particular importance when the intended shoeing involves pads, glues, or large area coverage. Anaerobic organisms can be found in the crevices of the frog, which can cause disease when provided an air-deprived environment (such as glues, or covered crevices) [10]. Trimming of extraneous keratin and rasping/smoothing ragged edges help prevent diseases such as thrush [41]. Farriers are even known to use a torch to further dry the keratin in an effort to prevent disease and/or local pockets of moisture.

2.5.2 Shoeing the Hoof and Final Adjustments

Once the hoof has been prepared, shoeing may commence. A traditional, hand-forged metal shoe is first shaped to match the outer circumference of the hoof, where the most important match points are located at the toe and quarters. This shoe adjustment should also consider the heel expansion during the horse's step such that the contact between the ground plane and the hoof surface of the shoe maintain contact during the weight bearing stages [4]. A general skill test developed by The American Farriers Association states that the shoe branches should compensate for heel expansion by extending beyond the hoof wall no more than the "thickness of a dime" (~1.5 mm) [79]. Additionally, the heel length of the shoe should not extend beyond the palmar/plantar location more than the distance earmarked for heel expansion. This is to help prevent the

shoe from being stepped on by another shod hoof, which can lead to the shoe loosening or being complete ripped off [4]. This goes to show that the activity of the horse will drive shoeing decisions, as athletic horses (rodeo, racing, etc.) are often shod "tight", leaving minimal room for heel expansion to avoid "throwing a shoe"; at such speeds and tight turns, shoe loss during activity can prove to be catastrophic. However, if the horse is shod "tight", the shoe must be adjusted on the hoof more frequently to avoid the dangers of the quarters/heels overgrowing the ledge of the shoe [4]. Other methods to avoid shoe loss is to fillet the square ledge of the shoe (called "boxing"), or even fill the space with a flexible glue to remove the ledge overhand [41] [80] [81].

The traditional metal shoe is fastened to the hoof via six steel nails with rectangular profiles. Since the nail is driven through the SM, it is best to use the smallest nails possible to minimize splitting the hoof wall [41]. The part of the nail that protrudes out of the top of hoof wall are bent down, essentially hooking the nail over the hoof wall. These "nail clinches" should be embedded into the wall and smoothly finished so it does not feel rough to the touch [79] [41]. Excessive rasping of the nail clinches should be avoided, as doing so could weaken the connection between the shoe and the hoof—this is because the strength of the fastening depends upon the friction between the nail shaft and the SM, and on the nail clinches "hooking" action [4]. Metal shoes with "clips" (metal stubs that form small vertical lips on the outer rim of the shoe) can help reduce shear forces acting on the nails, which can help stabilize the shoe on the foot (especially is the hoof wall is particularly soft and/or weak) [4]. Nails are acknowledged to potentially weaken the hoof capsule wall, especially on hooves that are split/fractured or have a very thin SM [4]. However, on a healthy hoof, so long as the nails are placed no further back than the widest point of the

circumference, it is believed that nailing and interactive reshoeing does no harm beyond the superficial—and hand-forged shoes carefully set the nails specific to the hoof capsule geometry.

Commercial, mass-produced metal shoes (sometimes called “keg” shoes) do not have such careful nail placement as a custom forged shoe. The nail holes are punched in a uniform distance from the outer edge of shoe, which does not take into account how the hoof wall (and thus the SM wall region) thins closer to the heels [4]. The nail holes on a keg shoe are also often set further back to the heels (past the widest point in the hoof circumference) which increases the likelihood of the shoe interfering with the heel expansion. Finally, most keg shoes come with a beveled heel, which reduces the surface area that contacts the ground plane and shifts the bearing surface forward toward the dorsal region of the hoof [4]. While keg shoes are cost effective and more readily available than hand-forged shoes, there are many more drawbacks regarding hoof health.

Advancements in shoeing technology have progressed in recent times with the aim to eliminate the use of nails altogether by developing glue-on shoes. On one hand, these shoes do not pierce holes through the hoof wall, thus weakening the structure and giving rise to local stress concentrations. On the other hand, the attachment is not always as secure as nailing, and the installation process is more involved with an additional challenge of “beating the glue setting” time limit. There is also additional risk of bacterial infection due to the glue sealing areas of the hoof wall [82]. One of the most effective products on the market is the Sigafoos Glue-On shoe by Soundhorse Technologies, which boasts an aluminum shoe with a polyurethane rim (to reduce impact shock) that is glued on via a

woven cloth cup that is soaked with acrylic adhesive. According to the product specs, this composite shoe system forms a holding strength twice that of traditional nailing [83].

Other available options involve pads that offer flexible support around and under the hoof with a wrapping adhesive similar in application to plaster cloth bandages. There is even a product that doesn't need to use a shoe at all, but instead encases the entire hoof in a glue using flexible molds. Angles and other "shoe" corrections are designed into the molds themselves and are reflected in the finished hoof encapsulation. The obvious benefit here is the natural wearing away of the glue as the horse works. Though of course, the more complex and advanced the solution, the more the shoeing service costs. Especially with shoeing solutions that require special tools, such as molds.

Table 2.2 Comparison of Qualities Between Horseshoes

Shoe Quality	"Keg" Metal Shoe	Custom Metal Shoe	Three-quarter Shoe	Glue Casting	Glue-On Shoes	Plastic Shoes	Padded and Wrapped Shoes
Nailed Shoe	✓	✓[1]	✓	X	X	✓	X
Fit Quality	X	✓	~	✓	~	✓	✓
Readily Available	✓	~	~[2]	✓	X[5]	✓	✓
Easy Installation	✓	✓	✓	X[4]	X[4]	✓	X
Circumferential Support	✓	✓	X[3]	✓	✓	✓	~
Cost	$	$$	~	$$$	$$-$$$	$-$$	$$-$$$

✓	Shoe has specified quality.	$	Low Cost
X	Shoe does not have specified quality.	$$	Med. Cost
~	Quality partially applies or is a special case.	$$$	High Cost

1 Less destructive nail placement [4].
2 Predominately available in the United Kingdom [80].
3 No medial support; reduces hoof soundness [4].
4 Gluing is time limited and is more challenging than nailing.
5 Only ~10% of farriers apply glue-on shoes in their practice [82].

This demonstrates the tremendous progress made thus far and the continuing efforts for improvement in the farrier world. Such products are on the rise; however, some believe that the use of nails will persist as the leading shoe attachment method because it is economic, convenient, easy, and has such a long track record in history. There is still much work to be done before nailing is truly pressed by the competition.

Plastic shoes have a number of attractive benefits, including but not limited to a lower overall stiffness to reduce hinderance of heel expansion. Depending on the shoe, plastic can run the gamut between inexpensive to quite pricey depending on specific material and manufacturing method. As plastic can often be easier to fabricate with, more customization options are available, such as closer circumferential fits. Additionally, farriers are able to rasp a standardized plastic shoe into a more custom fit with greater ease than blacksmithing a classic steel shoe. Of course, plastic shoes are less durable than their steel counterpart, and may be more vulnerable to a horse potentially throwing the shoe. However, in the event of a thrown shoe, one could postulate that a plastic shoe caught by a hoof would be more forgiving and less damaging than a steel shoe.

If material and method were not enough options in the horseshoe world, there is still the consideration of shoe shape. When the word “horseshoe” is uttered, one’s mind immediately pictures the class u-shaped steel shoe. However, there are other shapes, the most common of which are the bar shoe, the egg bar shoe, and the heart bar shoe. These shoes are represented in Figure 2.5.

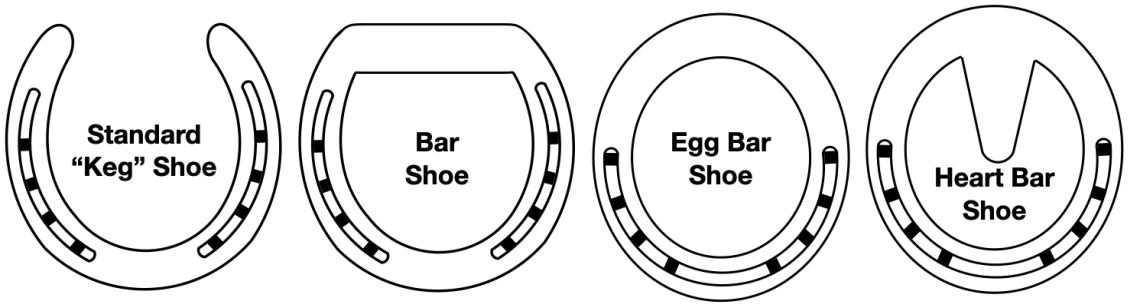

Figure 2.5 Typical Horseshoe Shapes

The bar shoe, for example, might be chosen when extra heel support is needed, or when an injury causes excessive heel expansion or contraction. The egg bar shoe also adds extra heel support, but also extends beyond the heel and provide more real estate to wedge the hoof when navicular disease other conformation issues arise. The heart bar not only provides heel support and space for wedging, but also a central bar that supports the frog. The center bar also provides opportunity to pad the hoof sole.

2.5.3 The Full Scope: Gaps in the Literature and Research Objectives

This literature review covered a myriad of relevant topics pertinent to the research goals. The horse hoof biology and step cycle were discussed in detail, as well as covering the typical loading a hoof may experience. The progress in charactering the material stiffness of equine hoof keratin was summarized, with respect to some changes in hydration, and strain rate. There seems to be sparse data density and study-to-study variation when it comes to the correlation between the elastic modulus and intermediate hydration levels, and no data reporting different elastic moduli via hydration in the same sample. Many factors affect the hydration level in the hoof, such as extreme environments, hoof care techniques such as rasping, and the natural RH gradients in the hoof capsule. This study aims to characterize the local tensile properties of the various stratums of the hoof wall and observe how the properties change with depth, hydration, temperature, and

strain rate, and tubule density. Additionally, the research will contribute in-depth data comparing the elastic moduli of equine keratin in orthogonal directions with respect to tubule placement under a range of hydration conditions and TDs. The study herein provides a model for evaluation of the equine keratin from different horses to standardize comparisons and contribute to gaps in the literature.

This chapter also presented both sides of the age-old debate of whether hooves with light pigmentation are "softer" than hooves with mixed or dark pigmentation. Additionally, a brief history of hide glue and potential modern benefits was discussed in detail. This study intends to track the pigmentation of the equine hoof samples and contribute more data to the body of knowledge in an effort to further the ongoing debate.

Once the local keratin properties are experimentally determined, they will then be used to model the stiffness of bulk wall specimens via FEA. The FEA results will be compared with experimental data of bulk wall keratin specimens to validate the results and prediction method. This prediction method can be applied to the entirety of a hoof capsule. A 3D model with specific stiffness properties for a particular horse can be analyzed and a 3D printed, custom horseshoe can be designed and manufactured. This concept will be tested in a clinical trial for validation. The method developed in this study will provide an easy, non-invasive, cost-effective method for farriers and horse owners to gain vital information about a specific horse that will guide shoeing practices in an animal-specific way.

CHAPTER 3

METHODOLOGIES

3.1 Introduction

This chapter presents the specimen preparation methods and testing techniques used in this research. Healthy hoof capsules used in this study were ethically sourced from horses (no ponies were used), who died for reasons other than this research. These horses ranged from 4 to 29 years in age, were of varying breeds (Tennessee Walking Horse, American Quarter Horse, Thoroughbred, Oldenburg). Feet were harvested within 4 hours after death and stored at 4 ºC in air-locked bags until sample preparation was undertaken. The hooves used during this research had a variety of keratin pigmentation, the spectrum ranging from light to darkly pigmented keratin, and many even had a mixture of dark and light keratin. During specimen fabrication and subsequent testing, several parameters were recorded, including but not limited to type of horse, fore- vs. hind-limb, keratin color, tubule distribution and growth angle, hoof capsule sample location, and hoof sampling depth.

3.2 Keratin Hydration

Thin specimens were manufactured to observe the general dehydration trend of various regions in the hoof wall. Hoof capsules were first cut proximodistally into sections 1-2 inches wide using a bandsaw. These hoof sections were secured in a wooden sleeve to orient the sample's outer hoof surface square to a flat surface (Figure 3.1). A tabletop mill (Sherline, Vista, CA, USA) with end mill was used to level the coronary band with the SE surface. Next, a slitting saw attachment was used to slice thin keratin samples (Figure 3.1) from the SE, SM, and SI of the hoof wall.

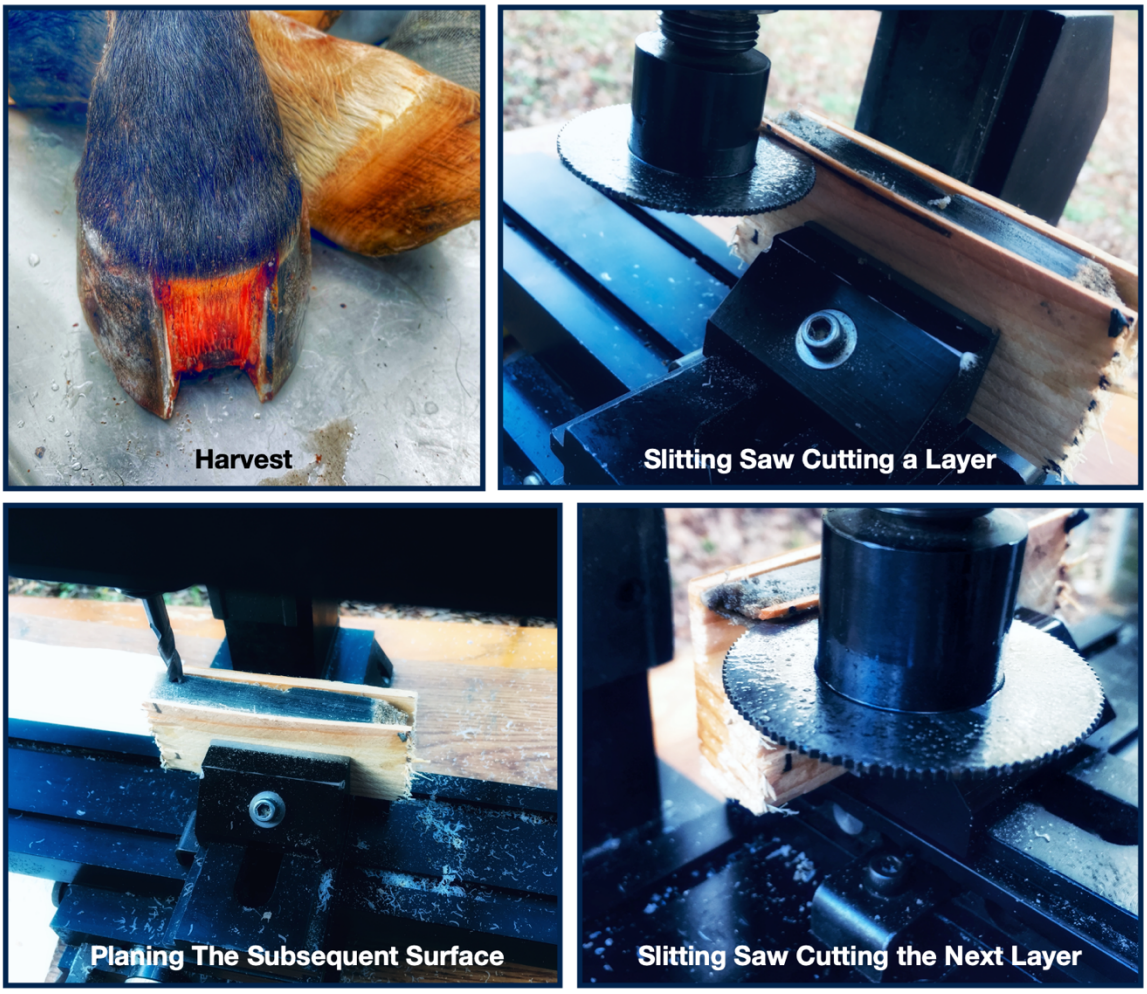

Figure 3.1 Fabrication Process for Keratin Dehydration Specimens

Cutting speeds were kept low, and no water lubricant was used in order to avoid heated liquids that would yield hide glue and/or scorched or burned keratin. Final geometry specifications for the dehydration samples were approximately 20 mm wide, 50 mm long, and 0.5 mm thick (Figure 3.2). Final dimensions for each sample were measured with calipers.

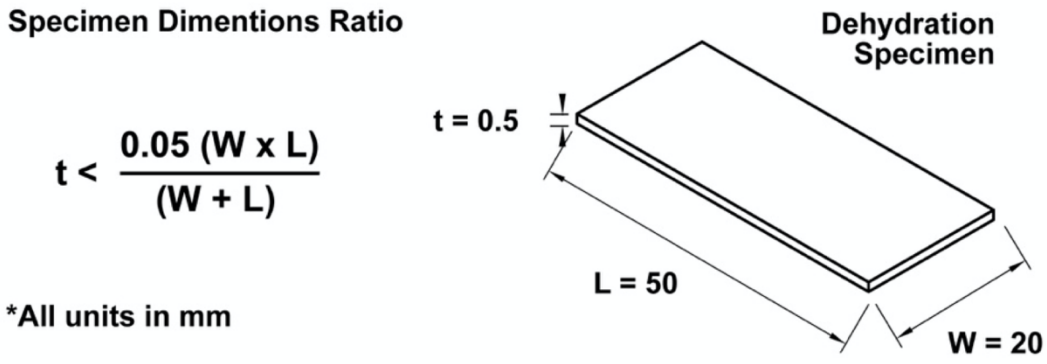

Figure 3.2 Geometry of Keratin Dehydration Specimens

Keratin specimens were hydrated in distilled water in a cold environment at ~3 ºC for a minimum of 72 hours prior to testing. Specimens were removed from the cold and allowed to equilibrate to ambient conditions (~21-23 ºC) in the distilled water for 24 hours. The weights of the hydrated specimens were then measured using a high precision electronic balance scale (Ohaus Pioneer, Ohaus Corp., Parsippany, NJ, USA), which read to the nearest 0.0001 g.

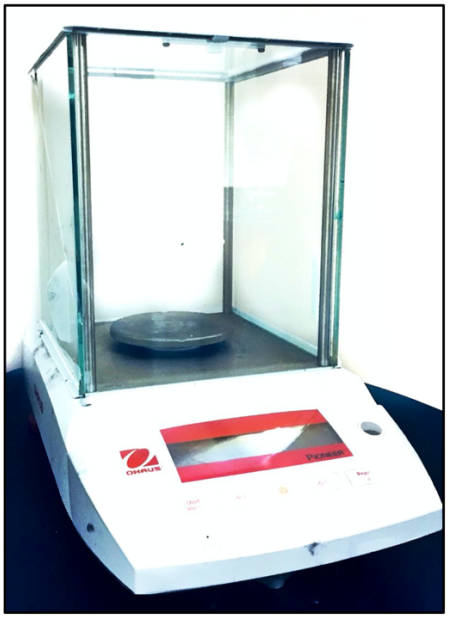

Figure 3.3 Ohaus Pioneer High Precision Electronic Balance Scale

The ambient laboratory temperature and humidity were determined using a hygrometer and thermometer (ThermoPro, Atlanta, GA, USA), respectively, which have uncertainties of +/-1 ºF and +/-2% RH. Each keratin specimen was then allowed to dehydrate naturally, and the time, specimen weight, and ambient temperature and RH were measured until the specimen hydration normalized to match the ambient RH. Afterwards, each sample was placed in a small oven heated to 80 ºC for 7 days until the keratin reached approximately 0% RH, at which point the final dry specimen weight was measured.

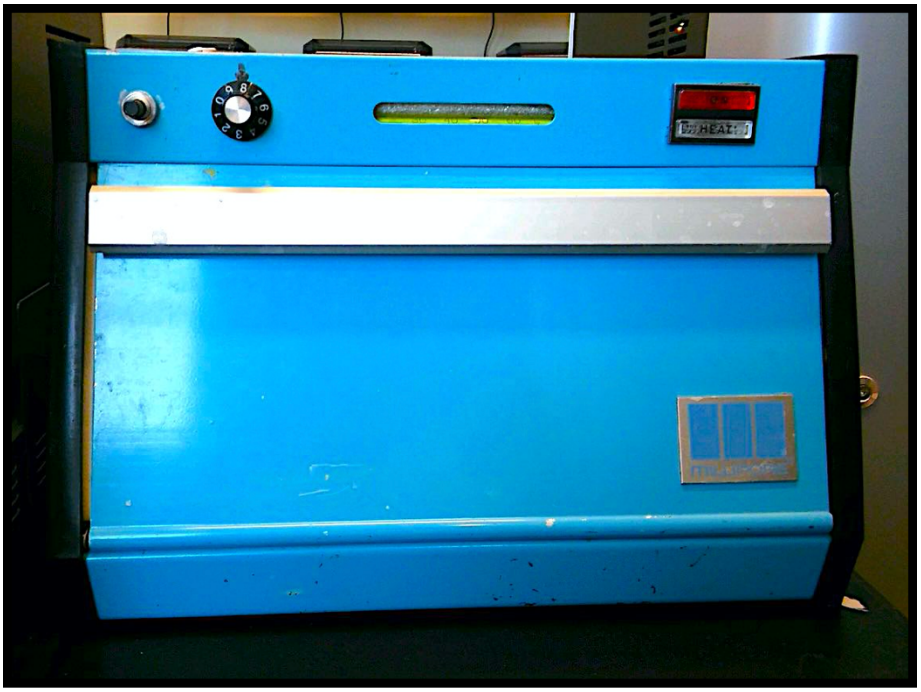

Figure 3.4 Millipore Lab Oven (Temperature Range 30-60 ºC)

Using the data obtained during the dehydration tests, specimen moisture concentration versus time curves were generated for keratin samples taken from the SE, SM, and SI regions of the hoof wall. To accomplish this, the following equation was used:

(Eq. 3.1) $$m(t) = M(t) - M_{dry}$$

Where m(t) is the water mass present in the specimen, M(t) is the time dependent mass of the specimen, and M_{dry} is the dry mass of the specimen after oven dehydration. The moisture concentration was calculated to eliminate minor variations in specimen volume:

(Eq. 3.2) $$C = \frac{m(t)}{V}$$

Where C is the moisture concentration, m(t) is the water mass present in the specimen at a specific time, and V is the specimen volume.

3.3 Uniaxial Tensile Testing Local Keratin Regions

3.3.1 Local Keratin Proximodistal Specimen Fabrication

Hoof capsules were first cut proximodistally into sections 1-2 inches wide using a bandsaw. These hoof sections were secured in a wooden sleeve to orient the sample's outer hoof surface parallel to a flat surface (Figure 3.5). A tabletop mill (Sherline, Vista, CA, USA) with square end mill was used to level the coronary band with the SE surface, and to cut the boundary lengths of each small specimen. This method ensured parallel edges for long, thin samples of testable keratin in both the proximodistal and mediolateral boundary cuts, respectively. Next, a slitting saw attachment was used to slice the long and slender keratin samples (Figure 3.5) from the SE, SM, and SI of the hoof wall. Finally, the new surface was planed and the previous steps were repeated until the available hoof material was exhausted.

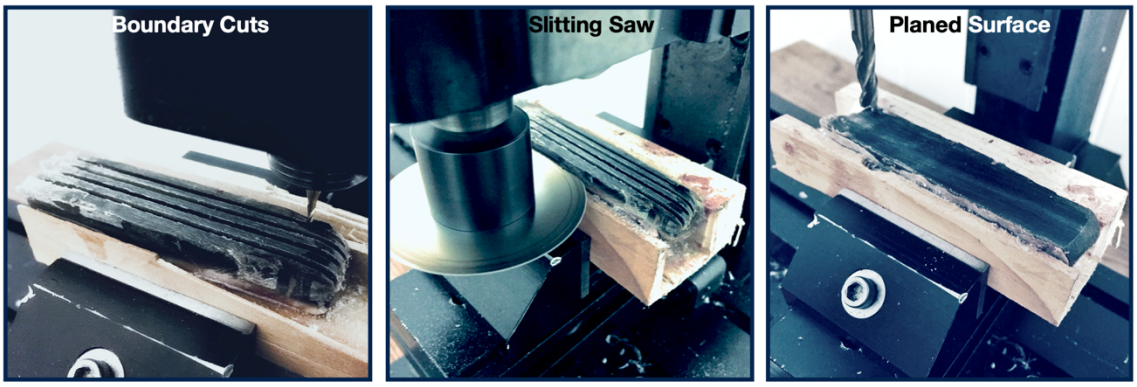

Figure 3.5 Fabrication Process for Local Keratin Proximodistal Specimens

Cutting speeds were kept low, and no water lubricant was used in order to avoid heated liquids that would yield hide glue and/or burned keratin. Lastly, specimen surfaces were carefully polished with progressively finer files and then cleaned to remove any small surface flaws or irregularities that may affect tensile testing. Proximodistally oriented specimens had a final geometry of approximately 40 mm in length and a cross-sectional area of 2 mm^2, as shown in Figure 3.6. Some variation in specimen length was seen across horses due to the limitations of source material (hoof size variation).

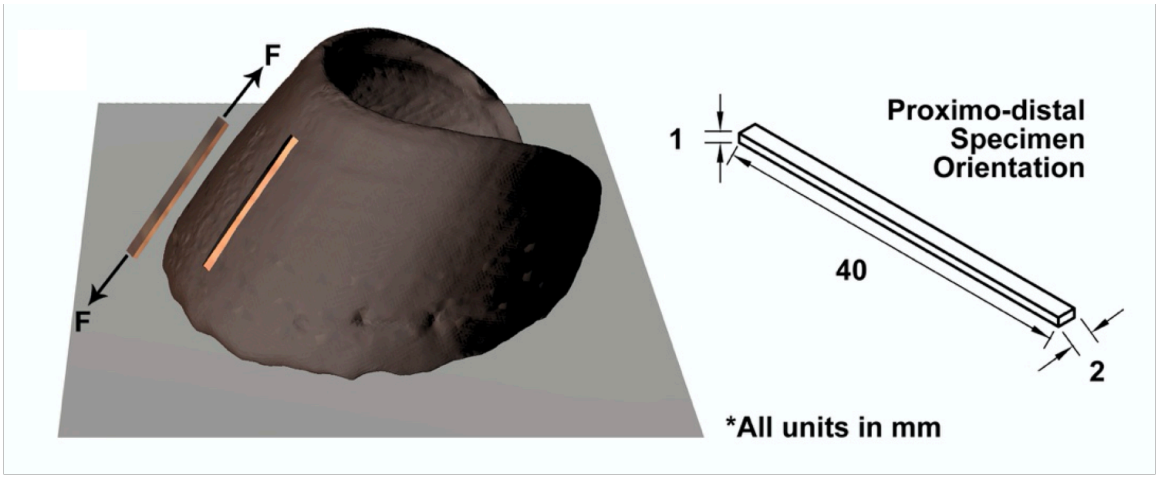

Figure 3.6 Geometry of Local Keratin Proximodistal Tensile Specimens

3.3.2 Local Keratin Mediolateral Specimen Fabrication

The hoof capsules were again cut proximodistally into sections 1-2 inches wide using a bandsaw. These hoof sections were secured in a wooden sleeve to orient the sample's outer hoof surface parallel to a flat surface. Similar to the proximodistal specimens, a tabletop mill (Sherline, Vista, CA, USA) with square end mill was used to level the coronary band with the SE surface and cut the boundary lengths of each small specimen, as illustrated in Figure 3.7. Next, a slitting saw attachment was used to slice the short and slender keratin samples from the SE, SM, and SI of the hoof wall. The new surface was then planed, and the small specimen boundaries cut again at the new depth. This was repeated until all the keratin material was used.

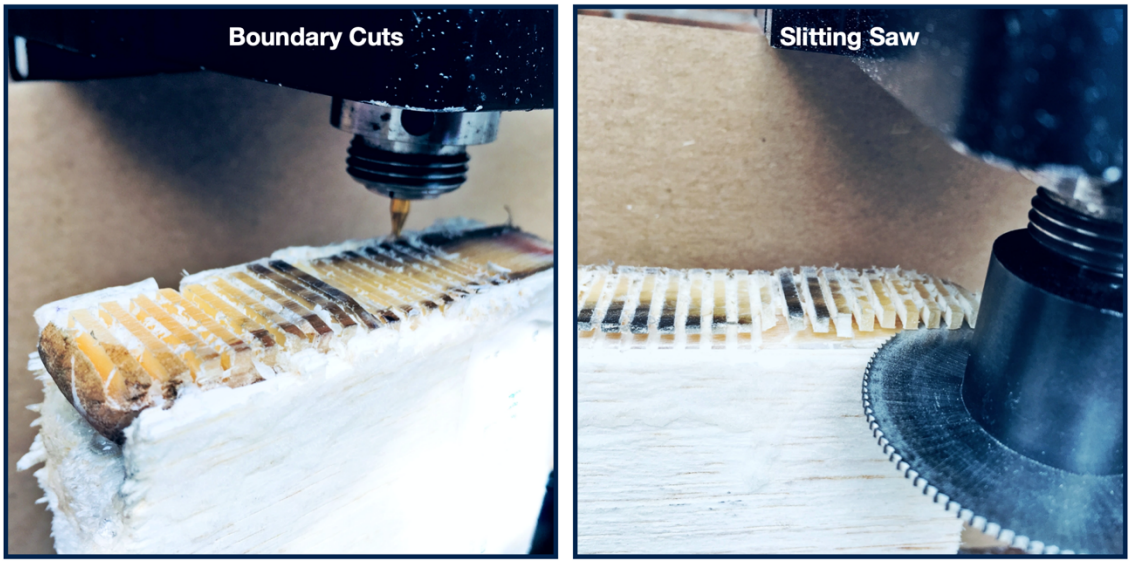

Figure 3.7 Fabrication Process for Local Keratin Proximodistal Specimens

The keratin specimen surfaces were polished with progressively finer files and then cleaned to remove any small surface flaws or irregularities that may affect tensile testing. Mediolaterally oriented specimens had a final geometry of approximately 20 mm in length and a cross-sectional area of 2 mm^2, as shown in Figure 3.8. Mediolateral specimens were

shorter than the proximodistal counterparts due to the length restrictions imposed by the curvature of the hoof capsule.

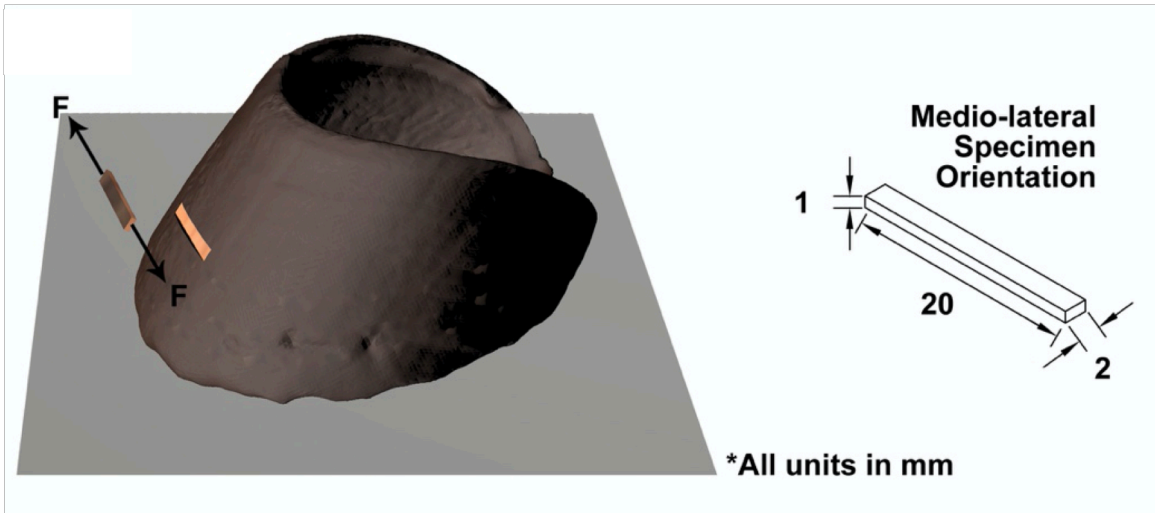

Figure 3.8 Geometry of Local Keratin Proximodistal Tensile Specimens

3.3.3 Tensile Testing Equipment

Before tensile testing commenced, specimen dimensions were measured with precision calipers (iGAGING OriginCal, San Clemente, CA, USA) and recorded. Stress-strain tensile tests were performed on a Wisdom Technology MT-200 tension/torsion micro-tester (Wisdom Technology, Canton, MI, USA), pictured in Figure 3.9. This tabletop instrument is optimized for loading small specimens, making it an ideal choice for such small and slender local equine keratin samples. The tensile tests were strain (stroke) controlled so the keratin stress responses could be compared for different equine physical activities. The instrument's axial displacement resolution of 0.1 micron is quite sufficient for this purpose. Roughened grip sections were used to avoid specimen slippage. The variables measured in the uniaxial tensile tests were the uniaxial force, F, time, t, and the measured crosshead displacement, δ. Ultimate tensile strength data were only collected from specimens that failed near the center of the gage length, away from the grips.

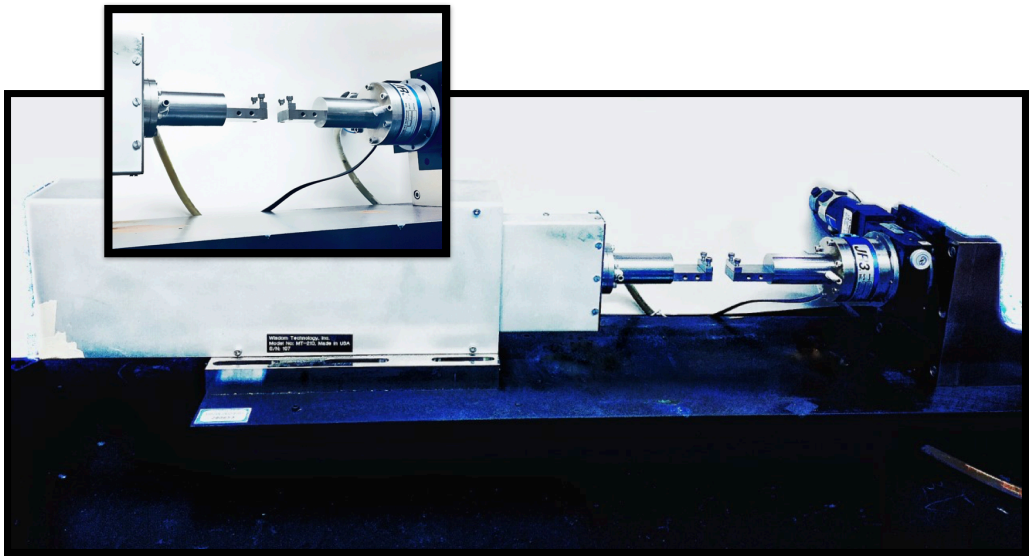

Figure 3.9 Wisdom Technology MT-200 Tension/Torsion Micro-tester

3.3.4 With Respect to Hydration

To quantify how the elastic modulus E changes with respect to its moisture content, an equine keratin specimen was fully hydrated in distilled water, tested at 100 %RH, and then tested systematically as the specimen naturally dehydrated in the ambient laboratory conditions. Tension was applied to the specimen such that the sample was never extended beyond the elastic region, allowing for multiple E measurements to be taken from the same specimen. The first fully hydrated test was performed with the specimen submerged in a bath of distilled water once both the specimen and water had equilibrated to the ambient conditions. The supplemental 3D printed plastic hydration chamber is pictured in Figure 3.10.

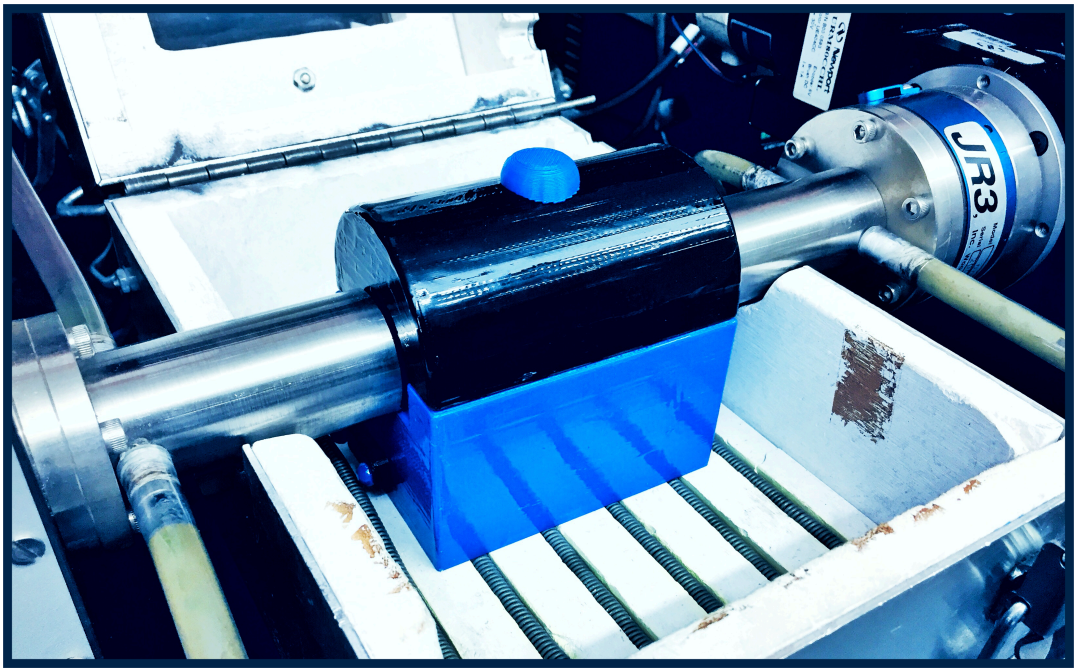

(a)

(b)

Figure 3.10 Distilled Water Bath Chamber (a) Assembled Onto the Tension Tester, and (b) Testing a Keratin Specimen at 100%RH Without the Lid

The weight of the specimen was measured and recorded at 100%RH, and then again directly before all subsequent tests at decreasing levels of hydration. Afterwards, the specimen was oven-dried, weighed at 0%RH, and finally tensile tested to failure at 0%RH. The hydration level was calculated using the following formula:

(Eq. 3.3) $$\%H_20 = (\frac{M(t)-M_{dry}}{M_{wet}}) \cdot 100$$

Where M(t) is the weight of the specimen at the time of testing, M_{dry} is the fully dehydrated weight of the specimen, and M_{wet} is the fully hydrated weight of the specimen.

The applied stress for any tensile loading was determined from the collected force data using the classic equation:

(Eq. 3.4) $$\sigma = \frac{F}{A}$$

Where $\boldsymbol{\sigma}$ is stress, F is the applied load, and A is the cross-sectional area of the local keratin specimen. As the tubule structures are, in essence, hollow straws, they would not contribute to the cross-sectional area resisting the load applied to the specimen. Individual tubules have an approximate diameter of 200 μm [20]. Hence, it stands to reason that the greater the local tubule population, the less surface exists to apply the loading upon for the same overall cross-sectional region. Therefore, an adjusted cross-sectional area, $A_{effective}$, must be determined for each specimen undergoing tensile testing:

(Eq. 3.5) $$A_{effective} = A - N_{tubule}(\frac{\pi}{4} D_{tubule}^2)$$

Where N_{tubule} is the number of tubules present in the specimen, and D_{tubule} is the approximate diameter of the circular tubule mouth. The equation used to calculate the stress response of proximodistal specimens throughout this study becomes:

(Eq.3.6) $$\sigma = \frac{F}{A_{effective}}$$

The axial strain was determined using the collected displacement data using the following equation:

(Eq. 3.7) $$\varepsilon = \frac{\Delta L}{L} = \frac{\delta}{L}$$

Where, ε is the uniaxial strain, L is the initial specimen gage length, and δ is the measured crosshead displacement.

The proximodistal specimen testing regime was repeated for three different strain rates: 10^2 s^{-1}, 10^3 s^{-1}, and 10^4 s^{-1}. After the specimen was tested to failure, the TD was observed and quantified. The TD measurements were conducted in the manner established in Section 3.5 and tracked throughout the study.

3.3.5 With Respect to Tubule Direction

The entire testing regime presented in Section 3.3.3 was repeated for the local keratin specimens of mediolateral orientation. The mediolateral specimen preparation process can be found in Section 3.3.2.

3.3.6 With Respect to Temperature

The effect of temperature on the stiffness of equine keratin was achieved using local proximodistal keratin samples fabricated via the process described in Section 3.3.1. All tensile tests were performed on keratin specimens with 100% RH, and so specimens were tested while submerged in a bath of distilled water (Figure 3.10) to achieve true, fully saturated results. Testing the keratin specimens at different temperatures was completed via the use of either heated or chilled distilled water. In the case of colder temperature testing, the supplemental hydration chamber walls and top were filled with distilled water and frozen in order to maintain the cold temperature of the bath throughout the tension test. The temperature of the specimens was measured and recorded during testing using a K-

type thermocouple (uncertainty: +/-2.2 ºC) (Omega Engineering, Norwalk, CT, USA) gently applied directly to the surface of the submerged keratin.

Figure 3.11 Omega Engineering K-type Thermocouple with Uncertainty of +/-2.2 ºC

3.3.7 Typical Testing Data for Local Equine Keratin Samples

A typical stress-strain curve is represented in Figure 3.12. The material response is elastomeric in nature, as indicated by the stress-strain curve shape. A hyperbolic tangent curve fit paired with an exponential growth term was used to model each stress strain curve:

(Eq. 3.8) $$\sigma = atanh(b\epsilon) + ctanh(d\epsilon) + f\epsilon + ge^{h\epsilon}$$

Where $\boldsymbol{\sigma}$ represents the stress term, $\boldsymbol{\epsilon}$ represents the strain term, and a, b, c, d, g, and h are coefficients supporting the curve fit. The elastic moduli were calculated using the following method:

(Eq. 3.9) $$E = ab + cd + f$$

Where a, b, c, d, and f are coefficients from the viscoelastic curve fit (Eq. 3.8).

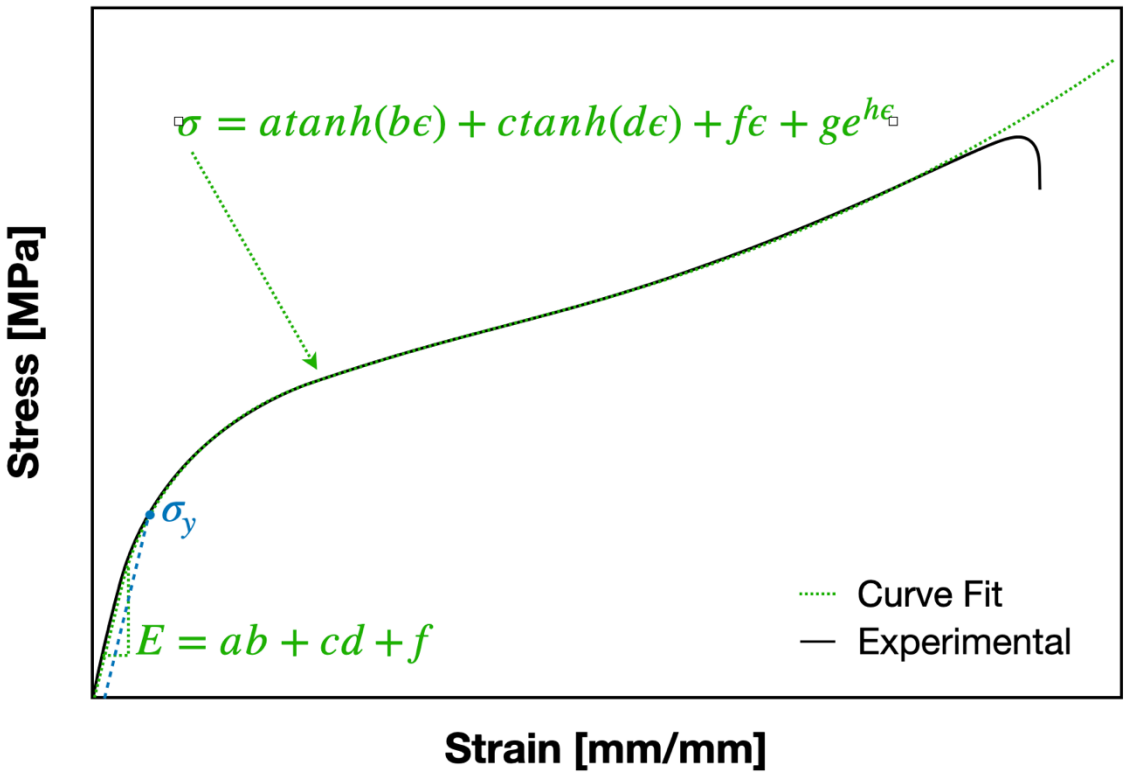

Figure 3.12 Typical Tensile Curve of Local Equine Keratin

3.3.8 Statistical Analysis

Standard deviation was difficult to obtain due to the complex, multi-variable nature of the study. There are limited comparable individual tests, as any comparison made has a minimum of three controlled variables (i.e. temperature, TD, strain rate, etc.), even with fluctuation of the %RH eliminated. This means that obtaining any meaningful standard deviation of "test batches" becomes very difficult. The published literature already offers a number of comparable individual tests which provide an understanding of standard batch variation [11] [16] [17] [29] [28] [30] [32] [33] [34] and is beyond the intended scope of

this study. Rather, the approach taken by this study is to describe the relationship between the variables under observation via best fit curves.

Curve fitting was used to describe the trends seen in the testing results. Statistical analysis of these curve fits are the primary focus and were obtained using the program CurveExpert Professional, version 2.6.5 (Hyams Development) [84]. Typical reported statistics were the standard error (s.e.) of the fit, and the coefficient of determination (r^2) to demonstrate the fit quality.

3.4 Tension and Compression Testing Bulk Hoof Wall Sections

3.4.1 Bulk Tensile Specimen Fabrication

Larger specimens were necessary to quantify the global stiffness of the equine hoof wall (i.e. specimens that spanned the SE, SM, and SI of the full wall thickness). Once the hoof capsule was separated from the leg, it was sectioned into several strips (~1 inch wide) along the proximodistal direction using a bandsaw. Strips were paired together by proximity and the region of the hoof capsule from whence they came. One of each pair was dedicated to analyzing the tubule density distribution (see Section 3.5), while the other was machined into a tensile specimen.

The equine keratin strip designated for tensile testing underwent further machining to the approximate specimen dimensions shown in Figure 3.13. Due to the variation in hoof wall geometry between animals, and even between legs on the same horse, the specimen dimensions may vary from the ideal.

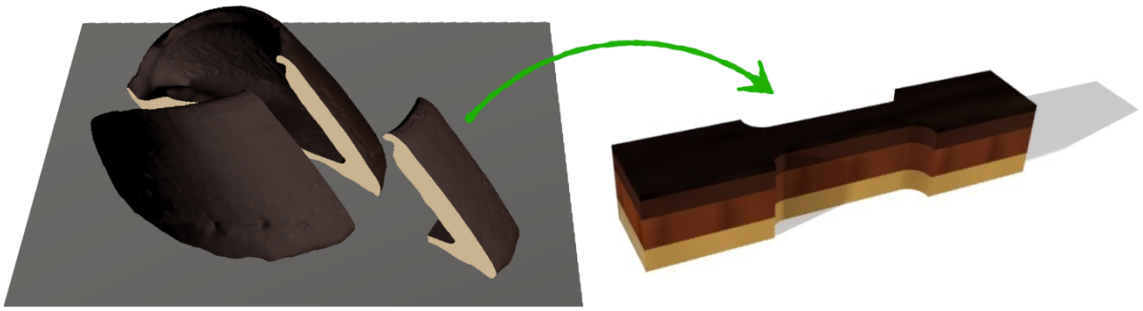

(a)

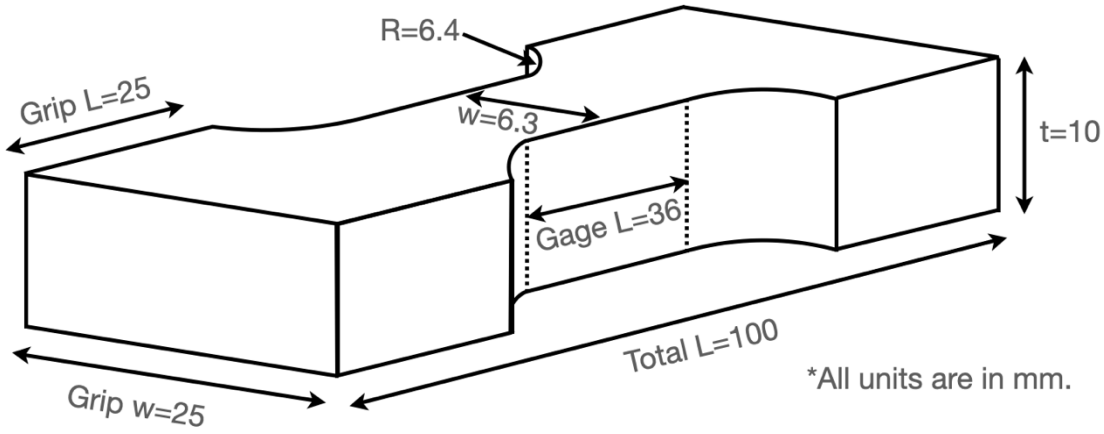

(b)

Figure 3.13 Bulk Keratin Specimen (a) CAD Rendering and (b) Ideal Geometry

A tabletop mill (Sherline, Vista, CA, USA) with square end mill was utilized to cut a uniform gage section (~6.5mm thick and ~30mm long) and smooth transition into the grip sections (Step 3 in Figure 3.14). The hoof wall surfaces (SE and SI) were left raw to preserve the surface effects that would naturally occur in the field.

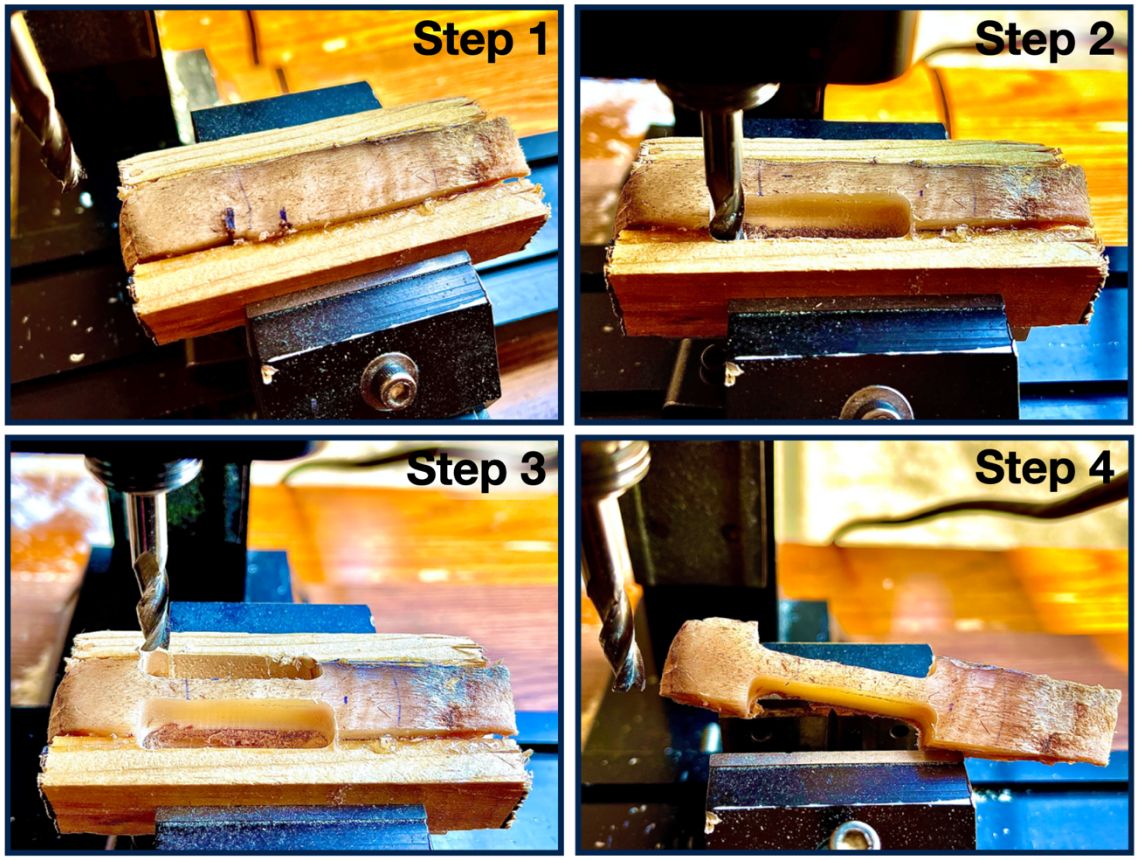

Figure 3.14 Bulk Keratin Specimen Fabrication Process

3.4.2 Tensile Testing Equipment and Procedure

Strain controlled tensile tests were performed on the bulk equine keratin specimens using an Instron Universal Testing Instrument (Model 5982, Instron, Illinois Tool Works Inc., Norwood, MA, USA) with dual column floor frames and a 100 kN capacity load cell. This freestanding instrument is optimized for loading standard to large specimens, making it an ideal choice for the bulk equine keratin specimens. The tensile tests were strain (stroke) controlled with a rate of 10^{-3} s^{-1} so the bulk keratin stress responses could be compared and correlated to the smaller, local keratin properties (see Section 3.3). Roughened grip sections were used to avoid specimen slippage in the flat, textured grips. The variables measured in the uniaxial tensile tests were the uniaxial force, F, time, t, and

the measured crosshead displacement, δ. Ultimate tensile strength data were only collected from specimens that failed near the center of the gage length, away from the grips.

Figure 3.15 Instron Universal Testing Instrument (Model 5982)

Prior to each tensile test, specimen dimensions were measured with precision calipers (iGAGING OriginCal, San Clemente, CA, USA) and recorded.

For the purposes of this study, the state of hydration of the keratin specimen at the time of testing was imperative to know. In order to control this time-dependent variable, specimens were soaked in distilled water (~3ºC) for 72 hours until the fully hydrated state (100%RH) was reached. The soaking specimen was removed from the cold conditions,

and the bath was allowed to equilibrate to ambient conditions for 24 hours. Finally, the specimen was removed from the bath and allowed to naturally dehydrate in the lab for a set time (15 minutes, 60 minutes, 5 hours, or 24 hours). During this process, the specimen weight was continuously measured, beginning at 100%RH and systematically throughout the timed dehydration window. At the time of testing, the specimen was loaded into the tensile machine and was pulled to failure. Directly after the specimen fractured, the weight was measured again so the dehydration during the actual testing period could be later determined. Finally, the specimen weight was measured periodically until the specimen hydration state equilibrated to the ambient humidity, after which the specimen was placed in a small oven (heated to 80 °C for 7 days) until 0%RH was achieved. Once the final, dry weight of the bulk specimen was known, the timeline of the decreasing %RH could be calculated using Equation 3.3.

The bulk wall tensile properties obtained from the tension test could then be matched with the testing conditions (specimen %RH and temperature). The ambient laboratory temperature and humidity were determined using a hygrometer and thermometer (ThermoPro, Atlanta, GA, USA), respectively, which have uncertainties of +/-1 ºF and +/-2% RH. The specimen temperature was measured and recorded during testing using a K-type thermocouple (uncertainty: +/-2.2 ºC) (Omega Engineering, Norwalk, CT, USA) gently applied directly to the surface of the bulk keratin specimen. Through this method, the approximate %RH and temperature of the equine specimen is known at the time of tensile testing, and the bulk wall stiffness can be correlated to the tensile properties of the local regions in the hoof wall (SE, SM, and SI).

Compression tests were conducted on a limited number of specimens. The fabrication method, equipment, and procedure are the same as with the tension tests, the only different being the testing direction.

3.4.3 Typical Testing Data for Bulk Equine Keratin Specimens

The data trend for the bulk keratin tension tests are similar to the viscoelastic tensile curves presented in Section 3.3.7. The same data analysis and curve fitting method was utilized as well (Eq.s 3.8 and 3.9).

3.5 Tubule Density Distribution

The tubule density (TD) distribution was quantified for several parts of this study, including the local tensile tests, bulk wall tensile tests, and several samples unrelated to mechanical testing that contributed to the correlation between TD and keratin pigmentation. Due to the important link between TD and stiffness, an aim of this study was to develop a simple and economical method of determining the TD distribution that would make this animal-specific information more accessible to farriers in the field and/or the average horse owner.

3.5.1 Tubule Density Distribution Measurement Equipment and Method

Each equine keratin strip designated exclusively for TD measurement (and not mechanical testing) were cut in half orthogonal to the tubule direction of growth. After the testing and weighing of the tensile specimens concluded, the TD distribution was measured and recorded. The area of interest on the dry tensile specimen was trimmed flat orthogonal to the tubule growth direction. The surface was then polished with progressively finer sandpaper and subsequently submerged in pigmented water. The cut surface was then polished with progressively finer grits until the tubule diameters were revealed. Finally,

the specimen was soaked in water mixed with gentian purple ink (as per the procedure explained in Section 3.5), which resulted in a high contrast between the tubule hollows/walls and the interstitial material.

The sample was examined and photographed at 30x magnification using light microscopy (Meiji Techno, San Jose, CA, USA), and the tubules were counted via a combination of Reilly et al's methods [18] [85]. The only difference in method was a millimeter grid that curved along the subtle arch of the hoof capsule wall, allowing for a more accurate measurement of TD at a particular point in the wall. The TD describes the number of tubules per square millimeter, which was plotted against each location's "percent distance" from the outer surface of the hoof wall (Figure 3.16). The color of each data point represents the pigmentation of the hoof keratin. The overlayed purple data points and dashed lines represent the average TD at a specific point within the hoof wall.

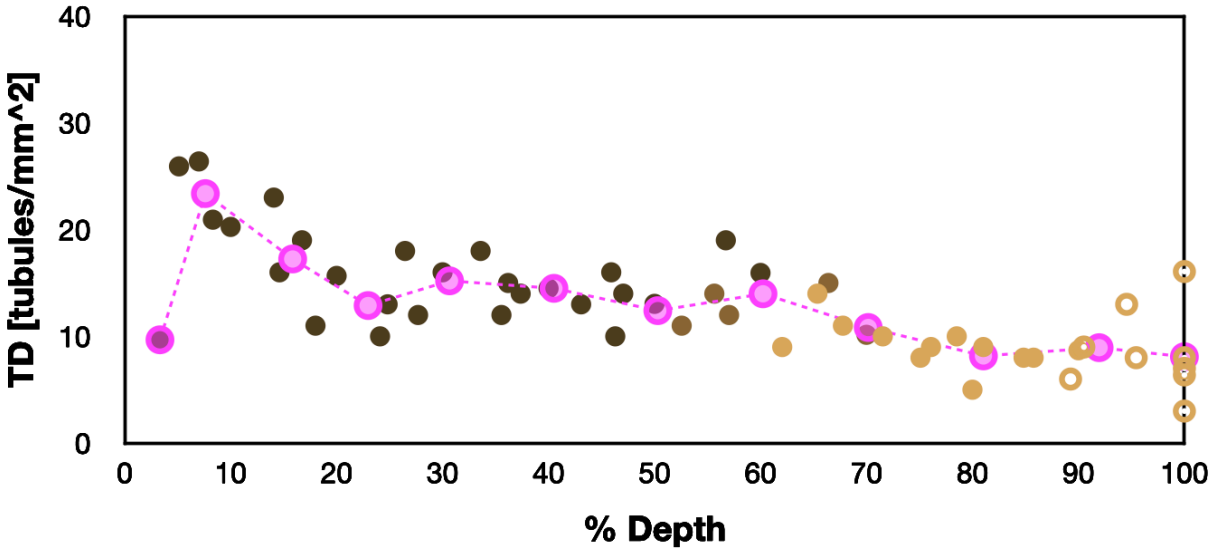

Figure 3.16 Typical Color-coded Tubule Density Distribution Profile

3.5.2 Typical Tubule Density Data for Equine Keratin

After testing and weighing were concluded, the TD distribution was measured and recorded for each mechanically tested specimen. The area of interest on the dry specimen was trimmed flat and polished with progressively finer sandpaper and subsequently submerged in pigmented water. The medullae around the tubule absorbed more pigmented liquid than the intertubular material, and the hollow tubule channels held more pigment than its surrounding medulla. Dark keratin was soaked in white artist's gouache (Horadam Schminke & Co., Erkrath, Germany) pigmented water, and light and mixed keratin was soaked in gentian purple diluted sheening ink (Vinta Inks). Utilizing light microscopy (Meiji Techno, San Jose, CA, USA), the pigmented tubules were clearly contrasted against the surrounding material and easily countable. This layman's method for TD determination is a cost-effective alternative to the more traditional, time intensive histological staining. Figure 3.17 provides some examples of the pigmented sample surfaces and the typical level of contrast achieved.

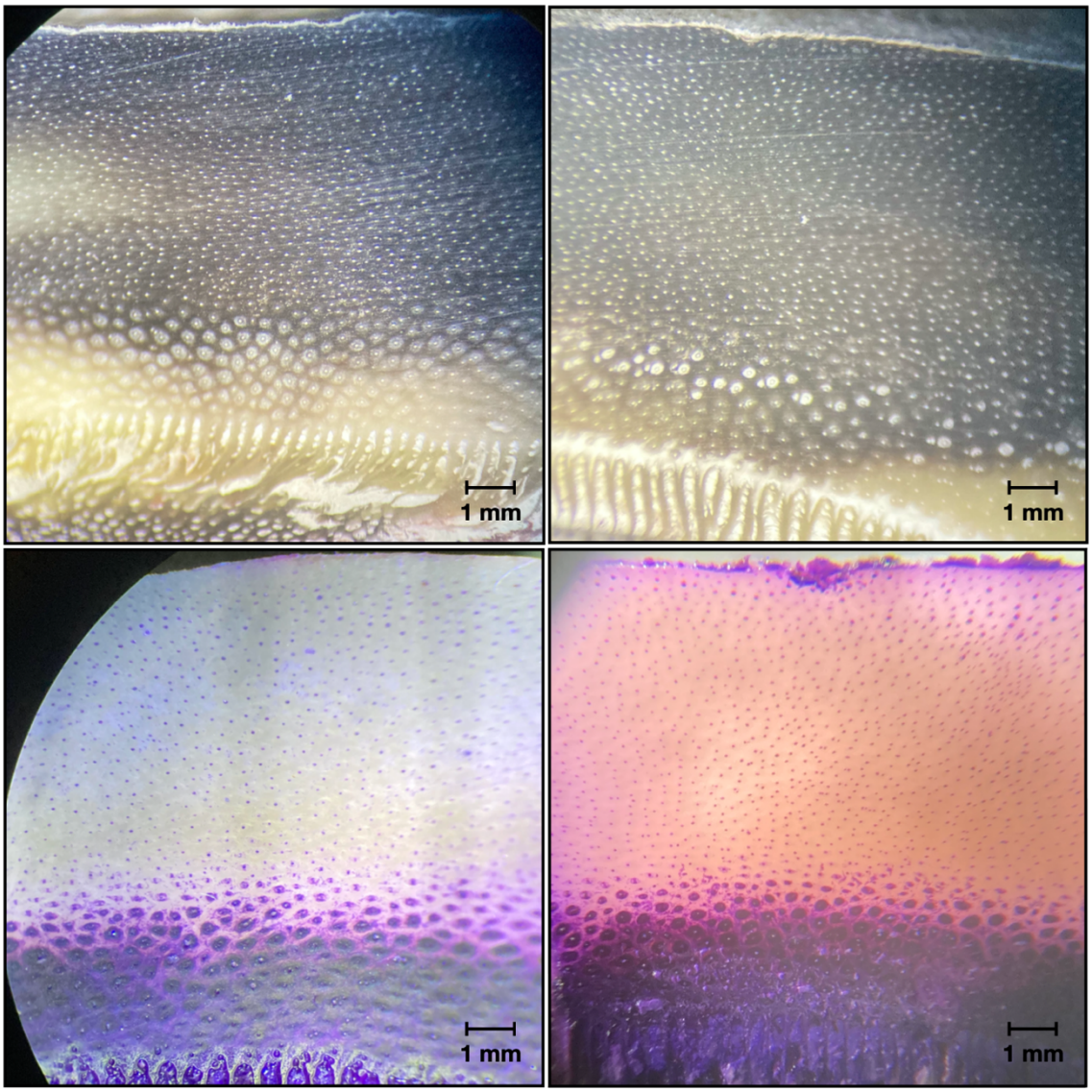

Figure 3.17 Equine Keratin Specimens Prepared for Tubule Counting

As the slender tensile specimens already had nearly constant TD across the entire specimen, the tubules were counted and divided by the entire area for the literature-standard TD units of tubules/mm^2. Larger specimens of the hoof wall spanning all three SE, SM, and SI regions were also cut, polished, and inked in the same manner to gather TD distribution data. This study followed a tubule counting method similar to the one

developed in the study by Reilly et al. [18], and these data were used to correlate mechanical properties to different regions of the hoof wall.

3.6 Tension Testing Additive ABS Specimens

The stiffness of additively manufactured Acrylonitrile Butadiene Styrene (ABS) was determined for a range of infill patterns and densities in an effort to determine which pattern(s) would yield favorable properties for 3D printing a horseshoe. Additionally, the tensile properties of two print orientations were explored in order to account for three-dimensional loading in the final horseshoe orthotic design process.

3.6.1 ABS Tensile Specimen Fabrication

Specimens were designed to meet ASTM standard D638-14, the Standard Test Method for Tensile Properties of Plastics [86]. The specimen geometry is displayed in Figure 3.18. The specimen was digitally modeled using a Computer Aided Design (CAD) program called Fusion 360 (Autodesk Inc., San Raphael, CA, USA) and subsequently exported as a standard .stl file.

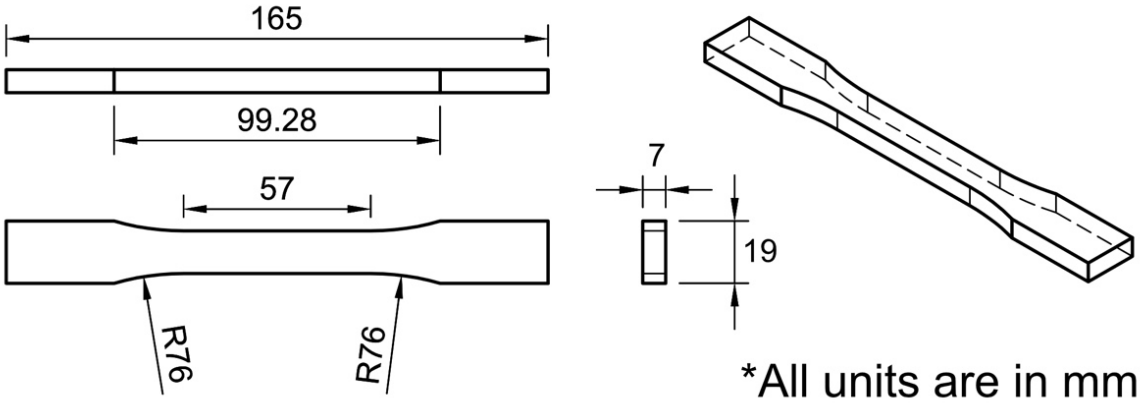

(a)

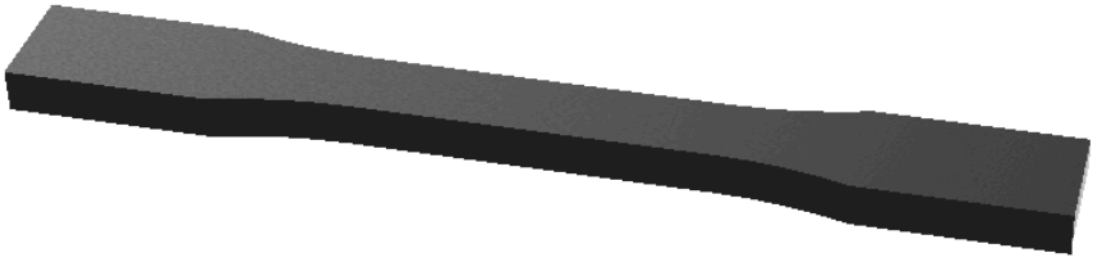

(b)

Figure 3.18 3D Printed ABS Tensile Specimen (a) Dimensions, and (b) CAD Model

The .stl file was imported into an additive manufacturing preparation program called GrabCAD Print (Version 1.56.11.9996, Stratasys Ltd.), which generates the g-code to direct the extruder travel path layer by layer. The automated "slice program" print settings utilized are displayed in Table 3.1.

Table 3.1 Print Settings for ABS Tensile Specimens

Tray Setting	Setting Selection
Model Material	F123 ABS
Slice Height	0.0111 in | T14
Slice Style	Constant
Support Material	F123 QSR Support
Support Tip	T14
Part Build Style	Normal
Purge Part Type	Full Height
System Mode	Normal
First Layer Material	Support

The 3D printer utilized for specimen fabrication was a Stratasys F370 Precision 3D Printer (Stratasys Inc., Eden Prairie, MN, USA), which has a maximum build space of 10 in x 10 in x 10 in. The ABS filament and QSR Support material was purchased from the same company (Stratasys Inc., Eden Prairie, MN, USA).

Figure 3.19 Stratasys F370 Precision 3D Printer

Specimens were printed with a range of infill patterns and density, which are listed in Table 3.2. Density ranges per infill pattern were limited in selection due to the automated settings of the GrabCAD Print program. Two print orientations were explored for each type of specimen: the x-plane orientation and y-plane orientation. The z-plane orientation was not included in this study as the print direction would not be desirable for the ultimate end goal of additively manufacturing a horseshoe (due to the loading direction applied when installed on the hoof).

Table 3.2 Infill Patter and Density Setting for ABS Tensile Specimens

Infill Pattern Type	Set Pattern Densities	Body Thickness	Support Angle
Sparse	17%, 25%, 35%, 50%	0.06 in	45º
Sparse—Double Dense	50%, 60%, 70%, 80%	0.06 in	45º
Hexagram	46%, 50%, 60%	0.06 in	45º
Solid	100%	0.02 in	45º

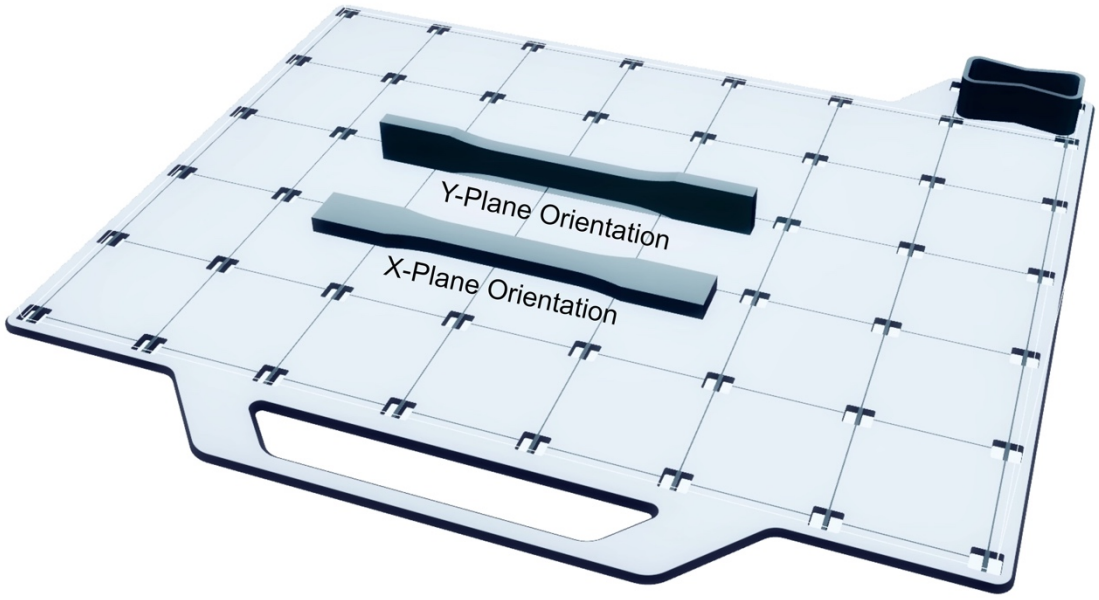

Figure 3.20 Print Orientations of ABS Tensile Specimens.

3.6.2 Tensile Testing Equipment and Procedure

Prior to testing, specimen dimensions were measured using precision calipers (iGAGING OriginCal, San Clemente, CA, USA), and the mass was determined using a a high precision electronic balance scale (Ohaus Pioneer, Ohaus Corp., Parsippany, NJ, USA), which read to the nearest 0.0001 g. Once the geometric measurements were recorded, the specimen was then tested to failure. The strain (stroke) controlled tension testing of additively manufactured ABS was conducted using an Instron Universal Testing Instrument, the same equipment described in Section 3.4.2. The testing rate was 10^{-3} s^{-1}. The variables measured in the uniaxial tensile tests were the uniaxial force, F, time, t, and the measured crosshead displacement, δ.

3.6.3 Typical Testing Data and Analysis

Stress and strain responses were calculated using the same method and equations presented in Section 3.3.7. As each testing condition was repeated three times, a best fit curve was applied to all three tensile data sets to obtain a representative stress-strain curve. Figure 3.21 presents a typical data set of this nature. These average representative stress-strain curves were compared with each other for analysis and were used to extract various mechanical properties for each condition.

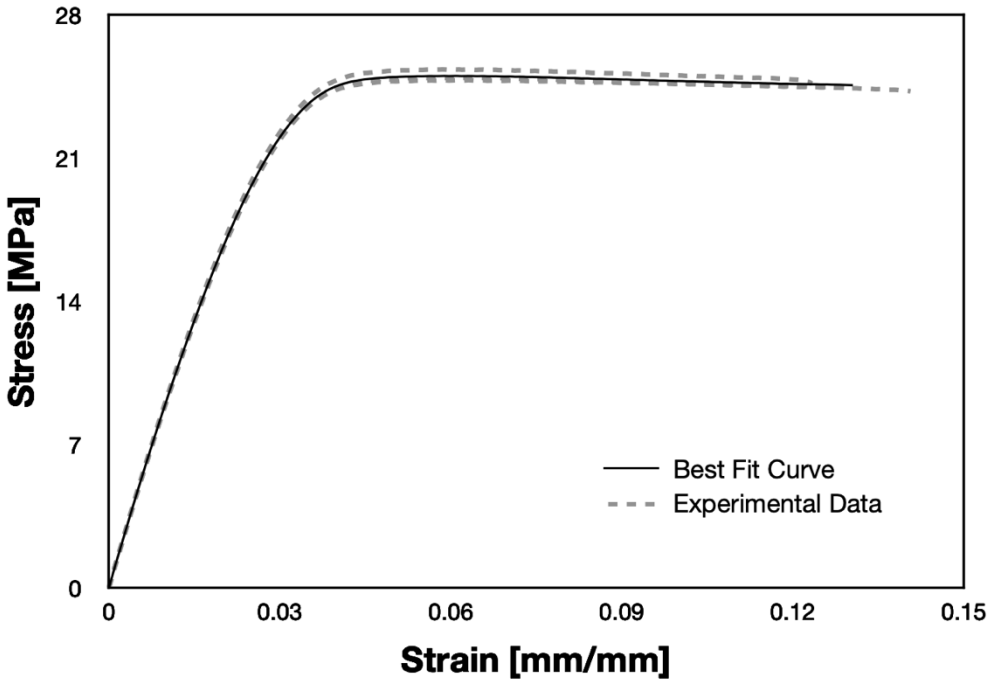

Figure 3.21 Representative Tensile Data of Additively Manufactured ABS.

Density represents the relationship between mass and the volume it occupies. As the 3D printed specimens had different types and amounts of infill for the same theoretical volume, it is sensible to compare the tensile properties to the specimen density. The volume of the as-designed specimens was 18362.3 mm^3 and was obtained via the modeling software. The physical as-build specimen density was calculated using the following equation:

(Eq. 3.10) $$\rho_{calc} = \frac{m}{V}$$

Where ρ is the calculated specimen density, m is mass, and V is the special volume.

3.7 Tension Testing Formahoof Advanced Polymer Specimens

Formahoof Advanced Polymer is a glue-like substance that is used to encase the hoof in a protective polymer with flex and wear properties meant to be comfortable for the

horse. The material is stored as two separate materials in parallel tubes and is only mixed directly before application in a process similar to many epoxies. The stiffness of the Formahoof material was determined for a number of curing times ranging from 1 day to 2 months, the typical expected service life of a hoof shoed with the material.

3.7.1 Formahoof Advanced Polymer Specimen Fabrication

Specimens were manufactured as typical flat plate tension coupons and shared the same geometry specifications as those presented in Figure 3.18. A three part mold was fabricated and 3D printed into which the Formahoof Advanced Polymer mixture could be injected and allowed to cure. The mold was fabricated out of ABS plastic, which was sufficient to withstand the heat generated during the initial curing without warping or melting together. There was a hole at one end to serve as the injection point, and three small channels at the other end to allow air pockets and excess material to escape the mold. Small divots were placed along the seams so that a standard flathead screwdriver could assist in separating the mold layers without damaging the Formahoof specimen. Figure 3.22 presents a CAD model representation of the mold and specimen setup. The mold layers were assembled and held together by four bolts, effectively creating an airtight seal.

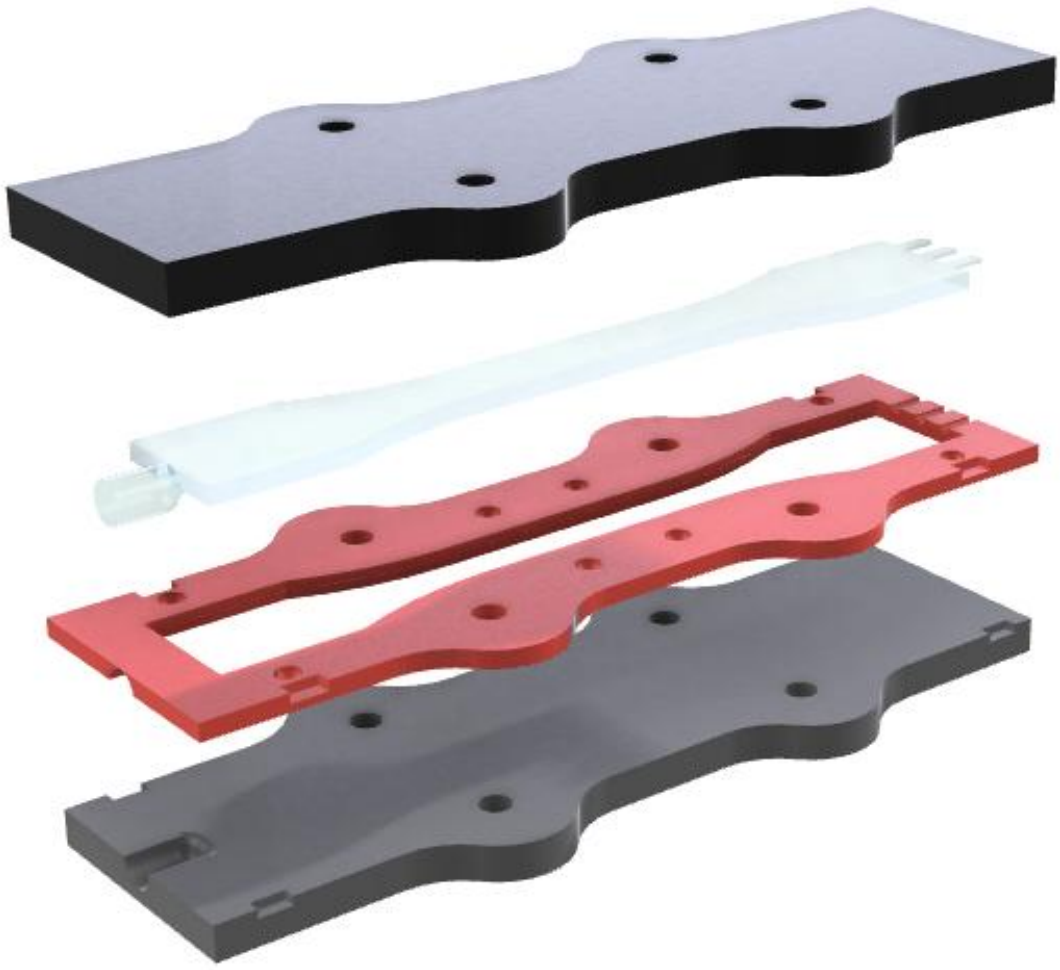

Figure 3.22 CAD Model Representing the Mold and Cured Specimen Removal.

Once the specimen had solidified in the mold for an hour, it was carefully removed and stored in steady ambient laboratory conditions for the allotted aging time. Figure 3.23 presents a backlit view of a typical cured Formahoof specimen prior to removal from the center mold piece. Striations can be clearly seen in the specimen where mixing was not fully homogenized by the applicator nozzle. The striation patterns also indelicate the flow pattern of the material into the mold space.

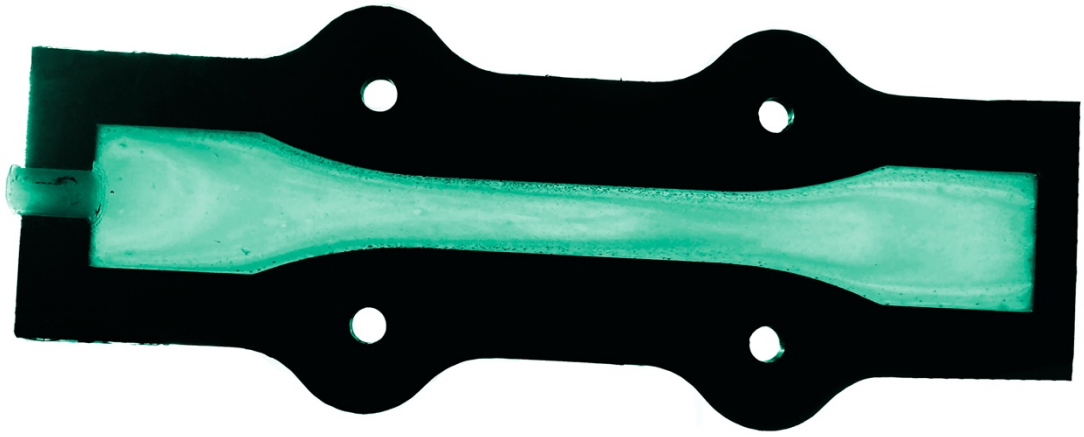

Figure 3.23 CAD Model Representing the Mold and Cured Specimen Removal.

3.7.2 Tension Testing Equipment, Procedure, and Typical Data

The strain (stroke) controlled tension testing of the Formahoof specimens was conducted using an Instron Universal Testing Instrument, the same equipment described in Section 3.4.2. The testing rate was 10^{-3} s^{-1}. The variables measured in the uniaxial tensile tests were the uniaxial force, F, time, t, and the measured crosshead displacement, δ. The stress and strain were calculated using the same procedure as earlier. A typical tensile curve for Formahoof material is presented in Figure 3.24. A hyperbolic tangent curve fit was applied to the raw tensile data, using the following equation:

(Eq. 3.11) $$\sigma = a\tanh(b\epsilon) + c\tanh(d\epsilon) + f\epsilon$$

Where σ represents stress, ϵ represents strain, and a, b, c, d, and f are fit coefficients. The elastic modulus was calculated using the fit coefficients as follows:

(Eq. 3.12) $$E = ab + cd + f$$

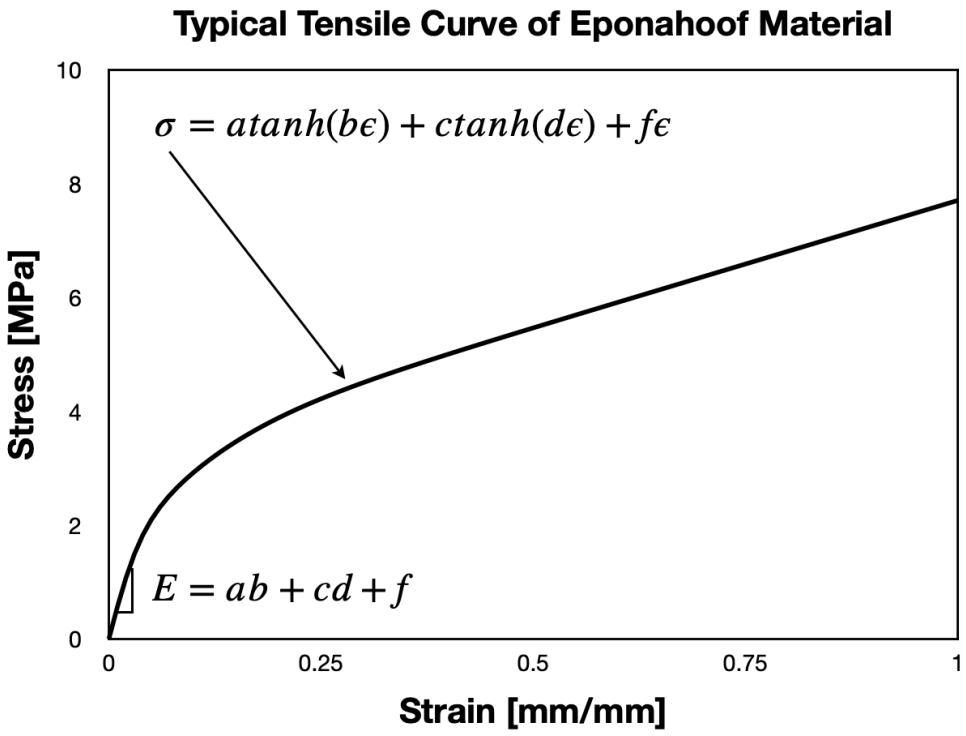

Figure 3.24 CAD Model Representing the Mold and Cured Specimen Removal.

CHAPTER 4

LOCAL KERATIN BEHAVIOR WITH RESPECT TO TUBULE DENSITY

4.1 Introduction

Equine hooves widely vary from animal to animal, even geometry and thickness will differ between horses of the same breed. Studies focusing on the tensile behavior of equine hoof wall keratin across the years have seen diverse results that are often difficult to relate to one another. This seems to be due to the complex, multivariable nature of the topic. This portion of the study seeks to explore the local variation of equine keratin stiffness at the localized level, i.e. isolated behavior of hoof wall regions (SE, SM, and SI). This approach may reveal a method to relate the bulk hoof capsule behavior to the local regions and TD in the wall, yielding a more animal-specific understanding of foot conformation.

In this chapter, several local specimens were milled (see Section 3.3) and tension tested at different levels of hydration. A number of local keratin tensile specimens were tested to failure at 100%RH in order to establish general material behavior. Afterwards, several more tension tests were performed on local keratin specimens that were limited to the elastic region so each specimen could be tested several times under different hydration conditions. The stiffness of equine keratin has been explored for different states of hydration ranging from ~1%-100% RH for keratin specimens with different TDs within the range of ~13-27. Additionally, tension tests were conducted at three different strain rates of 10^{-2} s^{-1}, 10^{-3} s^{-1}, and 10^{-4} s^{-1}. Finally, tubule orientation was explored in by testing specimens manufactured in both the proximodistal and mediolateral orientation.

4.2 Initial Investigation of Tubule Density Distribution

A through-wall sample was sourced from the toe region of an equine hoof capsule to provide general TD pattern context for this portion of the study. A more extensive TD analysis was performed on several specimens in Chapter 6 to contribute an additional data set to the body of knowledge. Figure 4.1 illustrates the hoof wall sample sourced from the foremost dorsal area of the hoof capsule, which was polished and pigmented (see Section 3.7). The surface clearly shows the tubule locations as they were highlighted by the absorbed white artist's gouache. There is an obvious increase in tubule population towards the outer surface of the hoof wall (i.e. near 0% depth of SE), though the papillae surrounding each tubule is much thinner, and TD reaches upwards of 30 tubules/mm^2. Towards the inner hoof wall (i.e. towards 100% depth of SI), the tubule population decreases to as low as 5 tubules/mm^2, though the papillae are larger with a greater capacity to absorb liquid.

A close examination of the surface shows some fluctuations of the tubule population distribution pattern, particularly in the SM—this is to be expected in any biological material. This "scatter" is better depicted by the graph in Figure 4.1, where the local TD is plotted against the hoof wall depth. As reflected in the photomicrograph, the TD is lowest at the SI (nearest to the dermis and internal soft tissue) and increases towards the outer hoof wall surface. As the percent depth approaches 0 (i.e. the SE), the TD appears to quickly drop off again, which is expected as the SE layer does not host any tubules. This indicates a need to determine how the tensile properties of equine keratin are affected by TD, as it is yet another variable necessary to untangle this complex material.

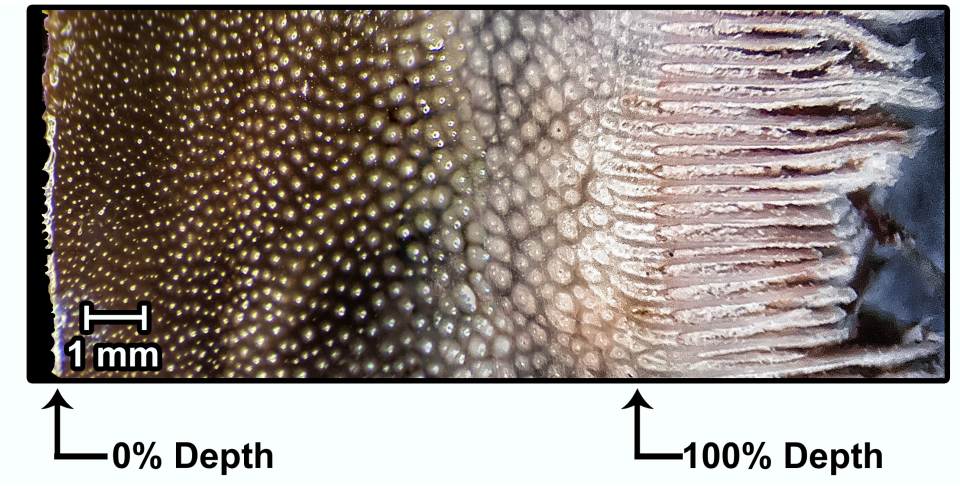

(a)

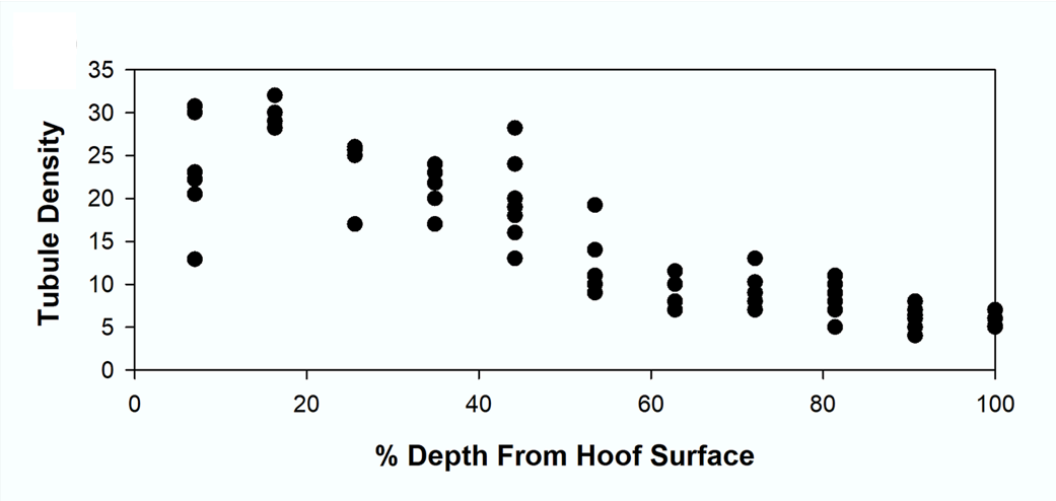

(b)

Figure 4.1 Equine Keratin Dorsal Wall Sample (a) Polished and Pigmented to Reveal the TD, and (b) Data Plot Showing the TD Distribution

4.3 Keratin Dehydration Behavior

Four equine keratin samples were sourced from the same horse at the dorsal area of the hoof capsule but extracted from different depths of the wall. One sample was of the SE, two were taken from SM, and one was extracted from the SI. The maximum moisture

concentrations of each sample correspond with the tubule population trend of each hoof wall region, as demonstrated in Figure 4.1.

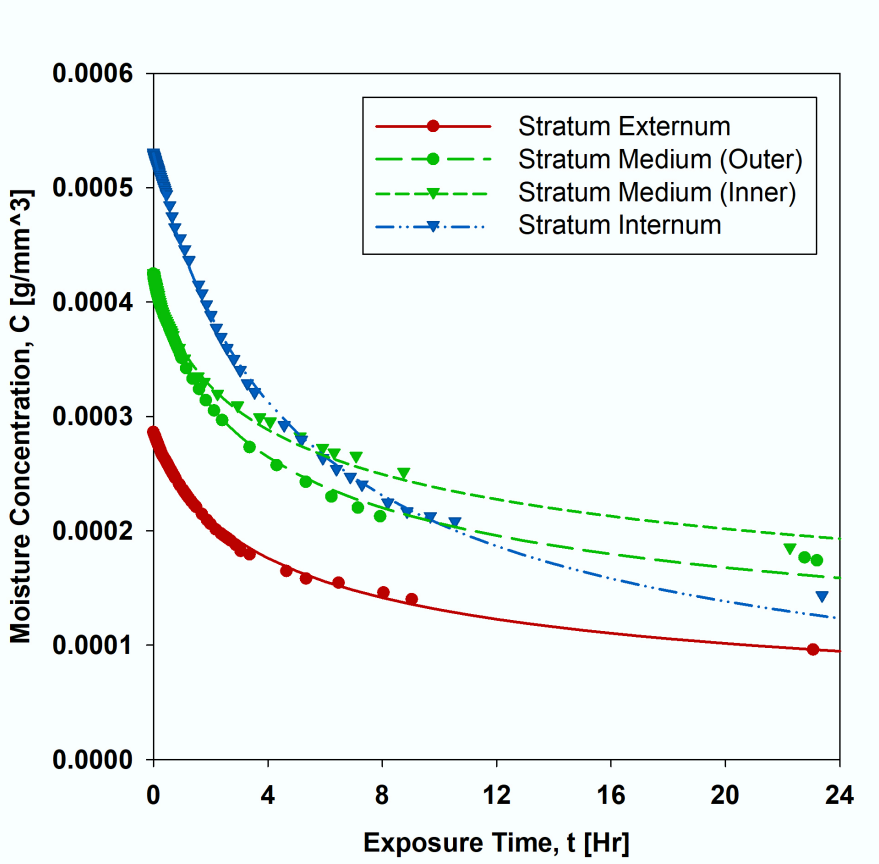

Figure 4.2 Dehydration Curves of Equine Keratin Hoof Wall Regions

The SE sample held the lowest moisture capacity, which is the region of the hoof without tubules. The two SM samples saw an increased moisture capacity over the SE and were on the same magnitude as each other. Finally, the highest moisture capacity was seen in the SI sample. While there is a lower reported TD in the SI, the tubules in this region are surrounded by larger, soft medullae, which would facilitate greater moisture retention than the tubules located closer to the hoof surface. Additionally, the SI is the region of transition between the hard keratin hoof wall and the softer internal biology, which would naturally hold more liquid overall.

The SE and both SM had the same dehydration rate, which makes sense as both regions make up the bulk of the horny keratin hoof wall. The SI had a swifter dehydration rate, which, again, is intuitive because the material is more supple and transitions into the soft tissue.

These results provide context for the dehydration rates of tested keratin for future comparative studies. This also allowed for predictions regarding the timing of the different tensile tests performed on the local specimens—greater control was given to testing at specific intervals to achieve a high-resolution data set of stiffnesses for different %RH conditions. While the weight was tracked in order to report accurate %RH status of each test, the dehydration curves are incredibly helpful in planning such experiments.

4.4 Tensile Data Comparing Tubule Density and Strain Rates

Several local keratin specimens were tension tested to failure while submerged in a distilled water bath to achieve a consistent %RH state. This approach held the %RH variable constant while exploring the variances of hoof wall region and strain rate. Three strain rates were used (10^{-2} s^{-1}, 10^{-3} s^{-1}, and 10^{-4} s^{-1}), and the TD of each specimen was quantified.

Resulting tensile curves were compared in batches where the strain rate was held constant, and the hoof wall sampling depth was varied (Figure 4.3). The material response is elastomeric in nature, as indicated by the stress-strain curve shape. A hyperbolic tangent curve fit paired with an exponential growth term was used to model each stress strain curve:

(Eq. 4.1) $$\sigma = atanh(b\epsilon) + ctanh(d\epsilon) + f\epsilon + ge^{h\epsilon}$$

An interesting detail is that the lowest strain rate of 10^{-4} $s^{-1}$was slow enough to manifest as less elastomeric, and the exponential growth term that creates the tail on the end of the elastomer curve becomes 0 and is canceled out.

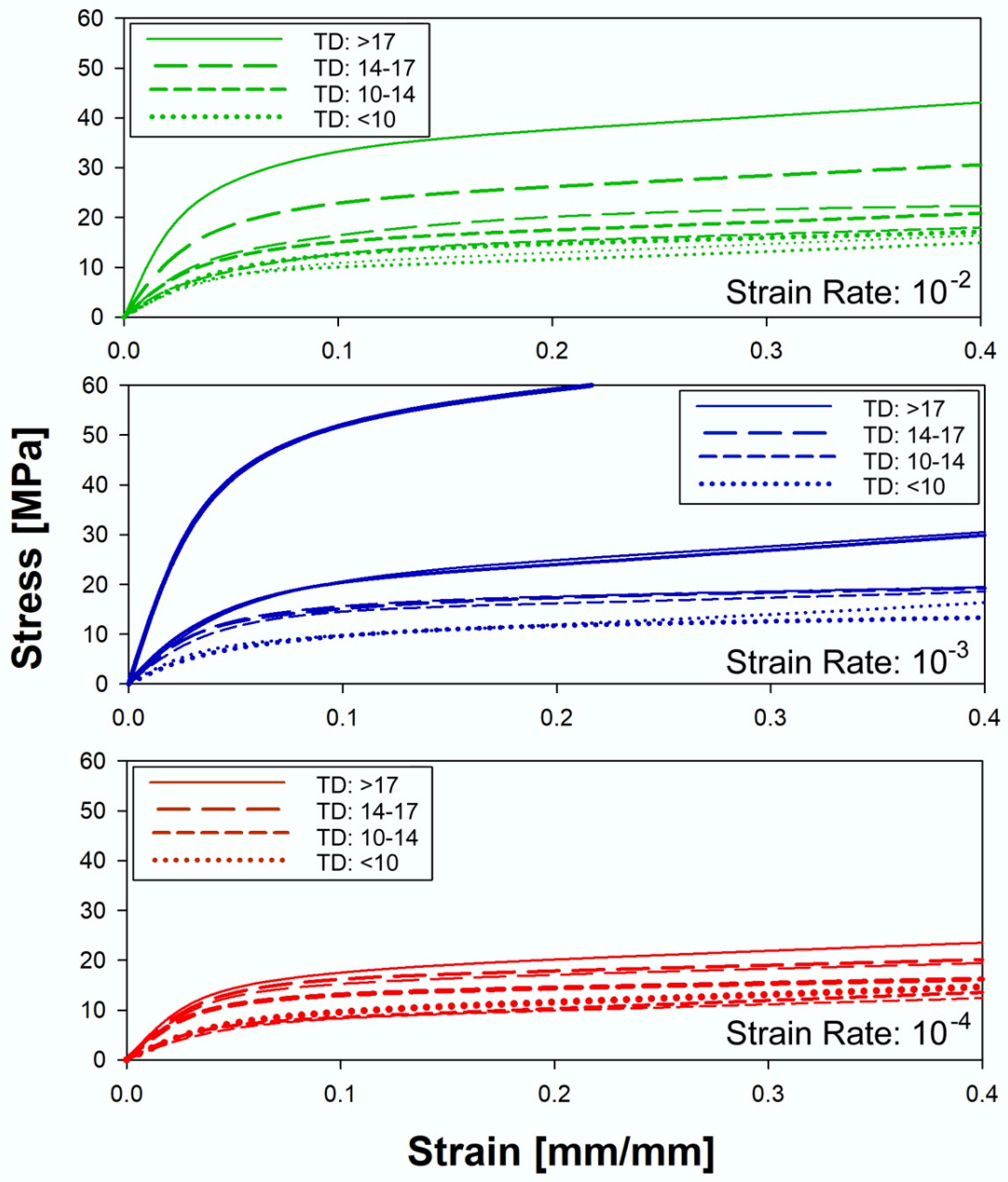

Figure 4.3 Stress-Strain Curves of Local Equine Keratin Specimens at 100%RH

On the surface, there seems to be a large spread in the tensile results from different specimens tested under the same conditions. While some variation is to be expected from

any biological material, there was significant scatter that needed to be evaluated. The key to cracking the trend was the differing TDs between specimens. Specifically, the higher the TD, the greater the stress response. Figure 4.3 sorted the specimens of each strain rate into comparable groups with similar TDs, indicated by the different line styles. In the 10^{-2} s^{-1} specimen set, TD ranged between 5-19 tubules/mm^2 and E values between 0.257-1.016 GPa. The 10^{-3} s^{-1} regime saw a TD range of 6-25 tubules/mm^2 and E values between 0.216-1.354 GPa. The final test set with conducted at a strain rate of 10^{-4} s^{-1} saw TDs from 8-18 tumbles/mm^2 and yielded E values from 0.207-0.478 GPa. This discovery adds another variable to the myriad of factors that affect the behavior of equine keratin and must be a consideration during experimentation and the development of material behavior models.

The next comparison applied to this data set is between the elastic moduli of all the tensile tests conducted at 100% RH against the specimen TD (Figure 4.4). The elastic moduli were calculated using the following method:

(Eq. 4.2) $$E = ab + cd + f$$

Where a, b, c, d, and f are coefficients from the viscoelastic curve fit (Eq. 4.1). Additionally, three trend lines (Figure 4.4) represent the different testing strain rates, which were modeled using an exponential growth model:

(Eq. 4.3) $$y = ae^{bx}$$

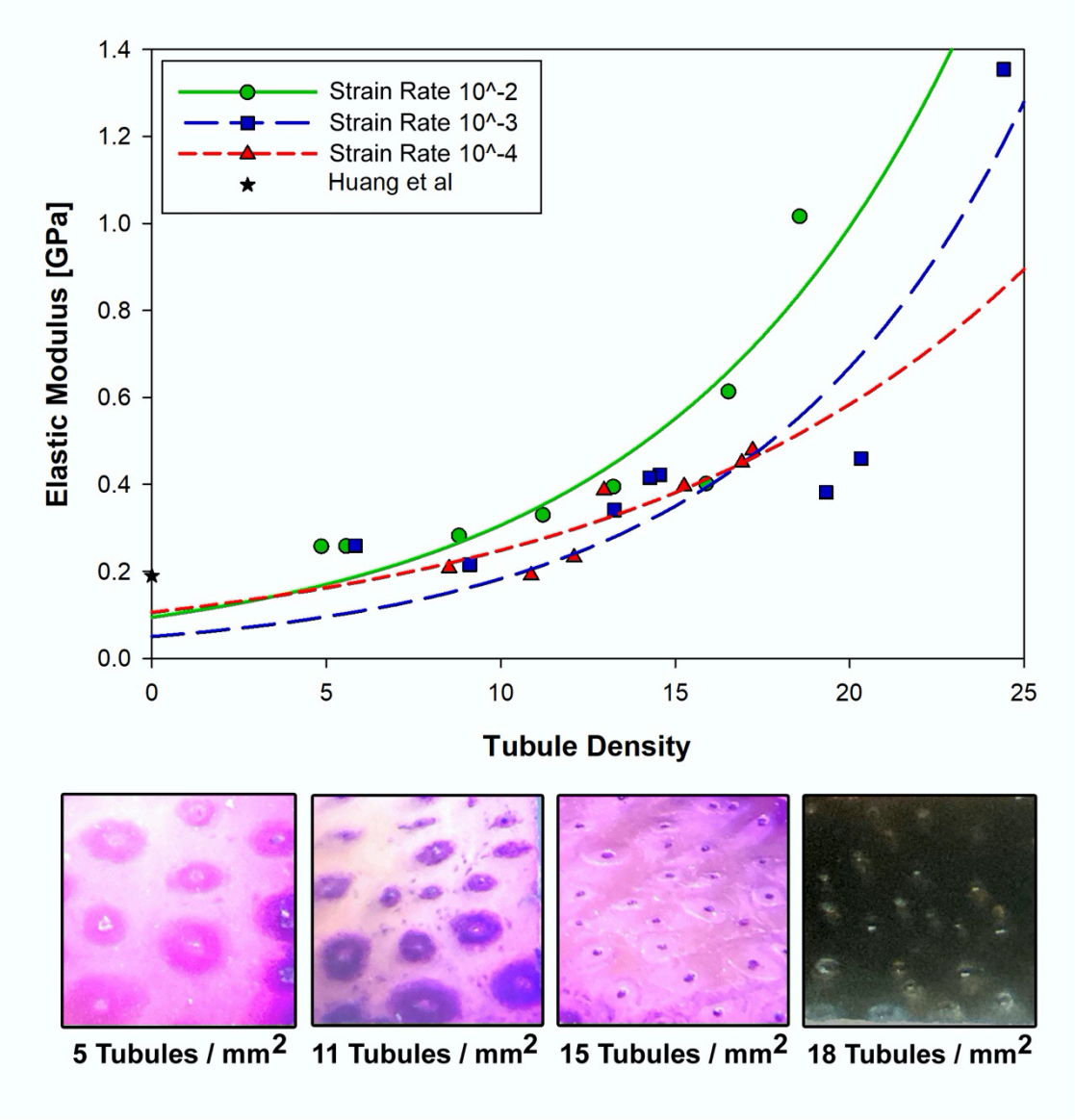

Figure 4.4 Stiffness vs TD Trends For Three Strain Rates (10^{-2} s^{-1}, 10^{-3} s^{-1}, 10^{-4} s^{-1})

There is an obvious trend where the elastic modulus increases with TD, and the tensile stress response generally increases with the strain rate. The exponential growth at 10^{-2} s^{-1} is described as $y=0.94e^{0.118x}$ (*s.e.*=0.123, r^2=0.801). The lower strain rate of 10^{-3} s^{-1} saw a generally lower response as $y=0.050e^{0.130x}$ (*s.e.*=0.172, r^2=0.793). Finally, at 10^{-4} s^{-1}, the final trend can be described as $y=0.106e^{0.086x}$ (*s.e.*=0.061, r^2=0.792). In light of the TD distribution characterized earlier, there is a general pattern of increased stress-strain

response the closer the keratin specimen was sourced to the hoof wall surface, i.e. the SE and SE adjacent material consistently saw the highest tensile properties, and the SI saw the lowest tensile properties regardless of the strain rate.

4.5 Tensile Data Comparing Tubule Density, Hydration, and Strain Rates

Local keratin specimens in the proximodistal orientation were tension tested at several levels of hydration. The elastic modulus of each specimen was dramatically affected as the keratin's moisture content decreased from 100 %RH to ~0 %RH. Linear regression fitting was used on the stress-strain results (which did not extend beyond the elastic strain region) to determine the moduli of elasticity.

A representative set of measured elastic moduli for a proximodistal specimen is presented in Figure 4.5, and clearly displays the increase in stiffness corresponding to the decrease in %RH.

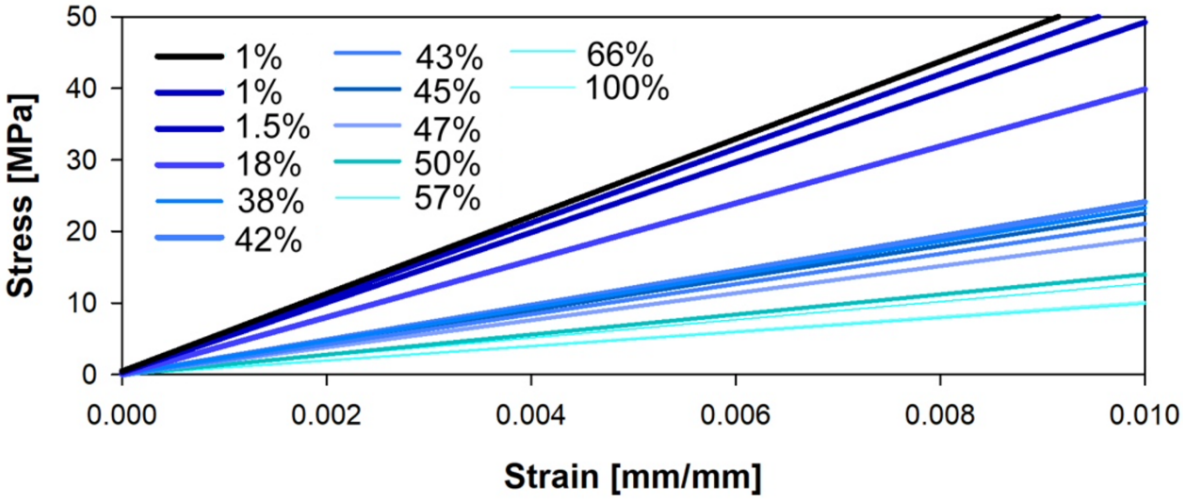

Figure 4.5 Elastic Regions For One Equine Keratin Specimen Tested At Various %RHs

By plotting the elastic moduli against the %RH, a trend can be seen in the form of an exponential decay:

(Eq. 4.4) $$y = a(1-b)^x$$

Where y represents E as predicted by the trend, a is the original, stiffest E value at 0 %RH, b is the factor of decay, and x is %RH. Figure 4.6 shows a representative exponential decay fitted to the collected E data.

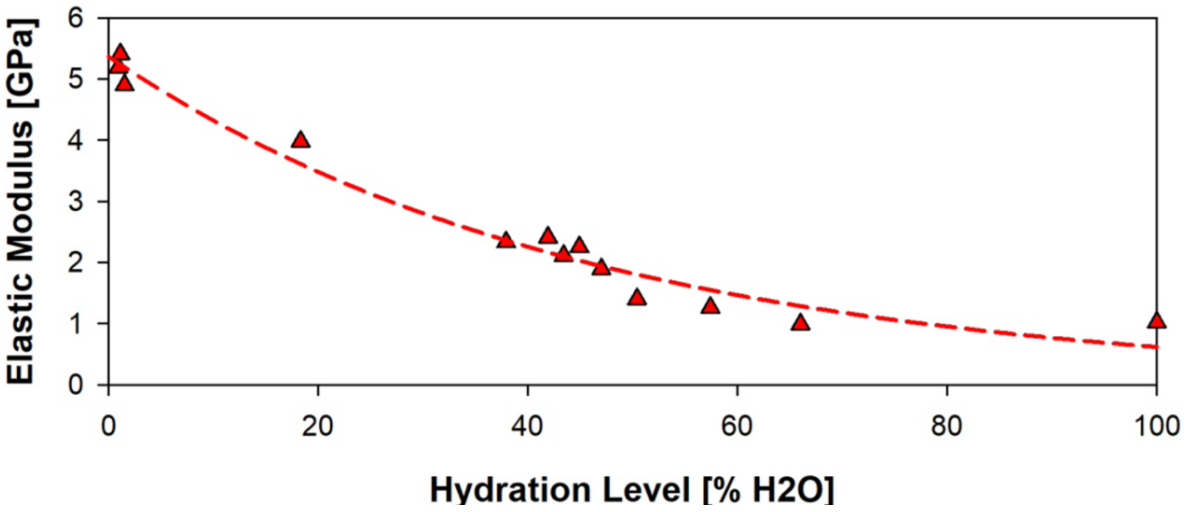

Figure 4.6 Elastic Moduli vs %RH For One Proximodistal Equine Keratin Specimen

This method was repeated for all proximodistal specimens. The elastic moduli of specimens tested at various %RH levels and subjected to three different strain rates; specimens were sampled throughout all of the hoof wall regions (SE, SM, SI), which resulted in different specimens consisting of different TDs. Figure 4.7 displays the entire data set and trendlines for the proximodistal orientation.

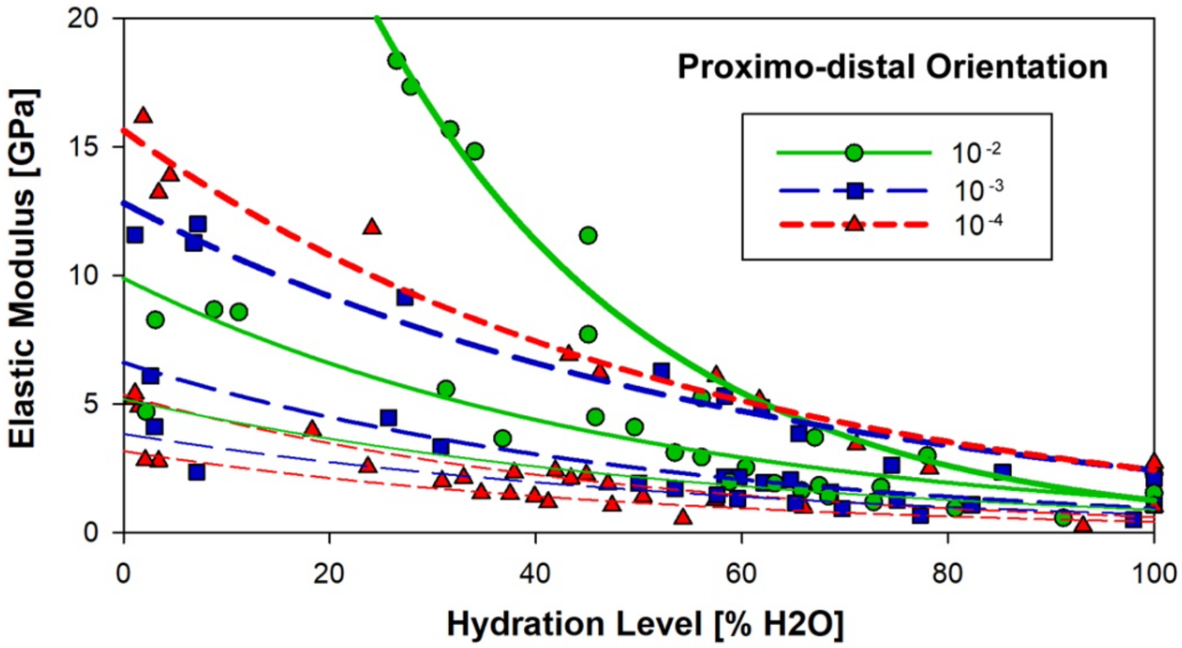

Figure 4.7 Elastic Moduli vs %RH For One Proximodistal Equine Keratin Specimen

At first glance, the trend lines vary widely, and there does not seem to be an obvious pattern beyond the known inverse relationship between E and %RH. However, the "scatter" is explained by the different TDs observed for each specimen. Upon evaluating this additional variable, two sets of specimens of similar TD were pulled for isolated comparison (Figure 4.8).

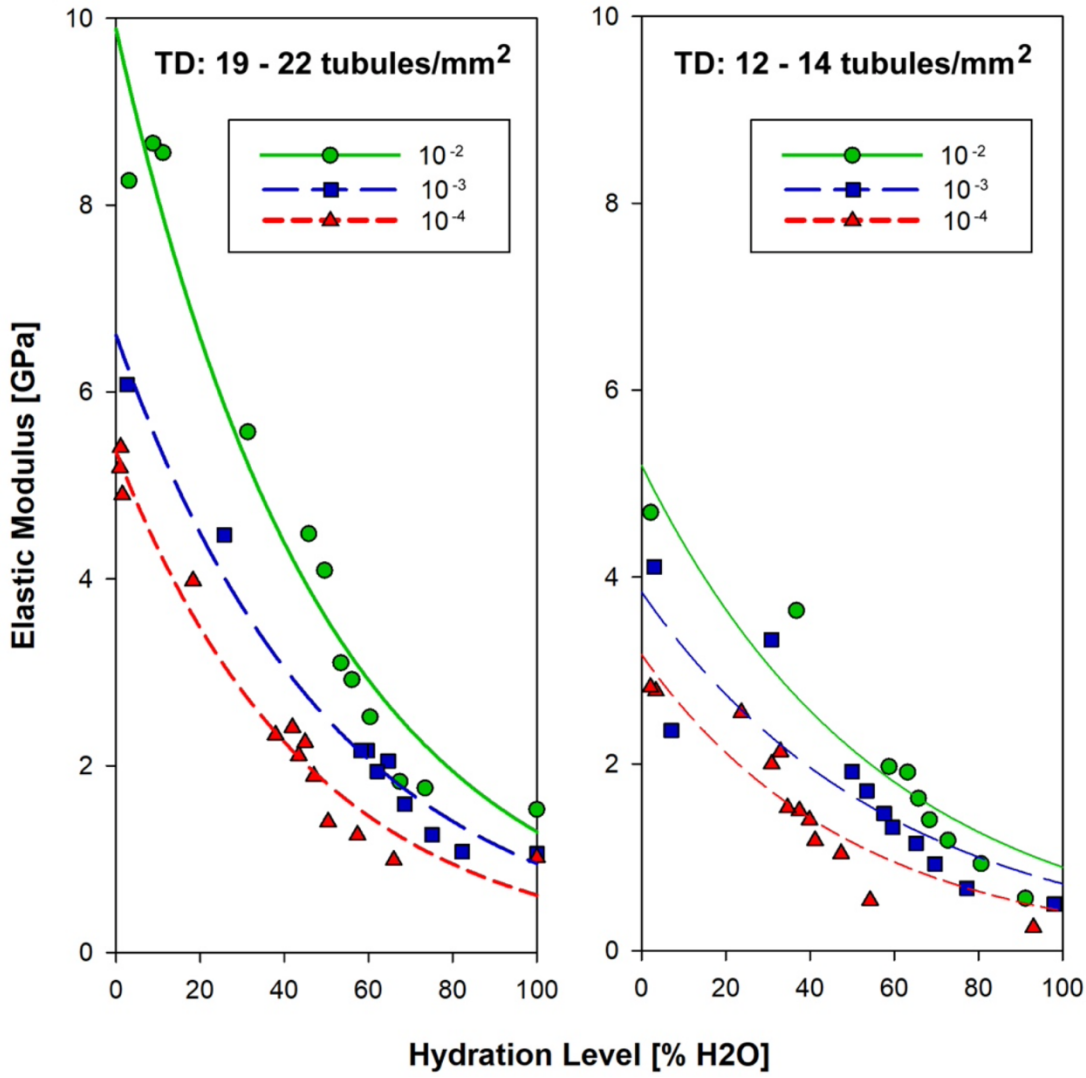

Figure 4.8 Elastic Moduli vs %RH For One Proximodistal Equine Keratin Specimen

One specimen set was comprised of specimens with TDs ranging between 19-22 tubules/mm^2 with resulting E values ranging from approximately 1-9 GPa. The second isolated test set saw TDs between 12-14 tubules/mm^2 with approximate E values between 0.2-5 GPa. In both comparisons, there is a clear increase in resulting E values as the strain rate is increased from 10^{-4} to 10^{-2}. This trend is expected and in agreement with the general behavior of viscoelastic materials. Table 4.1 provides a summary of the observed trend lines.

Table 4.1 Trendlines Describing Stiffness vs TD of Proximodistal Keratin Specimens

Strain Rate	Curve Fit [y=a(1-b)^x]	*s.e.*	r^2	TD
10^{-2}	y=5.194(1-0.017)^x	0.4526	0.8999	13
10^{-2}	y=9.886(1-0.020)^x	0.5776	0.9588	22
10^{-2}	y=49.346(1-0.036)^x	1.0901	0.9940	28
10^{-3}	y=3.839(1-0.017)^x	0.5556	0.7775	14
10^{-3}	y=6.610(1-0.019)^x	0.2419	0.9803	22
10^{-3}	y=12.813(1-0.017)^x	0.7880	0.9624	26
10^{-4}	y=3.170(1-0.020)^x	0.3410	0.8488	12
10^{-4}	y=5.361(1-0.022)^x	0.2803	0.9721	19
10^{-4}	y=15.637(1-0.018)^x	1.0326	0.9597	27

4.6 Tensile Data Comparing Hydration, Tubule Orientation, and Strain Rates

The experimental process analyzing local keratin stiffness with respect to various %RH conditions (Section 4.5) was repeated for specimens fabricated in the mediolateral orientation. Figure 4.9 displays the entire data set and trendlines for the mediolateral orientation.

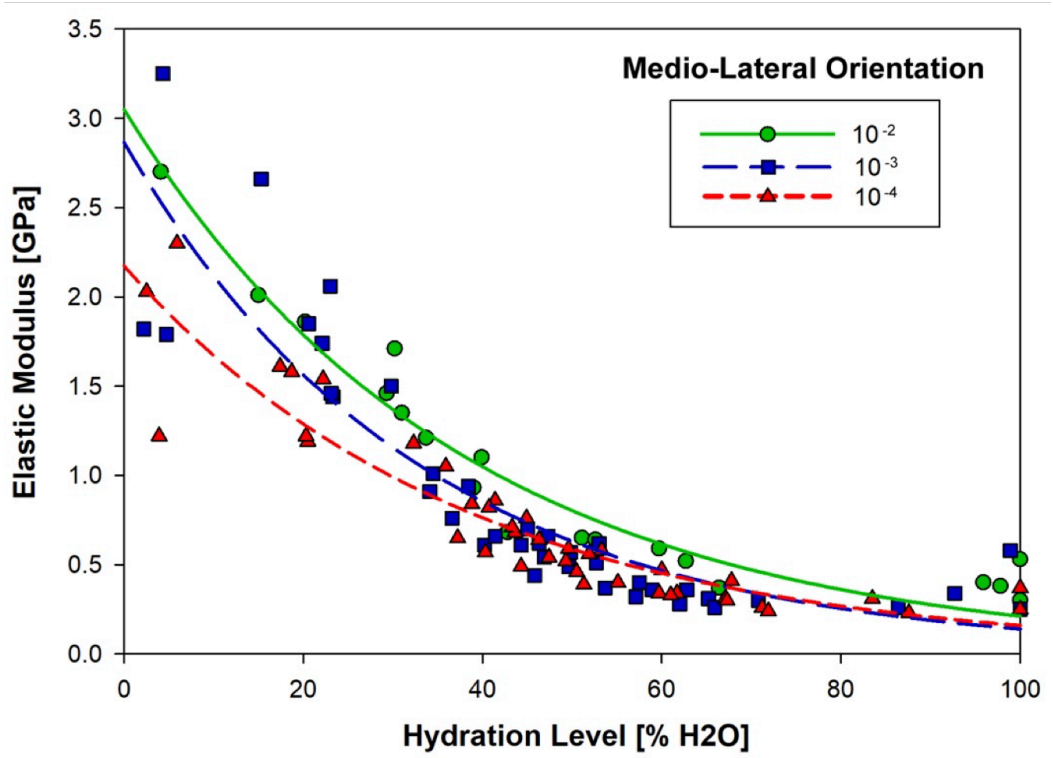

Figure 4.9 Elastic Moduli vs %RH For One Proximodistal Equine Keratin Specimen

Again, strain rates appear to have an impact on the elastic moduli of equine keratin at all levels of hydration. Hence, the faster the strain rate, the stiffer the elastic modulus. However, this effect seems less pronounced when compared with the proximodistal orientation results. There is also much less scatter in the mediolateral orientation data, indicating that much of the variation in the proximodistal orientation mechanical properties could be attributed to the changing TD throughout the hoof wall thickness. Resulting elastic moduli ranged between 0.23-3.25 GPa, which is a significantly smaller range than that of the proximodistal orientation stiffnesses. A summary of the observed trend lines is presented in Table 4.2.

Table 4.2 Trendlines Describing Stiffness vs TD of Mediolateral Keratin Specimens

Strain Rate	Curve Fit [$y=a(1-b)^x$]	*s.e.*	r^2	TD
10^{-2}	$y=3.050(1-0.026)^x$	0.1645	0.9435	N/A
10^{-3}	$y=2.865(1-0.030)^x$	0.3232	0.8034	N/A
10^{-4}	$y=2.173(1-0.026)^x$	0.1894	0.8620	N/A

4.7 Tensile Data Comparing Tubule Density, Temperature, and Strain Rates

Temperature also has a large effect on the mechanical properties of equine keratin. All of the tensile tests were conducted on proximodistal specimens submerged in distilled water that was heated or chilled to the desired temperature, ranging from approximately 1-70 °C. The strain rate was held at 10^{-3}, and all keratin specimens were sourced from the SM. The material response was elastomeric across the entire tested temperature range. When comparing all the stress-strain tensile curves tested at various temperatures (Figure 4.10), there is an overall increase in stress response as the temperature decreases. Additionally, the general shape of the curve changes with the temperature. The higher the temperature, the lower and longer the curve becomes which is evidence of a more ductile

material behavior and elastic moduli as low as 0.095 GPa. Conversely, the colder the temperature, the higher and shorter the curve became, demonstrating a more brittle response with elastic moduli as high as 3.079 GPa.

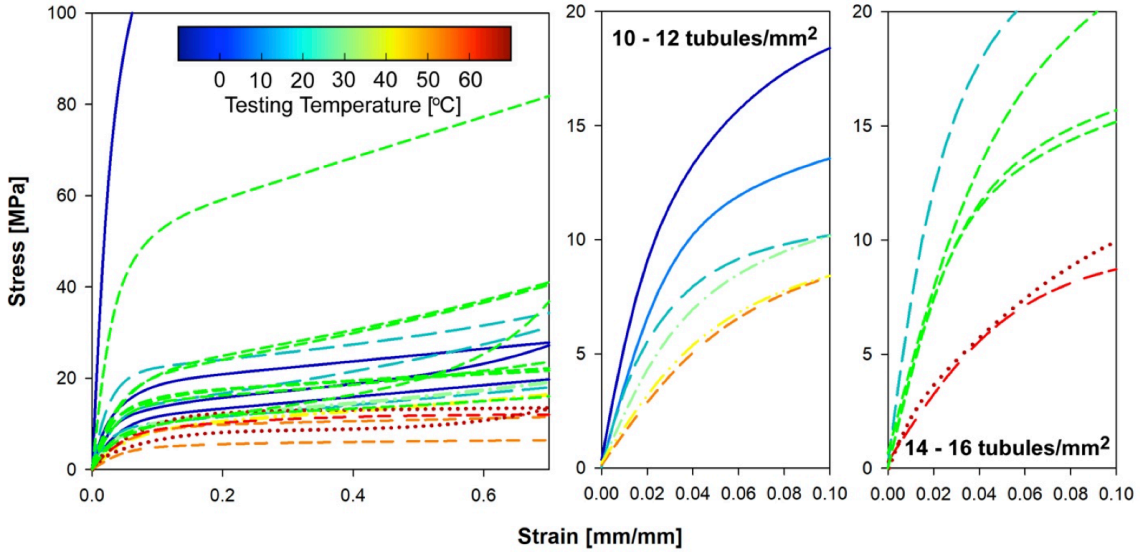

Figure 4.10 Stress-Strain Curves for Equine Keratin at Various Temperatures and TDs

Initially, there seems to be significant scatter in the results, but the trend becomes much clearer with less spread when samples of similar TD are sorted and compared. Two specimen sets with TDs of 10-12 tubules/mm^2 and 14-16 tubules/mm^2 were isolated and compared in Figure 4.10, and there is a clear trend where a decrease in temperature results in an increased stress response. The first specimen set (TD=10-12 tubules/mm^2) resulted in elastic moduli ranging between 0.142-0.532 GPa for a temperature range of 1.7-51.7 ºC (+/-2.2 ºC), while the second set (TD=14-16 tubules/mm^2) saw resulting elastic moduli of 0.137-0.750 GPa for the temperatures of 10-66.1 ºC (+/-2.2 ºC).

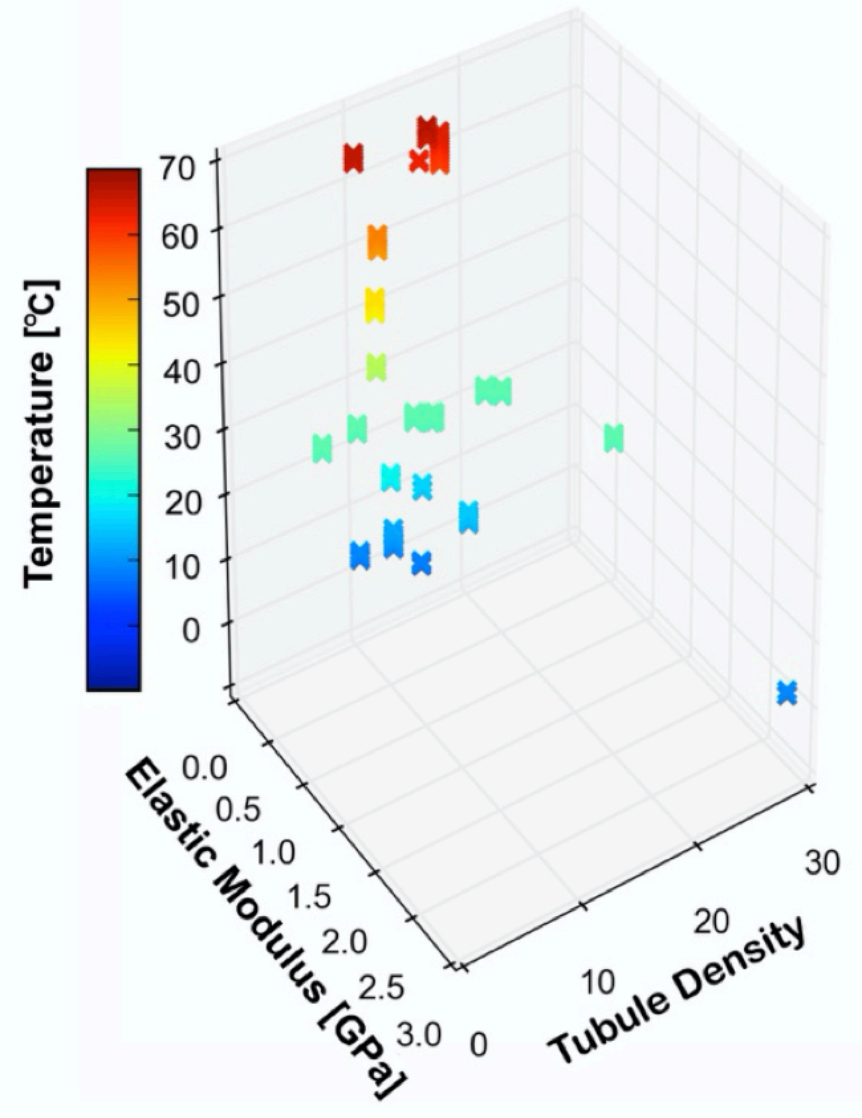

Figure 4.11 Stiffness vs TD vs Temperature for Local Equine Keratin

All three variables of temperature, TD, and E are compared in Figure 4.11. Figure 4.12 provides an isolated view of the data comparing temperature versus TD. The two groupings of specimens with comparable TD are plotted alongside each other, comparing temperature and the resulting elastic moduli.

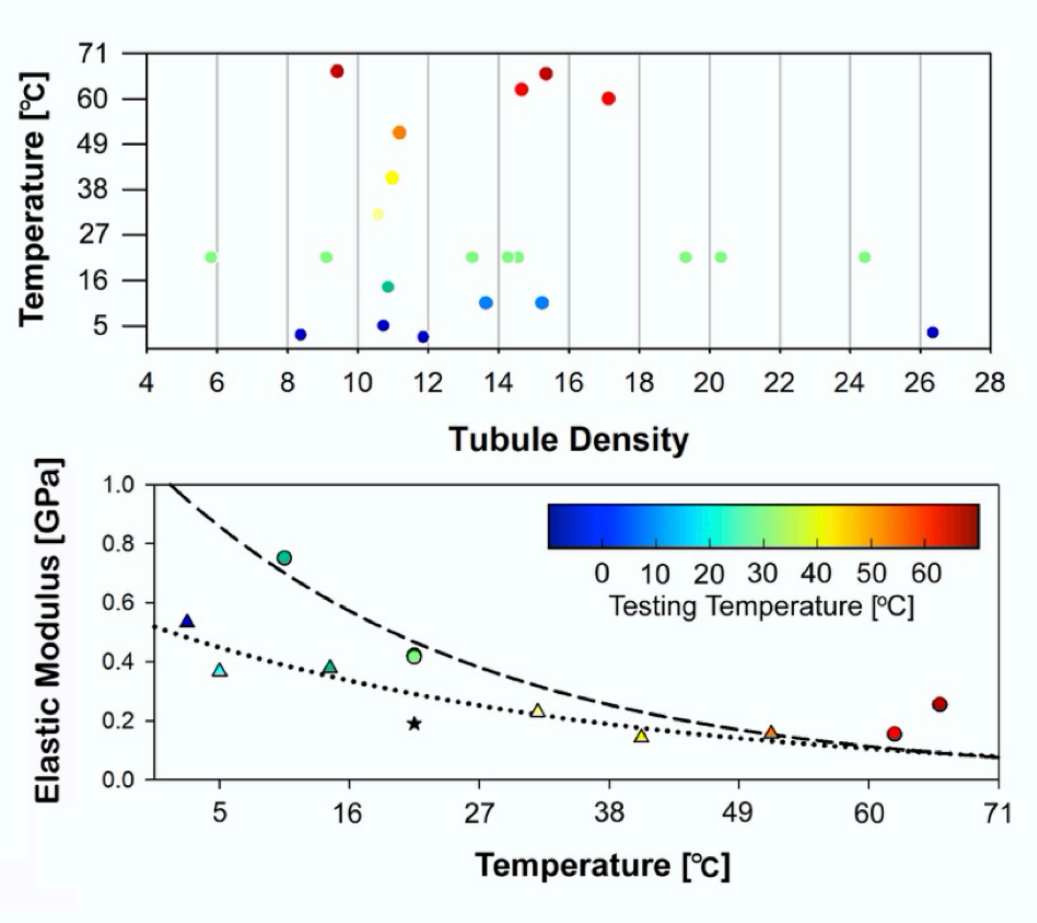

Figure 4.12 Stiffness vs TD vs Temperature for Local Equine Keratin

An exponential decay model was used to model the two data sets:

(Eq. 4.5) $$y = a(1-b)^x$$

Where y represents the elastic modulus E as predicted by the trend, a is the coldest, stiffest E value, b is the factor of decay, and x is the temperature T.

Two trends are made apparent: first is the inverse relationship between temperature and E, and second, as E increases, TD increases. More specifically, when $10 \leq TD \leq 12$, there was a resulting trend described by $y=0.800(1-0.014)^x$ (*s.e.*=0.051, $r^2=0.908$), and when $14 \leq TD \leq 16$, the trend became $y=1.93(1-0.020)^x$ (*s.e.*=0.062, $r^2=0.954$). A summary of the observed trend lines are presented in Table 4.3.

Table 4.3 Trendlines Describing Stiffness vs Temperature for Limited TD Ranges

Strain Rate	Curve Fit [y=a(1-b)^x]	*s.e.*	r^2	TD
10^{-3}	y=0.800(1-0.014)^x	0.051	0.908	10≤TD≤12
10^{-3}	y=1.93(1-0.020)^x	0.062	0.954	14≤TD≤16

This is vital information. Shoeing practices can be individually tailored to accommodate specific stress responses, such as increases and decreases in environmental temperature/humidity, workload of the horse, type of activity (jumping, racing) and/or cargo. Trimming the toe is a common practice when changing horseshoes. The castoff material could easily be assessed for TD of the horse hoof to monitor changes in the hoof wall that can result due to disease states and alterations in exercise and nutrition. Hoof wall trimmings can be utilized to analyze the hoof wall TD distribution of the specific horse, detect problems with the formation of the hoof wall, and can be a way to compare therapeutic outcomes over a period of time.

4.8 Compiled Mechanical Properties

The stiffness for equine keratin with different TDs and temperatures can be compiled to form a 3D contour graph. The "sheets" representing the stiffness vs TD vs %RH at a specific temperature are formed from the data sets collected from the local keratin tension tests described throughout Chapter 4. The plot represents keratin behavior at the strain rate of 10^{-3} s^{-1} because it had the largest data set available.

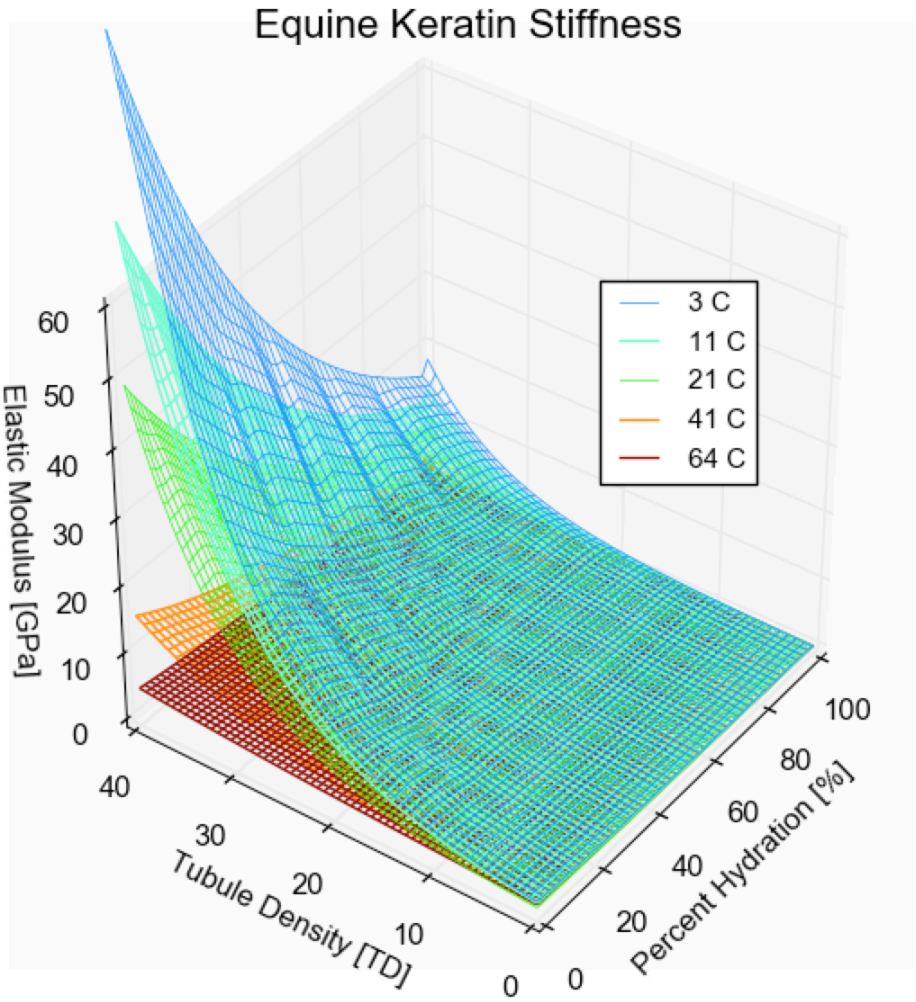

Figure 4.13 Stiffness vs TD vs Temperature for Local Equine Keratin

The contour plot sheet representing the T=3 ºC data set becomes visibly "rough" in the high TD/low %RH region—this is due to the limited data available for the "extreme" boundaries of the plot. The rest of the sheets have smoother, better defined surfaces because of the sufficiently dense population of data. An opportunity for future research is to expand this data set and those of the other strain rates (10^{-2} s^{-1} and 10^{-4} s^{-1}) in order to improve the curve fits.

4.9 Discussion

The elastic modulus and %RH values for the entire specimen regime were examined by varying the following factors: TD (due to sampling from throughout the hoof wall), strain rate, and the axis of stress with respect to tubule orientation (i.e. proximodistal versus mediolateral orientations). All specimen results demonstrated an increase in data spread as the %RH is reduced. Specimens with higher TDs are generally stiffer than specimens tested under the same conditions but with lower TDs. This is noteworthy, as the different regions of the hoof wall have different TDs and different maximum moisture capacities. These results indicate anisotropy in equine keratin, which primarily varies by the tubule orientation with respect to the loading axis. The implications of these results suggest that the tubule component of keratin material is affected by strain rate, but the inter-tubular material component may not be affected in as significant a way, if at all. As the tubule orientation alters around the circumference of the asymmetric conical hoof capsule, the effective tensile properties will change with the different local loading conditions.

This study provided a more systematic approach to exploring the tensile properties with respect to variations in strain rate and hoof wall region/TD. Additionally, the temperature data generated here is a novel contribution to the body of knowledge and provided information at a variety of temperatures of both ambient and extreme environments. The primary strength of this study is demonstrating the relationships between TD, E, and temperature, with respect to three different strain rates, which helps isolate these trends from additional uncertainty stemming from % RH and other fluctuations in the testing environments. While the number of specimens tested in this study is limited simply by the challenging nature of biological material harvesting,

manufacturing, and testing, improvements could be made by expanding the data set via this new procedure. The beauty of the procedure developed by this study lies in its capability to produce comparable results between hooves of different size, shape, breed, and pigmentation. A convenient summary of conclusions are as follows:

The SE, SM, and SI regions of the equine hoof wall possess different maximum capacities for moisture. This supports the supposition that the SE is a significant hydration moderation mechanism for the hoof wall. Tubule density alters with hoof wall region, where the tubule population per mm^2 is lowest towards the SI, and increase throughout the SM towards the SE. Keratin specimens of the proximodistal orientation exhibit a higher stress response when the tubule density is increased; conversely, there is a lower stress response correlated with lower tubule densities. The trend demonstrated an exponential growth trend: at 10^{-2} s^{-1}, $y=0.94e^{0.118x}$ (*s.e.*=0.123, $r^2=0.801$); 10^{-3} s^{-1}, $y=0.050e^{0.130x}$ (*s.e.*=0.172, $r^2=0.793$); 10^{-4} s^{-1}, $y=0.106e^{0.086x}$ (*s.e.*=0.061, $r^2=0.792$). Increased strain rate is directly correlated to the increase in the modulus of elasticity and tensile stress response of equine keratin. The faster the strain rate, the higher the tensile response and the more polymeric the behavior becomes; conversely, if the strain rate is reduced enough (10^{-4} s^{-1} or slower), the tensile curve follows the more traditional, hyperbolic tangent behavior. The implication is that different hooves can handle different levels of stress and/or speed, depending on the animal's personal TD distribution; not all keratin is created equal. Knowing this information can inform the owner about what kind of work the animal should be doing and what type of shoe and hoof preparation method should be used. Some shoes, for example, are cast wraps or epoxy-type coatings, and the softer, more flexible hooves may need higher coverage profiles (to avoid bulging over the top rim) or a more open shoe

to avoid excessive circumferential constraints. During rehabilitation, this information is useful for understanding the proper limits to impose during the healing process. One horse may be able to withstand greater activity and/or diet without issue, while another animal with a different TD profile may need more conservative handling.

As the temperature increases, the more ductile the equine keratin behaves, just as the material becomes more brittle behaving as the temperature decreases. Lower temperatures resulted in stiffer elastic moduli, a trend that may be described as an exponential decay: when $10 \leq TD \leq 12$, $y=0.800(1-0.014)^x$ (*s.e.*=0.051, $r^2=0.908$); $14 \leq TD \leq 16$, $y=1.93(1-0.020)^x$ (*s.e.*=0.062, $r^2=0.954$). Environmental factors, such as temperature and humidity, have an effect on keratin behavior and overall hoof health. Management to reduce excessive temperature to the hoof wall might provide protection of the elasticity of the hoof wall and prevent breakage and potential subsequent episodes of lameness. Shoeing decisions can also be better informed based on the environment in which the horse lives and operates.

Trimmings taken from the hoof during the shoeing process may be used to determine an understanding of the tubule population specific to that horse and its individual hooves. This simple, noninvasive examination may inform the caretaker as to what type of loading the hoof wall experiences so shoeing and activity can be adjusted as necessary. Additionally, if this data is consistently collected over time, changes in the tubule shape and density could serve as an early alert system to developing hoof issues.

These trend curves, along with other data collected using this procedure [Sterling et al], provide a reference database for baseline comparisons of equine keratin useful to farriers, veterinarians, horse owners, and other equine caregivers. A greater number of specimens from multiple breeds with different hoof sizes and geometries might be analyzed and compared for further statistical comparisons. Additionally, harvesting specimens from trimmings of hoof can be utilized for TD analysis. Any caregiver could use the simple, cost-effective "kitchen-suitable" method of TD determination previously adapted by Sterling et al to better understand their animal's specific needs based on breed, environment, and expected activity.

4.10 Summary Conclusions

Major conclusions are summarized as follows:

- The SE, SM, and SI regions of the equine hoof wall possess different maximum capacities for moisture. This supports the supposition that the SE is a significant hydration moderation mechanism for the hoof wall.
- The modulus of elasticity, E, is inversely related to the hydration level, %RH, of the keratin specimen. The more hydrated the keratin is, the more ductile behaving this material becomes, just as the keratin behaves more brittlely as the material dehydrates.
- Increased strain rate is directly correlated to the increase in the modulus of elasticity and tensile stress response of equine keratin. The faster the strain rate, the higher the tensile response and the more polymeric the behavior becomes; conversely, if the strain rate is reduced enough (10-4 or slower), the tensile curve follows the more traditional, hyperbolic tangent behavior.

- Tubule density alters with hoof wall region, where the tubule population per mm^2 is lowest towards the SI, and increase throughout the SM towards the SE. Keratin specimens of the proximodistal orientation exhibit a higher stress response when the tubule density is increased; conversely, there is a lower stress response correlated with lower tubule densities.
- Equine keratin is anisotropic with respect to tubule orientation versus loading axis. There is a higher stress response in keratin loaded along the proximodistal orientation (loading applied parallel to the tubule direction) than in keratin loaded along the mediolateral orientation (loading applied orthogonally to the tubule direction). Additionally, there is greater spread and impact upon the proximodistal data as compared with the mediolateral results, as the proximodistal specimens are significantly impacted by local tubule density.
- Equine keratin specimens fabricated in the proximodistal orientation demonstrated higher material stiffness as TD increased; conversely, lower elastic moduli correlated with lower TDs. Because TD changes throughout the hoof wall region—where the tubule population per mm^2 is highest towards the SE, and decreases throughout the SM towards the SI—the material stiffness also alters throughout the hoof wall regions.
- As the temperature increases, the more ductile the equine keratin behaves, just as the material becomes more brittle behaving as the temperature decreases. Environmental factors, such as temperature and humidity, may have a significant effect on keratin behavior and thus overall hoof health. The temperature profile of the hoof wall may vary through the thickness, as the SE may be cool in certain

environmental conditions, but the SI is close to the internal biology of the digit and may be warmer due to the animal's body temperature.

- During the shoeing process, hoof trimming may be taken and could potentially be used to better understand the tubule distribution of that specific horse. By analyzing that hoof trimming for TD and consulting the material property trend lines based on what activities the horse is expected to perform, the caretaker may adjust shoeing practices. Additionally, habitual assessment of TD following changes in shoeing can be utilized to ascertain the effectiveness of the changes in shoeing practices. If hoof trimmings are routinely examined, and TD data is consistently collected over time, it will be easier for the caretaker to identify any alterations of the tubule shape/density. This could potentially act as an early alert system to developing hoof issues, allowing the horse to receive preventative treatment before the problem evolves/worsens.

CHAPTER 5

BULK HOOF WALL PROPERTIES

5.1 Introduction

Now that the local stiffness of equine keratin has been quantified, the next logical step is to explore how the differing local stiffnesses in the changing regions of the hoof wall work together. Since equine hooves vary dramatically between individual animals and species, there is an infinite combination of wall region thicknesses, TD, wall geometry, and orientation to the loading of the horse's step—meaning there are infinite possible combinations of local keratin properties merged to create the behavior of the bulk hoof wall capsule. This portion of the study aims to collect, quantify, and analyze data on the stiffness of bulk wall equine keratin specimens while tracking the different geometries, keratin pigmentation, TD distributions, %RH, and temperature of the specimens under examination. This data set will become a steppingstone in a path forward to relate the bulk hoof capsule behavior to the local regions and TD in the wall, yielding a more animal-specific understanding of foot conformation.

In this chapter, several bulk hoof wall specimens were manufactured with proximodistal orientation (see Section 3.4.1 for fabrication details) and tension tested at a limited number of hydration levels. The specimens were hydrated in distilled water to 100%RH in a chilled environment, and then dehydrated in a controlled manner prior to testing. The weight was recorded for each specimen in the 100%RH condition, and then the weight was systematically measured and recorded during the dehydration period of 15 minutes, 60 minutes, 5 hours, or 24 hours. Once the specimens were tension tested to failure, they were fully dehydrated and weighed in the 0%RH condition. For all specimens,

the testing strain rate was held at 10^{-3} s^{-1}, and the temperature at testing was measured and recorded.

19 bulk wall keratin specimens were sourced from the toe region of 19 different horse hoof capsules belonging to 12 different horses. The data set contained specimens of light, dark, and mixed keratin pigmentation. The %RH ranged from approximately 30%-95%. The TD distribution was obtained for each individual specimens using the process described in Section 3.5.

5.2 Observations and Tensile Data for Bulk Hoof Wall Keratin

During testing, the keratin specimens were gripped and pulled to final failure. The progressive cracking of the specimen was audible as the tension test was conducted, and cracks most commonly initiated in the SI region. The crack would then progress through the SM following a tortuous route, which lends some credence to the supposition that the SM structure acts in part as a crack inhibitor/staller. Finally, the SE would be the last to sever, leaving a jagged, angled fracture surface. This process is shown in more detail in Figure 5.1.

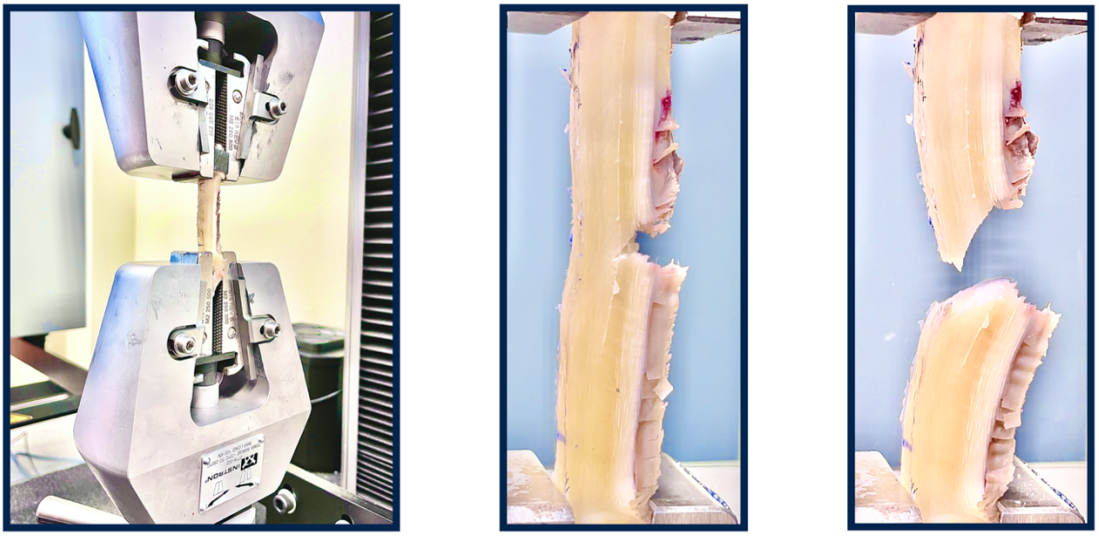

Figure 5.1 Typical Tensile Test Setup (left) and Specimen Final Fracture (Center, Right).

A typical tensile curve (Figure 5.2) demonstrated viscoelastic behavior with a slightly non-linear initial elastic region. The viscoelastic curve shape became more prominent as %RH decreased and TD increased.

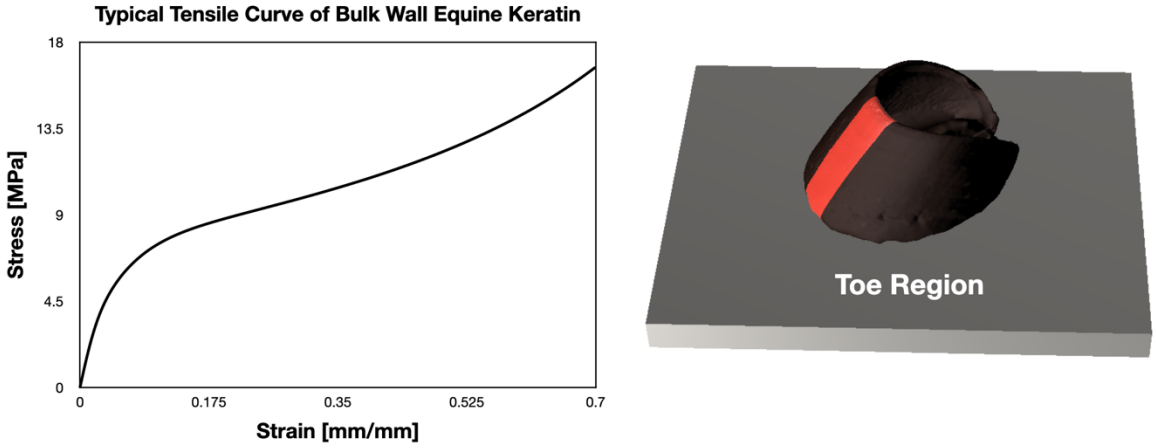

Figure 5.2 Typical Tensile Test Curve of a Bulk Wall Equine Keratin Specimen.

A comparison of the tension test data can be seen in Figure 5.3, with the view constrained to 0.1 mm/mm strain to enable a closer examination of the initial elastic regions. The testing conditions (temperature and %RH) and specimen TD vary widely, producing a wide range of results. The expected general trend is seen where the overall stress response increases as %RH decreases. Additionally, an inverse relationship between specimen hydration and initial stiffness is seen. These trends are better viewed in the three-dimensional graph in Figure 5.4, where the tensile curves are arranged by %RH for an easier comparison. This behavior is as expected and agrees with previous trends observed in the local tension testing data.

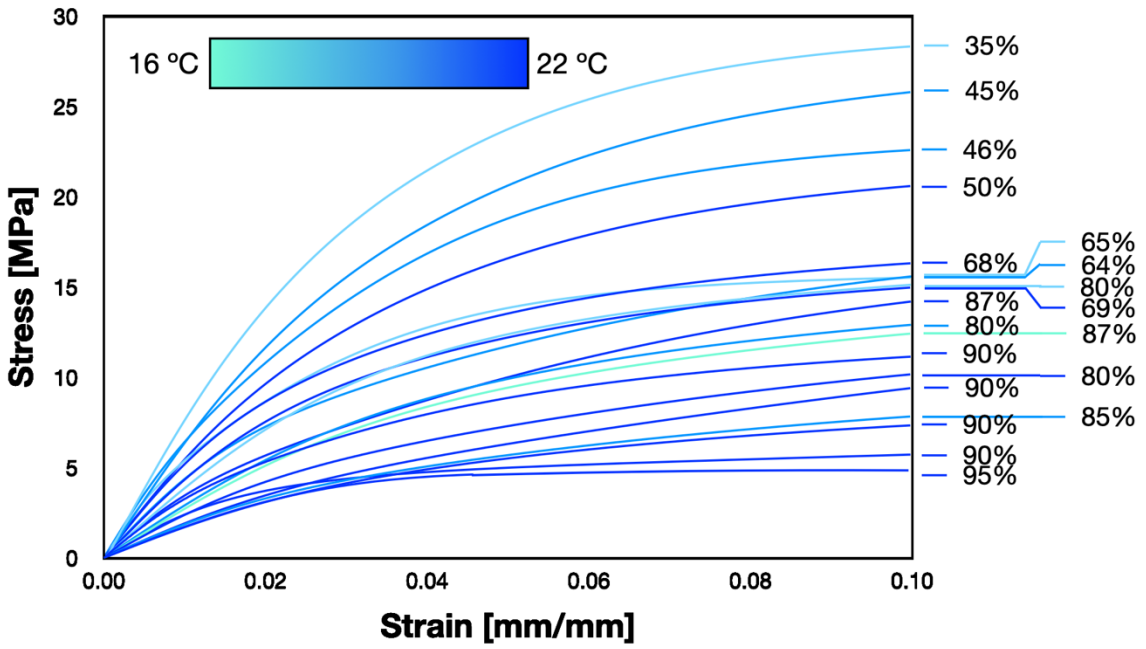

Figure 5.3 Comparison of Tensile Test Results of a Bulk Wall Equine Keratin Specimen.

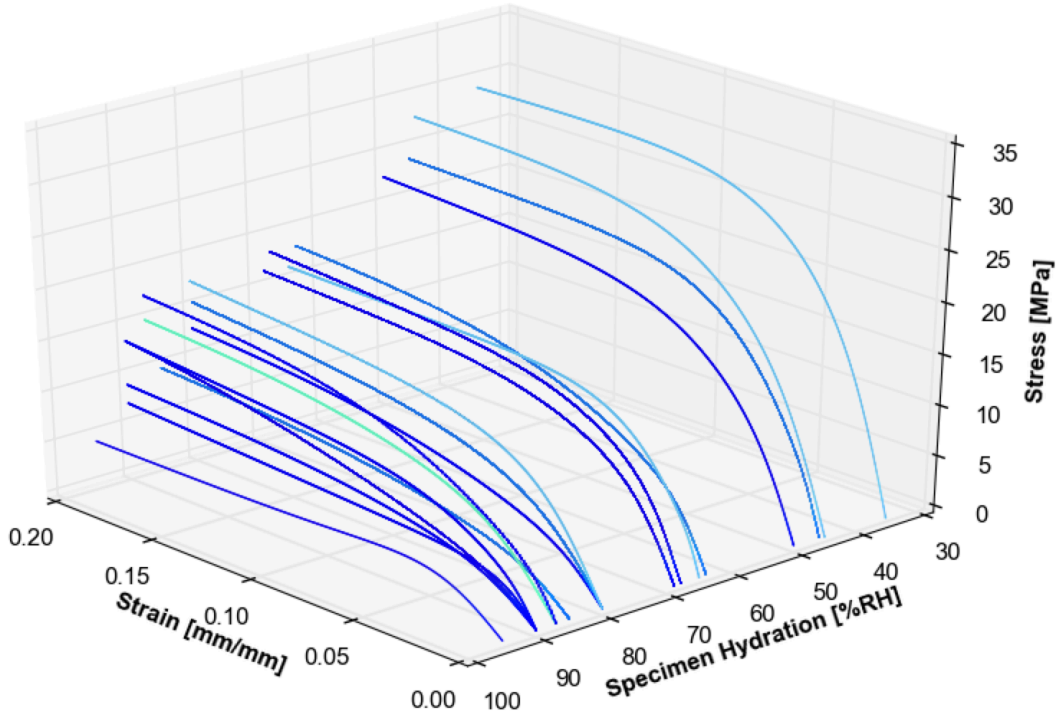

Figure 5.4 Bulk Wall Equine Keratin Tensile Test Results Arranged via %RH.

Overall, for the testing range, the elastic modulus ranged from 175.0-829.2 MPa. Even though the expected trends are seen when comparing the specimen stiffness with specimen hydration, there is variation in the tests with similar %RH. Figure 5.5 presents the equine specimen elastic moduli for the %RH conditions tension testing occurred at.

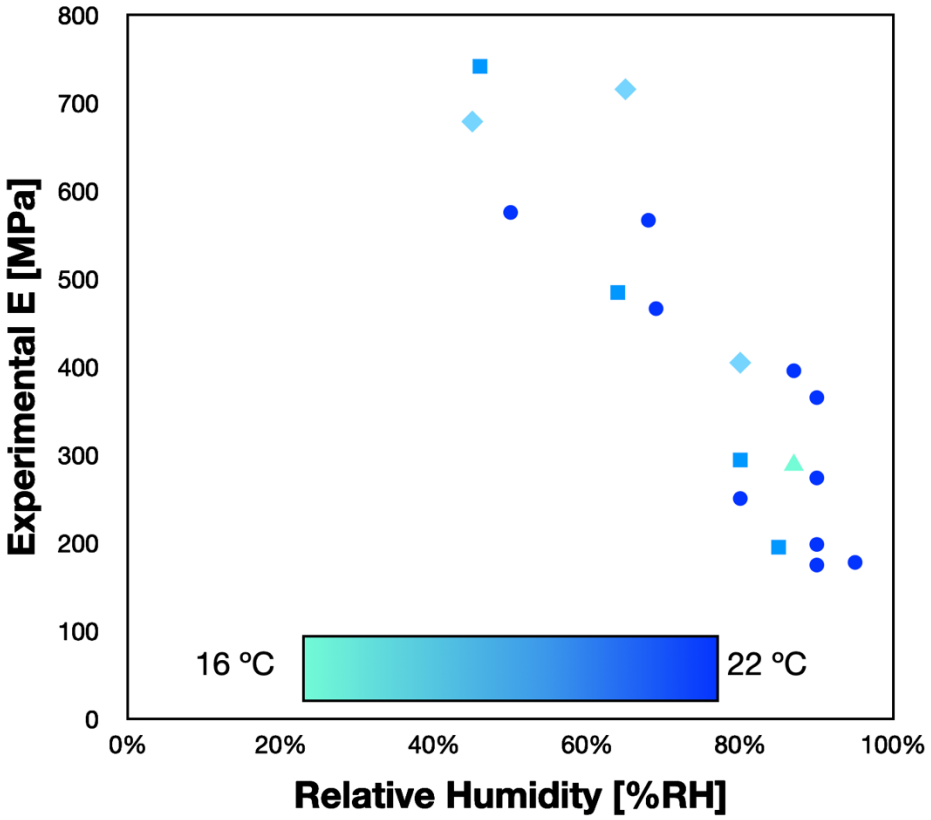

Figure 5.5 Elastic Moduli vs %RH of Tested Bulk Wall Equine Keratin Specimens.

For example, the 4 specimens tension tested at 90%RH (all at room temperature) saw elastic moduli ranging from 175-365.3 MPa. Other breaks in the pattern occur when temperature is considered. The 3 specimens tested at 80%RH demonstrate the expected trend of increasing stiffness corresponding to decreasing temperature, however, that established trend is not perfectly modeled in the 85-87%RH range. To account for this deviation, the TD distribution of the specimens in question must be examined (Figure 5.6).

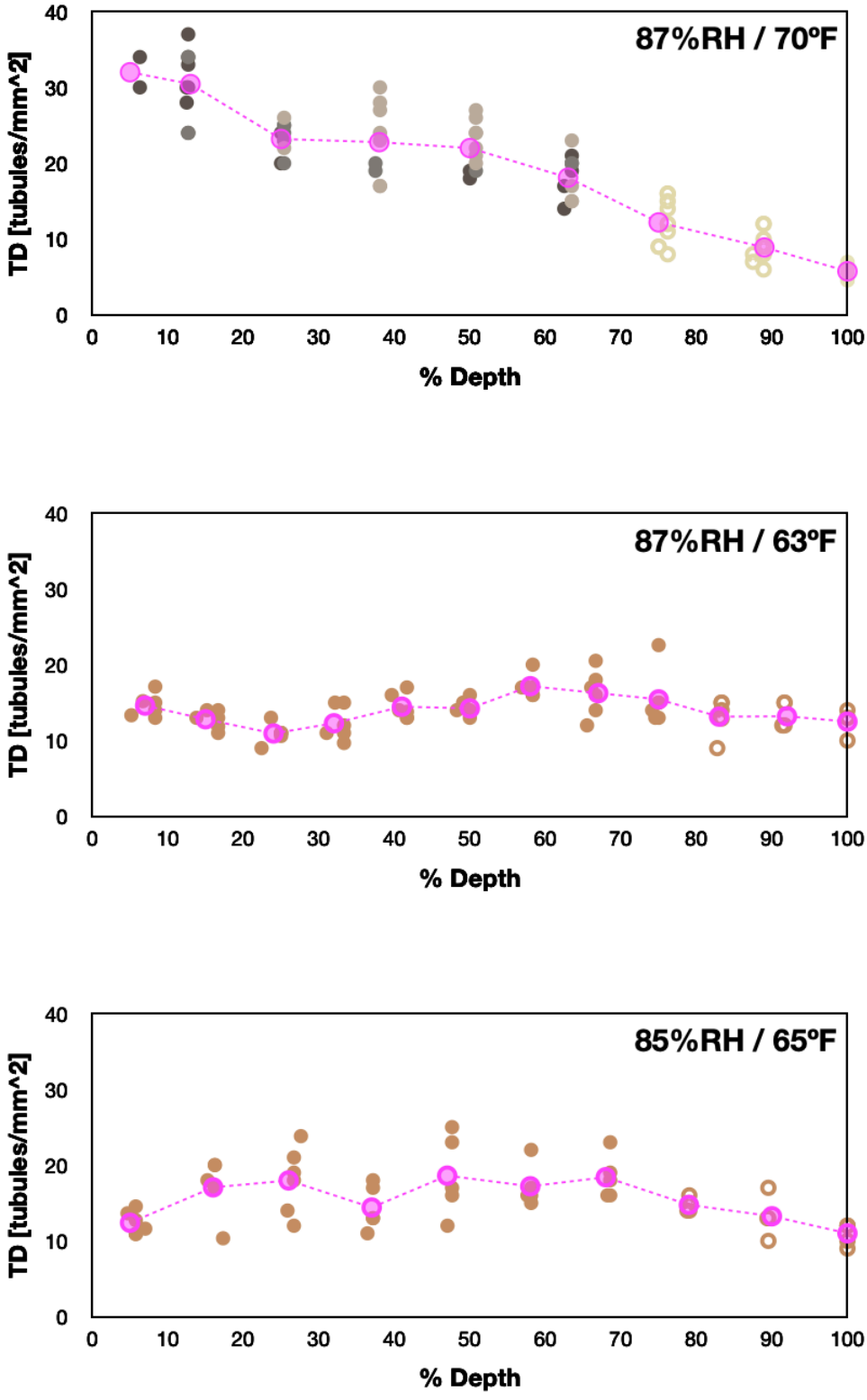

Figure 5.6 Tubule Density Distributions of Tension Specimens Tested in the 85-87%RH and 63-70ºF Condition Ranges.

On the surface, the specimen with the lowest temperature for the same or similar %RH condition would be expected to produce the lowest stress response. However, in this case, that specimen produced the highest stress response and an elastic modulus of 395.8 MPa. This can be explained by the TD distribution of the specimen, which had significantly higher peaks of up to ~35 tubules/mm^2, and a higher overall presence of tubules through most of the wall thickness. The second highest stress response was produced by the specimen tested at 87%RH and 63ºF, with an elastic modulus of 250.1 MPa. The TD distribution of this specimen sees peaks of ~15-20 tubules/mm^2 and maintains a lower average TD throughout the wall thickness than the other 2 specimens in this testing range. Additionally, the %RH is slightly lower than the other specimens, and these factors should result in the lowest stress response of this comparison. However, the lower temperature increased the stress response just enough to achieve second place. It is also interesting to note that the TD distribution is more consistent along the width of the specimen, as is indicated by the reduced scatter in the TD data plot. The lowest performing specimen (85%RH and 65ºF), which had an elastic modulus of 195.3 MPa, saw more scatter in the TD data, despite having slightly higher peaks and averages through the wall thickness.

This data set comparison is representative of the competing variables that determine the stress response and material behavior of equine hoof keratin. Hydration conditions can determine the general trend of keratin stiffness. However, TD plays an important role in affecting the material behavior, and, when the TD peaks are high enough, can have a greater impact than temperature. Temperature also has a significant impact on the stress response of equine keratin, however, that appears to become more dominant when paired with mid to low TD values.

5.3 Summary Conclusions

Major conclusions are summarized as follows:

- The fracture surfaces of the equine hoof wall specimens were angled and tortuous. This supports the supposition that the SM serves as a crack growth inhibitor by forcing the crack to propagate in a non-linear fashion and travel a further cumulative distance.
- The modulus of elasticity, E, is inversely related to the hydration level, %RH, of the keratin specimen. The more hydrated the keratin is, the more ductile behaving this material becomes, just as the keratin behaves more brittlely as the material dehydrates.
- Keratin specimens of the proximodistal orientation exhibit a higher stress response when the tubule density is increased; conversely, there is a lower stress response correlated with lower tubule densities.
- Equine keratin specimens fabricated in the proximodistal orientation demonstrated higher material stiffness as TD increased; conversely, lower elastic moduli correlated with lower TDs.
- As the temperature increases, the more ductile the equine keratin behaves, just as the material becomes more brittle behaving as the temperature decreases. Environmental factors, such as temperature and humidity have a significant effect on keratin behavior, and thus, overall hoof health.
- TD plays an important role in affecting the material behavior, and, when the TD peaks are high enough, can have a greater impact than temperature. Temperature

also has a significant impact on the stress response of equine keratin, however, that appears to become more dominant when paired with mid to low TD values.

CHAPTER 6

TUBULE DISTRIBUTION AND KERATIN PIGMENTATION

6.1 Introduction

Twenty-two bulk hoof wall samples were extracted from the hoof capsule toe regions of 15 different horses. Each sample was prepared for TD analysis as per the procedure explained in Section 3.5. The TD profile of each sample was graphed in such a way where each point is colored to match the keratin pigmentation at that location. This allows for a both an understanding of the TD ranges a horse hoof may have, and the ability to track any pigmentation trends. One of the most hotly debated questions in the farrier world to this day is whether hooves with lighter pigmentation are "softer" than hooves with darker pigmentation. In this chapter, typical TD distributions trends are identified, and specific pigmentation comparisons are presented and discussed.

6.2 Linking Tubule Density Distribution to Keratin Pigmentation

Throughout the research conducted, pigmentation coloration was tracked whenever TD distribution data was collected. Of the 22 specimens, 10 had light pigmentation, 6 were darkly pigmented, and 6 were a combination of the two. The data points plotted in the TD distribution profile graphs were color coded to match that of the keratin in question. This is perhaps most pertinent when viewing a mixed pigmentation keratin sample, as the coloration altered through the thickness of the wall. One such instance is presented in Figure 6.1, where the outer surface of the hoof wall (SE and outer SM) shows dark pigmentation which becomes light towards the inside surface (inner SM and SI). There is also a small patch of dark pigmentation near the inside hoof wall surface. The specimen TD distribution profile shows the color coordination of the data points.

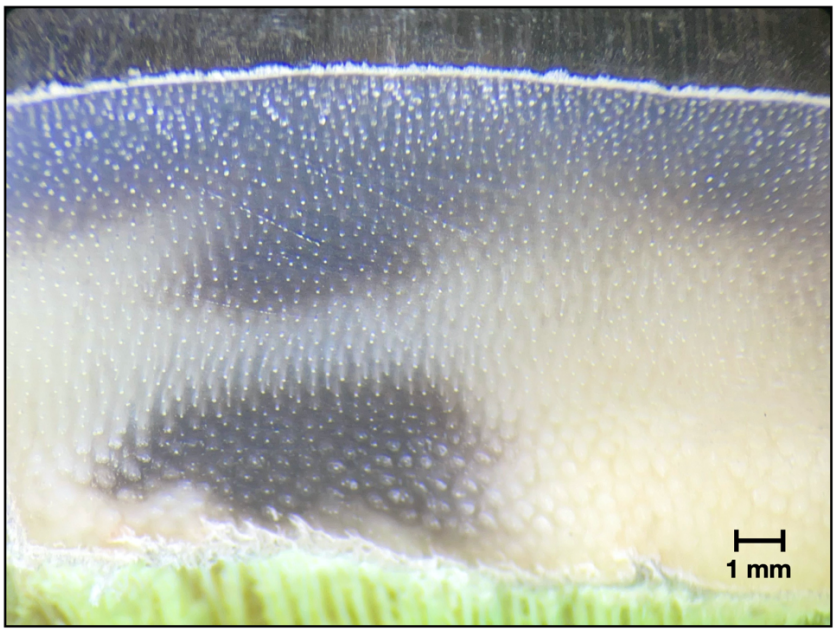

(a)

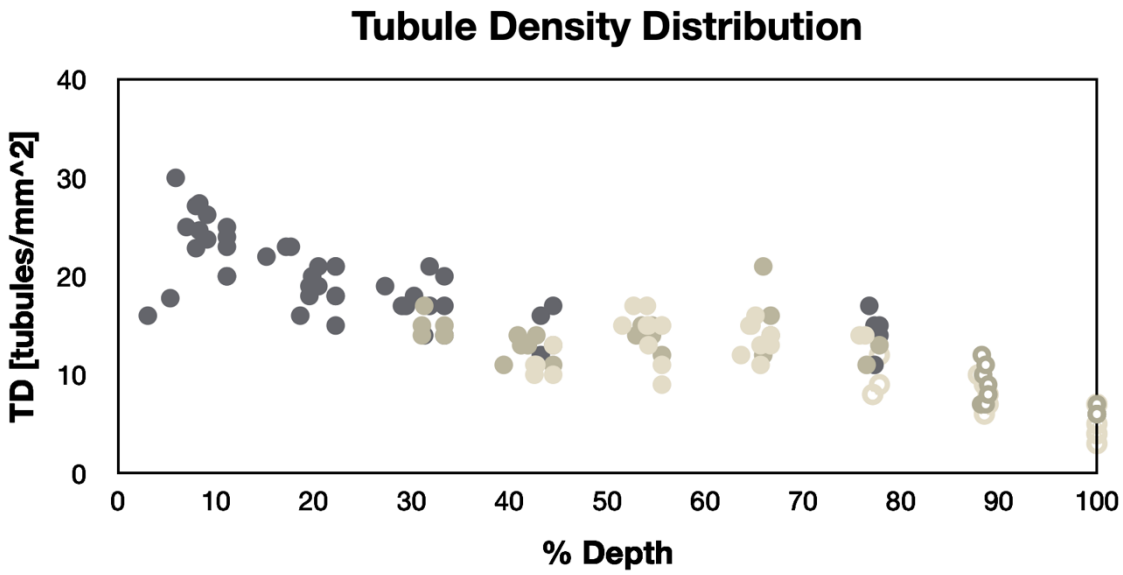

(b)

Figure 6.1 (a) Equine Hoof Keratin Cross-sectional Area with Mixed Pigmentation and (b) Associated TD Distribution Profile

All TD distribution profiles are compared in Figure 6.2. There is visually apparent color trend where the light pigmentated keratin generally saw lower TD peaks and a less variable profile

overall. The dark pigmentated keratin saw higher TD peaks, most significantly in the outer 20% depth of the hoof wall. Keratin with combination pigmentation—medium browns and transition hues— had TD distributions that appear to land between the dark and light pigmented keratin.

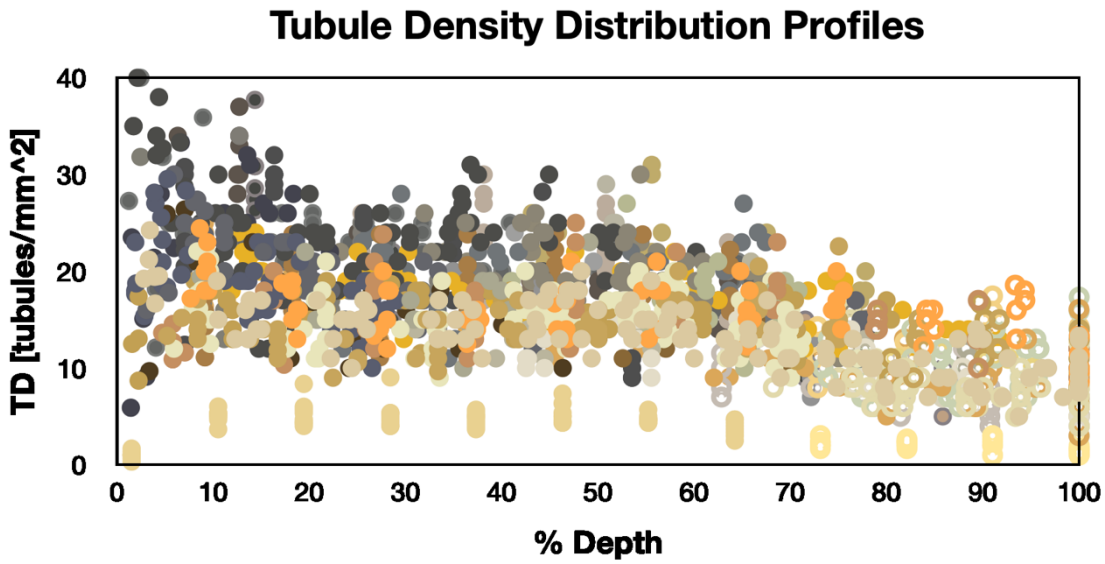

Figure 6.2 Cumulative Color-coded Tubule Density Distribution Profiles

The three pigmentation categories were isolated for further analysis, the TD distribution profiles for which are displayed in Figure 6.3. Each grouping of TD data was averaged through the hoof wall depth (0-100%) in increments of ~5%, which is represented on the plots via the larger, purple circles and dashed lines. The differences in the profile shapes are more easily examined when isolated by pigmentation coloration. An interesting thing to note is the spread of data per pigmentation color. The dark pigmentation saw a denser data population in the outer half of the hoof wall, and the combination pigmentation was commonly found at ~20-70% depth. The light pigmentation was abundant throughout, which is expected due to the larger sample size of specimens. However, there was still a denser data population from ~70-100% wall depth.

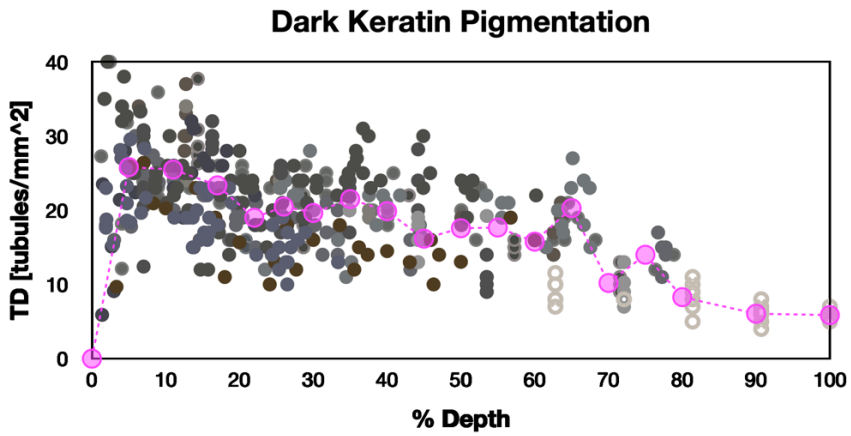

(a)

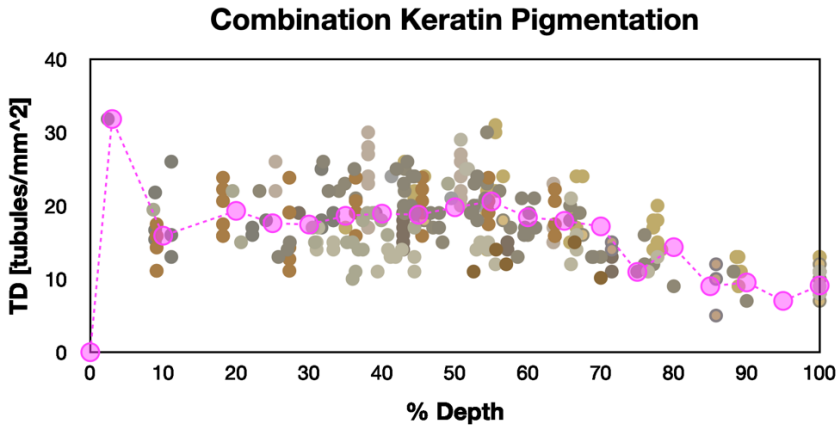

(b)

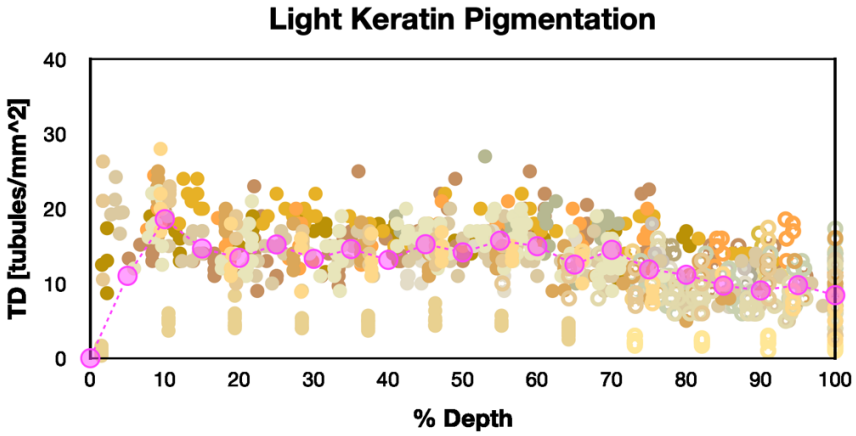

(c)

Figure 6.3 Cumulative Tubule Density Distributions of Keratin with (a) Dark Pigmentation, (b) Combination Pigmentation, and (c) Dark Pigmentation

The averaged TD distribution profiles were extracted and compared, which can be found in Figure 6.4. All profiles saw an initial peak occur in the outer ~10% of the hoof wall. The dark pigmented keratin profile saw the most fluctuation—that is to say, it had the most peaks and valleys—and the light pigmented keratin had the steadiest profile. The average TD distribution profile for combination pigmentation showed an initial peak and valley in line with the dark keratin trend, but it seemed to become steadier throughout the rest of the hoof wall thickness. The light keratin generally appeared to be lower than that of the dark and combination pigmentation in the first 0-70% of the hoof wall thickness. All three trends of the TD distribution profiles appeared to converge during the innermost 30% of the hoof wall thickness (70-100%). This makes sense because all equine hoof keratin sees a reduction in TD closer to the SI, as that is the region where the hard keratin material begins transitioning into soft tissue.

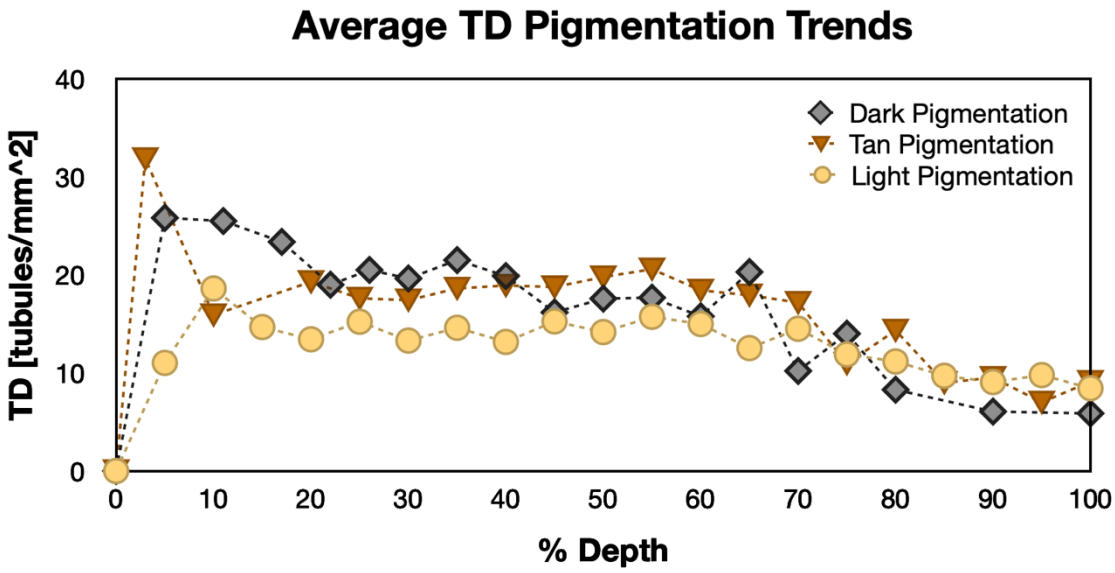

Figure 6.4 Average Tubule Density Distribution Profiles for Light, Dark, and Combination Keratin Pigmentation

Overall, the most prominent difference between the light pigmented keratin TD profile and the dark and combination pigmented keratin is the magnitude of the initial peaks (outer 10% hoof depth). The dark and combination keratin saw significantly higher initial peaks of TD than that of the light keratin. While this may not seem significant upon first glance, that initial TD peak has an impact on the stress response of equine keratin in tension. This becomes clear when considering the rapid increase of local material stiffness as TD increases. If this line of thought is followed through to its inevitable conclusion, then it would seem that hooves with dark or combination pigmentation are likely to be stiffer than light hooves. Correlation, however, does not necessarily equal causation. Keratin pigmentation may potentially be an indication of how "soft" a horse hoof is, but that does not necessarily mean it is the cause. The cumulative dark pigmentation TD distribution profiles shown in Figure 6.3 widely vary with initial TD peaks ranging from ~20-40 tubules/mm^2, implying that some dark hooves may be much stiffer than others. Likewise, the light keratin cumulative TD distribution profiles see a handful of initial peaks reach upwards of ~28 tubules/mm^2, though this occurrence is rarer. The wide variation away from the average TD distribution profiles may explain some of the conflicting observations regarding the "softness" of light hooves. To come to a definitive conclusion on this subject would require expanding the current data set, which is a goal set for future research. However, the results presented here make a strong argument for pursuing this theory further.

6.3 Summary Conclusions

In this chapter, equine hoof keratin with light, dark, and combination pigmentation were examined to obtain TD distribution profiles. These profiles were graphed with color-coded

data points for ease of comparison between samples with different pigmentations. Major conclusions are summarized as follows:

- A correlation was found between higher TDs and dark keratin pigmentation. Additionally, the TD distribution profiles of dark keratin generally display more peaks and valleys than other keratin coloration. Initial TD peaks occurring at the outer ~0-20% depth reached upwards of 40 tubules/mm^2.
- A correlation was found between lower TDs and light keratin pigmentation. Additionally, the TD distribution profiles of light keratin generally display a less variable profile than other keratin coloration. Initial TD peaks occurring at the outer ~0-20% depth reached upwards of ~28 tubules/mm^2.
- Keratin with combination pigmentation generally saw trends between that of the light and dark keratin TD distribution profiles.
- When considering the observed relationship between higher material stiffness and higher TDs, there is an implication that equine keratin with dark pigmentation will tend to exhibit higher stiffnesses than that of light keratin.
- The wide variation away from the average TD distribution profiles may explain some of the conflicting observations regarding the "softness" of light hooves.
- While there appears to be a potential correlation between light keratin pigmentation (which, on average, appear to have lower TD distribution profiles) and "softer" hooves, correlation is not causation. The results here present a strong case to pursue this theory by expanding the data set in future research.

CHAPTER 7

UTILIZING FINITE ELEMENT ANALYSIS TO PREDICT LOCALIZED HOOF WALL BEHAIVIOR

7.1 Introduction

Now that the bulk wall stiffness of equine keratin has been quantified and experimental data obtained, the next logical step is to explore how material behavior can be predicted. By developing a process that can predict the stiffness of a specific horse's hoof based on field data obtained from hoof trimming (cast offs produced during shoeing preparations), any farrier can gain a deep knowledge of how that animal should be shoed. Furthermore, using a free, intuitive, readily available FEA program that is accessible by the average individual, will produce a method that can be utilized by the average farrier. This method of FEA would serve as the cornerstone for modeling the entire hoof capsule and simulating how different shoeing options would suit a specific horse.

This portion of the study aims correlate the local keratin stiffness trends (see Chapter 4) with the experimentally determined bulk wall stiffnesses (see Chapter 5) via TD distribution, %RH, and temperature conditions. This is an effort to clarify the complex, multivariable nature of the topic by forging relationships between TD distribution, local/regional keratin stiffness, %RH, temperature, and tubule orientation by utilizing FEA.

7.2 Digital Modeling Program and Approach

The keratin specimen model construction and subsequent FEA simulation was performed using Autodesk Fusion 360 (Autodesk Inc., San Raphael, CA, USA). The specimen CAD models consisted of 3-5 layers (Figure 7.1) corresponding with the unique specimen TD distribution profile.

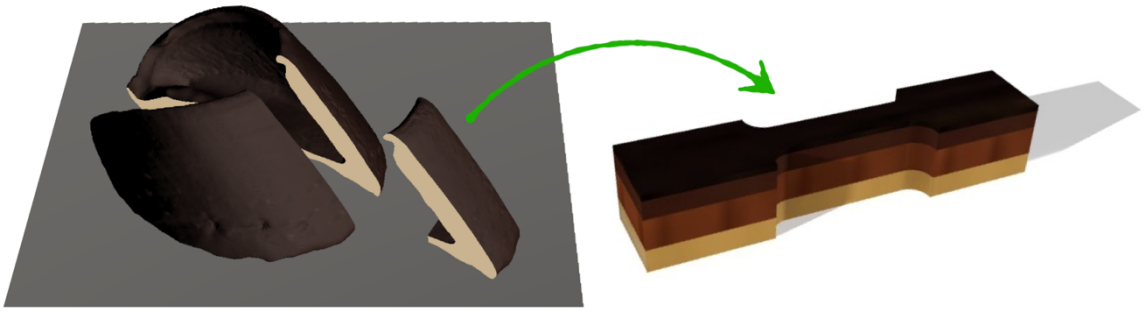

Figure 7.1 Representative CAD Model of an Equine Keratin Bulk Wall Tensile Specimen Comprised of 4 Layers

The TD fluctuates through the thickness of the hoof wall, from outer surface (SE) to the transition between keratin and soft tissue (SI). Since different stiffnesses are associated with different TDs, the material stiffness will change throughout the hoof wall thickness, and this must be accounted for in the FEA simulation. To model all of the tubules in the specimen CAD model would require greater time and effort per specimen in the modeling stage and require a significantly smaller element size utilized during FEA simulations. This would increase computational time and resources beyond the average individual. A more streamline approach was taken to avoid these issues. First, only the gage section was modeled, allowing for a simpler element distribution throughout a rectangular body, as opposed to modeling in the grip section and radial fillet transitions. Secondly, rather than model each tubule, an "effective cross-sectional area" was determined for each layer of the specimen. This effective cross-sectional area was obtained by reducing the original specimen cross-sectional area by that of the hollow tubules present, while maintaining the original aspect ratio. Figure 7.2 shows the relationship between the original specimen cross-sectional area and the TD distribution profile. The TD distribution profile was

divided into four approximate regions of similar TDs, ranging the full wall thickness (from 0% depth of the SE to 100% depth of the SI).

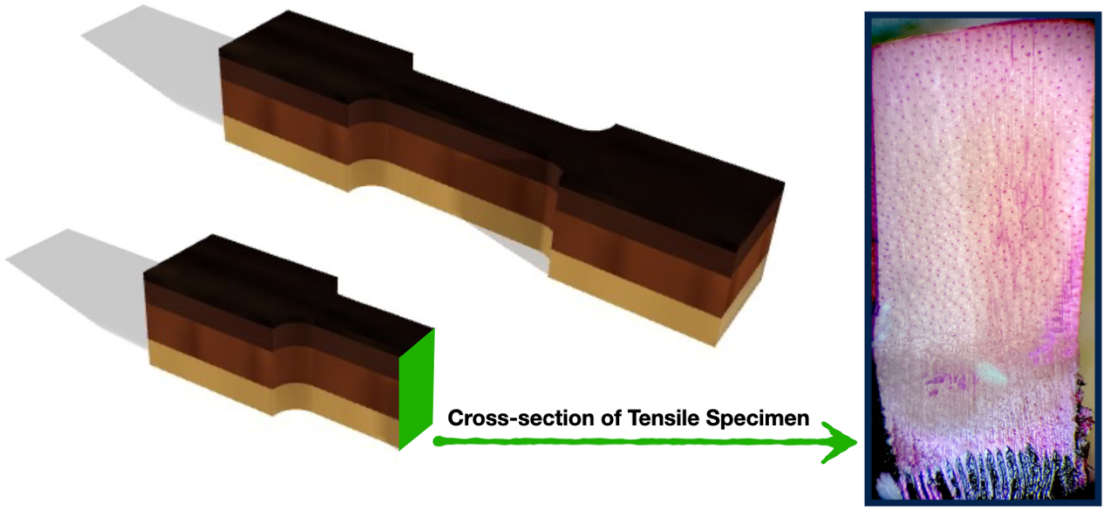

(a)

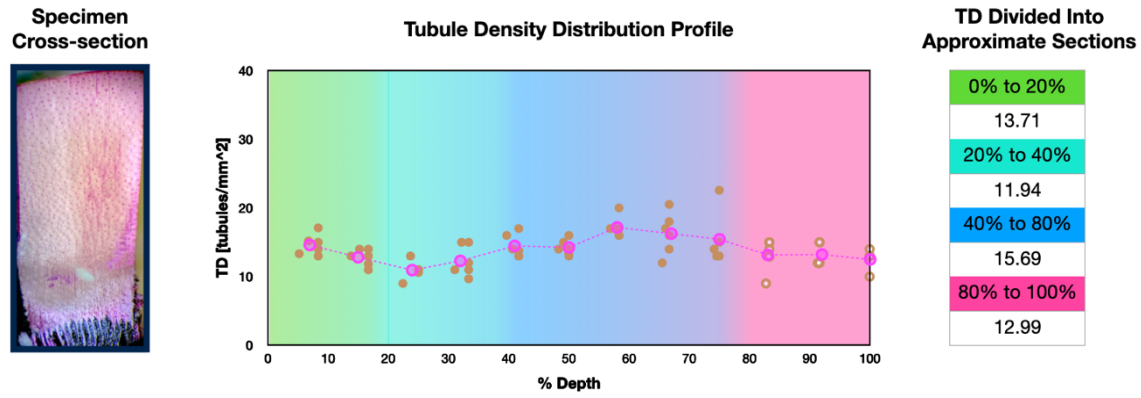

(b)

Figure 7.2 Representative Tensile Specimen (a) Cross-sectional Area, and (b) Associated TD Distribution Profile and Approximated Layer Data

Once the sections have been delineated, an average TD is obtained for that section of the wall thickness. Following the example shown in Figure 7.2, the four layers from outer to inner surface have average TDs of 13.7, 11.9, 15.7, and 13.0, respectively. These TDs can be linked to the local keratin properties presented Chapter 4. Those local stiffnesses

associated with the testing conditions of that specific tensile specimen can then be assigned to each layer of the CAD model as customized material properties (Figure 7.3).

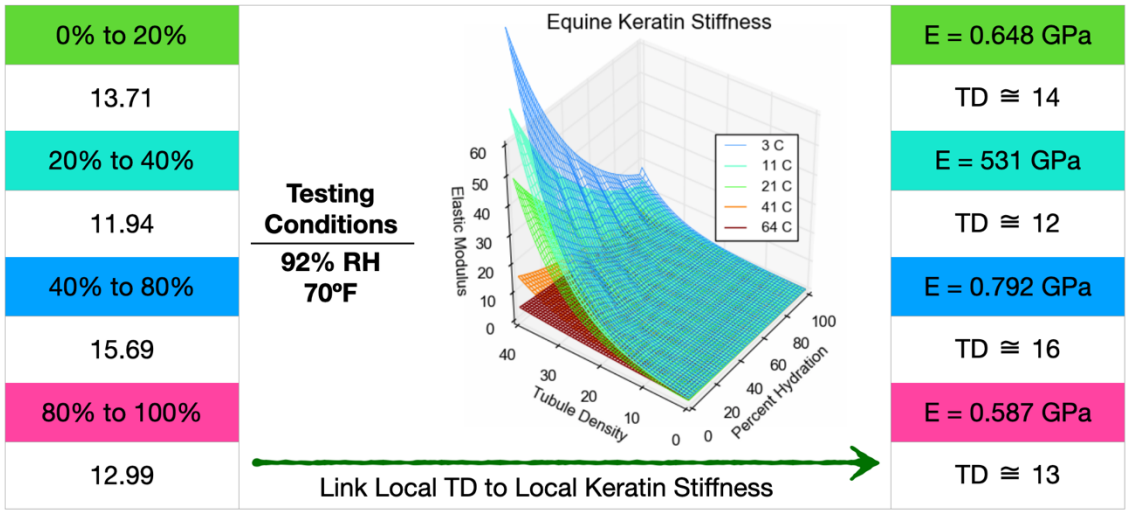

(a)

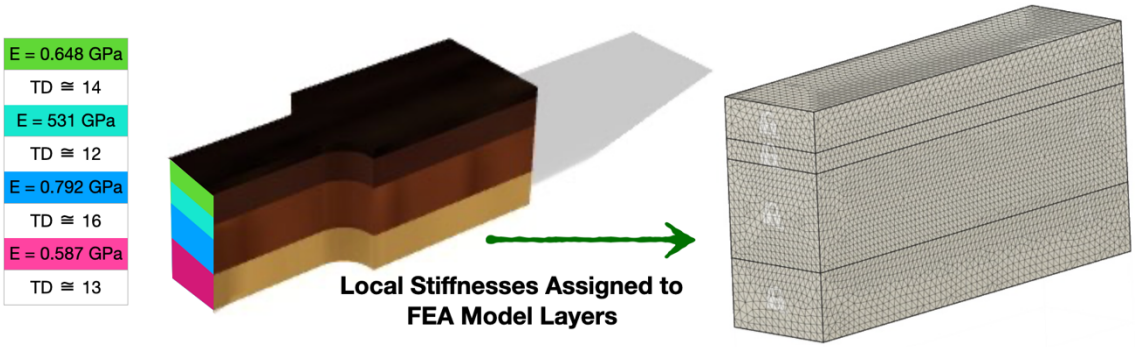

(b)

Figure 7.3 (a) Association Between Local TDs and Local Keratin Stiffness, and (b) Custom Stiffnesses Assigned to FEA Model

To calculate the size of the total effective cross-sectional area, the following equations can be applied:

(Eq. 7.1) $$A_{total_{effective}} = A_{total_{nominal}} - N_{tubule}\left(\frac{\pi}{4}D_{tubule}^2\right)$$

Where $A_{total\ effective}$ is the total effective cross-sectional area, $A_{total\ nominal}$ is the original cross-sectional area of the specimen, N_{tubule} is the total number of tubules present in the specimen, and D_{tubule} is the approximate diameter of the circular tubule mouth.

The effective cross-sectional area of each individual layer of the model can be determined by the following equation:

(Eq. 7.2) $$A_{effective_i} = A_{nominal_i} - A_{tubule_i}$$

$A_{nominal\ i}$ and $A_{tubule\ i}$ can be expanded into Equations 7.3 and 7.4, respectively, and be combined with Eq. 7.2 to generate the fully expanded expression in Eq. 7.5:

(Eq. 7.3) $$A_{nominal_i} = w(d_i t)$$

(Eq. 7.4) $$A_{tubule_i} = (TD_i A_{nominal_i})\left(\frac{\pi}{4} D_{tubule}^2\right)$$

(Eq. 7.5) $$A_{effective_i} = w(d_i t) - \left(TD_i\left(w(d_i t)\right)\right)\left(\frac{\pi}{4} D_{tubule}^2\right)$$

Where w is the nominal cross-sectional width, t is the nominal cross-sectional thickness, d_i is the layer proportion of the nominal cross-sectional thickness, and TD is the tubule density of the layer. The challenge, however, is to maintain the original specimen cross-sectional aspect ratio with the new, effective cross-sectional area. The effective width, $w_{effective\ total}$ and the effective thickness, $t_{effective\ total}$, can be determined using the following two equations:

(Eq. 7.6) $$w_{effective_{total}} = \sqrt{\frac{wA_{total_{effective}}}{t}}$$

(Eq. 7.7) $$t_{effective_{total}} = \sqrt{\frac{tA_{total_{effective}}}{w}}$$

Finally, to obtain each effective layer thickness required to dimension the CAD model:

(Eq. 7.8) $$t_{effective_i} = d_i t_{effective_{total}}$$

Once the effective specimen geometry is calculated and modeled, each layer is assigned the custom material property. As stated previously, the elastic modulus was determined from the local keratin property characterization discussed in Chapter 4. Because equine keratin has direction-dependent properties, the sheer modulus was determined for an orthotropic case using Huber's equation:

(Eq. 7.9) $$G_{12} = \frac{\sqrt{E_x E_y}}{2\left(1 + \sqrt{v_{xy} v_{yx}}\right)}$$

Where E_x and E_y are the directional elastic moduli determined from the local keratin properties, and v_{xy} and v_{yx} are the directional Poisson's ratios assumed to be 0.4 (sourced from the literature [34] [87]).

The mesh was comprised of tetrahedral elements, with an assigned "absolute size" of 0.3 mm. The element size was selected through a mesh refinement study, where the same simulation was iteratively conducted for various element sizes. Once the simulation results no longer fluctuated, that element size was chosen. This approach identified the most economic element size (that still produced steady state results) in terms of computation time. Figure 7.4 presents the findings of the mesh refinement study. The simulation constraints were imposed upon the model. One end of the specimen was held static in all directions while a prescribed displacement was applied to the opposite cross-section. For each specimen, five simulations were conducted with a prescribed displacement of 0.01 mm, 0.05 mm, 0.1 mm, 0.15 mm, and 0.2 mm. Representations of a typical mesh, prescribed displacement, strain, and stress simulation details are illustrated in Figure 7.5.

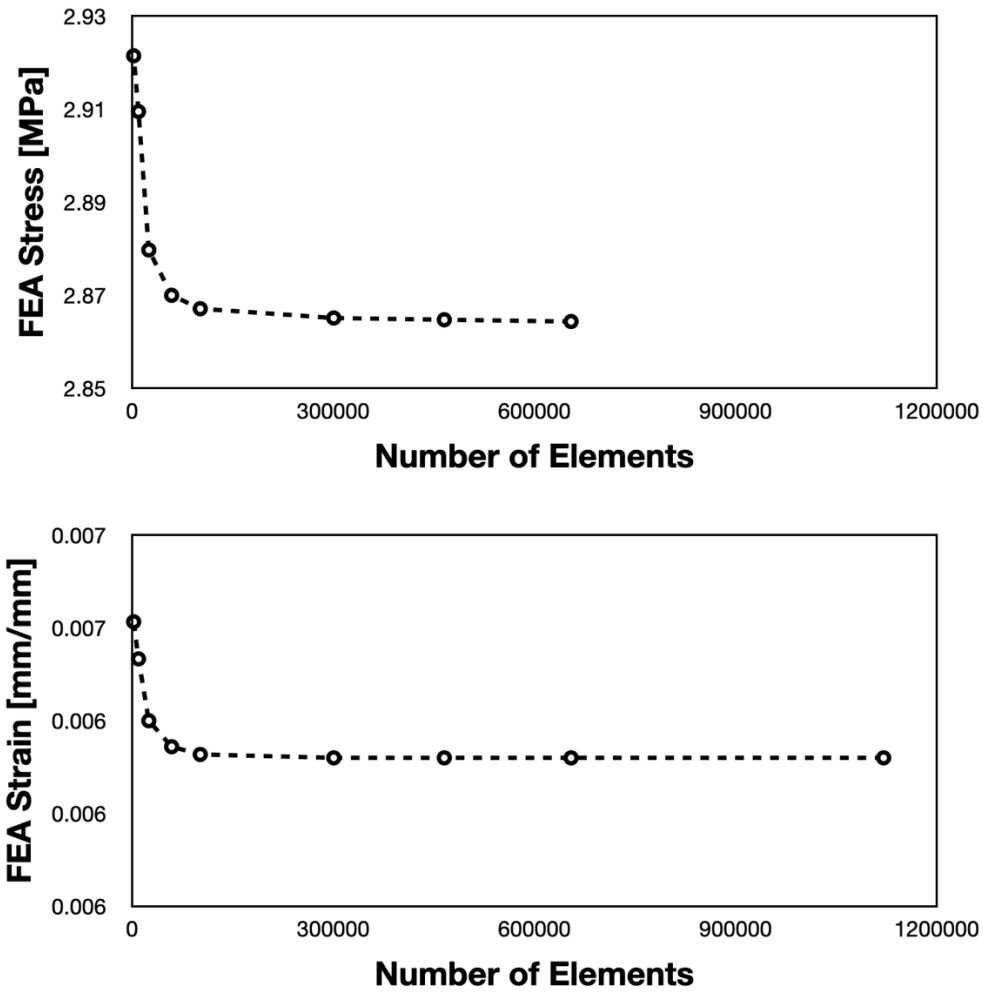

Figure 7.4 Mesh Refinement Study to Determine Best Element Size

Von Mises stress and strain was obtained for each simulation by using the average values of each segment from the center of the gage section. A slice plane view was created and an inspection point probe was placed in the center of each layer's cross-sectional area, an example of which can be found in Figure 7.6. Equation 7.10 was used to calculate the average Von Mises stress in the multi-layer specimen models.

(Eq. 7.10) $$\sigma_{avg} = \frac{\sum_{i=1}^{N} \sigma_i A_{effective_i}}{A_{effective_{total}}}$$

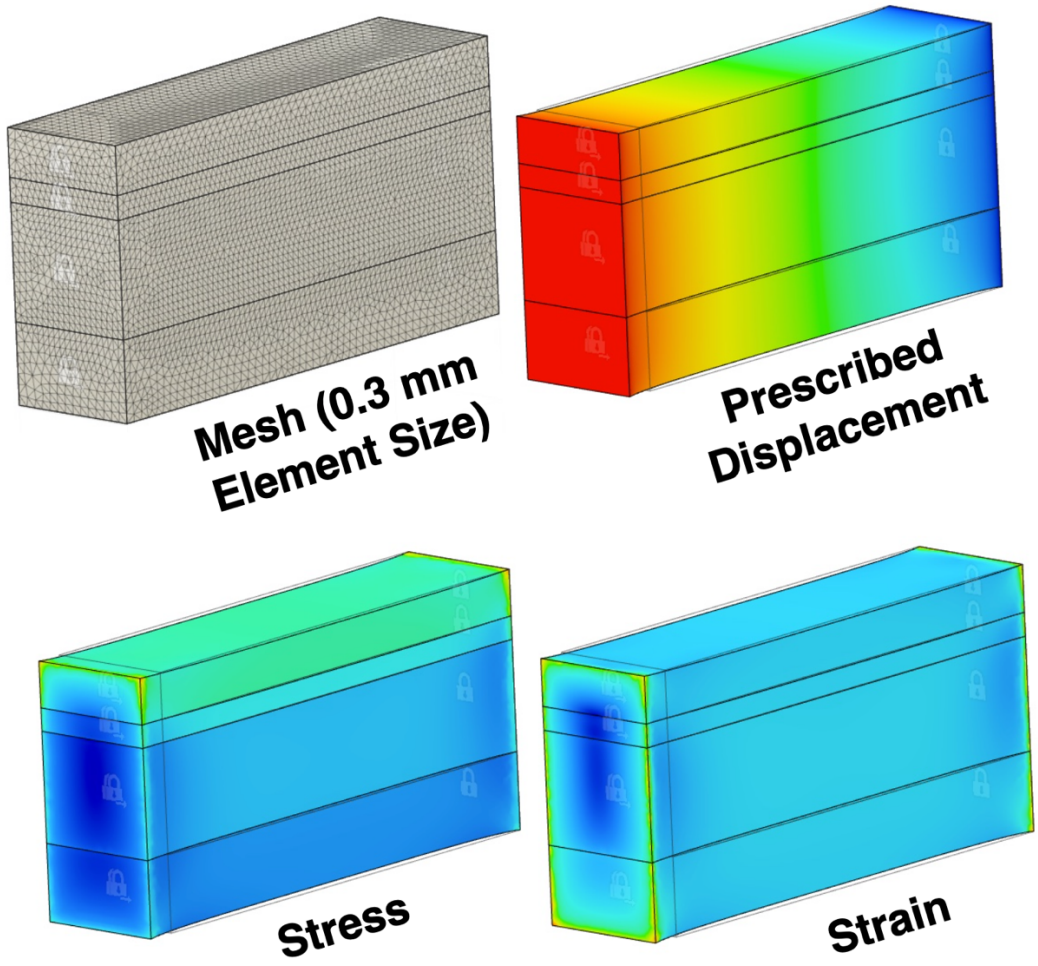

Figure 7.5 Typical Mesh, Prescribed Displacement, Stress, and Strain Simulation Details

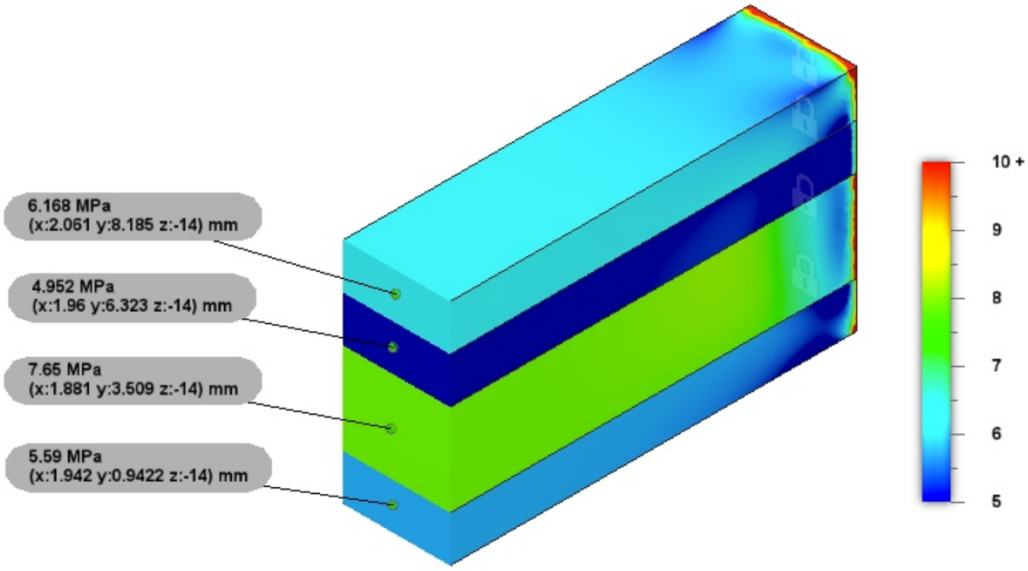

Figure 7.6 Slice-Plane View of Resulting Simulated Von Mises Stress

The strain was calculated using the following equation:

(Eq. 7.11) $$\epsilon_{FEA} = \frac{\delta}{L}$$

Where **δ** represents the prescribed displacement and L represents the gage length.

To determine how well the simulation results compared to the experimental results of the same specimen, the simulated stress-strain results were superimposed onto the experimental tensile curve so the initial elastic moduli could be qualitatively and quantitatively compared. Figure 7.7 displays a typical comparison between experimental and simulated results.

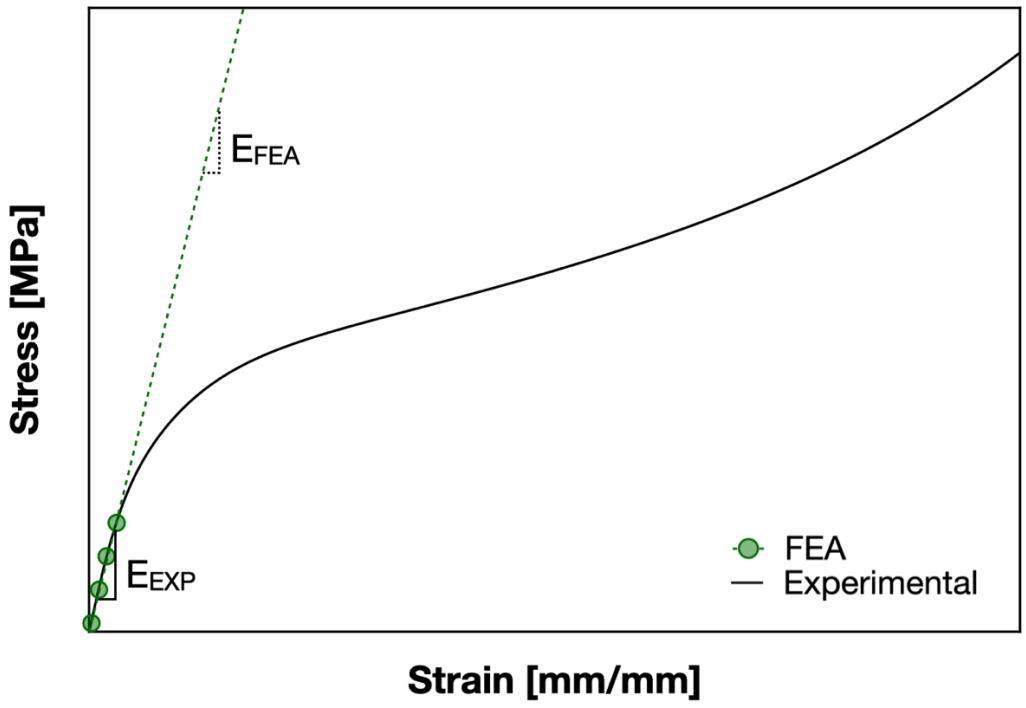

Figure 7.7 Typical Comparison Between Experimental and Simulated Results

7.3 Comparing Experimental Data with the Analytical Model

The simulation of each bulk hoof wall tensile specimen tested in Chapter 5 was assigned a series of prescribed displacements between 0.01 mm-0.2 mm. The simulated elastic modulus was superimposed onto the experimentally obtained tensile curves.

Specimen 1 was tested at 90%RH and 21ºC, and the simulated stiffness is compared with the experimental tensile curve in Figure 7.8. The initial elastic modulus appears reasonably well predicted.

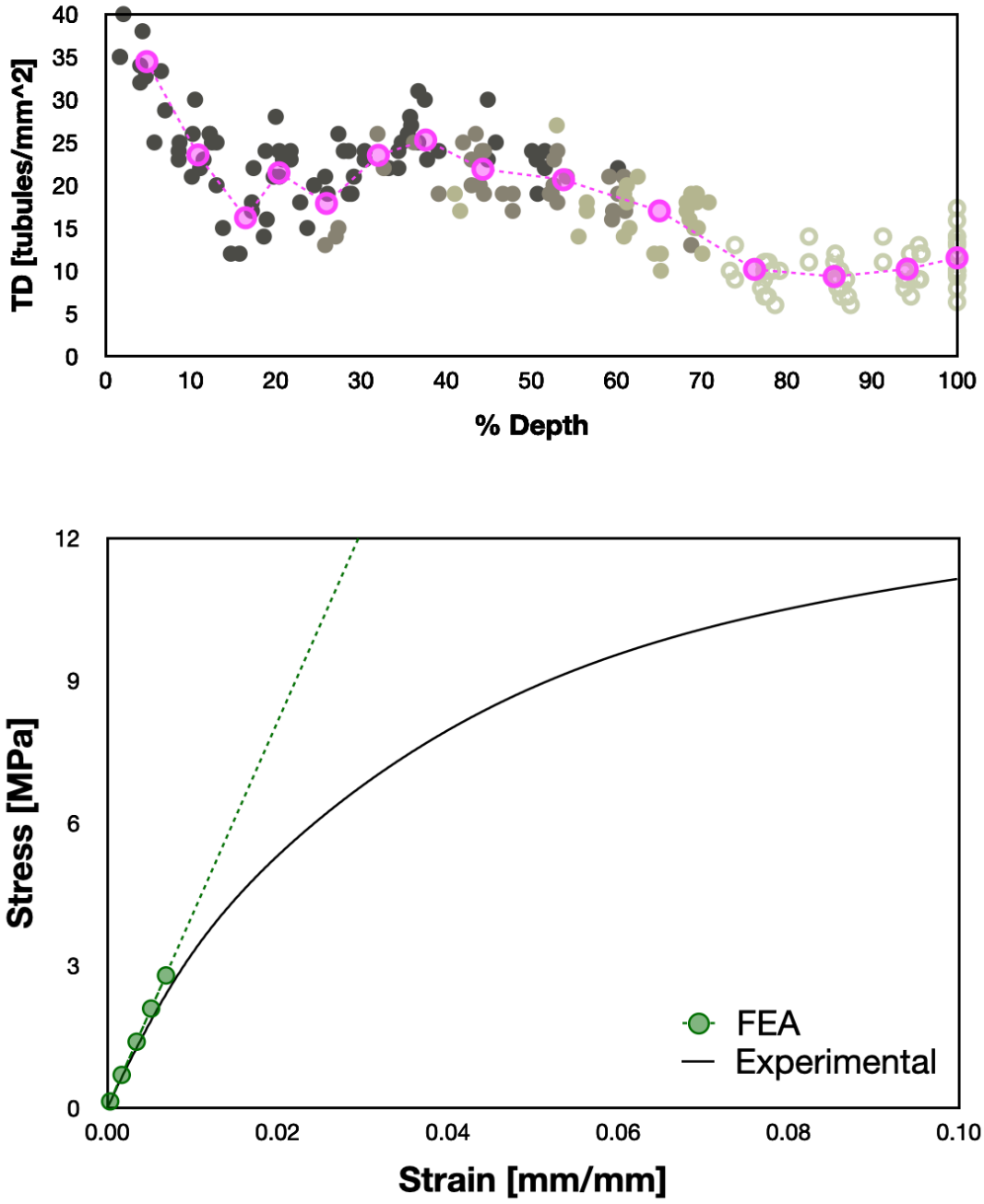

Figure 7.8 Comparison Between Experimental and Simulated Results of Specimen 1

Specimen 2 was tested at 95%RH and 21ºC, and the simulated stiffness is compared with the experimental tensile curve in Figure 7.9. The initial elastic modulus appears reasonably well predicted.

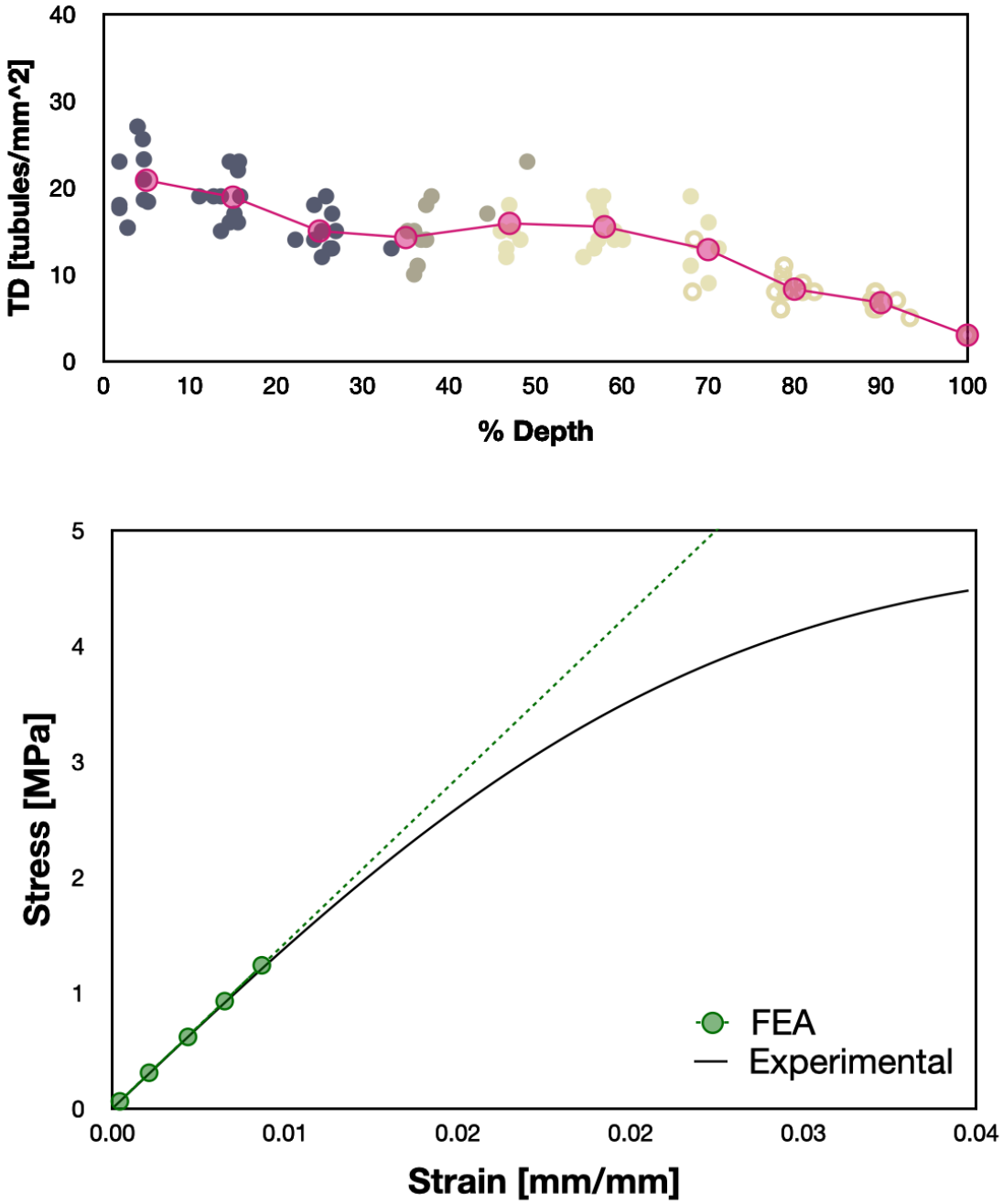

Figure 7.9 Comparison Between Experimental and Simulated Results of Specimen 2

Specimen 3 was tested at 87%RH and 21ºC, and the simulated stiffness is compared with the experimental tensile curve in Figure 7.10. The initial elastic modulus appears reasonably well predicted.

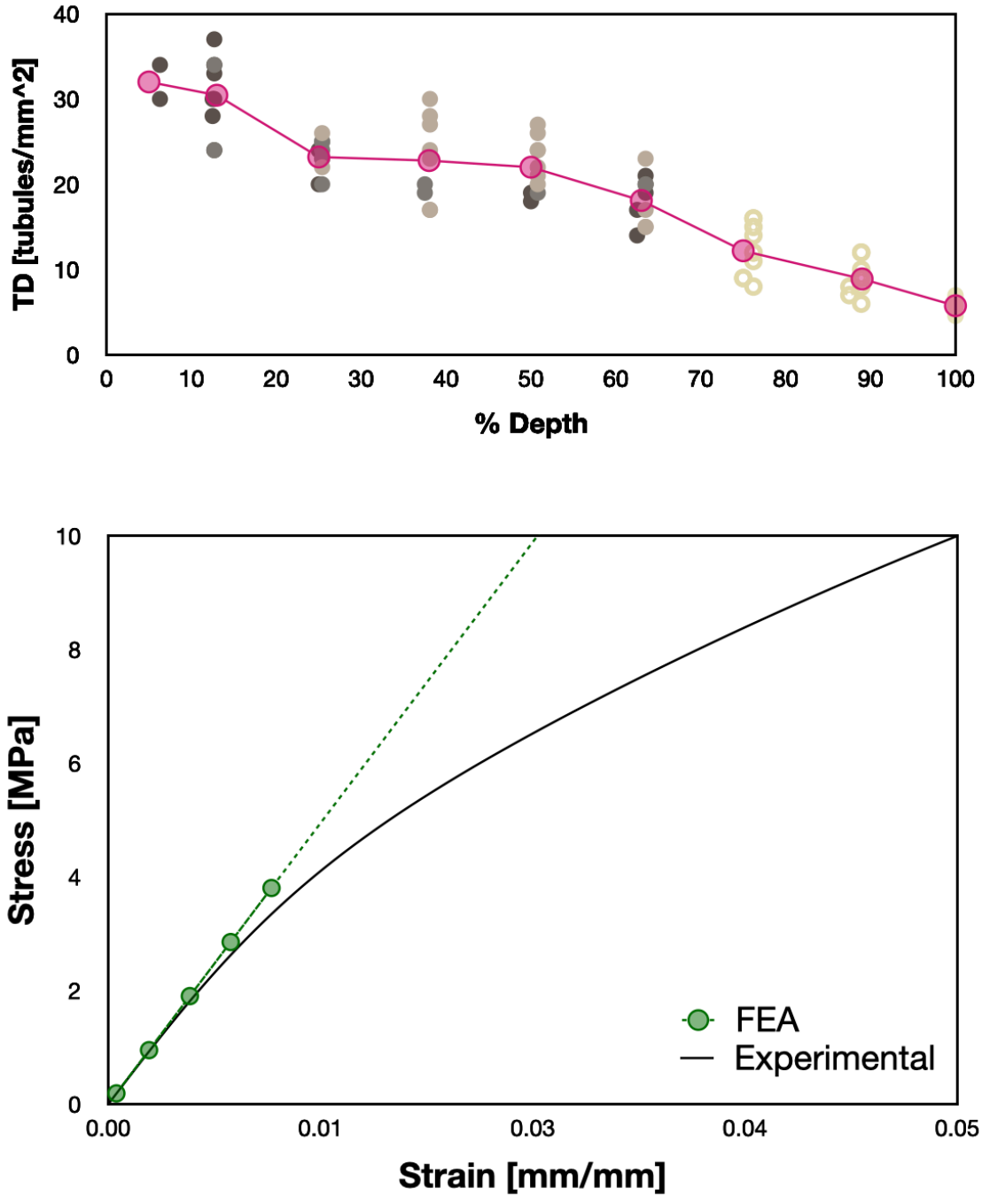

Figure 7.10 Comparison Between Experimental and Simulated Results of Specimen 3

Specimen 4 was tested at 90%RH and 21ºC, and the simulated stiffness is compared with the experimental tensile curve in Figure 7.11. The initial elastic modulus appears reasonably well predicted.

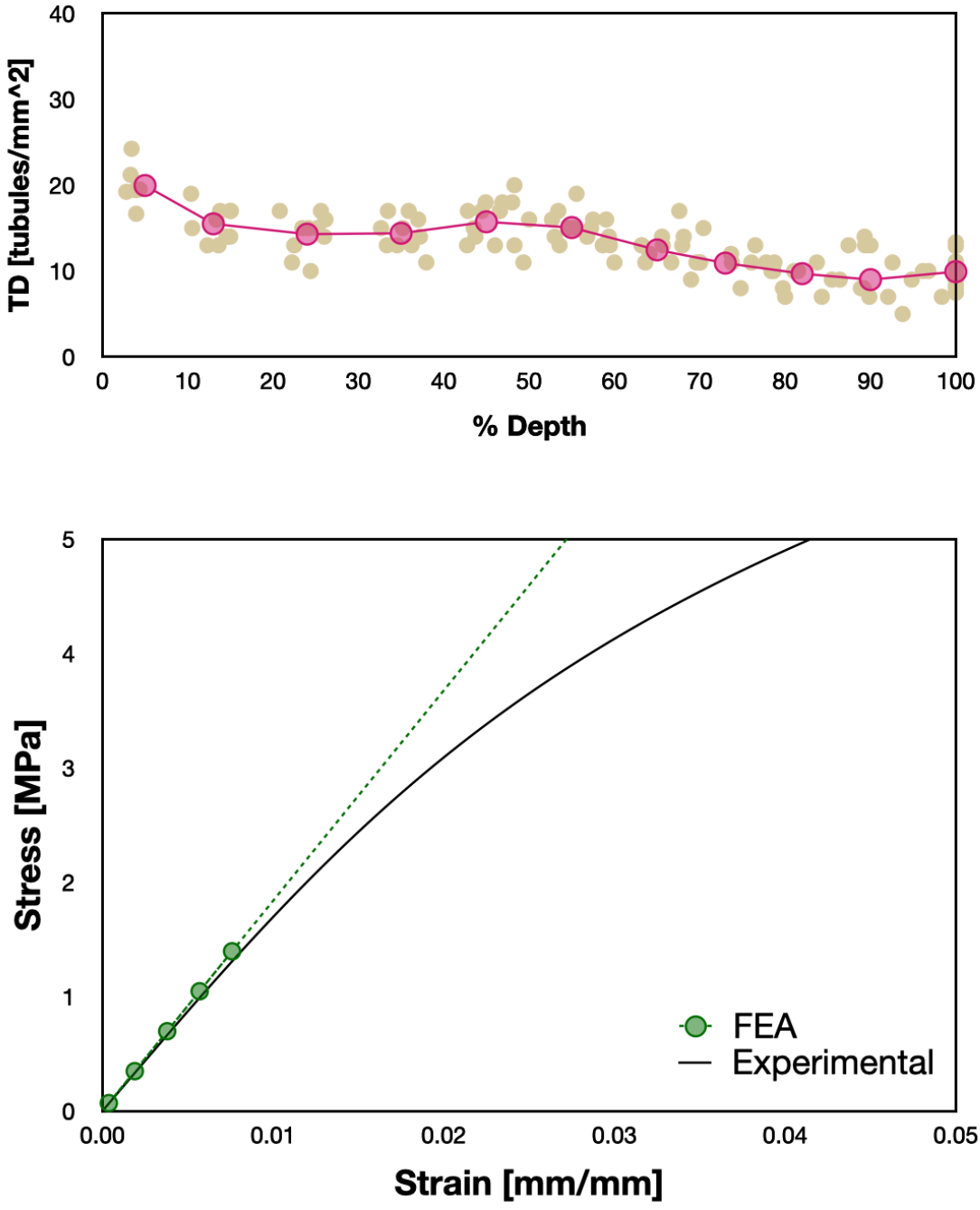

Figure 7.11 Comparison Between Experimental and Simulated Results of Specimen 4

Specimen 5 was tested at 80%RH and 21ºC, and the simulated stiffness is compared with the experimental tensile curve in Figure 7.12. The initial elastic modulus appears reasonably well predicted.

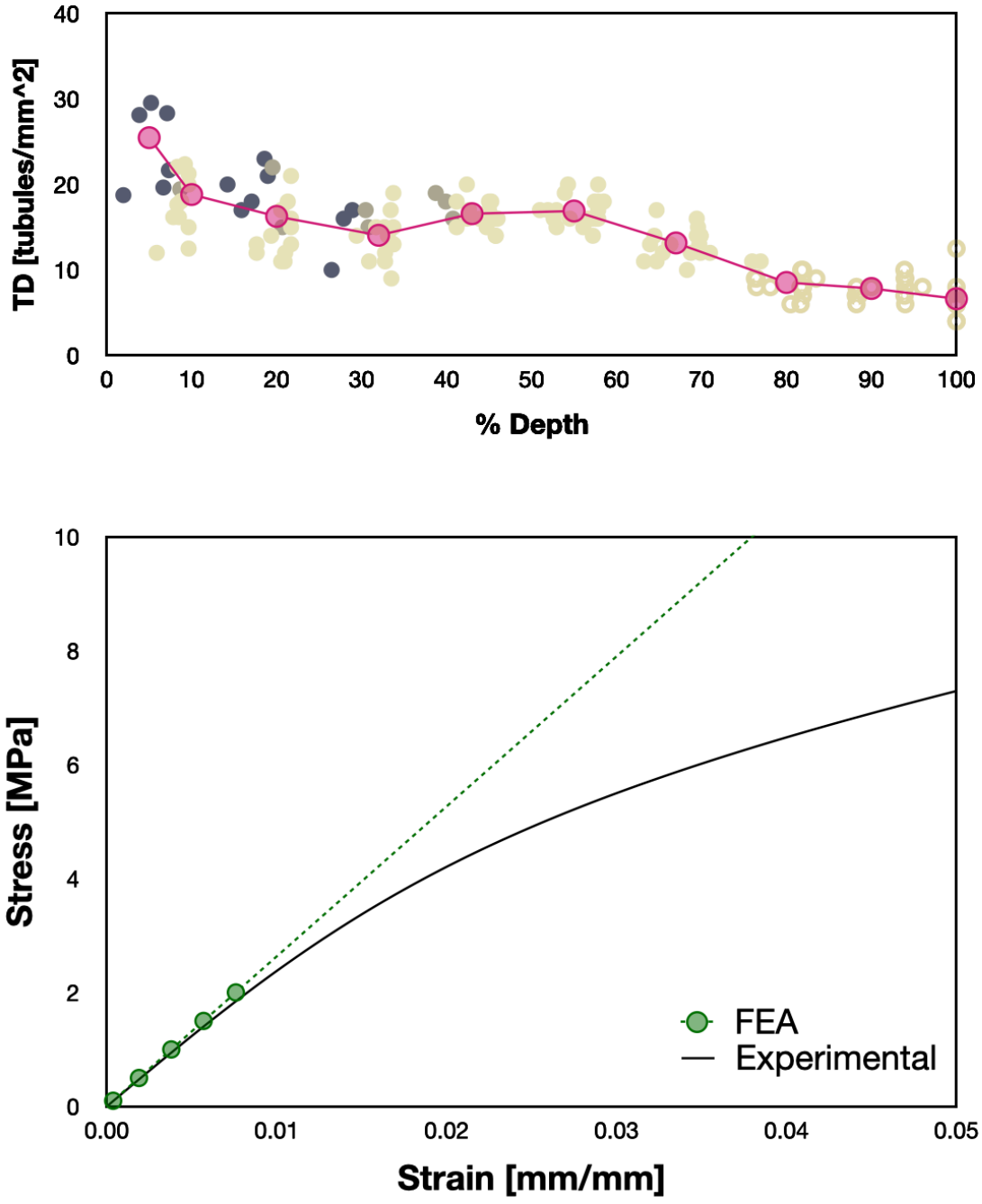

Figure 7.12 Comparison Between Experimental and Simulated Results of Specimen 5

Specimen 6 was tested at 90%RH and 21ºC, and the simulated stiffness is compared with the experimental tensile curve in Figure 7.13. The initial elastic modulus appears reasonably well predicted.

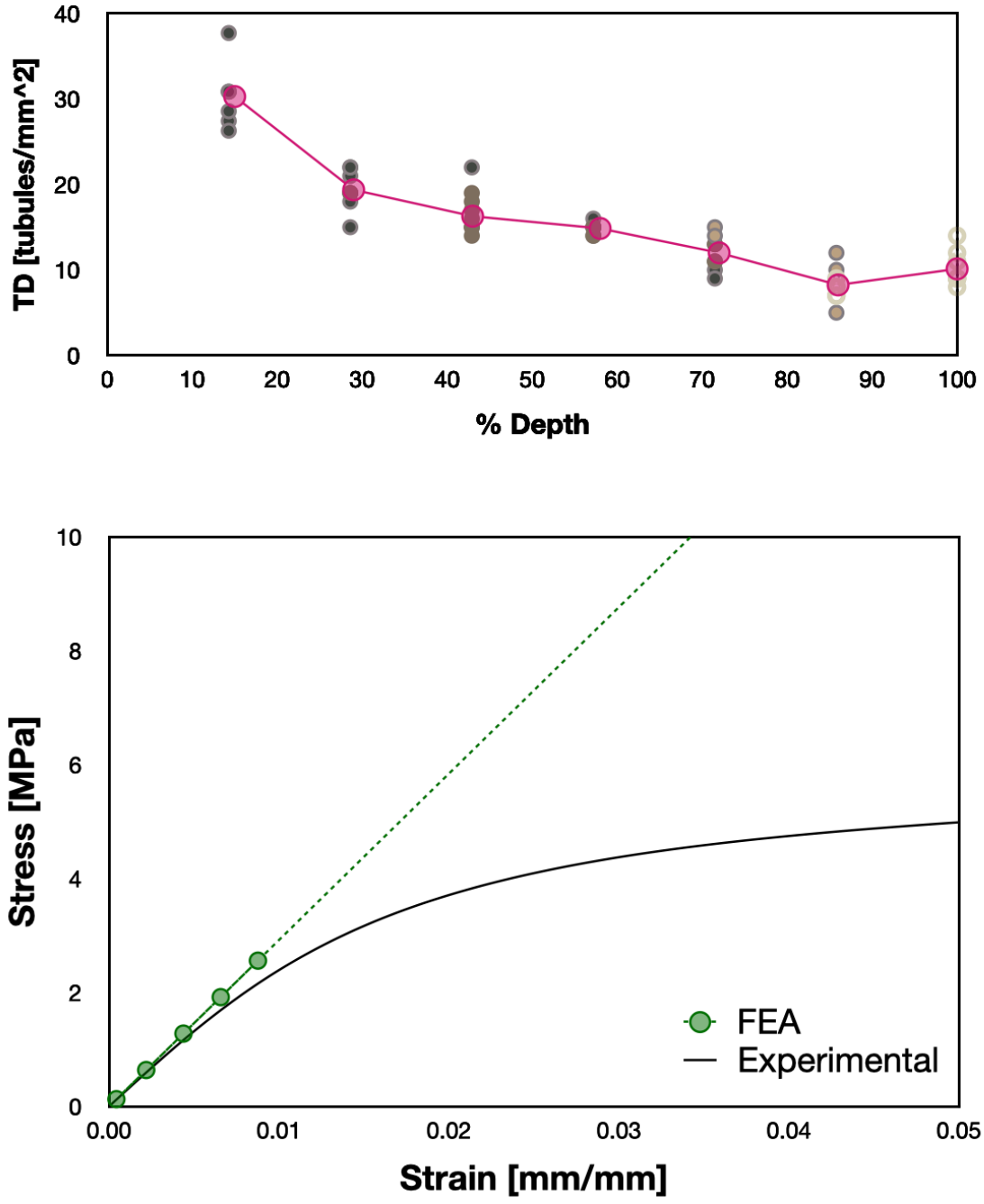

Figure 7.13 Comparison Between Experimental and Simulated Results of Specimen 6

Specimen 7 was tested at 50%RH and 21ºC, and the simulated stiffness is compared with the experimental tensile curve in Figure 7.14. The initial elastic modulus appears reasonably well predicted.

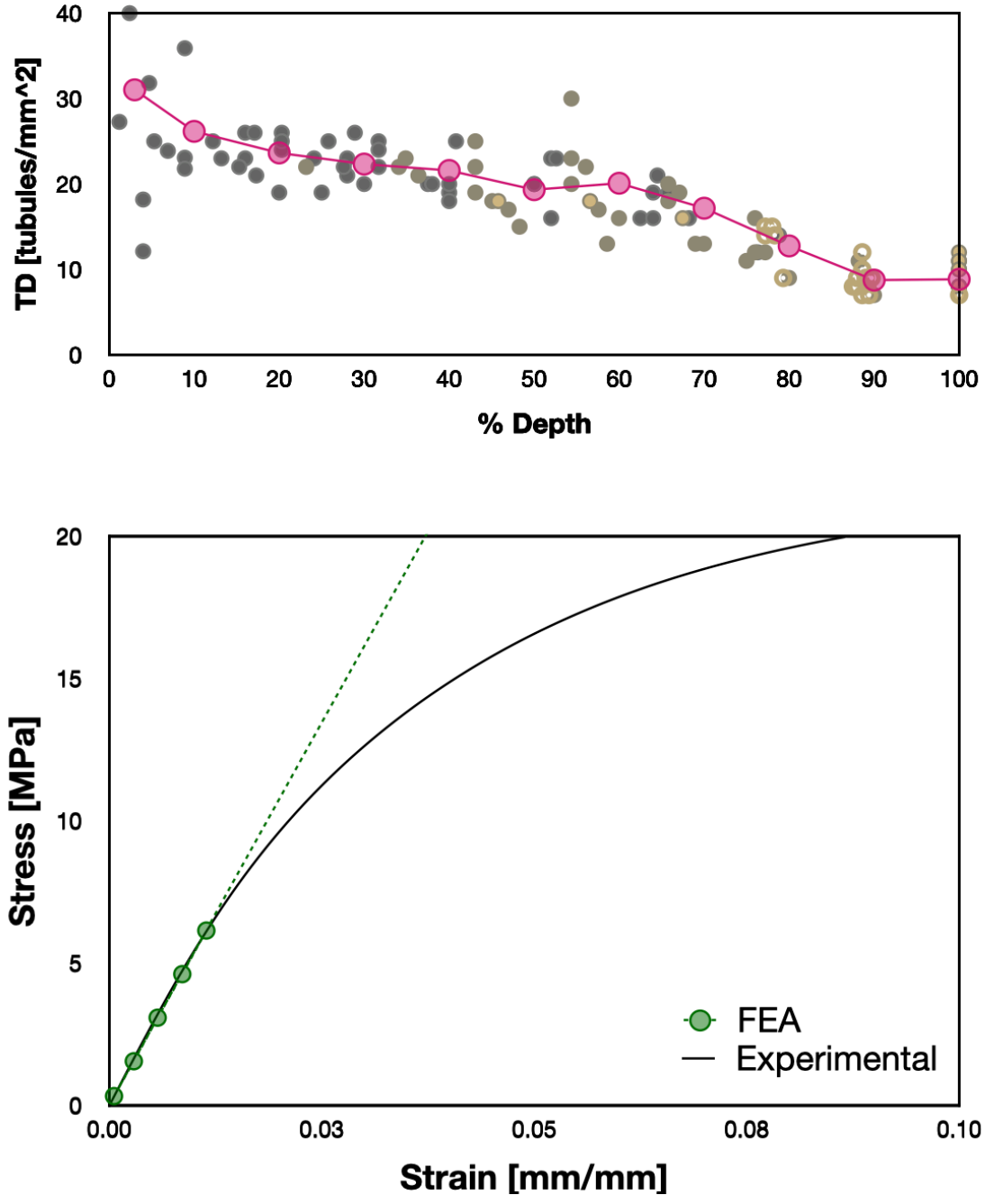

Figure 7.14 Comparison Between Experimental and Simulated Results of Specimen 7

Specimen 8 was tested at 90%RH and 21ºC, and the simulated stiffness is compared with the experimental tensile curve in Figure 7.15. The initial elastic modulus appears slightly overpredicted.

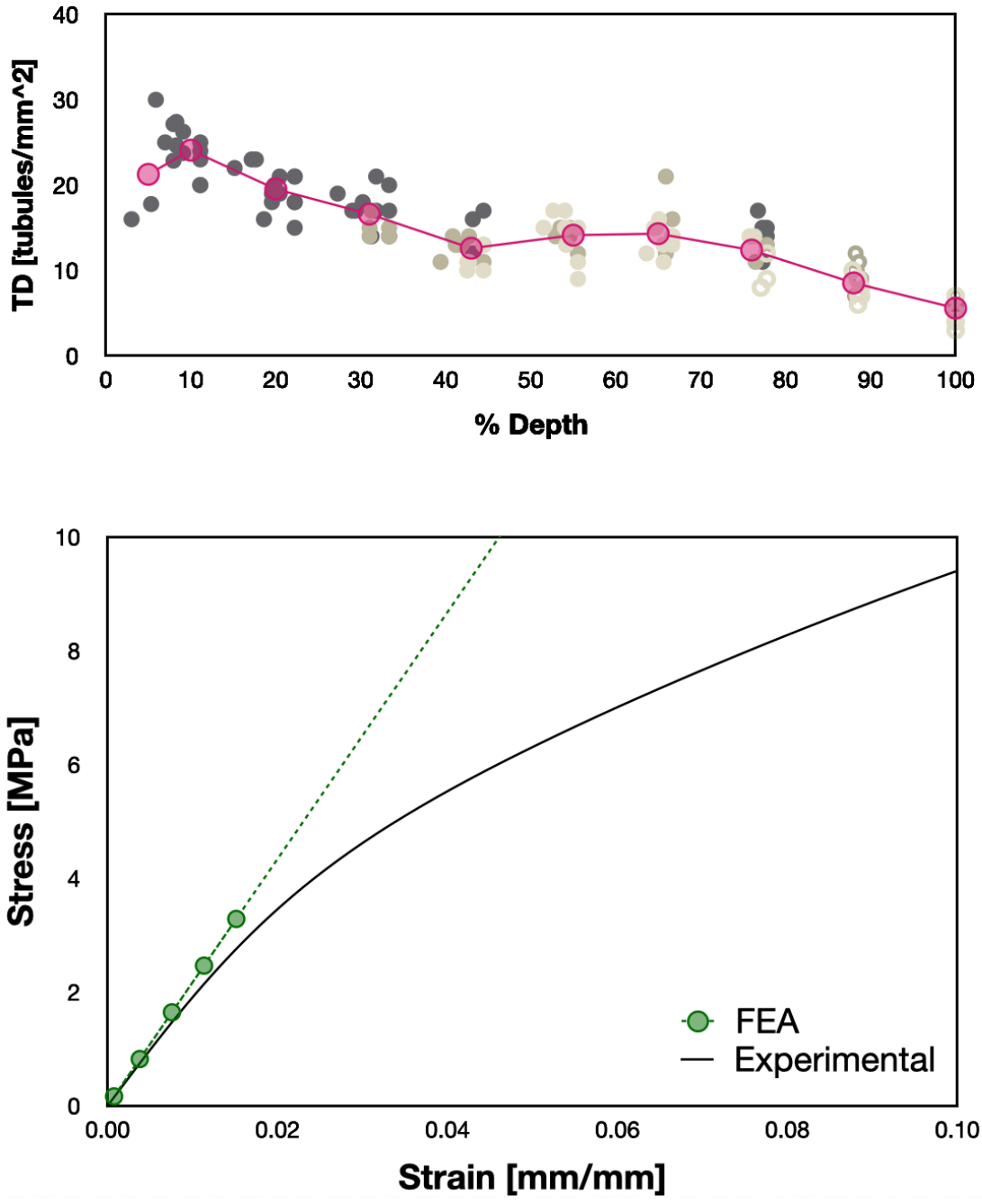

Figure 7.15 Comparison Between Experimental and Simulated Results of Specimen 8

Specimen 9 was tested at 46%RH and 18.3ºC, and the simulated stiffness is compared with the experimental tensile curve in Figure 7.16. The initial elastic modulus appears reasonably well predicted.

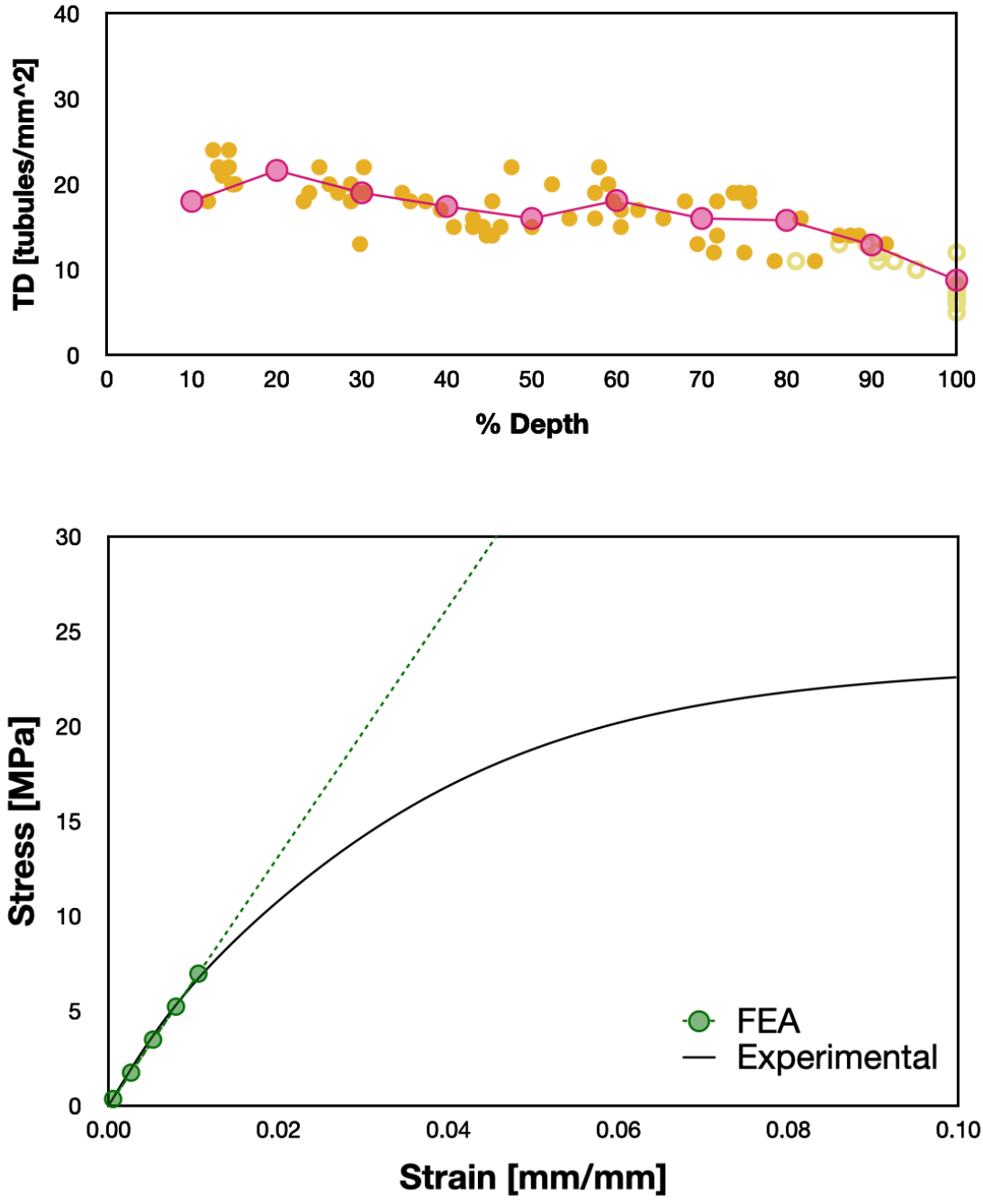

Figure 7.16 Comparison Between Experimental and Simulated Results of Specimen 9

Specimen 10 was tested at 65%RH and 17.8ºC, and the simulated stiffness is compared with the experimental tensile curve in Figure 7.17. The initial elastic modulus appears slightly underpredicted.

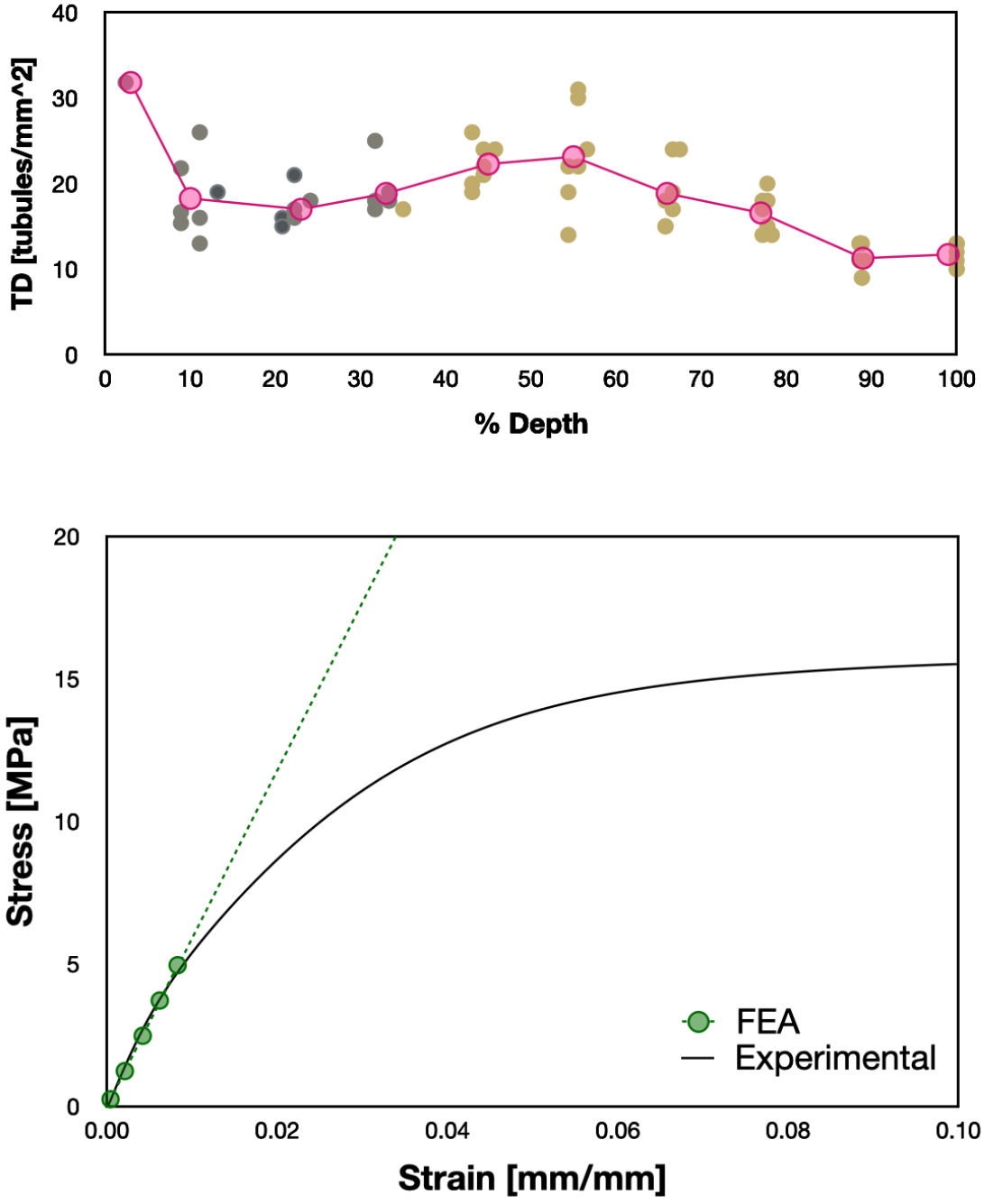

Figure 7.17 Comparison Between Experimental and Simulated Results of Specimen 10

Specimen 11 was tested at 68%RH and 21ºC, and the simulated stiffness is compared with the experimental tensile curve in Figure 7.18. The initial elastic modulus appears reasonably well predicted.

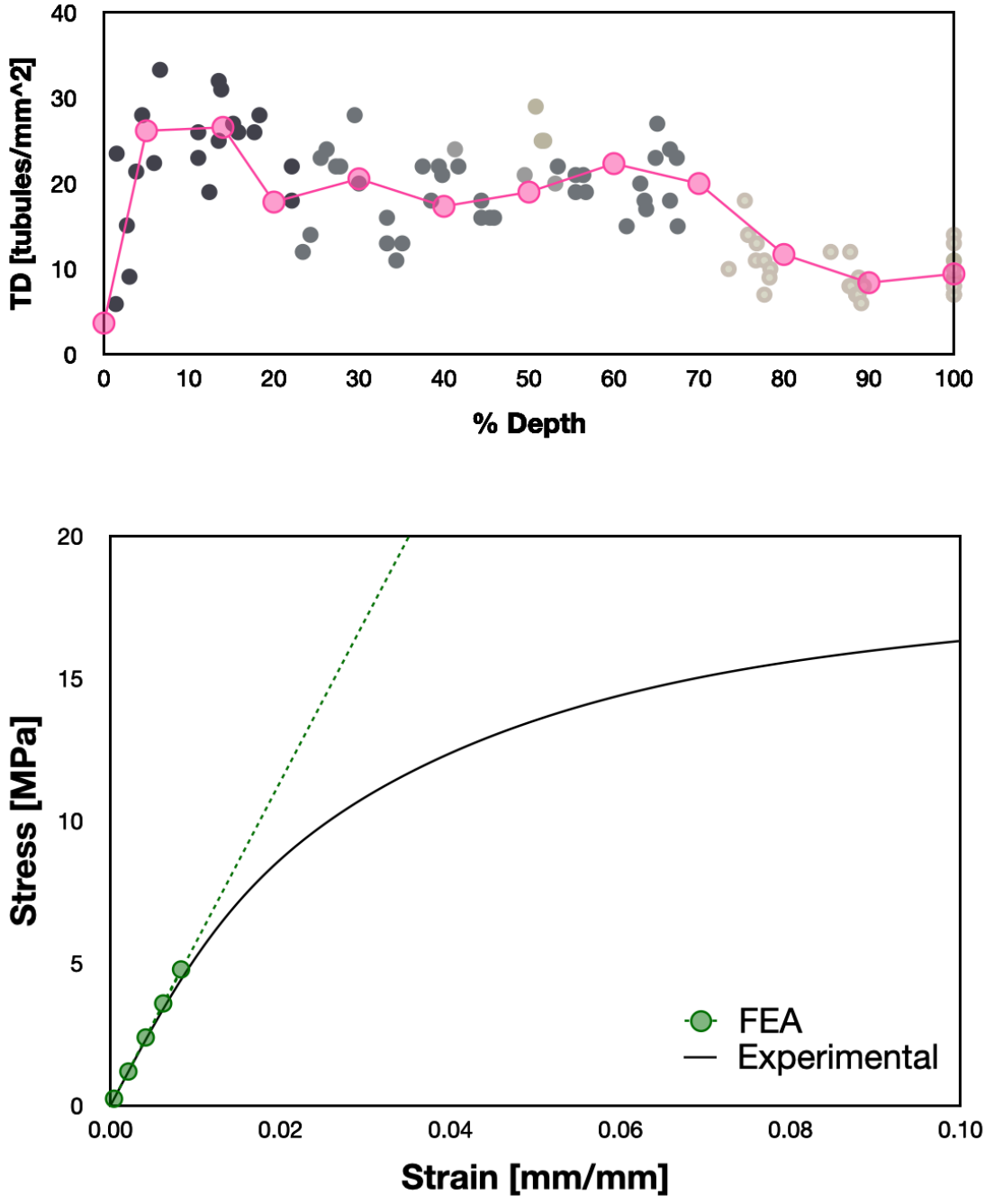

Figure 7.18 Comparison Between Experimental and Simulated Results of Specimen 11

Specimen 12 was tested at 45%RH and 17.8ºC, and the simulated stiffness is compared with the experimental tensile curve in Figure 7.19. The initial elastic modulus appears reasonably well predicted.

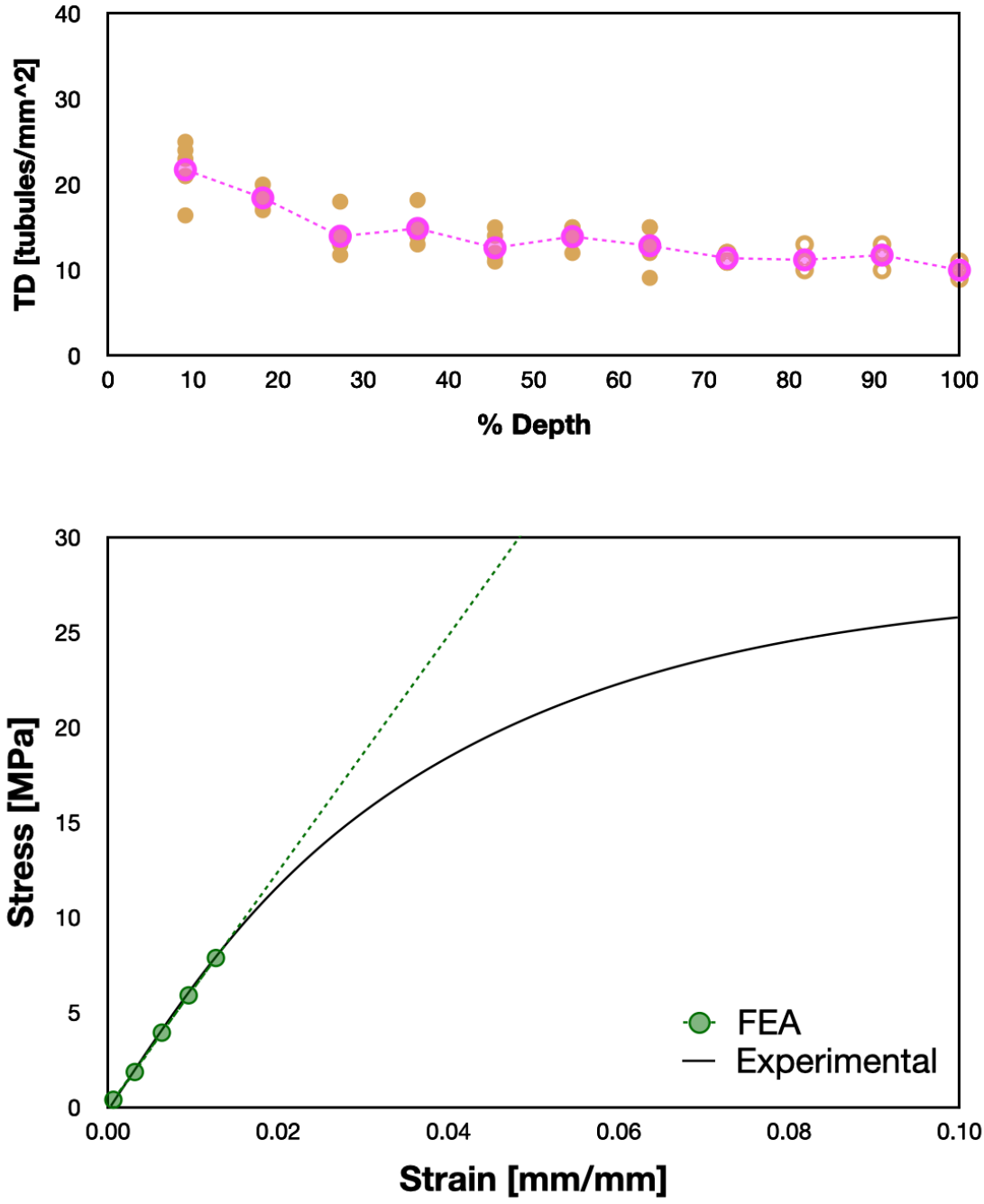

Figure 7.19 Comparison Between Experimental and Simulated Results of Specimen 12

Specimen 13 was tested at 64%RH and 18.3ºC, and the simulated stiffness is compared with the experimental tensile curve in Figure 7.20. The initial elastic modulus appears reasonably well predicted.

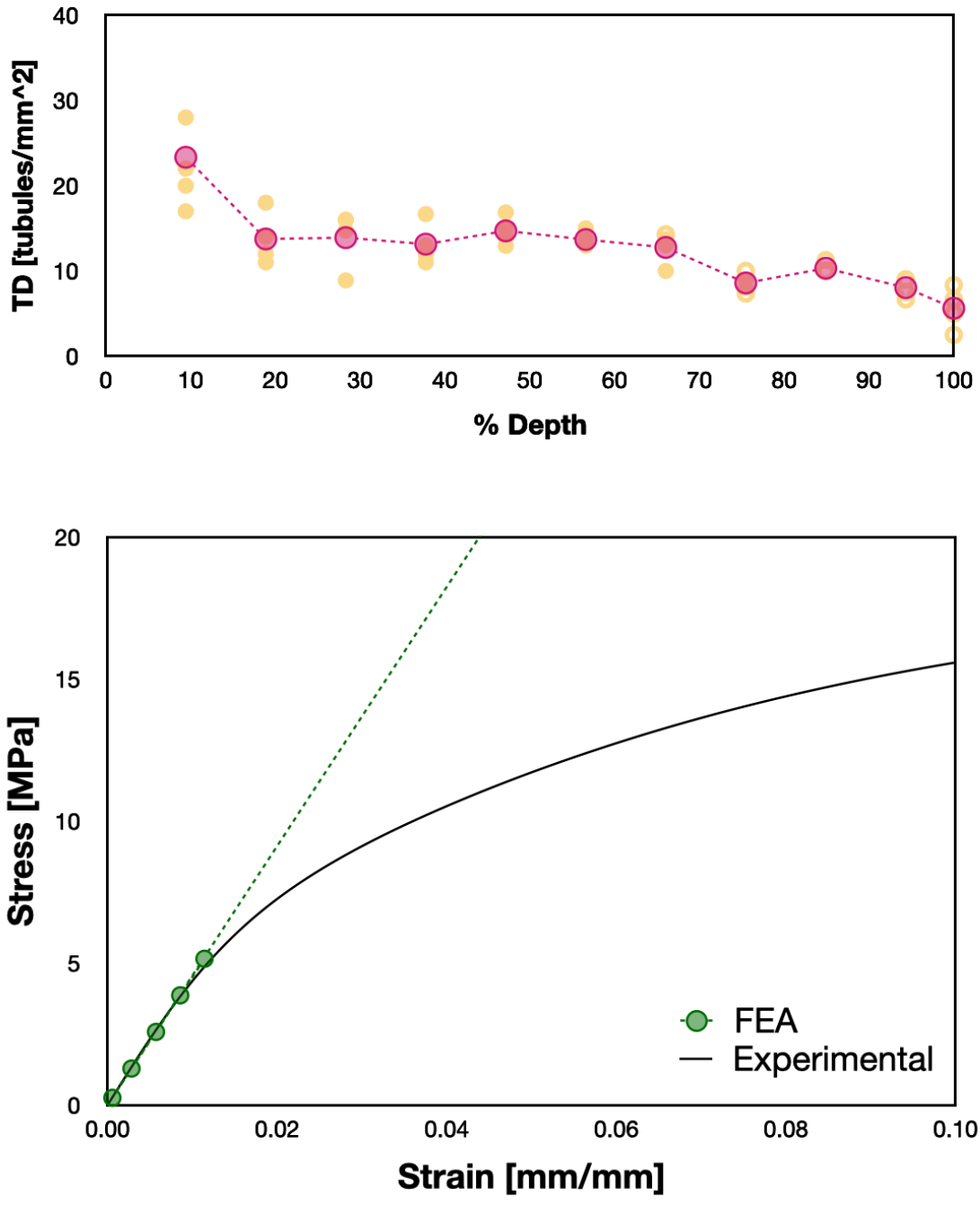

Figure 7.20 Comparison Between Experimental and Simulated Results of Specimen 13

Specimen 14 was tested at 69%RH and 21ºC, and the simulated stiffness is compared with the experimental tensile curve in Figure 7.21. The initial elastic modulus appears slightly overpredicted.

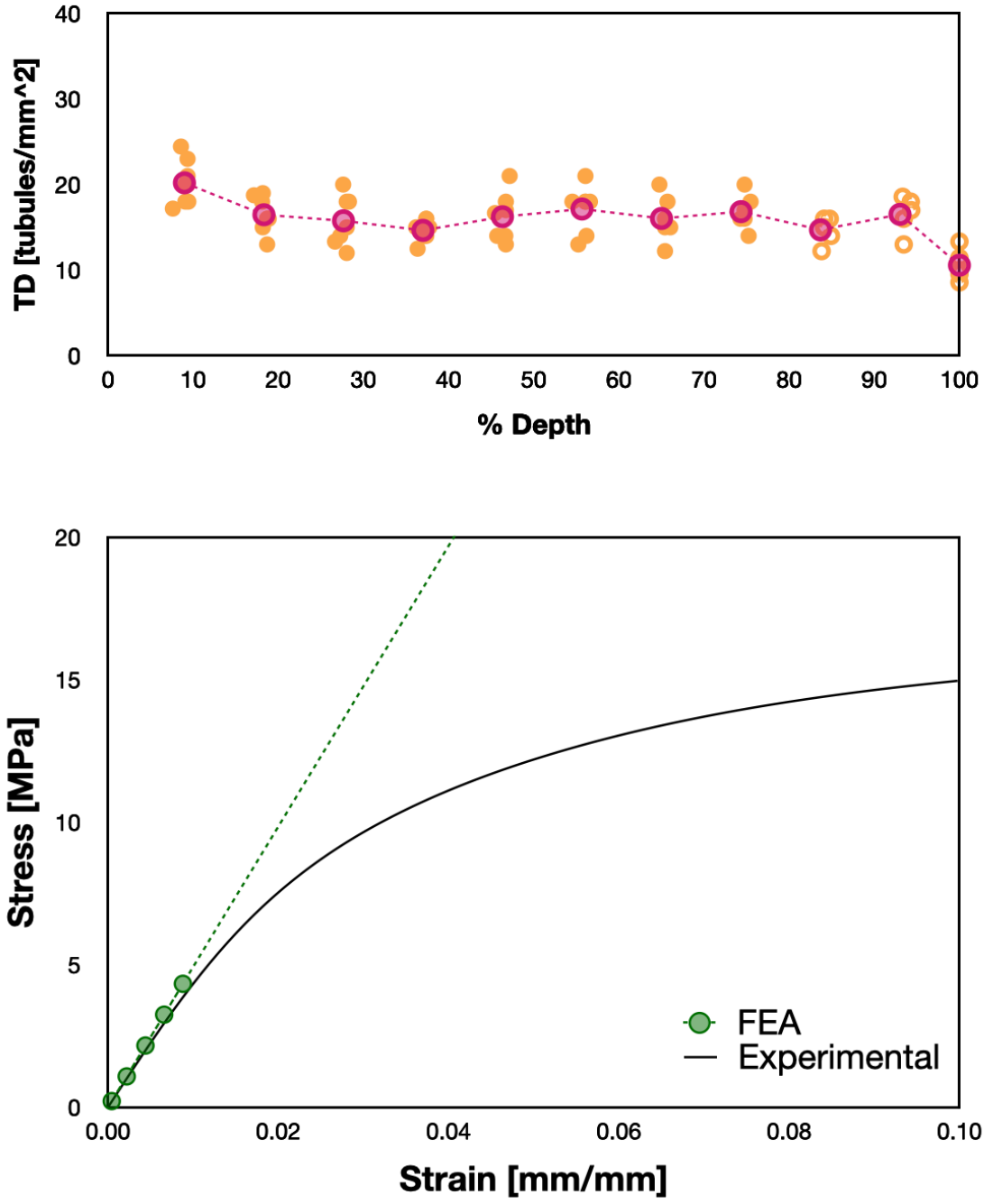

Figure 7.21 Comparison Between Experimental and Simulated Results of Specimen 14

Specimen 15 was tested at 35%RH and 17.8ºC, and the simulated stiffness is compared with the experimental tensile curve in Figure 7.22. The initial elastic modulus appears slightly underpredicted.

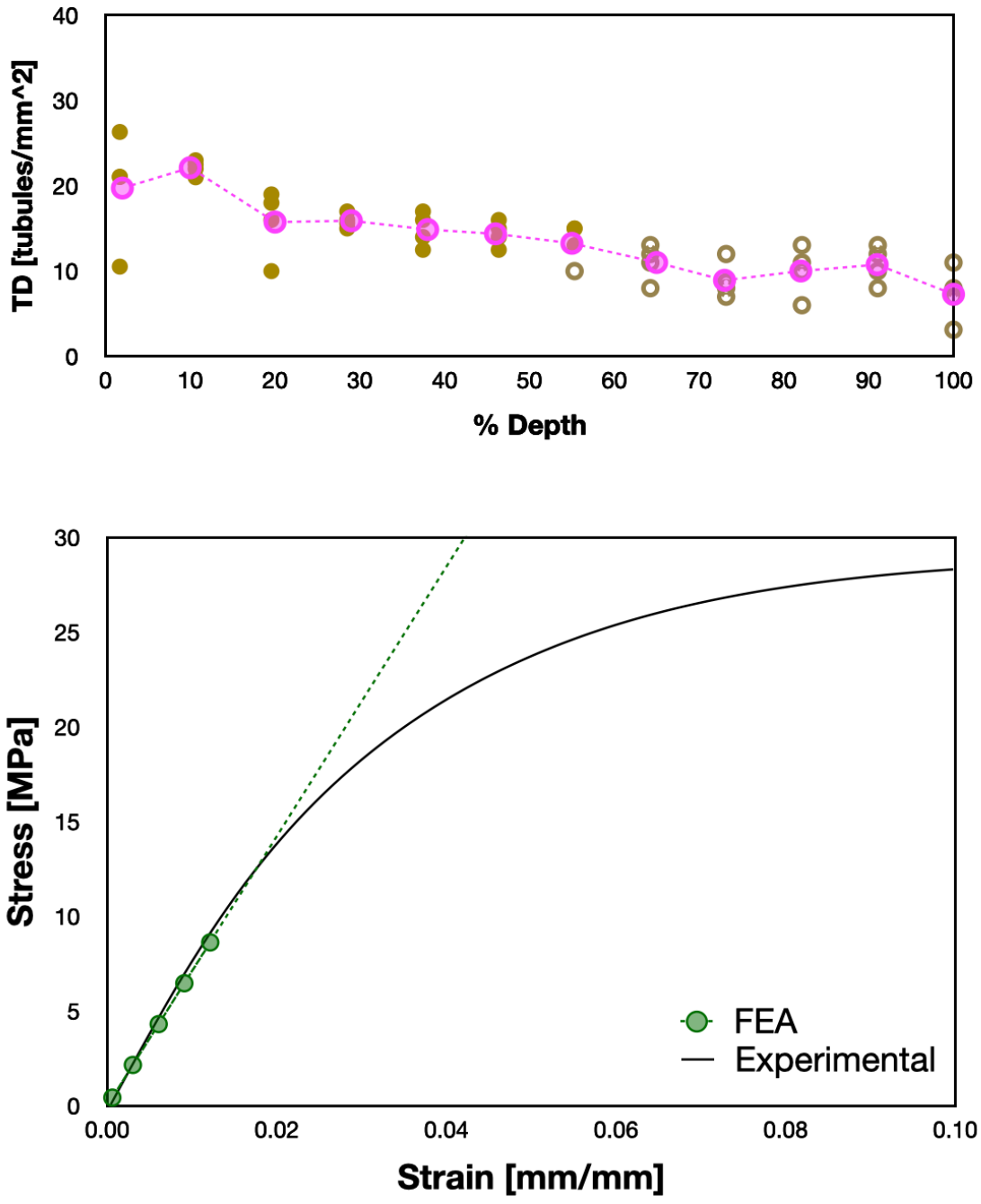

Figure 7.22 Comparison Between Experimental and Simulated Results of Specimen 15

Specimen 16 was tested at 80%RH and 18.3ºC, and the simulated stiffness is compared with the experimental tensile curve in Figure 7.23. The initial elastic modulus appears reasonably well predicted.

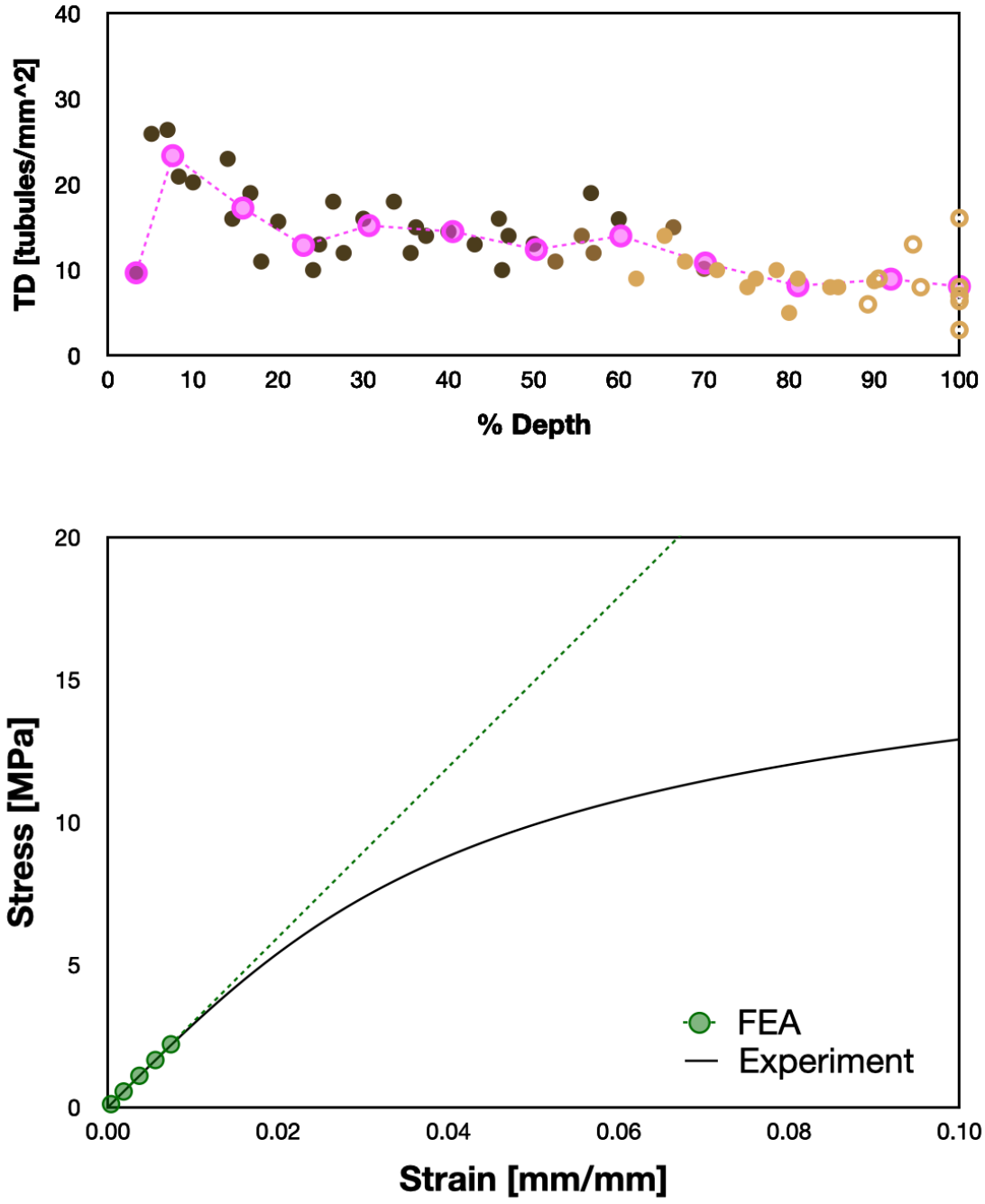

Figure 7.23 Comparison Between Experimental and Simulated Results of Specimen 16

Specimen 17 was tested at 87%RH and 17.2ºC, and the simulated stiffness is compared with the experimental tensile curve in Figure 7.24. The initial elastic modulus appears slightly underpredicted.

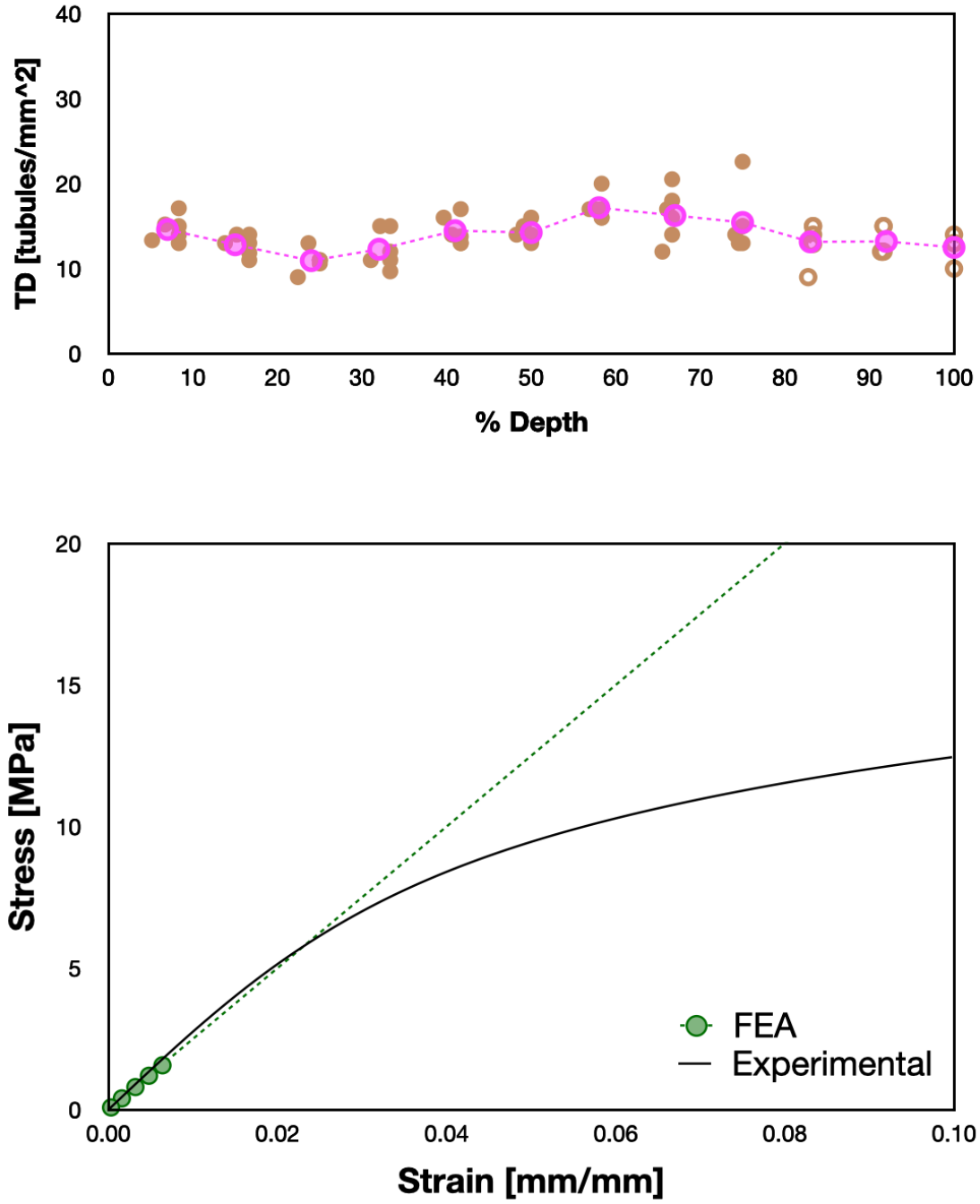

Figure 7.24 Comparison Between Experimental and Simulated Results of Specimen 17

Specimen 18 was tested at 80%RH and 17.8ºC, and the simulated stiffness is compared with the experimental tensile curve in Figure 7.25. The initial elastic modulus appears slightly underpredicted.

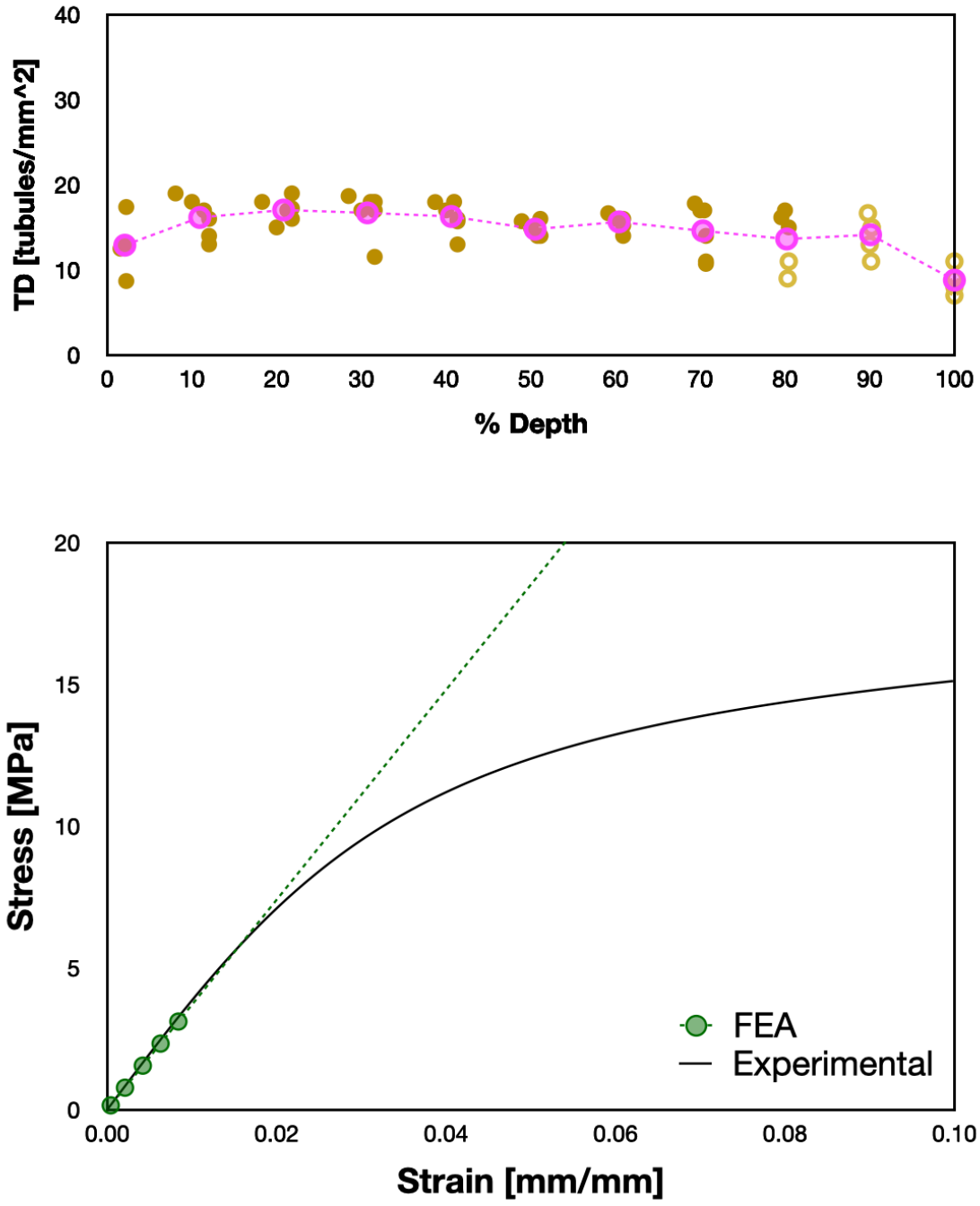

Figure 7.25 Comparison Between Experimental and Simulated Results of Specimen 18

Specimen 19 was tested at 85%RH and 18.3ºC, and the simulated stiffness is compared with the experimental tensile curve in Figure 7.26. The initial elastic modulus appears reasonably well predicted.

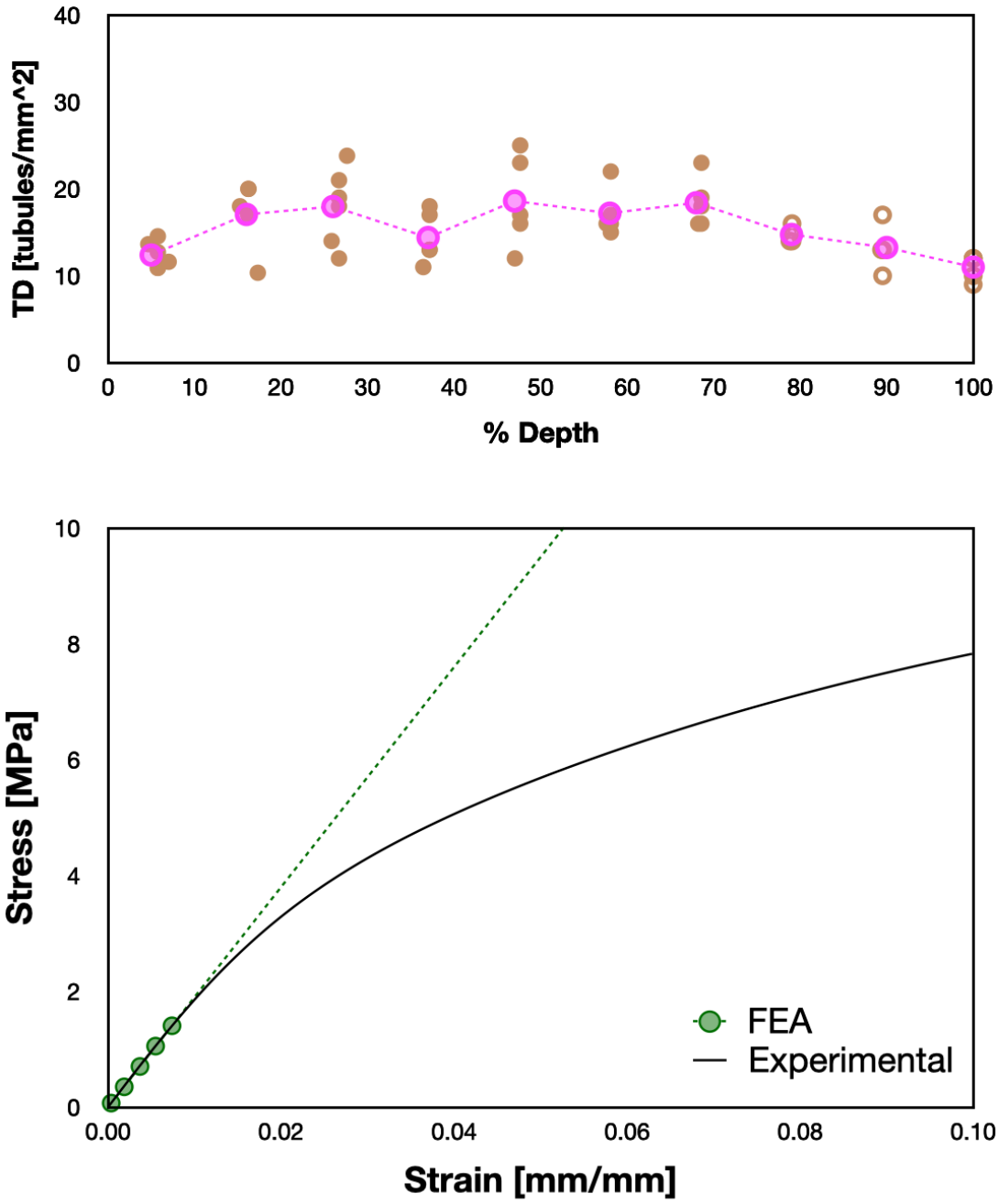

Figure 7.26 Comparison Between Experimental and Simulated Results of Specimen 19

The cumulative experimental data is compared to the FEA results in Figures 7.27-29. Figure 7.27 compares the experimental strain with the FEA strain for a given prescribed displacement. The center diagonal line with a slope of 1 represents an ideal correlation. The data points above the centerline represent an instance of overestimation, while data points below the centerline represent instances of underestimation. As expected, the data hugs the ideal line very closely.

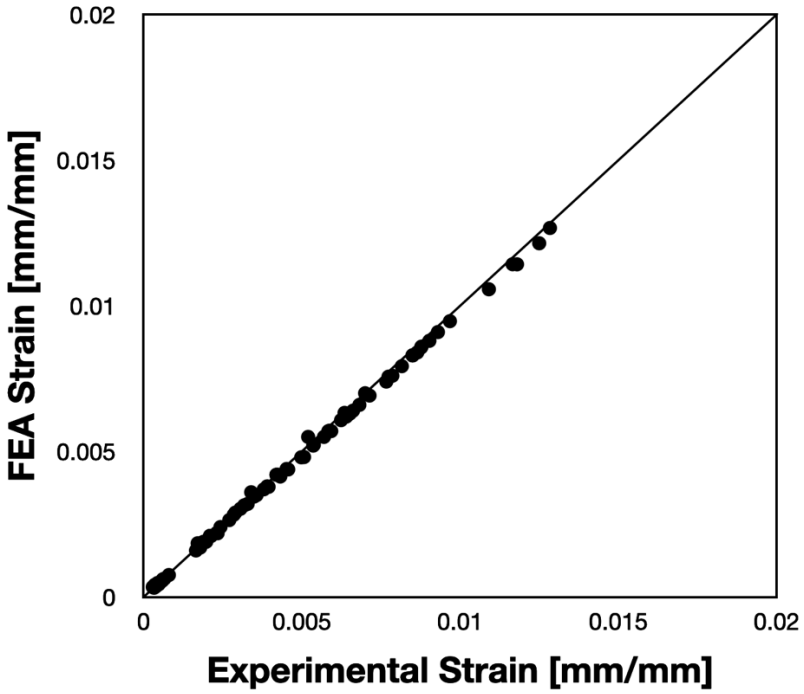

Figure 7.27 Comparison of Cumulative Experimental Strain Data and FEA Results

Figure 7.28 compares the experimental stress with the FEA stress for a given prescribed displacement. The data falls within a +/-10% envelope. There are several potential sources of uncertainty that could explain the scatter in the fit. The first to mention is the simplification of the TD distribution profile used to construct the layers of the specimen CAD model. Some TD distribution profiles are more complex, with more peaks and valleys, than others, and this simplification process will lend different amounts of uncertainty to the prediction. There is also some uncertainty in the assumed layer

properties determined from the local keratin stiffness trends. Other uncertainty arises from the experimental process. The bulk %RH of the keratin bulk hoof wall specimens was determined by measuring the weight of the specimen at varying levels of hydration. However, as the specimen dehydrated, it is not guaranteed that the loss of water was uniform throughout the specimen. The water would evaporate via the exposed surfaces of the specimen, likely having a more hydrated core than the outer surface. Furthermore, as the specimen dehydrated, there would be minor shrinkage in the cross-sectional area while the tubule diameters may increase (due to the "tightening" of the surrounding material).

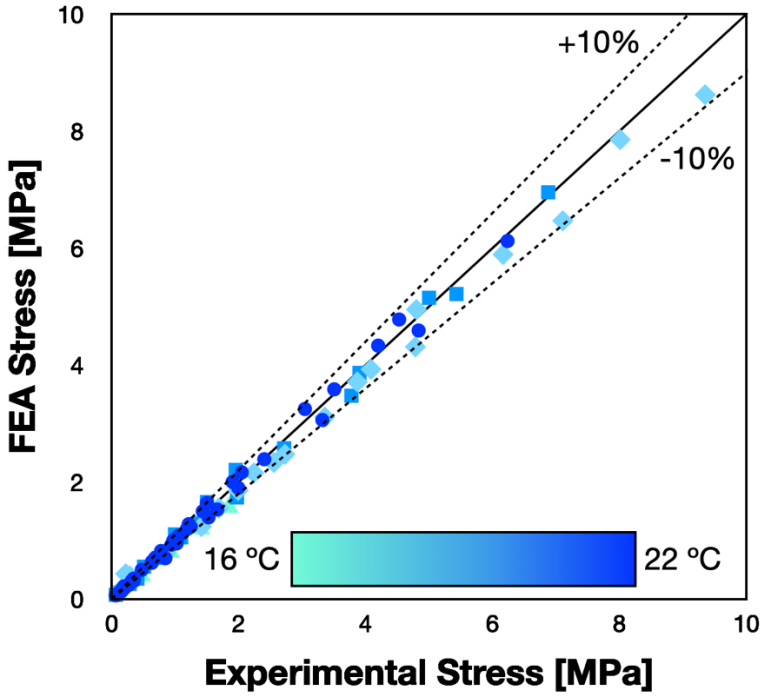

Figure 7.28 Comparison of Cumulative Experimental Stress Data and FEA Results

Figure 7.28 compares the experimentally obtained elastic moduli with the simulation predictions. Again, the center diagonal line represents the ideal 1:1 correlation, and the dashed lines represent the envelope containing the scatter in the data set. The material stiffness maintained a +/-10% envelope for most of the explored boundaries,

however, the method underpredicted the experimental elastic modulus an additional -6% as the stiffness increased past 700 MPa. An additional trend of note is that specimens whose stiffness was underpredicted outside of the +/-10% envelope were those with lower temperatures and/or lower hydration. This makes sense, as those quadrants of the local keratin stiffness properties have fewer experimental data points, increasing the potential uncertainty stemming from the properties assigned to the CAD model layers.

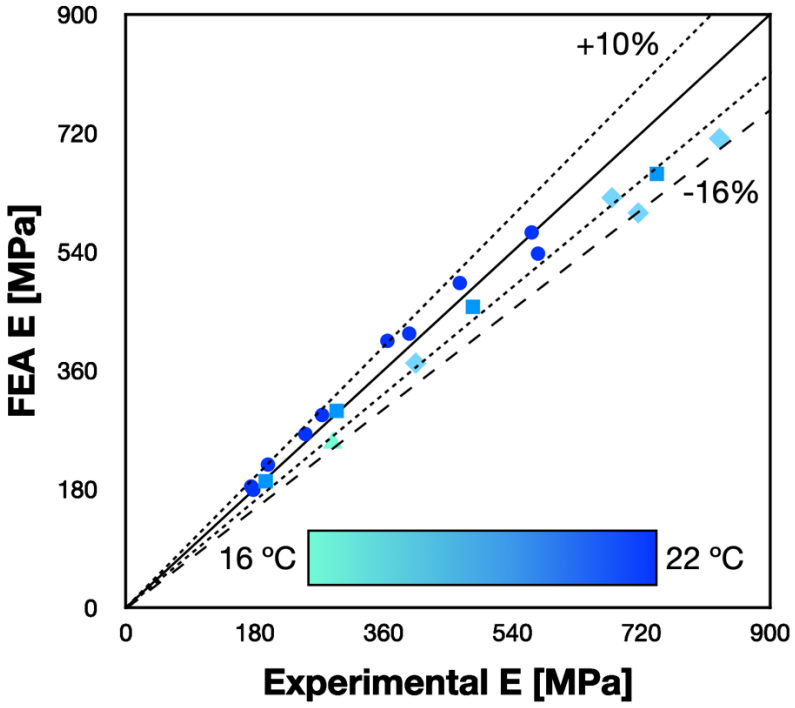

Figure 7.29 Comparison of Experimental Bulk Hoof Wall Stiffness Data and FEA Results

Considering the nature of biological materials and the numerous variables (material conditions and environmental factors) that are potential sources of uncertainty, this method can be considered as useful for predicting the elastic modulus of equine keratin. One must simply remember to assign appropriate %RH and temperatures to the different layers of hoof keratin when modeling a live hoof. The outer layers (SE to outer SM) would likely

have a temperature and %RH that reflects the environmental conditions. The innermost layers (inner SM to SI), however, would have an increased %RH due to proximity to the soft tissue and a temperature closer to the animal's body temperature.

7.4 Summary Conclusions

Major conclusions are summarized as follows:

- This method of predicting stresses in equine hoof keratin based on TD, %RH, and temperature is demonstrably successful for applications robust enough to withstand +/-10% envelope.
- This method of predicting equine hoof keratin stiffness based on TD, %RH, and temperature is demonstrably successful for applications robust enough to withstand +10/-16% envelope.
- The method of prediction appears to experience increased uncertainty for temperatures lower than 21ºC and lower levels of hydration. This is because less experimental data is available in those quadrants of the local keratin stiffness data regime. Expanding the experimental data used to construct the local keratin stiffness data set is an excellent opportunity for future research to improve the accuracy of this method of prediction.

CHAPTER 8

MODELING THE HOOF CAPSULE

8.1 Introduction

CAD modeling of hooves under different shoeing conditions is of interest to the veterinary and farrier fields because it can qualitatively describe the hoof capsule reaction. The equine digit is structurally complex with a myriad of moving parts, including but not limited to bones, tendons, soft tissues, and keratin. Some studies have used simplified setups with idealized geometries and limited loading in order to predict hoof behavior under various conditions [88] [89] [90]. These instances only included the keratinous hoof capsule, with loading applied to selected internal surfaces in an effort to mimic appropriate loading along the coffin bone, navicular bone, and third phalanx. Another study included regions of internal biology within the hoof capsule, but for the purpose of exploring the laminar juncture as a veterinarian specialists' tool in the treatment of laminitis [91].

The loading a hoof capsule can experience is quite significant. The standing force on one hoof can be greater than or equal to a horse's own body weight depending on the shift in the animal's stance. Horses typically weigh anywhere between 900-2000 pounds, depending on age, breed, and activity. An average trotting horse can see loading on the hoof upwards of 8000 N [6], even reaching 9000 N at gallop [11]. Depending on the hoof capsule geometry, the average contact area with the ground is ~20 cm^2, working out to an applied stress of nearly 5 MPa at a gallop [11]. Table 8.1 summarizes the general "rule of thumb" for determining the loading on an equine hoof. This, of course, can change depending on the activity, hoof conformation and geometry, and which limb is under analysis. For example, during a gallop, the forelimb will see the greatest vertical load [92].

But if instead, the horse is hauling a load, the hindlimb will see the highest load in the horizonal direction [93]. With so many variables to consider, it is no wonder that scientists have turned to FEA simulations to better understand and treat equine hoof issues.

Table 8.1 Approximate Loading on Equine Hoof

Activity	Equation	Sources
Waling	0.6 x body weight	[9]
Trotting	(0.9 to 1.0) x body weight	[9] [94]
Galloping	1.75 x body weight	[95]

This chapter describes a simplified CAD model of an equine hoof that can qualitatively predict the hoof capsule's reaction to a number of shoeing scenarios under walking conditions. The model hoof wall is customizable for specific properties of a particular horse based on the TD analysis of cast-off keratin trimmings. Additionally, the internal biology of the equine forelimb digit is included in simplified, approximate form in order to include the resistance to deformation this would provide.

8.2 Model Construction and Assigned Properties

The CAD program Fusion360 (Autodesk Inc., San Raphael, CA, USA) was utilized to construct the simplified, typical, healthy front equine hoof capsule geometry. The dorsal hoof wall formed a 50º angle between the toe and the ground surface. At the widest point of the hoof capsule, the medial and lateral walls formed an 80º angle with the ground surface. The dorsal hoof wall (center of the toe) had a maximum cumulative thickness of 14 mm, and it was divided into an outermost thickness of 2 mm, a central thickness of 8 mm, and an internal thickness of 4 mm. The hoof wall thickness steadily decreased towards the heel to a minimum cumulative thickness of 7 mm, which was divided into an outermost thickness of 1 mm, a central thickness of 4 mm, and an internal thickness of 2 mm. The

frog was level with the heels and the sole was concaved to be raised off the ground surface. The heel walls were parallel with the front-most toe wall, and the hoof capsule model was symmetrical. Figure 8.1 provides a view of the overall hoof capsule structure.

Figure 8.1 Simplified CAD Model of a Typical Equine Hoof Capsule

The internal tissues and skeletal structure present in the hoof were modeled as simplified, approximated geometries to provide qualitative behavior without requiring an overwhelming number of elements during simulation. This simplified approach maintains accessibility to the average individual with typical resources. The coffin bone and middle phalanx were modeled as one component, and no navicular bone was directly present—however, the downward pressure of the coffin joint and navicular bone upon the digital cushion were represented with an applied loading. A deep digital flexor tendon was attached to a shelf at the base of the coffin bone, and the surrounding tissue was divided into medial and lateral cartilage, a digital cushion over the frog, and dermis layer between the bone and wall. Figure 8.2 illustrates the simplified internal biology present in the equine hoof CAD model.

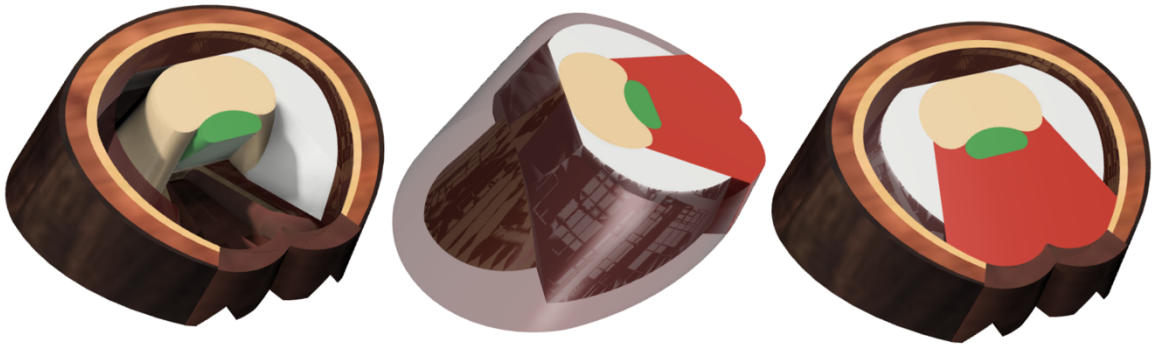

Figure 8.2 Simplified CAD Model of a Typical Equine Digit with Biology

While equine hoof keratin is anisotropic with respect to tubule orientation, a previous study demonstrated that the difference this detail makes when applied to a full hoof capsule FEA model is under 15% [96], and for this reason, other studies have determined that assuming the hoof material to be isotropic, homogenous, and linear elastic is sufficient for qualitative analysis [88] [91] [89] [96] [90]. For the purposes of both simplification and comparison with the literature, the hoof material was assigned to be isotropic, although it is known to be otherwise. The material properties assigned to the model are summarized in Table 8.2.

Table 8.2 Material Properties Assigned to an Equine Hoof CAD Model

Hoof Part	Material Property	Sources
Hoof Capsule	ν=0.4	
Outer Wall Thickness	E=10.4 GPa	Ch. 4
Central Wall Thickness	E=1.8 GPa	Ch. 4
Internal Wall Thickness	E=451 MPa	Ch. 4
Bulk Wall Thickness	E_{avg}=0.697 GPa	FEA Analysis
Frog and Heel Bulbs	E=9.9 MPa	[32]
Sole	E=230 MPa	[32]
Bars	E=10.4 GPa ; ν=0.4	Ch. 4
Internal Biology		
Bones	E=10 GPa ; ν=0.3	[97] [89]
Digital Cushion	E=25 MPa	[91]
Deep Digital Flexor Tendon	E=1 GPa	[98]
Solar Dermis	E=20 MPa	[97] [89]
Cartilage	E=12 MPa ; ν=0.45	[91]

All loading conditions were held constant for all models analyzed in this chapter and were selected to mimic a horse in walk. The primary applied load mainly followed the pulling force of the suspension of the coffin bone [88] and middle phalanx and was approximately 80% of a 3000N walking load (2.4 kN) [99] [100] [101] [102]. The rest of the walking load was distributed evenly over the digital cushion, frog, and sole roughly underlying the approximate location of a navicular bone [90]. An upward force of 0.875 kN was applied to the deep digital flexor tendon [91]. Interactions between model parts were considered via two types of contacts. Material regions with coincident faces were assigned bonded contacts to mimic the tissue acting as one body. The deep digital tendon was assigned sliding contacts everywhere except the point of attachment to the coffin bone, which was a bonded surface [91].

The first scenario explored was the hoof wearing a keg shoe with eight nails, the furthest back of which was located just beyond the widest point of the hoof. The steel keg shoe was attached to the hoof perimeter via nodes representative of nails, and the bottom shoe surface was constrained in all directions to mimic placement upon the ground surface. Figure 8.3 displays the simulation results for the keg shoe scenario.

Heel expansion was approximately 0.24 mm, which agrees with the expected range in the literature of 0.28 mm [90]. Outer dorsal wall dropped 0.11 mm and the inner wall dropped 0.13 mm, which is reasonably close to the literature (0.09 mm and 0.19 mm, respectively [90]). The slight differences in the hoof capsule geometry, thicknesses, and applied properties can explain the differences in results. The stresses at the nail junction on the load bearing surface were as follows, beginning with the frontmost nails to the backmost nails: 5.5 MPa, 5.2 MPa, 8.87 MPa, and 13.14 MPa. The literature reported

reasonably similar values of the nail stresses of 6.1 MPa, 13.3 MPa, and 16.6 MPa, listed in order from toe to quarter most nails [90].

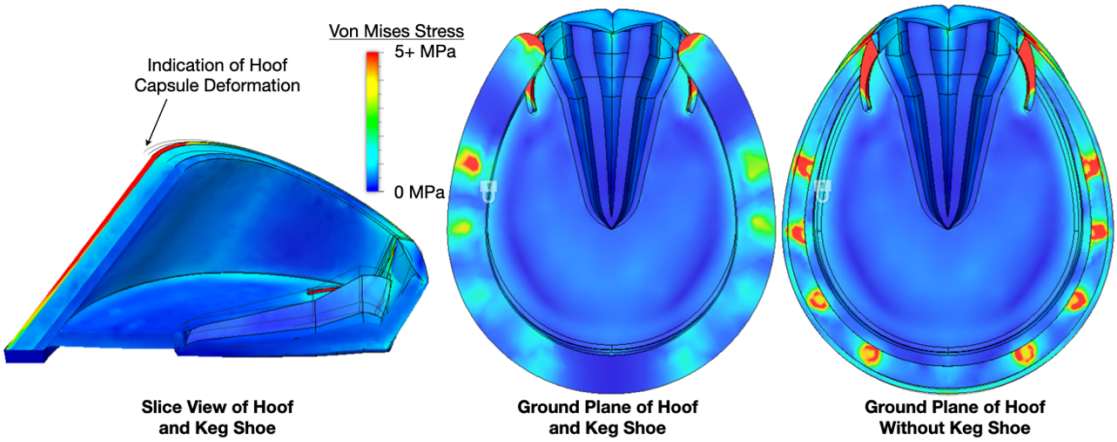

(a)

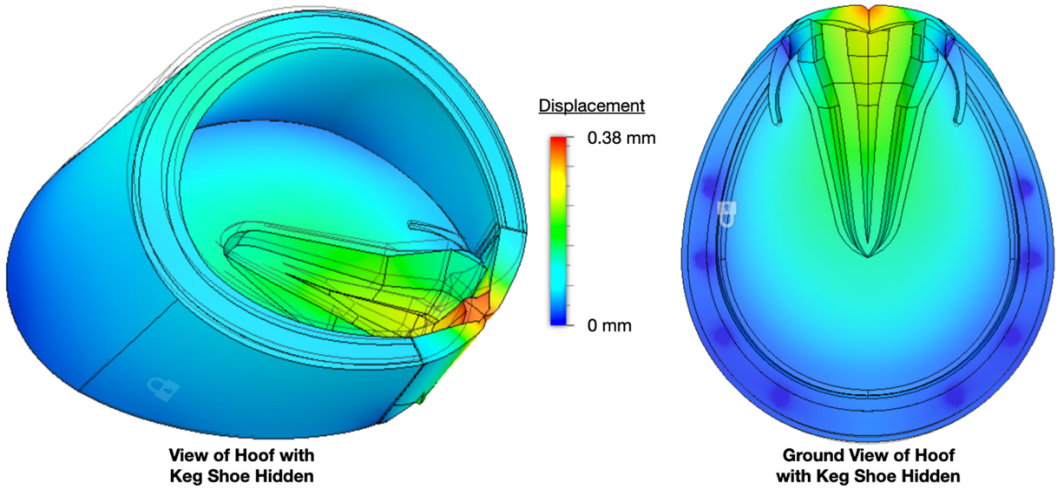

(b)

Figure 8.3 Simulation of Keg Shoe Nailed to a Typical Walking Equine Hoof With (a) Von Mises Stress and (b) Displacement Distributions.

The second scenario explored was the same hoof capsule and internal biology under the same loading conditions, except the hoof was barefoot instead of wearing a keg shoe. Figure 8.4 displays the simulation results of the barefoot scenario.

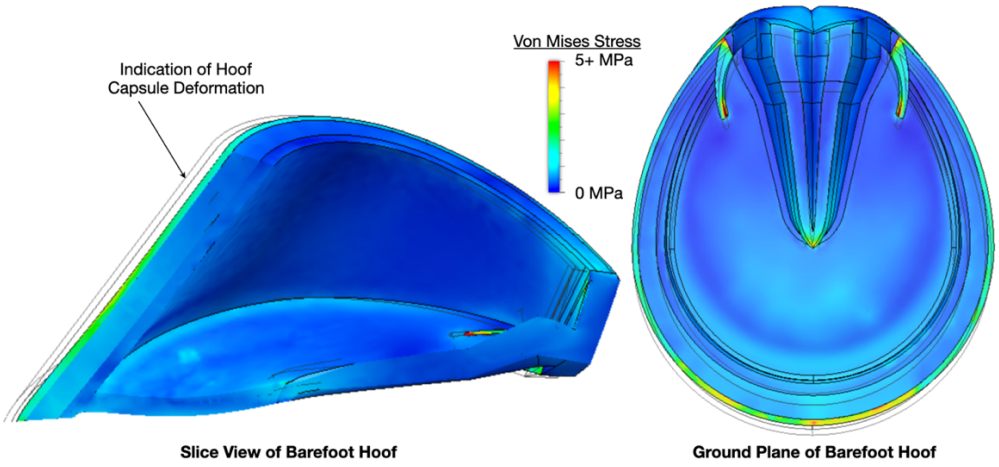

(a)

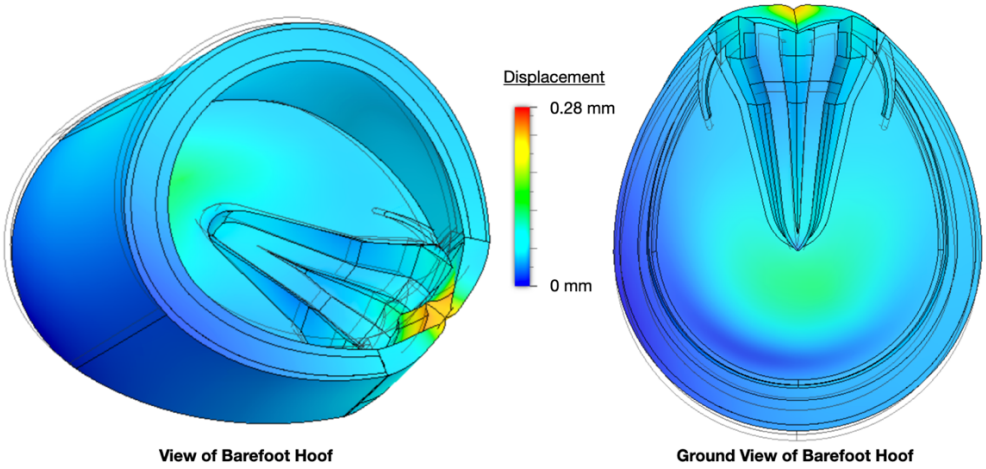

(b)

Figure 8.4 Simulation of a Barefoot Typical Walking Equine Hoof With (a) Von Mises Stress and (b) Displacement Distributions.

Heel expansion was approximately 0.26 mm. Both the outer and inner dorsal wall saw 0.12 mm of displacement. The stress along the perimeter where nails would have been present saw stresses ranged between 1.5-2.0 MPa at the outer hoof wall thickness, which is lower than the stress experienced with a keg shoe. The central and inner wall thickness saw stresses ranged from 0.1-0.5 MPa.

Figure 8.5 shows a comparison of the Von Mises stress distribution for the barefoot and keg shoed hoof under walking loading conditions.

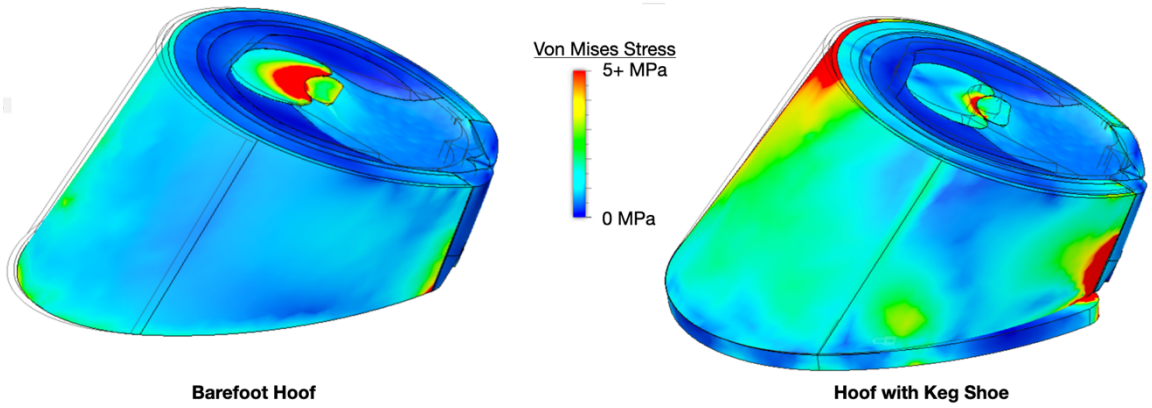

Figure 8.5 Simulation Comparison of a Typical Walking Equine Hoof in the Barefoot and Keg Shoe Conditions

The barefoot hoof experienced less drop in the sole and frog region than the shod hoof. This makes sense because the lack of perimeter constraints would allow a more uniform expansion of the heels and hoof perimeter. The constriction from the keg shoe would force the hoof to drop further down in the arch of the hoof. The barefoot hoof also saw less deformation in the dorsal wall, and there was more uniform displacement through the thickness. Additionally, there was a general reduction of stress in the barefoot hoof all around, particularly in the heel region. One of the more noticeable differences is the lack of stress risers on the loading perimeter of the barefoot hoof from the lack of nails. This led to a more even distribution of stress along the medial and lateral hoof walls in the barefoot hoof. The keg shoe and nails caused localized areas of higher stress in the walls.

This approach to modeling the hoof appears to be a reasonable and accessible method that does not require excessive resources to accomplish. The most notable benefit, however, is the ability to customize this model to match the specific hoof wall properties

as predicted by the TD distribution. Some hooves, such as the example displayed in Figure 8.6, have multi-toned keratin sections, and each region has its own TD distribution. For example, the dark pigmentation regions of the hoof have a TD distribution with a maximum peak of 32 tubules/mm^2 in the outer wall, approximately 18 tubules /mm^2 in the central wall thickness, and a lowest valley of 10 tubules/mm^2 in the innermost wall thickness. The light pigmentation regions of the hoof have a TD distribution with a maximum peak of 18 tubules/mm^2 in the outer wall, approximately 10 tubules /mm^2 in the central wall thickness, and a lowest valley of 7 tubules/mm^2 in the innermost wall thickness.

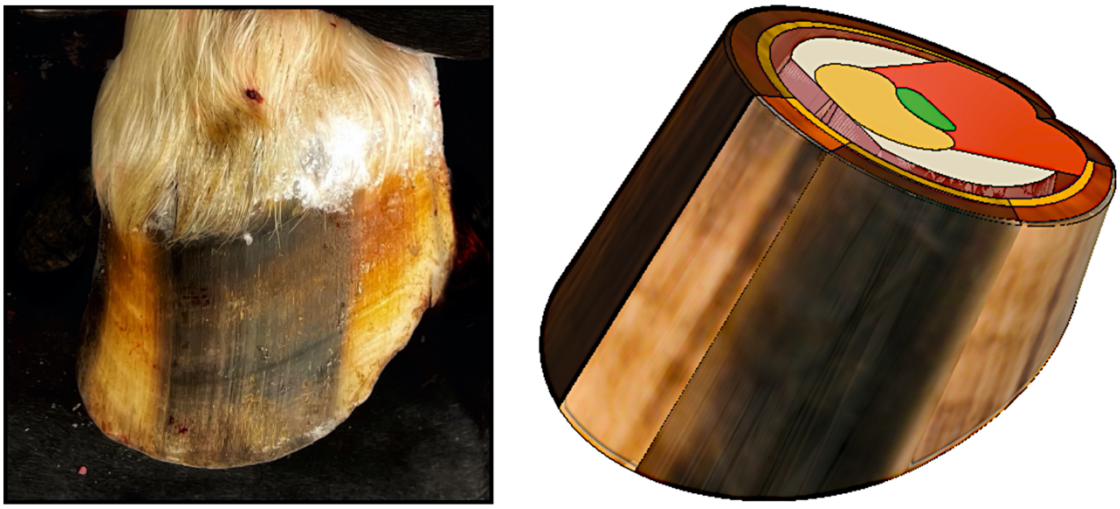

Figure 8.6 Equine Hoof with Multitoned Keratin and Corresponding CAD Model

Different TD distributions in the various regions of the hoof wall capsule means there will be a change in the stresses the hoof experiences under loading. Figure 8.7 displays the Von Mises stress distribution for a barefoot hoof under the same walking conditions as previous models, only with the hoof wall capsule customized to match the different stiffness properties associated with the TD of each pigmentation. The stresses in the hoof capsule can be seen to clearly change depending on the region of pigmentation.

The dark pigmentation regions see higher stresses than the lighter keratin. While the previous barefoot model also saw peak stresses in the central dorsal region in the outer thickness, the change in pigmentation here has led to higher stress in that location due to the proximity of a less stiff region of the hoof capsule. Additionally, the ground plane view of the pigmented barefoot hoof simulation shows that one side of the hoof experiences higher stress than the other, which could cause uneven deformation of the hoof capsule and eventual skeletal misalignment. When stiffness differs though the hoof capsule beyond the minor fluctuations of typical monotoned keratin, hoof conformation can be affected, and hoof issues can arise over time. Understanding the relationship between stiffness and TD of the hoof capsule is critical for not only treating hoof issues but preventing those issues well before they manifest as damaging. Prevention is better than a cure.

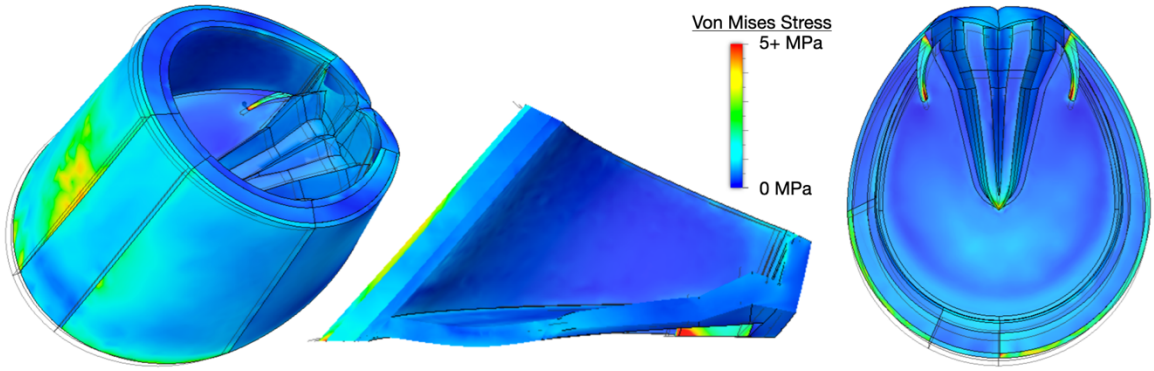

Figure 8.7 Von Mises Stress Distribution of Simulated Multi-toned Barefoot Hoof

8.3 Summary Conclusions

In this chapter, a CAD model of the equine digit was constructed and used to simulate a handful of scenarios: a barefoot uniform hoof, a uniform hoof with a keg shoe, and a barefoot hoof with multi-toned keratin. The hoof capsule was divided into three regions that could be customized with local stiffness properties derived from the TD distribution profile of the horse in question. Major conclusions are summarized as follows:

- The simulated barefoot hoof experienced less drop in the arch and frog region than the shoed hoof due to the lack of constriction from the keg shoe. The barefoot hoof also saw less deformation in the dorsal wall and a more uniform displacement through the thickness.
- A general reduction of stress was seen in the simulated barefoot hoof, especially the lack of stress risers on the loading perimeter from the absence of nails. The keg shoe and nails caused localized areas of higher stress in the walls.
- This approach to modeling the hoof appears to be an accessible method with the ability to straightforwardly customize this model to match the specific hoof wall properties of monotoned and multitoned keratin as predicted by the TD distribution.
- A custom multitoned hoof capsule was modeled and simulated in the barefoot condition, and the stresses in the hoof capsule can be seen to clearly change depending on the region of pigmentation.

CHAPTER 9

DESIGNING INTO 3D: QUADRUPED ORTHOTICS

9.1 Introduction

The end goal of this research is to leverage the equine keratin material properties and their correlation to hoof TD, hydration state (biological and environmental), temperature (biological and environmental), and activity (related to strain rate) in order to design custom horseshoes and/or orthotics that accommodate animal-specific and hoof-specific conditions. A farrier could analyze hoof trimmings to obtain an approximate TD distribution profile of the hoof capsule. The TD distribution profile paired with the local environment temperature and humidity can be used to reasonably predict the stiffness of the hoof capsule wall. From there, a standard horseshoe geometry can be modeled and functionally graded to match the changing stiffness of the hoof capsule perimeter.

If the hoof has conformation issues or injury, this process can be leveraged for a more detailed and powerful solution. The hoof capsule wall geometry can either be obtained via a three-dimensional exterior scan, an x-ray, manual measurements, or a combination of all three, and a CAD model can be constructed. An orthotic can then be designed to assist in correcting and healing a myriad of hoof issues, including but not limited to correcting skeletal alignment, keratin capsule growth/reshaping, promoting specific heel expansions/frog engagement, and improving the digital cushion.

9.2 Project Specifications

The beginning of any design method is defining and clarifying the project by compiling user needs, defining constraints, functional needs, and identifying the target

metrics. By taking these considerations into account at the beginning of the design process, time and resources can be saved by avoiding extraneous prototype iterations.

9.2.1 Product Users and Design Needs

A number of individuals have an interest in the product, whether as consumers and end users or as intermediaries, such as those who will be involved in fabrication. Table 9.1 presents a summary list of the users, their interest in the project, and their individual needs.

Table 9.1 Product Users' Interests and Needs

User	Interest	Product Needs
Customer	The horse owner who will use this product to maintain or improve the health of their animal.	≥ 2 Month Service Life
		Cost Effective
		Modularized for Reusable Parts
		Aesthetically Pleasing
Farrier	The farrier will install this product onto the horse, and possibly provide key measurements to the veterinarians.	Mimic Hoof Stiffness
		Ergonomic/Simple Installation
		Robust Design
		Customizable
		Correct Skeletal Alignment
		Aesthetics /Business Branding
		Limited Number of Parts
Manufacturer	The manufacturer will fabricate the final design.	Readily Available Material
		Limited Number of Fabrication Steps
		Limited Number of Parts
Horse	The animal will wear the product.	Comfortable Shoe/Hoof Interface
		Lightweight
		Shoe Should Naturally Wear Away
		Supports Hoof Capsule
		Mimic Natural Hoof Flex
Veterinarian	The individual who will track the health of the animal over time, and potentially prescribe treatment.	Correct Skeletal Alignment
		Exercise the Digital Cushion
		Support/Mimic the Natural Hoof
		Enable Record Keeping of Hoof Health/Therapy Progress

The owner of the horse has a vested interest in the product as they are the end users who will purchase the shoes. This leads to the obvious preference that the horseshoes be

affordable. The product cost is primarily driven by material selection, fabrication fees, and size. If the horse simply needs a shoe that will help prevent issues that arise from overuse of classic steel horseshoes, then a common plastic material and a passive/automated fabrication method would help keep the cost down. However, if the horse needs any long-term therapeutic hoof adjustments, a modularized shoe design would help keep costs down. For example, the base shoe that will deteriorate due to wear may attach to a reusable wedge/angle adjustment part, limiting the amount of material that is expended every shoe change. Additionally, the customer would prefer the shoe last at least as long as the classic steel shoes, which is approximately 6-8 weeks.

The farrier has a number of needs, as they will be the ones to install the shoe onto the animal, and sometime prescribe treatment. The shoe should be robust and reasonably simple to install onto the hoof. A limited number of parts is desirable in scenarios that require long-term therapeutic hoof treatment. The shoe design should be customizable so that the perimeter fit is clean and with little to no overhanging edges to avoid the horse snagging and tearing off ("throwing") a shoe. Aesthetics is a minor need, but one that may be of interest to the farrier if they wish to provide business-specific branding on a custom-designed shoe. The needs of the veterinarian begin to overlap with the farrier's need at this point. Along the lines of customizable shoes, the shoe stiffness should match that of the natural hoof, and the shoe geometry should be able to adjust any necessary skeletal alignment issues. Additionally, the shoe structure should support the heels and frog as needed while still allowing for natural heel expansion and flexing. Enabling these considerations will yield the added benefit of working the digital cushion, which can improve the overall health of the hoof. The material selected should also be able to wear

away as the hoof continues to grow. This would ensure that the loading from the step is directed down through the center of the shoe, rather than offset due to the growth of the hoof. As the hoof lengthens over time, the shoe should shorten to maintain proper balance.

The horse itself has a stake in the product as it will wear the shoe. In this, the horseshoe should be comfortable. Matching the hoof stiffness goes a long way towards a comfortable shoe, but keeping it lightweight will also help mimic a barefoot experience. Good hoof support and flex are imperative. Perhaps of most concern, however, is the method of installation. Nails can be painful if not placed correctly—too far in and the nail will pierce the soft tissue, and too far out makes the shoe more prone to loosening and/or ripping off entirely and may lead to splitting the hoof capsule.

The final individual of note is the manufacturer, who will be fabricating the shoe along with any customized details. The material selected should be readily available and readily manufacturable by the chosen method of fabrication. The method of fabrication should be selected to reduce the number of steps needed to make the parts, and the shoe design should be driven by the goal of reducing the overall number of parts needed to be made.

Once all these needs are analyzed, design and manufacturing decisions can be made. In order to achieve the hoof-specific shoe geometry, additive manufacturing is most likely the best choice. Not only can the shoe shape and stiffness be tailored to match the hoof via different infill patterns, but any medical information/business logos can easily be embossed into the shoe design itself. ABS is a material that lends itself well to this fabrication method and is a cost-effective plastic that can mimic equine keratin stiffness. The print-on-demand aspect of additive manufacturing makes it a cost-effective method,

as one can produce any number of shoes, which, in the event of therapeutic shoes, may be only one. It is suitable for the manufacturer as it reduces the number of steps and effort necessary to produce a custom horseshoe. With 3D printing technology fast becoming a household capability, the veterinarian, farrier, and even horse owner may not need to go out of house to produce the horseshoes.

Gluing the shoe on is a viable choice, as there are a number of available products on the market that can accommodate this approach. This allows the user to avoid nails altogether. However, in cases where the hoof is strong and healthy, and the longevity of the shoe is the highest concern, nails are an option. Choosing additive manufacturing to fabricate the shoe is the best choice as the location and orientation of the nail holes can be tailored to the animal's hoof wall thickness and capsule shape. Additionally, the nail holes can be inset into the shoe so that the plastic can still wear away during the service life without exposing the nail heads on the bottom surface. The more flexible plastic would also relieve some of the stress placed on the areas where nails pierce the hoof wall.

9.2.2 Functional Requirements of Hoof Prosthetics

The driving functional goal of a horseshoe is to protect the hoof. However, this seemingly simple goal can mean many things, to an overwhelming level. Functionally decomposing the primary purpose can help organize the functional needs of a product. Figure 9.1 presents a generalized functional decomposition of a horseshoe. Note that traditional functional decompositions do not include repeated appearance of the same subfunction, but the one used here deviates from this standard in order to utilize it as an accessible, easily understandable organizational flow chart.

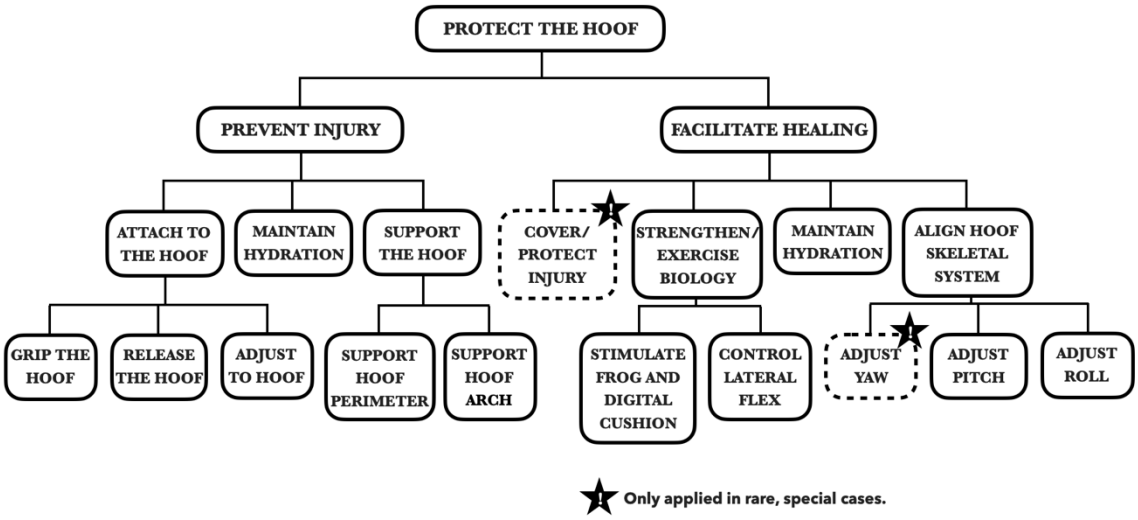

Figure 9.1 Functional Decomposition of Hoof Prosthetic.

The driving functional need of protecting the hoof can be divided into two categories: prevention and correction. A shoe that can prevent an injury will have the same functional needs as a therapeutic orthotic, only without corrective adjustments. The shoe must attach to the hoof in such a way that limits damage and should also support the perimeter and arch of the hoof. This support should reflect a similar stiffness as the natural hoof keratin. In some cases, maintaining a target level of hydration on the hoof may be desirable if the horse is located in a particularly dry climate and the hoof is at risk of severe cracking.

To facilitate healing an injury of the equine digit, a therapeutic orthotic might need to serve several functional needs. Not only must it accomplish all of the preventative needs (perimeter and arch support, attachment, etc.), but it may be required to provide a number of corrections to the digit. Skeletal alignment may need adjustment by raising the heels, restoring mediolateral balance, or correcting a twist. Another consideration is to stimulate the frog to encourage keratin development. Finally, allowing flex can exercise the digital

cushion and enlarge the critical impact-dampening tissues. In rare cases, there may be a need to cover a vulnerable injury in order to protect it from the surrounding environment.

The required functionality of a horseshoe must be judged on a case-by-case basis. Some of the functional requirements described in the functional decomposition may be needed, not many cases will need everything listed. The functional decomposition is a useful design tool to do the due diligence when making shoeing decisions.

9.2.3 Measuring Success: Metrics and Qualitative Analysis

Once the functional requirements for a particular horseshoe have been identified, the target metrics of success must be determined. For example, if the skeletal alignment needs adjustment, to what height and angle should the hoof be tilted? If the horseshoe must mimic the hoof keratin, then the target metric will be the stiffness of the actual horse's hoof as determined via the TD distribution. Consider the multi-toned horse hoof in Figure 8.6 that was under analysis in Chapter 8. The hoof wall thickness was divided into three regions, each with an associated TD (see Table 9.2).

Table 9.2 Multi-toned Hoof TD Information

Capsule Region	Wall Thickness Region	TD [tubules/mm^2]	Hydration [%RH]	Temperature [^{o}C]
Dark Pigmentation Region	Outer	32	40%	21
	Central	18	60%	21
	Inner	10	90%	38
Light Pigmentation Region	Outer	18	40%	21
	Central	10	60%	21
	Inner	7	90%	38

The hydration levels were selected based on a humid southern U.S. environment affecting the outer layer of the hoof capsule, with increasing hydration to the inner layer where the transition into wet soft tissue begins. The temperature levels were selected based on a

warm U.S. southern environment affecting the outer hoof wall layer, with increasing temperature at the inner thickness based on a horse's typical body temperature.

To determine the approximate stiffness of the light and dark keratin pigmentation regions, and FEA analysis was run on hoof wall layers. Figure 9.2 displays the simulation Von Mises stresses in the modeled hoof wall strips under a prescribed displacement of 0.2 mm.

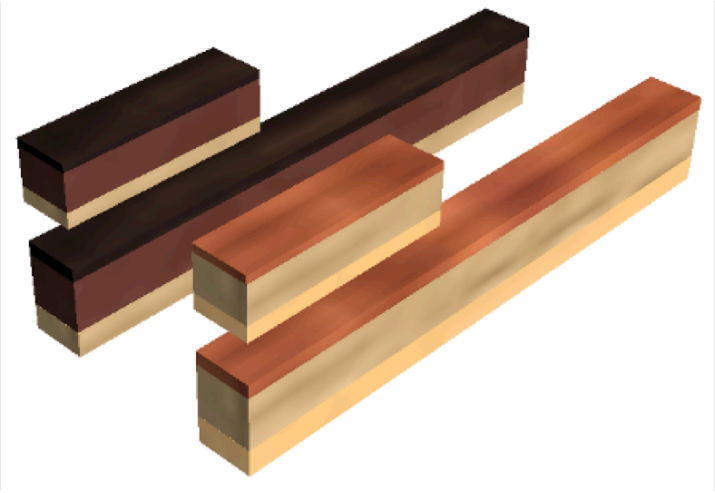

(a)

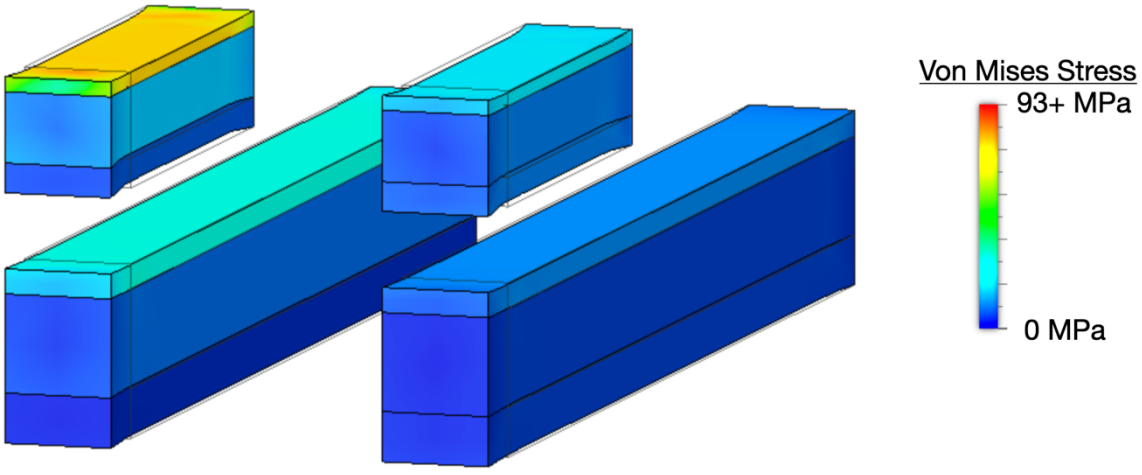

(b)

Figure 9.2 Simulated Hoof Wall Strips (a) Rendering and (b) Von Mises Stress

The long strips represent a keratin section from the toe regions, and the short strips represent a keratin section from the shorter side walls of the hoof capsules. A series of prescribed displacements were analyzed (0.01 mm, 0.05 mm, 0.1 mm, 0.15 mm, 0.2 mm) and the resulting strain and Von Mises stress recorded. The effective stiffness of the dark keratin region was determined to be ~699 MPa, and the effective stiffness of the light keratin region was determined to be ~275 MPa.

In order to design a horseshoe that mimics the natural behavior of the hoof in question, the shoe must be made of a material that has a functionally graded stiffness from 275-699 MPa. Additionally, the strain properties of the material must support the necessary displacement requirements of a barefoot hoof. In this case, the barefoot simulation predicted a maximum strain on the loading surfaces of 0.006 mm/mm. As discussed in Section 9.2.1, the horseshoe is intended to be additively manufactured to accommodate the hoof-specific contour and the functionally graded stiffness (via varied infill densities), and both glue and/or nails should be considered for attachment method.

9.2.4 Additively Manufactured ABS Target Metrics

A series of ABS specimens additively manufactured in two orientations were tension tested to failure. The testing setup, specimen details, and data analysis methods are discussed in detail in Section 3.6.2. The series of specimens explored a range of infill patterns and densities, which can be reviewed in Figure 9.3. The infill pattern types tested were solid, honeycomb, double dense, and sparse. The honeycomb pattern is reportedly the best choice for parts that need structural integrity while limiting weight. The sparse infill is meant to limit weight when structural integrity is not a primary concern. The double dense infill pattern is similar to the sparse pattern, but with thicker interior struts.

(a)

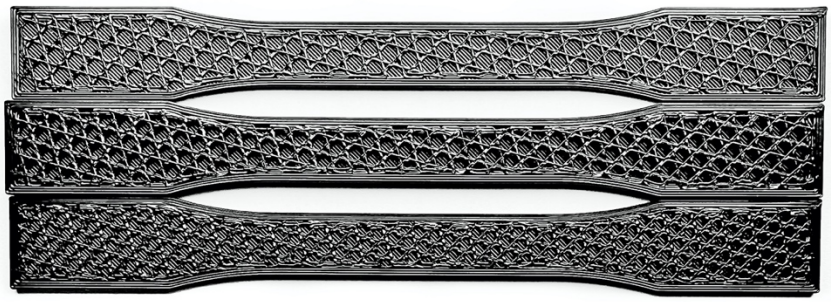

(b)

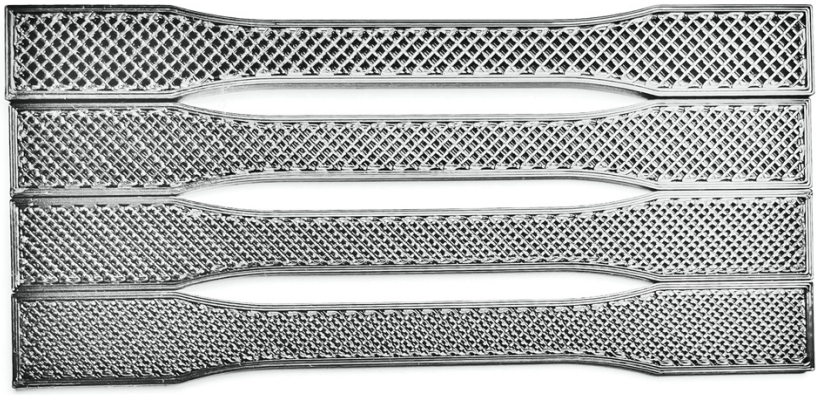

(c)

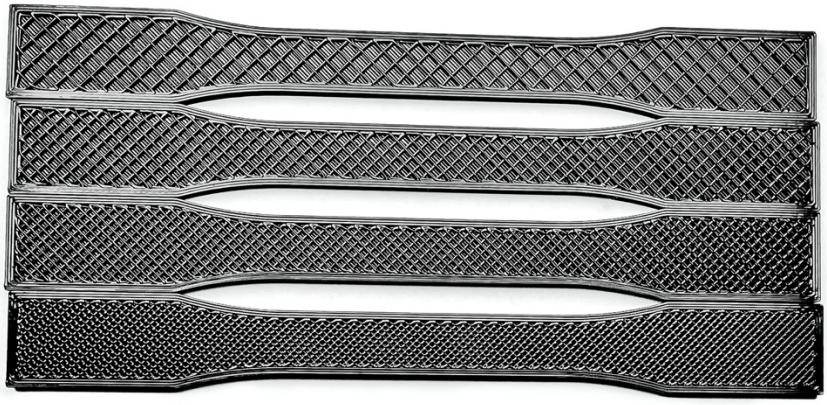

(d)

Figure 9.3 Infill: (a) Solid, (b) Honeycomb, (c) Double Dense, and (d) Sparse

The tensile curves for the additively manufactured ABS specimens with a variety of infill patterns and density settings can be found in Figures 9.4-5. Specimens printed in the x orientation produced tensile curves with a classic hyperbolic shape. The solid specimens clearly produced the highest stress response, while specimens with the sparse infill pattern saw the lowest stress response. The double dense infill pattern demonstrated the most variation when it came to varying the density settings. Specimens with the honeycomb infill pattern were the only specimens in the x orientation to exhibit lower stresses after yielding, though the downward slope of the tail was not exaggerated.

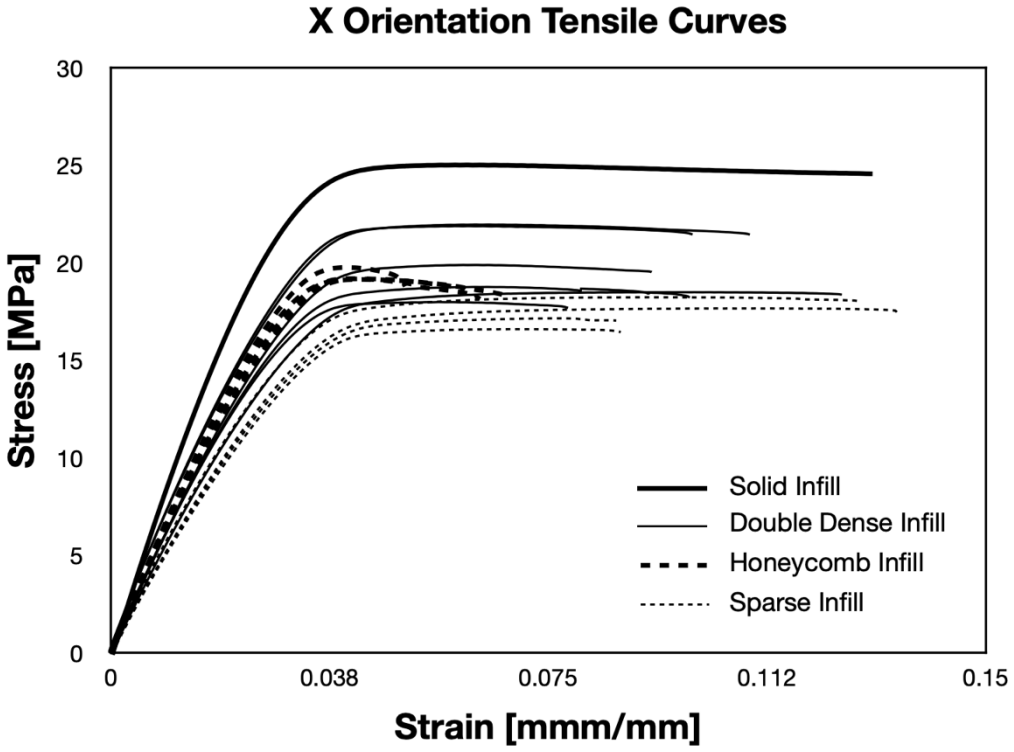

Figure 9.4 Tensile Curves for Additively Manufactured ABS in the X Orientation

The y orientation results, which are shown in Figure 9.5, produced shorter curves with a dip beyond the yield point typically indicative of polymeric ductility with minor strain softening. Like the x orientation data set, the solid specimen produced the highest stiffness, but the double dense infill pattern produced the highest ultimate tensile strength.

Specimens with the sparse infill pattern consistently produced the lowest stress response, and again, the double dense infill pattern demonstrated the largest variation in data across different densities. The honeycomb infill pattern was the most consistent across the density settings but exhibited the greatest strain softening. Overall, the y orientation specimens produced noticeably shorter percent elongation to failure than any of the specimens fabricated in the x orientation.

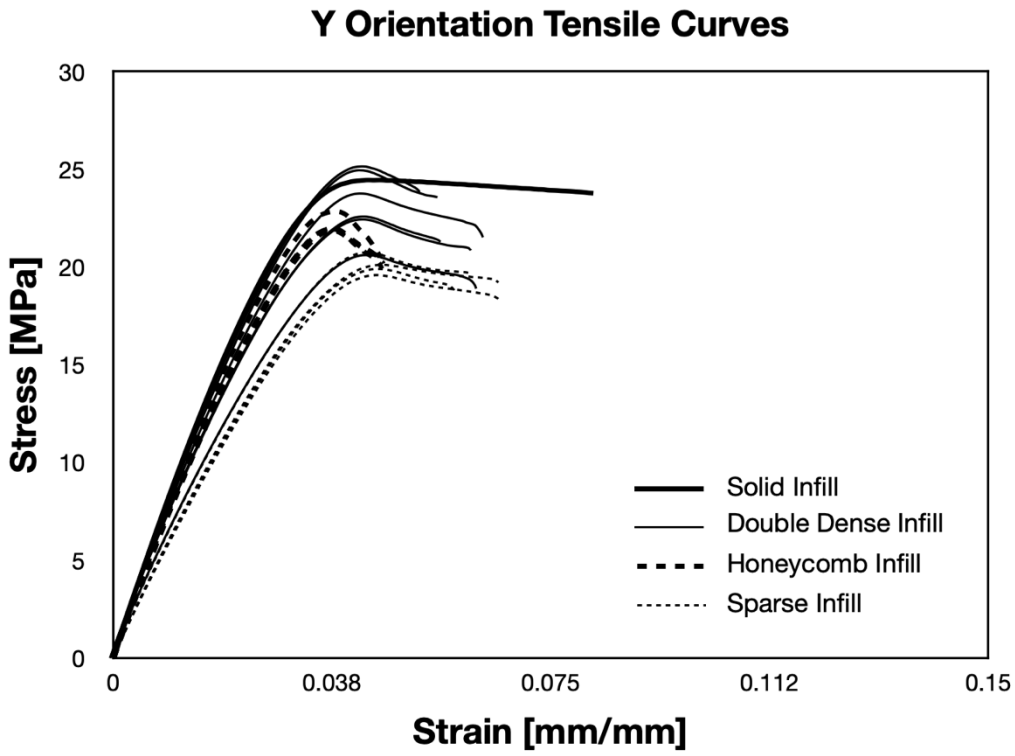

(b)

Figure 9.5 Tensile Curves for Additively Manufactured ABS in the Y Orientation

The resulting elastic moduli ranged from 0.53-0.93 GPa, and the material was generally stiffer as the specimen weight increased (Figure 9.6). Specimens 3D printed in the y orientation tended to yield higher material stiffnesses for the same amount of material as compared to specimens printed in the x orientation.

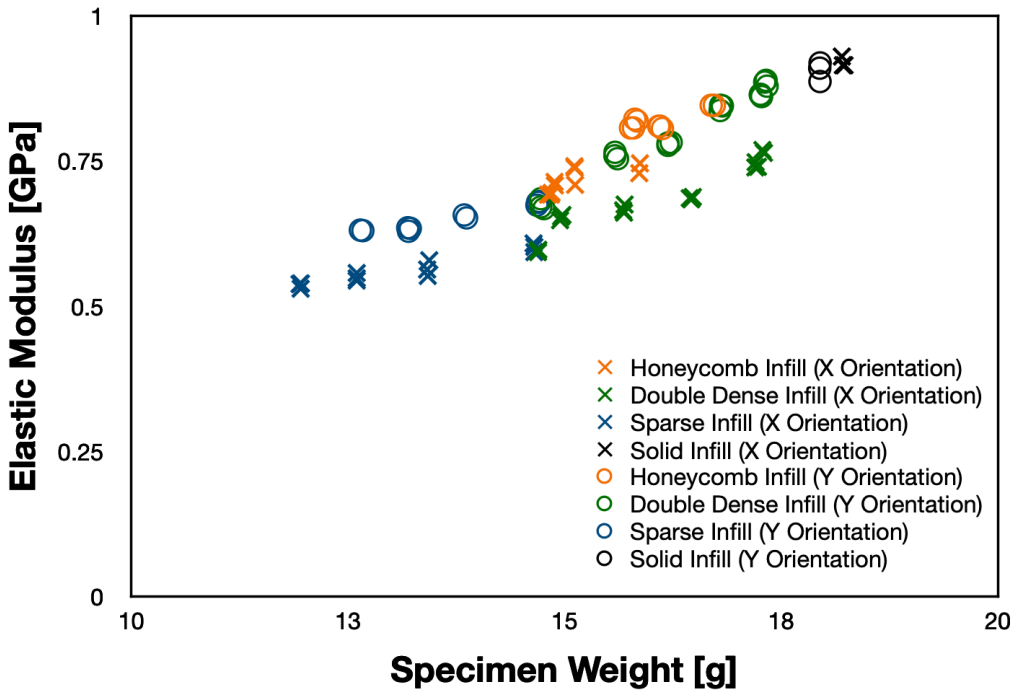

Figure 9.6 Stiffness of 3D Printed ABS For Various Infill Patterns and Densities

The strain response at the point of material yielding was similar across all infill patterns and densities. This can be seen in Figure 9.7. The strain at yield ranged between 0.006-0.016 mm/mm, with an average of 0.009 mm/mm. The most noticeable variation was a slight increase of yield strain for the sparse infill pattern on the lowest density setting. The strain at fracture, on the other hand, exhibits significantly more variation, with values ranging from 0.046-0.146 mm/mm. In general, the x orientation saw higher fracture strains than the y orientation specimens. The honeycomb infill pattern exhibited the lowest performance when compared with all others.

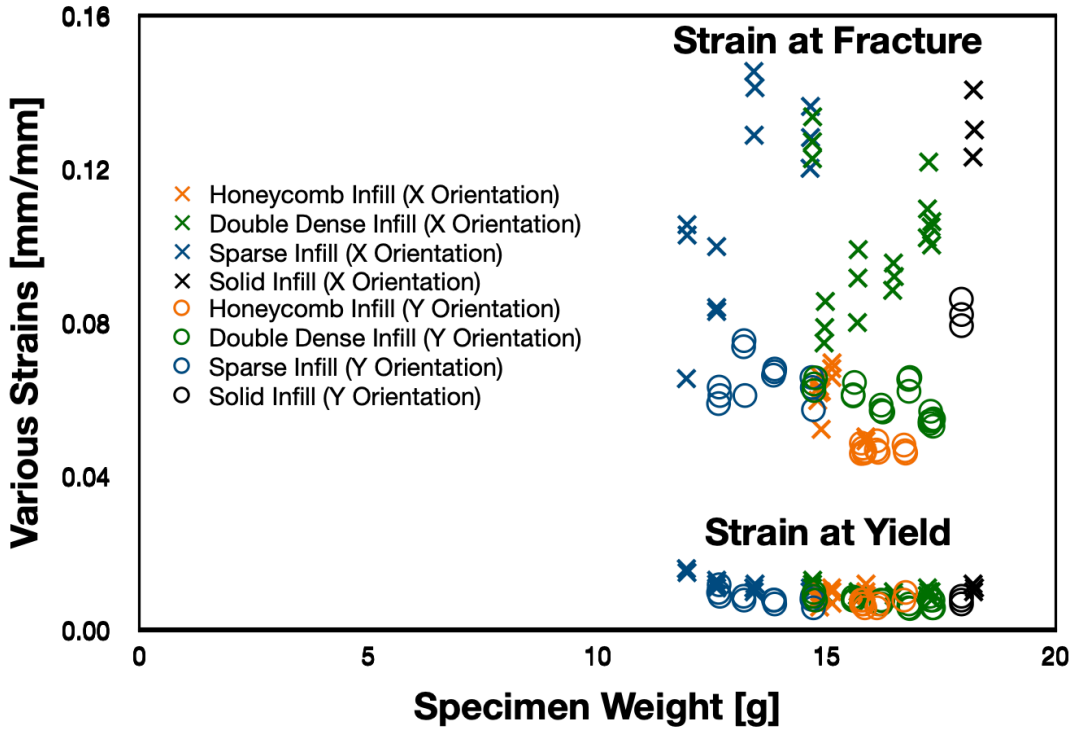

Figure 9.7 Strain Properties of 3D Printed ABS For Various Infill Patterns and Densities

The yield stress and ultimate tensile stress for the various additive infill patterns and densities are displayed in Figure 9.8. The yield stress ranged between 4.29-10.39 MPa with an average of 6.40 MPa. Overall, the specimens fabricated in the x orientation exhibited higher yield stresses than those printed in the y orientation. The sparse infill pattern appears to provide the best yield stress for the most economic use of material. The ultimate tensile stresses ranged from 16.5-25.3 MPa with an average of 20.77 MPa. There is a clear trend where the ultimate tensile stress increased with the material usage. The specimens printed in the y orientation tended to exhibit higher ultimate tensile stresses than those printed in the x orientation.

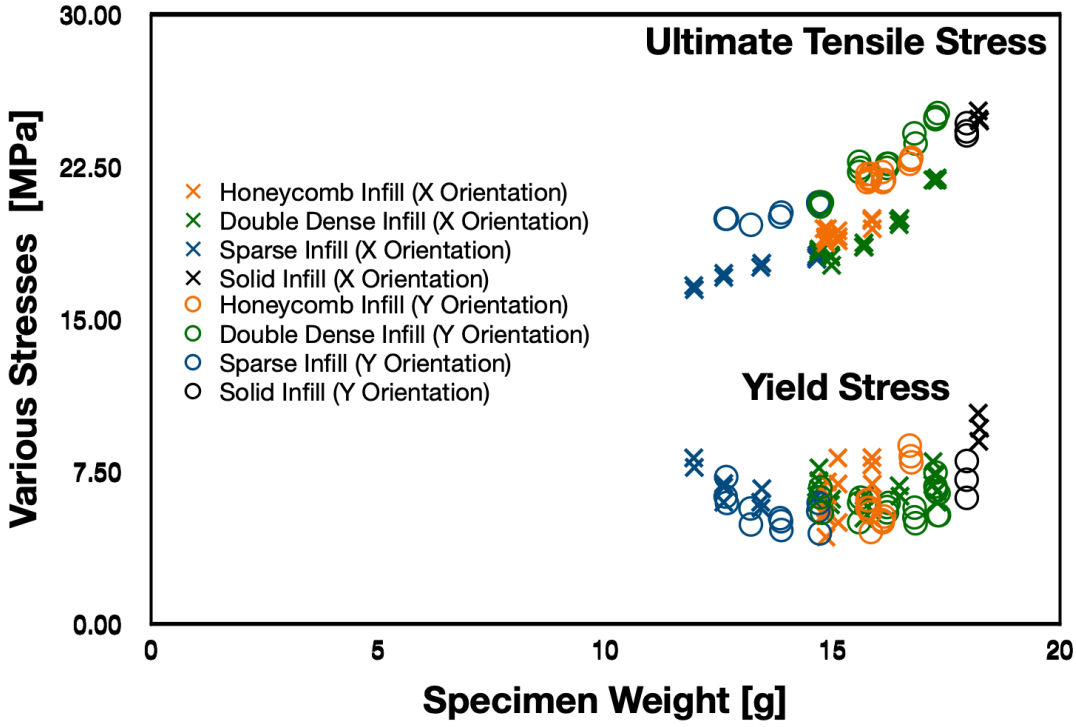

Figure 9.8 Stress Properties of 3D Printed ABS For Various Infill Patterns and Densities

A small batch of open-faced specimens were tension tested to failure in order to observe the deformation and final fracture behavior. Figure 9.9 displays one such example, where the specimen under tension was 3D printed in the x orientation with the sparse infill pattern and a 17% density setting. The blue ABS material tint allowed for clear observation of plastic deformation occurring on the exposed surfaces. As the specimen was stretched, the plastic deformation initiated at the points where the infill struts attached to the perimeter of the specimen. Further tension caused the plastic deformation bands to increase in the strut windows along the perimeter, where the diamond shape of the lattice was only half present. This is, logically, due to those locations have greater freedom of displacement in the absence of struts connected to the perimeter wall. Final fracture initiated at the edge of one of these plastic strain bands and tore through the body along the strut angles until it

reached the other side—and the corresponding plastic strain band. This failure sequence is representative of all additively manufactured ABS specimens tested in the study.

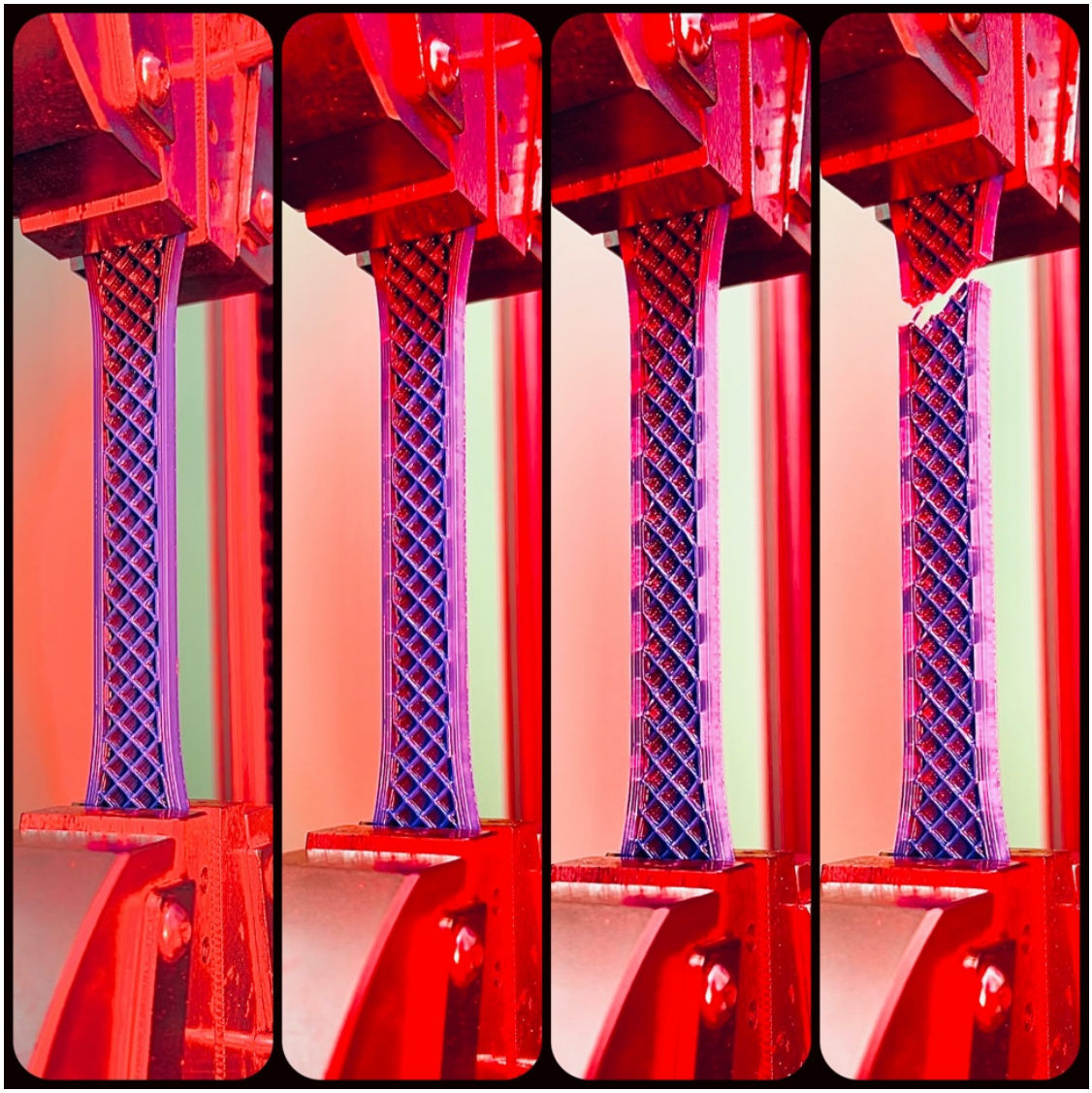

Figure 9.9 Tension Test Performed on Open-faced ABS Specimen with Sparse Infill

Now that the general material behavior of additively manufactured ABS has been quantified, the data can be used to determine the best print settings for a customized horseshoe with functionally graded stiffnesses. The effective stiffness of the dark keratin region of the barefoot hoof was determined to be ~699 MPa, and the effective stiffness of the light keratin region was determined to be ~275 MPa. Figure 9.10 shows the review of

the stiffnesses for various print settings of the ABS settings, and the properties that best match the desired hoof stiffness. A close match for the dark keratin was found to be ABS plastic 3D printed in the x orientation with a honeycomb infill patter and a 46% density setting. The light keratin, however, did not have an ideal match in stiffness, and so the settings associated with the lowest elastic modulus must be selected. In this case, ABS 3D printed in the x orientation using a sparse infill pattern and a 17% infill density setting will be utilized.

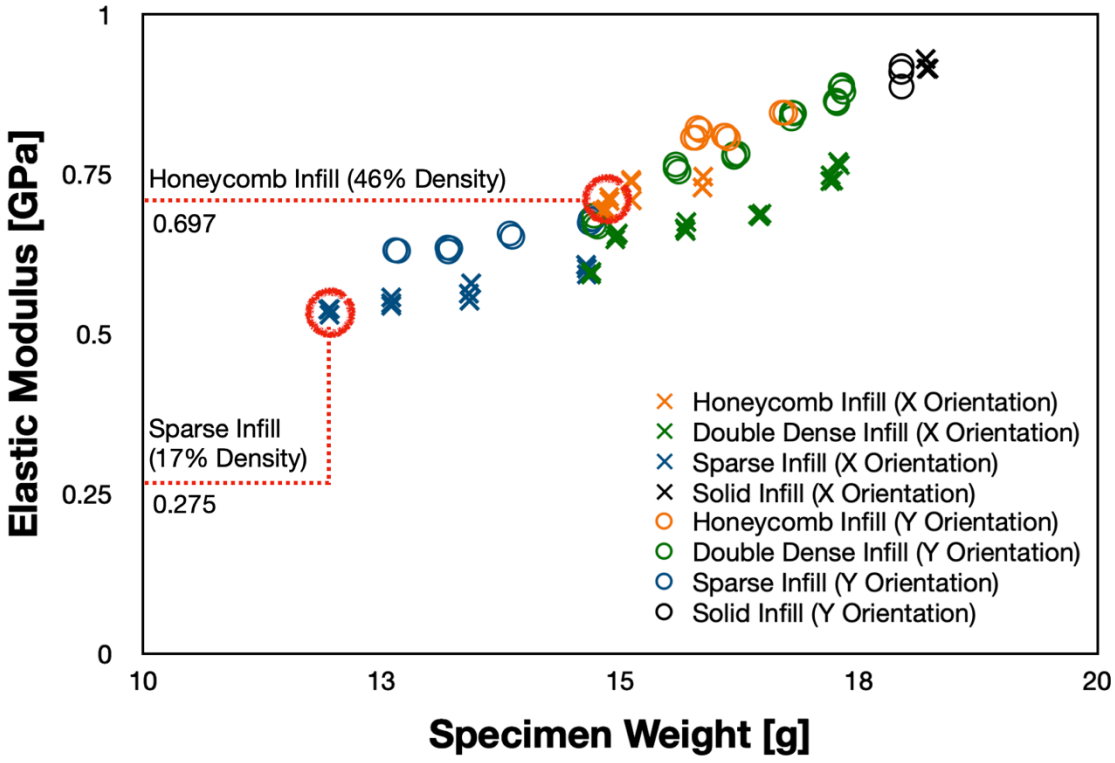

Figure 9.10 Target Elastic Moduli Metrics

Now that the infill patterns and density settings have been selected it is best practice to ensure that the other corresponding material properties are sufficient for the intended product use. The barefoot hoof simulation revealed the maximum strain along the capsule perimeter that will interact with the shoe to be 0.0085 mm/mm. Figure 9.11 identifies the

yield and fracture strains for the selected infill and density settings. The sparse infill setting demonstrated a yield strain of 0.011 mm/mm, which is greater than the maximum predicted strain. The honeycomb infill setting has a yield strain of 0.009 mm/mm, which is on par with the predicted strain of 0.0085 mm/mm. The fracture strains are sufficiently high that the ABS horseshoe should not experience a catastrophic amount of plastic deformation during the target service life of ~2 months.

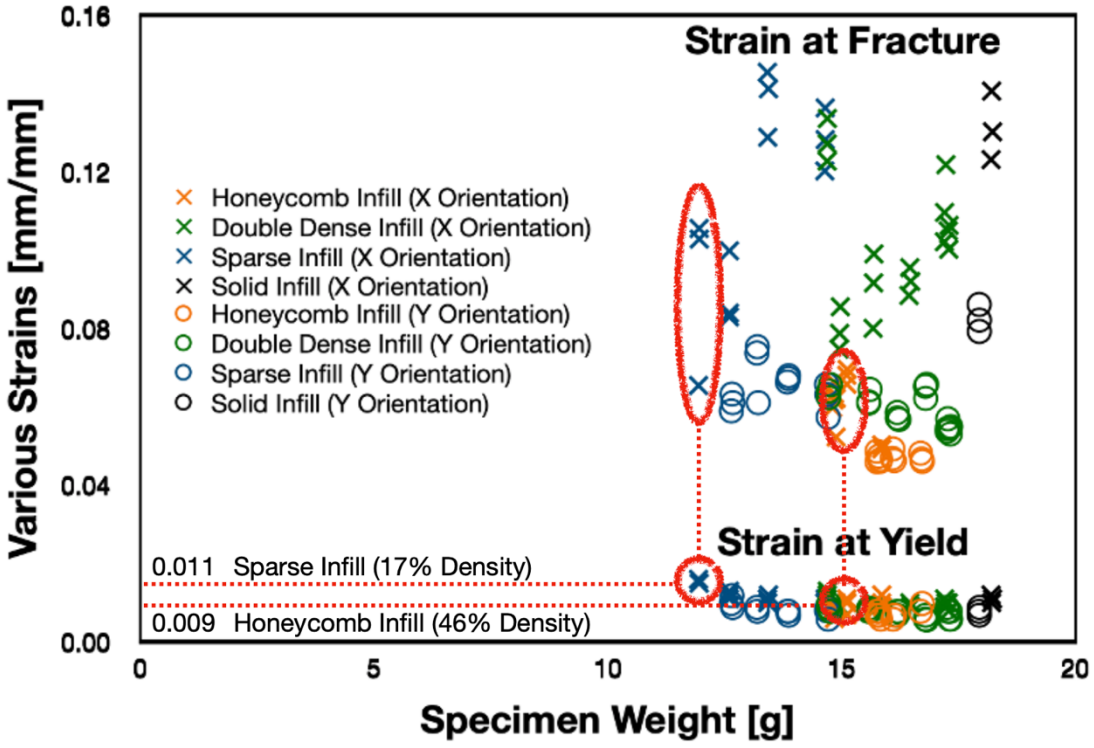

Figure 9.11 Target Strain Metrics

Finally, the stress properties must be analyzed as well to ensure the predicted stress in the barefoot hoof will not overload the ABS horseshoe. Figure 9.12 identifies the yield and ultimate tensile stresses for the selected infill and density settings. The barefoot hoof simulation predicted the maximum stress along the capsule perimeter that will interact with the shoe to be 5.04 MPa. Both the sparse and honeycomb infill yield stresses (8.026 MPa

and 5.714 MPa, respectively) are below the predicted simulation stress. The ultimate tensile strength in both cases is sufficiently high as to avoid any necking effects in the ABS shoe.

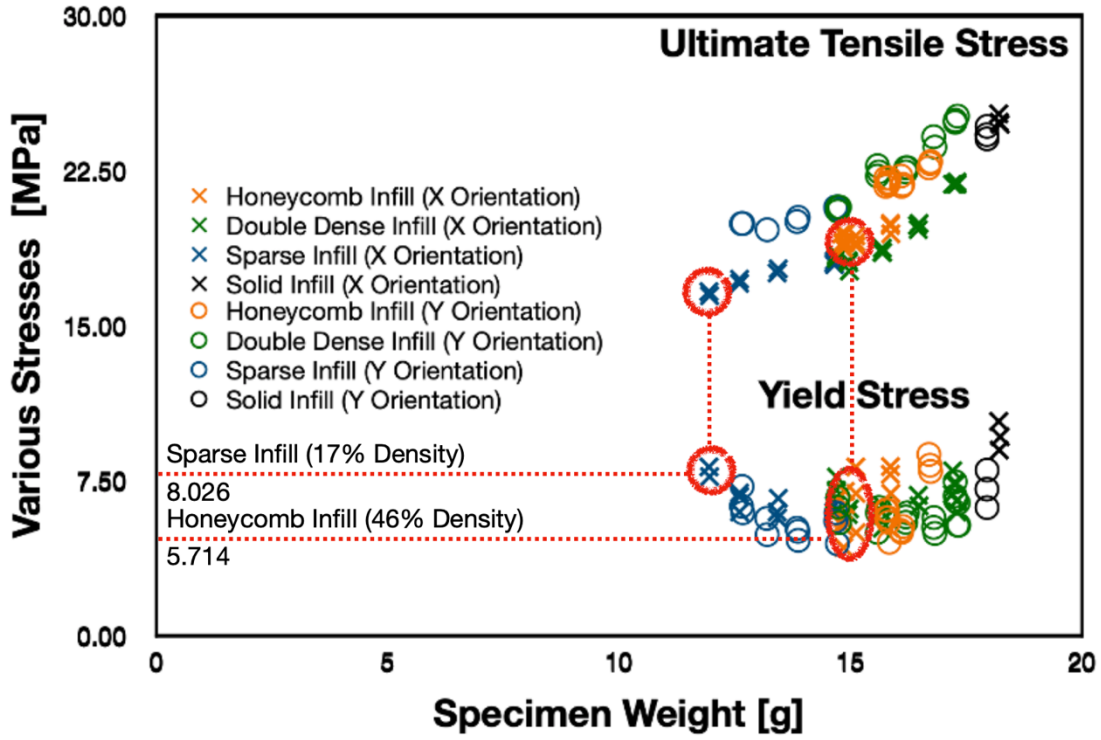

Figure 9.12 Target Stress Metrics

These material parameters are appropriate to serve as a shoe for a typical walking horse. The honeycomb infill material has yield stress and strain values close enough to the simulation predictions that some minor plastic strain effects might be experienced by the shoe, but the target service life of ~2 months should not accumulate enough damage to cause a catastrophic failure in a typical walking horse. However, if harder activities or environments are expected, such as galloping or hauling cargo, then other parameters must be selected. This underlines the imperative to carefully analyze and select materials on a hoof-by-hoof basis for the best results.

9.2.5 Formahoof Advanced Polymer Target Metrics

Gluing the ABS shoe to the hoof is one of the attachment methods under consideration, and as such, the material properties must be understood. For this purpose, a series of Formahoof Advanced Polymer specimens were manufactured and tension tested to failure. Formahoof Advanced Polymer is a flexible two-part polyurethane resin used to coat and protect a horse's hoof capsule. The testing setup, specimen details, and data analysis methods are discussed in detail in Section 3.7. To fabricate the tensile coupons, the Formahoof Advanced Polymer was injected into a mold to cure into the desired geometry, and the specimens were tracked based on the order of fabrication. All specimens in the testing batch were manufactured at the same time, and then tested at different time intervals in order to quantify any aging effects that might occur during the target service life of ~2 months. Figure 9.13 displays the tensile curves obtained during testing, with color coordinated lines to represent the variation in specimen age. The typical curvature has a hyperbolic tangent shape. There is no apparent relationship between the stress response and aging period within the examined time frame spanning 1-60 days.

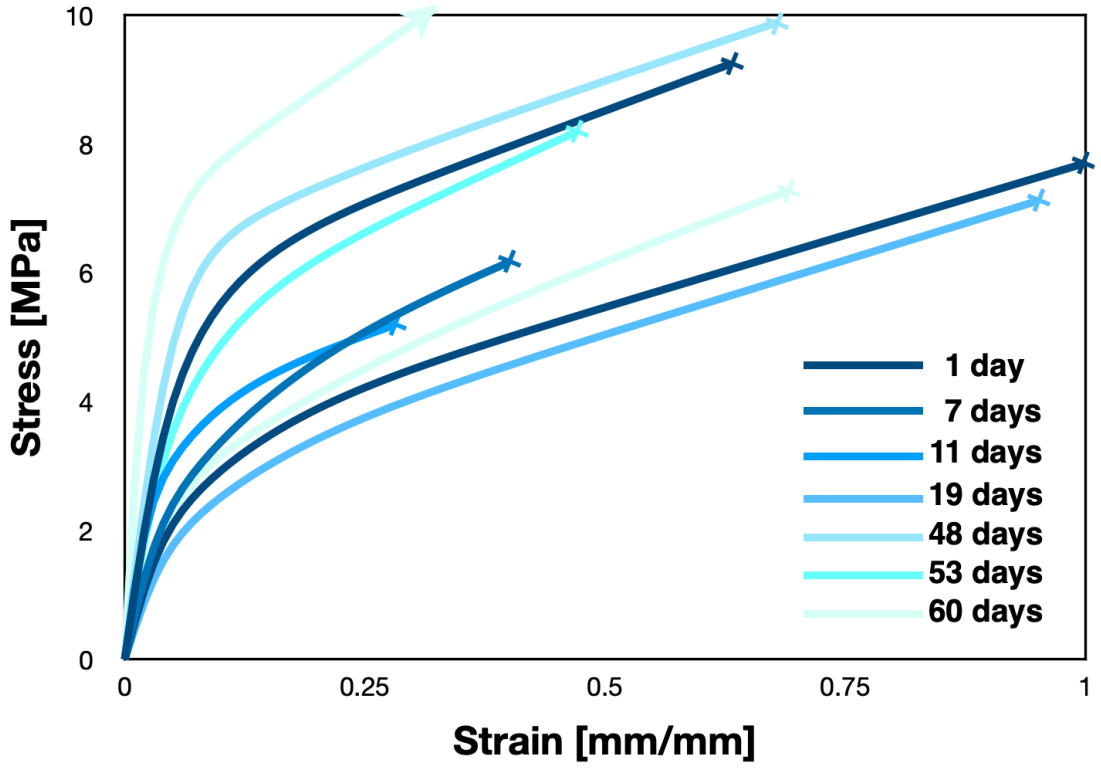

Figure 9.13 Tensile Curves of Formahoof Advanced Polymer Specimens

Figure 9.14 displays the elastic moduli of the specimens across the 60 day aging period. There was a range of variation in the Formahoof stiffness between 0.048-0.327 GPa with an average of 0.114 GPa. The resulting stiffness maintained a consistent variation between 0.048-0.131 GPa across all 60 days with the notable exception of the highest stiffness 0.327 GPa. The results indicate that it is not aging that affects the Formahoof stiffness properties, but the resulting homogeneity of the mixing process. The higher the stiffness, the "clearer" and "brighter" the polymer coloration with fewer striation tails and bubbles—which is indicative of how well the two components were mixed in the injection nozzle. What this means for field application is that the farrier should cast off the first amount of Formahoof injected from the nozzle before using the polymer for shoeing

purposes. For simulation purposes, the average material properties may be utilized to predict the behavior of various shoeing setups.

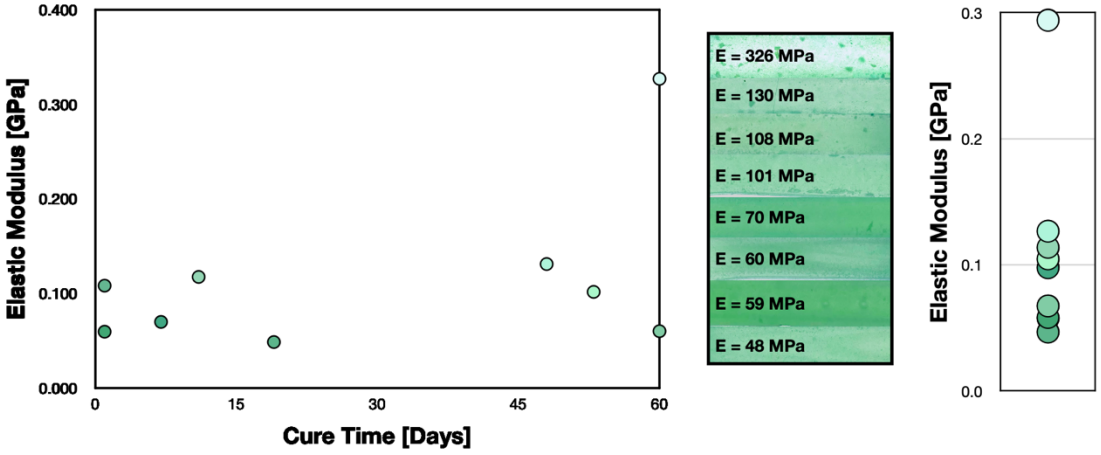

Figure 9.14 Elastic Moduli of Formahoof Advanced Polymer Specimens

9.3 Shoeing Simulations and Results

Prior to prototyping, it is best practice to evaluate the shoeing scenarios under consideration using FEA simulations. The first scenario explored here was to model a functionally graded ABS horseshoe that will be attached to the hoof using Formahoof Advanced Polymer as glue. Figure 9.15 compares the stress distributions of a classic nailed steel shoe with the simulated ABS horseshoe glued onto the capsule perimeter.

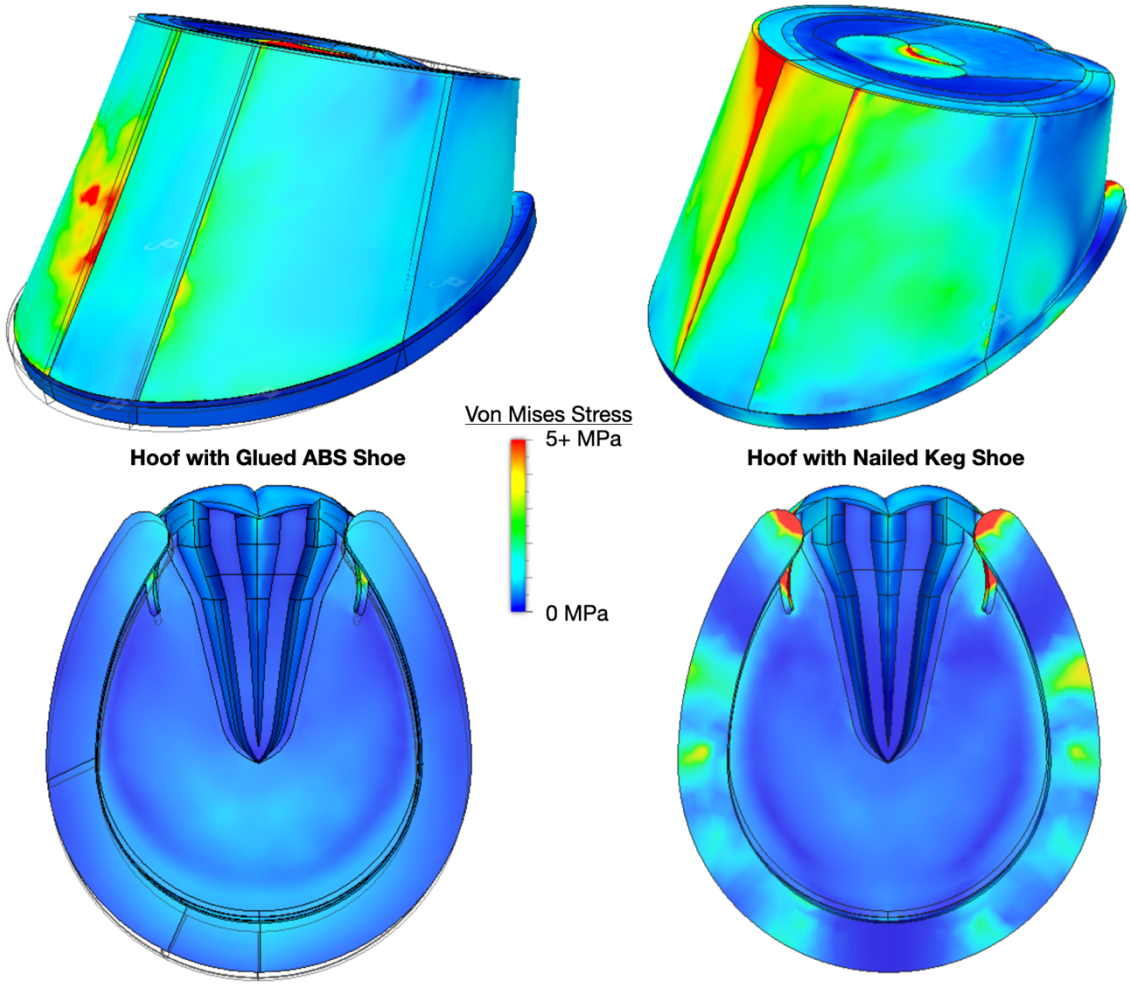

Figure 9.15 Simulation Comparison of a Typical Walking Equine Hoof in the Keg Shoe and ABS Glued Shoe Conditions

The steel shoe has a peak of ~7.8 MPa in the dorsal wall, and an average stress of 2.4 MPa across the majority of the hoof capsule outer wall. There are clear stress concentrations both along the perimeter at the nail sites and corresponding locales or increased stress in the wall above the nail locations. The ABS shoe glued onto the perimeter caused a peak stress of ~5.86 MPa in the central region of the outer dorsal wall, and an average stress across the outer wall of ~1.2 MPa. There is, comparatively, a distinct reduction in stress

concentrations in the outer capsule wall, and stress is distributed across the capsule in a much smoother gradient.

Reordering the stiffness of the ABS glued shoe in such a way that the lighter, more supple keratin is supported by stiffer ABS properties and vice versa, the stress distribution throughout the hoof capsule can be further manipulated. Figure 9.16 compares the previous simulation where the shoe matched the keratin stiffness and an adjusted shoe with opposing stiffness properties. The stress concentration at approximately the center of the toe wall has been further reduced, though the general stress across the front of the hoof wall capsule is somewhat elevated. Despite the general stress elevation, the distribution of that stress is furthered balanced, particularly along the front of the coronary band. This is simply a useful demonstration of how the stress throughout the hoof capsule can be managed through careful arrangement of the shoe stiffness gradient for specific purposes and applications.

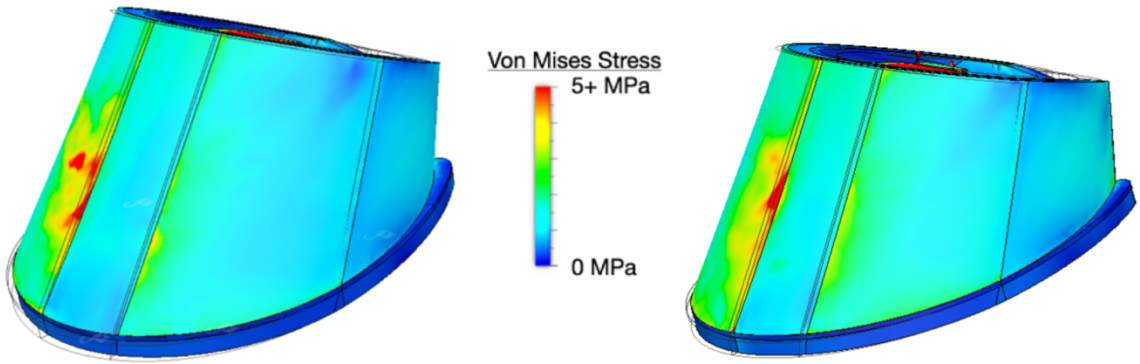

Figure 9.16 Simulation Comparison of a Typical Walking Equine Hoof in the ABS Glued Shoe Conditions with Matching Stiffnesses and Opposing Stiffnesses

The second scenario explored was to model a functionally graded ABS horseshoe that will be attached to the hoof using nails. Figure 9.17 compares the stress distributions

of a classic nailed steel keg shoe with the simulated ABS horseshoe nailed onto the capsule perimeter.

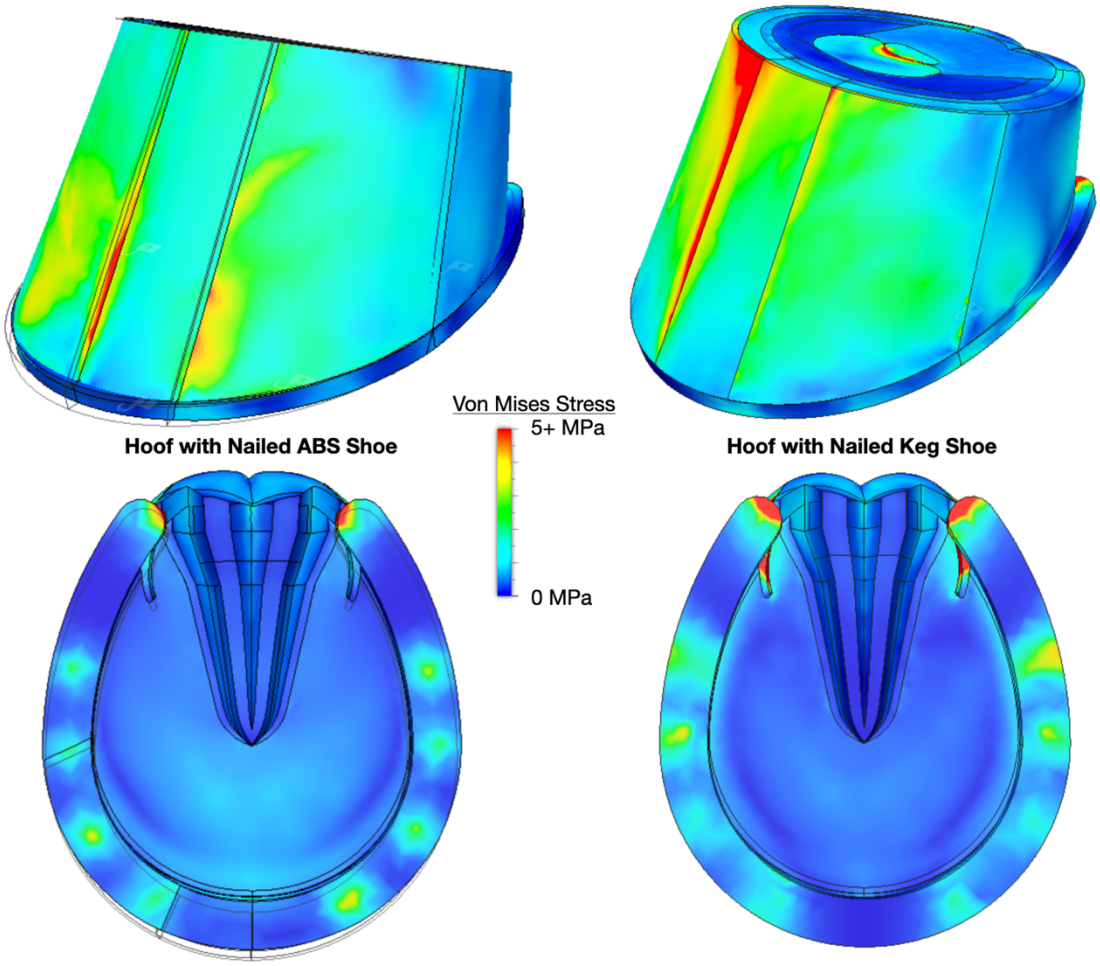

Figure 9.17 Simulation Comparison of a Typical Walking Equine Hoof in the Keg Shoe and ABS Nailed Shoe Conditions

In the nailed ABS shoeing condition, approximate stresses of the nail locations along the loading perimeter of the hoof capsule were 6.9 MPa, 2.7 MPa, 2.0 MPa, 2.6 MPa, listed from toe to heel. The flex in the ABS shoe, even when attached via nails, reduces the stress as compared to the classic keg shoe (nail stresses: 5.5 MPa, 5.2 MPa, 8.87 MPa, and 13.14 MPa, toe to heel). The maximum stress of the nail slots shifted to the frontmost position in the ABS shoe as opposed to the heel-most location that resulted in the keg shoe. This is

likely due to the heels and sidewalls being freer to expand naturally. Even when nailed to a healthy hoof, the simulation indicates that an ABS horseshoe would protect the hoof while exhibiting behavior that better mimics equine hoof keratin.

9.4 Designing Into 3D: Fit, Form, and Function

Before a design can be prototyped for testing, there are still many considerations to attend to specific to the additive manufacturing solution space. One of the most obvious fabrication details to account for is the layer orientation of 3D printed parts. When loading is applied orthogonally to the layers, the part is weakest and will fail along the fusion zone. If the horse's activity is walking and trotting, then the maximum loading from the hoof will be applied vertical to the ground plane, and the horseshoe should be printed in such a way that the layers are oriented to be strong in that direction. If, however, the horse's activity to hauling cargo, then the maximum loading may be nearly parallel along the ground plane, and a different print orientation would be needed.

A secondary concern regarding print orientation is the wear properties of the part. The rate of wear of a 3D printed part is dependent upon the layer orientation. If one of the desired functions of the ABS shoe is to be worn away on the toe and edges as the hoof continues to grow, then the print orientation must be arranged to accommodate this. However, if the bottom of the shoe is to be long-lasting and provide continuous friction for a steady step, then a different orientation may be required. Sometimes different desired functions of a part may require competing layer orientations, at which point the hierarchy of functional needs may be utilized to choose the most important one to satisfy. The other option is to orient the part at a non-orthogonal angle in an effort to satisfy both needs to some extent—if this route is chosen, a breakeven table is a useful approach. A firm

understanding of both material and tribological properties is imperative in order to leverage the layer orientation to work for the design.

Another consideration for the additive design space is geared toward lightweighting the manufactured part. The reduced material usage can also lead to reduced cost—especially in the case of larger batch production. Density and infill patterns can significantly reduce the material usage, but often at the cost of structural integrity. Using fillets in the design to round over sharp corners and edges is another simple way to remove material that is often excessive when the loading type and orientation is considered.

Finally, fracture behavior of the additively manufactured material should be understood and, whenever possible, leveraged to serve a useful purpose. Crack growth often follows along the layer boundaries of 3D printed materials, though this is not a universal rule. Adding design features that can potentially usher the crack growth along a more tortuous path could prolong the service life and increase opportunity for maintenance actions. Designing a part in such a way that the crack initiation sites are purposely located within convenient view of a regular observer could serve as an early warning signal for impending failure. With the design of equine orthotics as context, an alert function to service/replace the horseshoe before it fails in the field would be a very useful quality.

9.5 Summary

In this chapter, a CAD model of the equine digit was constructed and used to simulate a handful of shoeing scenarios. The hoof capsule was divided into three regions that could be customized with local stiffness properties derived from the TD distribution profile of the horse in question. Additively manufactured ABS was analyzed to obtain various mechanical properties of different infill patterns, density settings, and layer

orientation in an effort to match the typical material behavior of a barefoot equine hoof. Additionally, Formahoof Advanced Polymer was analyzed in order to obtain the mechanical properties needed to simulate gluing a horseshoe onto the hoof to determine its viability as an alternative to nails. An ABS horseshoe was designed with a gradated material stiffness throughout the part in an effort to lower the stress distribution caused by a keg shoe. The major conclusions are summarized as follows:

- Additively manufactured ABS specimens with various infill patterns and densities produced resulting elastic moduli ranged from 0.53-0.93 GPa, and the material stiffness generally increased with density. ABS specimens 3D printed in the y orientation tended to yield higher material stiffnesses for the same amount of material as compared to specimens printed in the x orientation.
- For all additively manufactured ABS tested in the study, the solid specimens produced the highest stress responses, while specimens with the sparse infill pattern saw the lowest stress responses. The double dense infill pattern demonstrated the most variation when it came to changing density settings.
- For all additively manufactured ABS tested in the study, yield strain ranged from 0.006-0.016 mm/mm, with an average of 0.009 mm/mm. The fracture strain saw greater data variation, and ranged from 0.046-0.146 mm/mm. In general, the x orientation saw higher fracture strains than the y orientation specimens. The honeycomb infill pattern exhibited the lowest performance when compared with all others.
- For all additively manufactured ABS tested in the study, yield stress ranged from 4.29-10.39 MPa, with an average of 6.40 MPa. Overall, the specimens fabricated

in the x orientation exhibited higher yield stresses than those printed in the y orientation. The sparse infill pattern appears to provide the best yield stress for the most economic use of material.

- For all additively manufactured ABS tested in the study, the ultimate tensile stress ranged from 16.5-25.3 MPa with an average of 20.77 MPa. The ultimate tensile stress tended to increase with density. Specimens printed in the y orientation tended to exhibit higher ultimate tensile stresses than those printed in the x orientation.
- Formahoof Advanced Polymer did not demonstrate any apparent relationship between the stress response and aging period within the examined time frame spanning 1-60 days. Instead, higher material stiffness seemed associated with the homogeneity of the mixture. For field application purposes, the farrier should cast off the first amount of Formahoof injected from the nozzle before use. Stiffness ranged from 0.048-0.327 GPa with an average of 0.114 GPa.
- The simulated equine digit with an ABS shoe glued to the hoof perimeter demonstrated a reduction and smoothening of the stress distribution in the outer capsule wall. No large stress concentrations on the side walls or loading perimeter due to the lack of nails. The flex in the ABS shoe, even when attached via nails, reduced the stress as compared to the classic keg shoe.

CHAPTER 10

CLINICAL TRIALS

10.1 Preventative Shoe

Two horseshoe designs were prototyped via additive manufacturing and field tested. A number of design choices were considered, such as the early options displayed in Figure 10.1. Some of the qualities of the early designs involved flexible heel supports, full arch supports, and a hoof wall cover to protect toe splits from further aggravation.

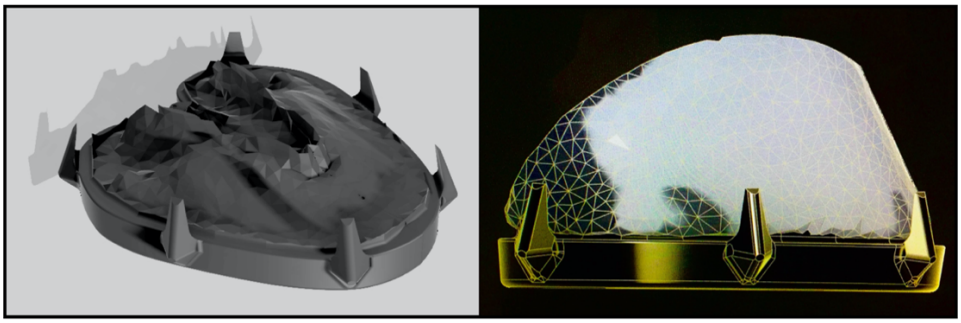

(a)

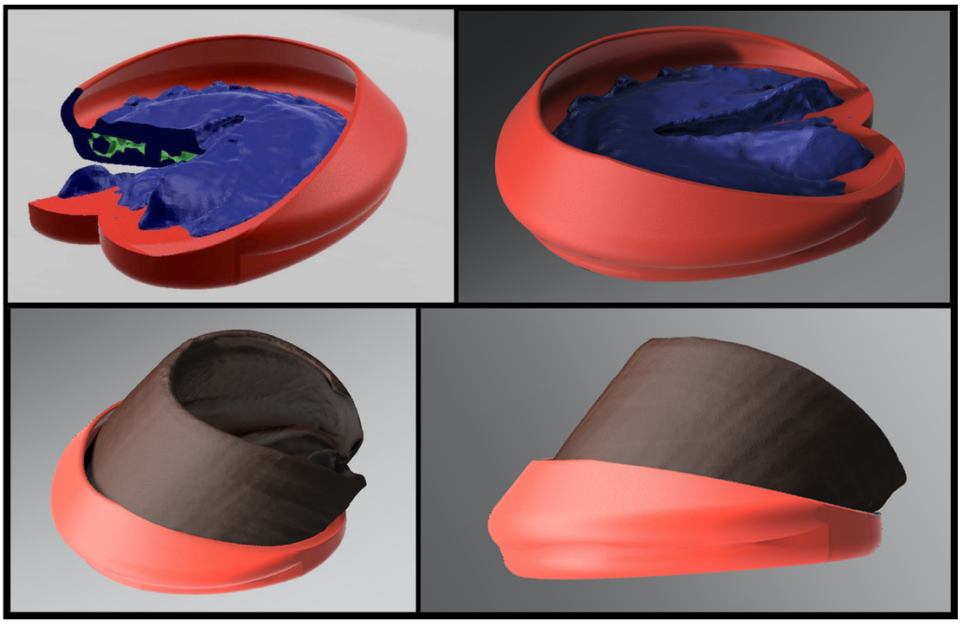

(b)

Figure 10.1 Various Horseshoe Designs That Utilize Additive Manufacturing

The shoe first selected for field testing was one of the simplest "preventative" designs. The minimalist split shoe was chosen for fabrication, and the 3D printed "universal" shoe is displayed in Figure 10.2. The spit nature of the shoe allows for full, natural heel expansion without the increased strain at the apex curvature under the dorsal wall at the toe. Additionally, the free lateral flex will exercise the digital cushion and improve the health of the internal biology of the equine digit. The ABS material generally reduces the stress on the hoof capsule, and the selected attachment method of Formahoof Advanced Polymer will avoid the stress concentrations and damage wrought by traditional nails. The leading toe edge is left free for continued growth and wear.

The breakaway supports from the additive manufacturing process can also be seen in Figure 10.2, which also represents the print orientation. By printing the part on the edge, the infill pattern is oriented in the x direction with respect to the loading direction of the hoof. If the shoe had a connecting arch beneath the toe region, a different print orientation would have been required instead. This particular minimalist split shoe has a generic topology as the hoof capsule was not known prior to shoeing. There are, however, two different textures on the top and bottom planes that the farrier may choose from depending on the ground plane friction requirements. One side is a tread geometry to increase grip, while the other side is comprised of inset semi-spheres in a pattern reminiscent of dominos, which is better for flat substrates, such as paved or concrete surfaces. Both patterns increase the surface area with which the Formahoof Advanced Polymer can hold the shoe to the hoof perimeter.

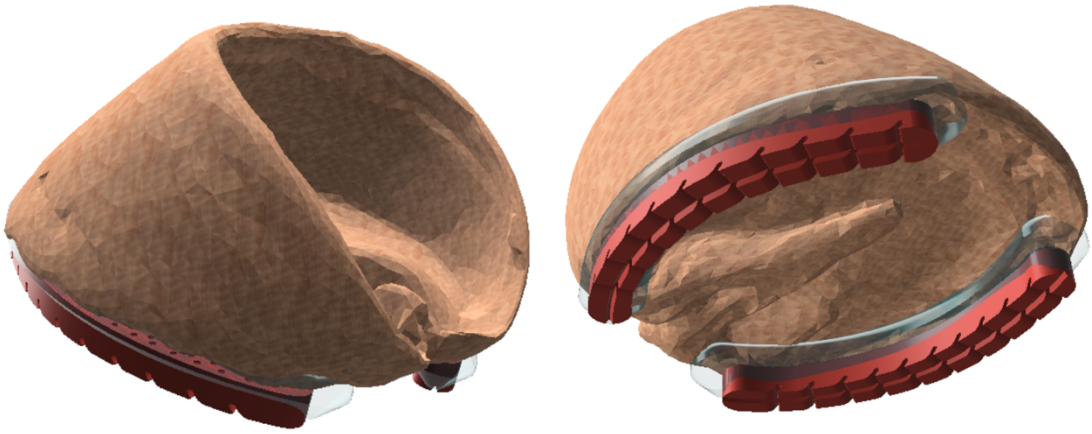

(a)

(b)

Figure 10.2 Minimalist Split ABS Horseshoe

10.1.1 Tooling and Application

Before the shoe may be applied, the hoof must be prepared. In this case, the hoof was first cleaned, trimmed, and rasped. Figure 10.3 demonstrates the hoof at various stages of the preparation process.

Figure 10.3 Preparing the Hoof for Shoeing

Once the hoof was fully prepared, the shoeing process was undertaken, the steps of which may be reviewed in Figure 10.4. The general shoe placement and tread orientation is chosen by the farrier, and then the hoof is wrapped to provide a rough surface to which the shoe was attached. The hoof wrap provided both the texturized surface area for attachment and some added support to the hoof capsule walls for the initial trial. Once the shoe was attached using Formahoof Advanced Polymer, the shoe and glue were rasped to achieve the ideal contour and remove any exposed leges that could lead the horse to throw the shoe.

Figure 10.4 Attaching the Minimalist ABS Split Shoe Onto the Hoof

The shoe appeared to have been a success overall. The horse walked well on the minimalist split shoe, and a series of chronological photographs describing the typical step sequence is shown in Figure 10.5. The hoof being reasonably healthy to begin with, an initial qualitative analysis can be made by comparing the horse's step before and after shoeing. The stride was approximately the same length, and the horse walked with confidence and did not demonstrate any hesitation to be led in different directions and to change speed. The animal seemed to be comfortable and was not disturbed by the shoeing process. The only drawback seen was a shorter service life than the desired 2 months. Without the front connecting bridge of the classic horseshoe shape, the split shoe was more susceptible to rocks and other large pulling items in the field. Overall, the design is promising, but needs further development to become a long-term shoeing solution for typical circumstances and activity.

Figure 10.5 Step Sequence of Horse Wearing Glued ABS Minimalist Split Shoe

10.2 Orthotic Shoe

The second shoe selected for field testing was a corrective design for a horse that was considered lame in the hindquarters. For this reason, only the forelimbs were shod. The equine digits in question can be viewed in Figure 10.6. The left forefoot had a dropped arch, and the lower heel is apparent when compared with the healthier right forefoot.

Figure 10.6 Various Views of the Hoof Prior to Shoeing

X-rays were taken of the barefoot hooves in order to assess the state of the equine digits and make a judgement regarding what corrections might be needed. As can be seen in Figure 10.7, the right forefoot had a full digital cushion and straight skeletal alignment. The left forefoot, however, shows an underslung heel, and the digital cushion is somewhat compressed and less full than that of the opposite hoof. Most notably, there is clear skeletal misalignment in the left forefoot, where the hoof angle is a little too low, and the hoof axis is broken back. The slight concavity of the dorsal wall suggests the beginning of an elongating toe, which means the shoe must be flexible enough to reduce the stresses in the hoof wall. Additionally, the hoof angle should be elevated, not only to begin adjusting the left forefoot skeletal alignment, but because the raised heels will reduce the overall stress in the hoof capsule [90]. Added support under the sole would help alleviate some of the dropped arch issues, and a split shoe would stimulate the digital cushion and frog region.

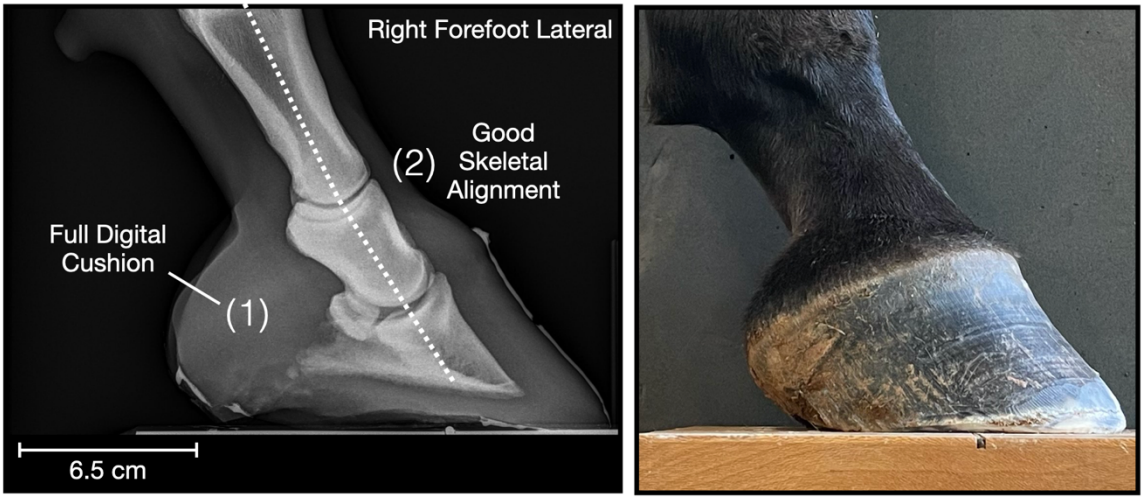

(a)

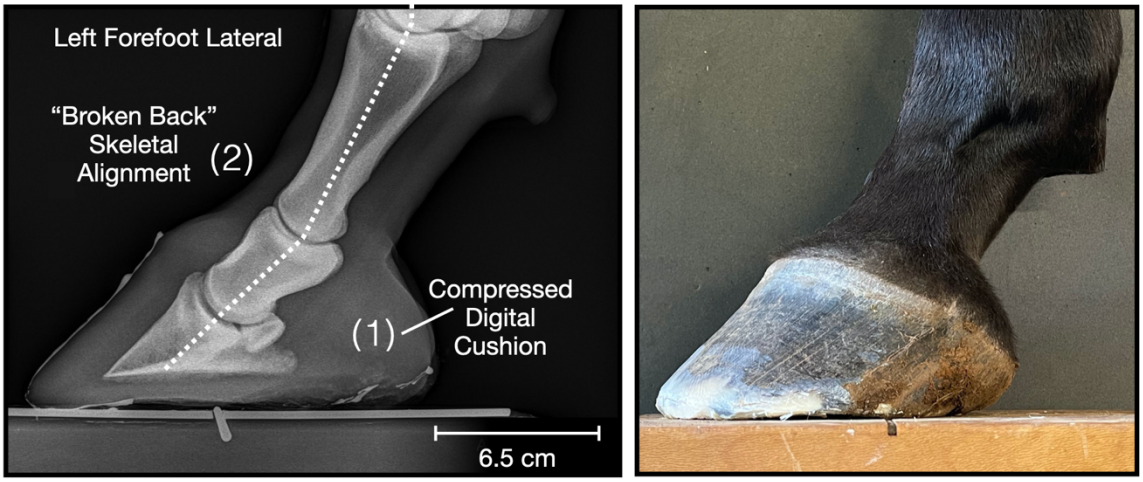

(b)

Figure 10.7 X-rays of the Hoof Prior to Shoeing

10.2.1 Tooling and Application

A CAD model of the corrective split shoe can be viewed in Figure 10.8. A 7º corrective angle was designed into the horseshoe in an effort to lift the heels and adjust the skeletal alignment. The body of the split shoe is comprised of additively manufactured ABS to hold the perimeter loading, and the central bridge is a latticework cushion 3D printed out of Thermoplastic Polyurethane (TPU) to support the arch of the hoof. A

secondary benefit of the lattice work is how it allows moisture to drain and evaporate so as not to saturate the hoof and/or promote bacteria growth. The nubs along the outer wall of the shoe are present for added surface area the Advanced Equine Polymer may attach to. Both ABS and TPU are malleable enough for the farrier to trim and rasp into a tight, custom fit along the hoof capsule. The split shoe aspect not only promotes lateral flex to stimulate the digital cushion, but also leaves the frog free to interact with the ground surface. Treads along the ground surface of the shoe deters slipping.

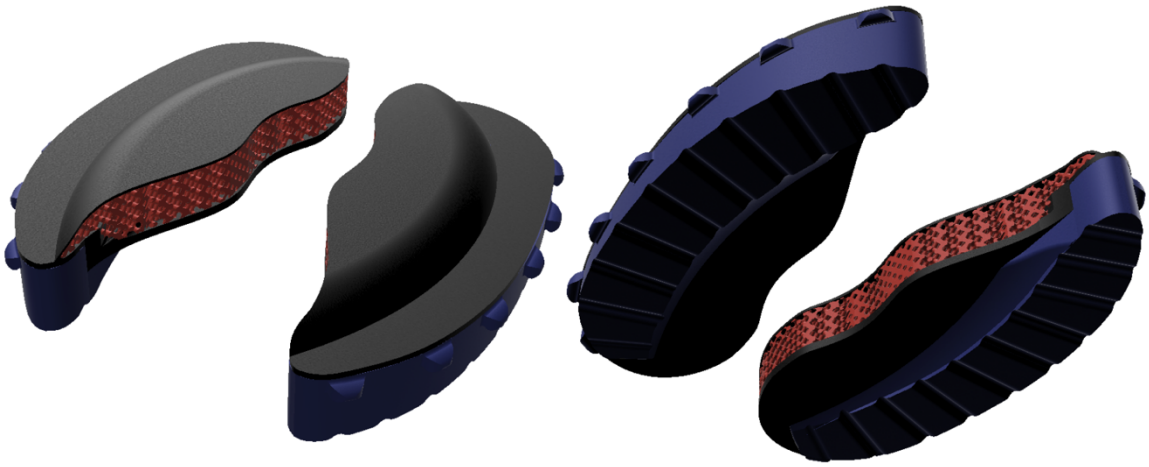

Figure 10.8 Angle-Correcting Shoe Design

The general steps for shoeing the prototype are presented in Figure 10.9. Prior to shoeing, the hoof must be prepared in the typical manner, including but not limited to cleaning, trimming, and rasping. Because the shoe incorporated arch support that covered a large portion of the sole, drying the hoof with a torch was also performed to discourage the growth of bacteria. The split shoe is aligned on the hoof perimeter and Formahoof Advanced Polymer is used to glue the shoe in place. Once curing was finished, the shoe and excess Formahoof Advanced Polymer were rasped into a cleaner profile along the hoof capsule. The shod hooves clearly show how the angled heel supports are present without interfering with the frog or overall flex of the hoof.

Figure 10.9 Shoeing Process

X-rays of the shod hooves were obtained and are presented in Figure 10.10. The added 7º lift of the heels improved the skeletal alignment and fetlock angle. This should also provide the added benefit of reducing the strain on the deep digital flexor tendon and superficial flexor tendon.

The shoe prototype appears to have been a success. The angle adjustment appears to have improved upon some of the existing hoof issues and the animal was receptive to the shoe. When comparing the stride of the horse before and after shoeing, there was an apparent increase in stride length, and the horse seemed to be more confident overall (Figure 10.11). The horse was even brought to a trot, which it was reticent to do before the front hooves were shod.

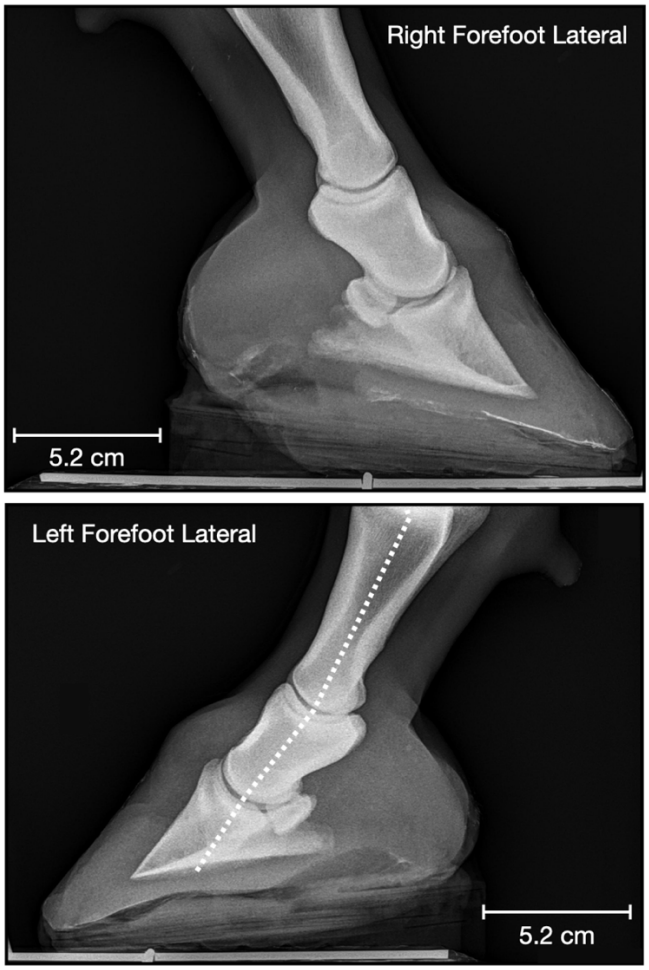

Figure 10.10 X-rays of the Shod Hoof

Figure 10.11 Comparison of Typical Step Prior to and Post Shoeing

CHAPTER 11

SUMMARY REMARKS AND FUTURE RESEARCH

11.1 Overview

In this work, the foundation was laid for a method that can predict the custom, functionally graded stiffness of a horse hoof based upon the TD distribution of the capsule walls. This TD information can be obtained from the trimmings that are material castoffs inherent to the shoeing process. The local keratin properties can be used to predict bulk hoof wall stiffness, which can be utilized in FEA analysis to predict the best shoeing practices for a specific animal. Various stages of this process were tested to prove the concept.

11.2 Local Keratin Behavior with Respect to Tubule Density

Equine hooves wildly vary from animal to animal, even geometry and thickness will differ between horses of the same breed. Studies focusing on the tensile behavior of equine hoof wall keratin across the years have seen diverse results that are difficult to relate to one another. This seems to be due to the complex, multivariable nature of the topic. Chapter 4 explores the local variation of equine keratin stiffness at the localized level, i.e. isolated behavior of hoof wall regions (SE, SM, and SI). This approach revealed a method to relate the bulk hoof capsule behavior to the local regions and TD in the wall, yielding a more animal-specific understanding of foot conformation.

The SE, SM, and SI regions of the equine hoof wall were seen to different maximum capacities for moisture. This supports the supposition that the SE is a significant hydration moderation mechanism for the hoof wall. Hydration has proven to have significant impact upon the stiffness of equine keratin. The modulus of elasticity, E, is inversely related to the hydration level, %RH, of the keratin specimen. The more hydrated the keratin is, the more ductile behaving this material becomes, just as the keratin behaves more brittlely as the material dehydrates. Another impactful variable is temperature. As the temperature increases, the more ductile the equine keratin behaves, just as the material becomes more brittle behaving as the temperature decreases. Environmental factors, such as temperature and humidity, may have a significant effect on keratin behavior and thus overall hoof health. The temperature profile of the hoof wall may vary through the thickness, as the SE may be cool in certain environmental conditions, but the SI is close to the internal biology of the digit and may be warmer due to the animal's body temperature. Activity also has an impact of the stiffness of keratin. Increased strain rate is directly correlated to the increase in the modulus of elasticity and tensile stress response of equine keratin. The faster the strain rate, the higher the tensile response and the more polymeric the behavior becomes; conversely, if the strain rate is reduced enough (10^{-4} s^{-1} or slower), the tensile curve follows the more traditional, hyperbolic tangent behavior. This means the hoof capsule will react and deform differently depending on what the animal is doing, such as walking, trotting, galloping, or hauling cargo.

The most useful link, however, is in the context of tubule density. Tubule density alters with hoof wall region, where the tubule population per mm^2 is lowest towards the SI, and increase throughout the SM towards the SE. Keratin specimens of the proximodistal

orientation exhibit a higher stress response when the tubule density is increased; conversely, there is a lower stress response correlated with lower tubule densities. Equine keratin is anisotropic with respect to tubule orientation versus loading axis. There is a higher stress response in keratin loaded along the proximodistal orientation (loading applied parallel to the tubule direction) than in keratin loaded along the mediolateral orientation (loading applied orthogonally to the tubule direction). Additionally, there is greater spread and impact upon the proximodistal data as compared with the mediolateral results, as the proximodistal specimens are significantly impacted by local tubule density. Equine keratin specimens fabricated in the proximodistal orientation demonstrated higher material stiffness as TD increased; conversely, lower elastic moduli correlated with lower TDs. Because TD changes throughout the hoof wall region—where the tubule population per mm^2 is highest towards the SE, and decreases throughout the SM towards the SI—the material stiffness also alters throughout the hoof wall regions.

The link between keratin stiffness and the TD distribution in the hoof is useful because it can be leveraged to predict the material behavior of a specific animal. During the shoeing process, hoof trimming may be taken and could potentially be used to better understand the tubule distribution of that specific horse. By analyzing that hoof trimming for TD and consulting the material property trend lines based on what activities the horse is expected to perform, the caretaker may adjust shoeing practices. Additionally, habitual assessment of TD following changes in shoeing can be utilized to ascertain the effectiveness of the changes in shoeing practices. If hoof trimmings are routinely examined, and TD data is consistently collected over time, it will be easier for the caretaker to identify any alterations of the tubule shape/density. This could potentially act as an early

alert system to developing hoof issues, allowing the horse to receive preventative treatment before the problem evolves/worsens.

Future research in this area should be focused on expanding the data set. The more data collected, the better the material property trends can be predicted with a clearer understanding of the uncertainty that can be expected. Also, the data collected and analyzed should be expanded to include useful properties other than the elastic modulus, such as yield stress.

11.3 Bulk Hoof Wall Properties

This chapter explores how the differing local stiffnesses in the changing regions of the hoof wall work together. Since equine hooves vary dramatically between individual animals and species, there is an infinite combination of wall region thicknesses, TD, wall geometry, and orientation to the loading of the horse's step—meaning there are infinite possible combinations of local keratin properties merged to create the behavior of the bulk hoof wall capsule. This portion of the study aims to collect, quantify, and analyze data on the stiffness of bulk wall equine keratin specimens while tracking the different geometries, keratin pigmentation, TD distributions, %RH, and temperature of the specimens under examination. This data set will become a steppingstone in a path forward to relate the bulk hoof capsule behavior to the local regions and TD in the wall, yielding a more animal-specific understanding of foot conformation.

A series of bulk wall specimens were tension tested to failure. The modulus of elasticity, E, was found to be inversely related to the hydration level, %RH, of the keratin specimen. The more hydrated the keratin is, the more ductile behaving this material becomes, just as the keratin behaves more brittlely as the material dehydrates. Equine

keratin specimens with higher TD ranges demonstrated higher material stiffness; conversely, lower elastic moduli correlated with lower TDs. In addition to stiffness, the overall stress response was elevated when specimens possessed higher TDs. TD clearly plays an important role in affecting the material behavior, and, when the TD peaks are high enough, can have a greater impact than temperature. As the temperature increases, the more ductile the equine keratin behaves, just as the material becomes more brittle behaving as the temperature decreases. The temperature variable appears to become more dominant when paired with mid to low TD values.

Future research in this area should be focused on expanding the data set. The more data collected, the better the material property trends can be predicted with a clearer understanding of the uncertainty that can be expected. Additionally, a wider range of environmental conditions should be explored, to test how well the local keratin properties can predict bulk wall behavior for different temperatures and humidity.

11.4 Tubule Density Distribution and Keratin Pigmentation

Chapter 6 analyzed a number of hoof wall specimens extracted from the toe region for typical TD distribution profiles. The TD profile of each sample was graphed in such a way where each TD data point was correlated to the local keratin pigmentation color. This allowed for both an understanding of the TD ranges a horse hoof may have, but also tracked any pigmentation trends. One of the most hotly debated questions in the farrier world to this day is whether hooves with lighter pigmentation are “softer” than hooves with darker pigmentation.

In this chapter, typical TD distributions trends were identified, and specific pigmentation comparisons are presented and discussed. A correlation was found between

higher TDs and dark keratin pigmentation. Additionally, the TD distribution profiles of dark keratin generally display more peaks and valleys than other keratin coloration. Initial TD peaks occurring at the outer ~0-20% depth reached upwards of 40 tubules/mm^2. TD distribution profiles of lighter colored keratin generally display a steadier profile than other keratin coloration. Initial TD peaks occurring at the outer ~0-20% depth reached upwards of ~28 tubules/mm^2. Keratin with combination pigmentation generally saw trends between that of the light and dark keratin TD distribution profiles.

When considering the observed relationship between higher material stiffness and higher TDs, there is an implication that equine keratin with dark pigmentation will exhibit higher stiffnesses than that of light keratin. The wide variation away from the average TD distribution profiles may explain some of the conflicting observations regarding the "softness" of light hooves. Future research in this area should be focused on expanding the data set. The more data collected, the better the pigmentation and property correlation can be predicted with a clearer understanding of the uncertainty that can be expected. The results herein indicate that this is a potential answer to an age-old debate, but the dataset must be expanded significantly to achieve statically definitive conclusions.

11.5 Leveraging Finite Element Analysis to Predict Localized Hoof Wall Behavior

Chapter 7 establishes a link between the local keratin property trends and the experimental bulk wall tensile results. FEA was used to simulate the tensile tests via a CAD model that included the individual wall thickness regions of the bulk specimens. Using an inexpensive, intuitive, readily available FEA program that is accessible by the average individual, will produce a method that can be utilized by the average farrier. This

method of FEA would serve as the cornerstone for modeling the entire hoof capsule and simulating how different shoeing options would suit a specific horse.

This method of predicting stresses in equine hoof keratin based on TD, %RH, and temperature was demonstrably successful for applications robust enough to withstand +/-10% envelope. The predicted elastic moduli saw an envelope of +10/-16%. There was increased uncertainty for temperatures lower than 21ºC and lower levels of hydration. This is because less experimental data is available in those quadrants of the local keratin stiffness data regime. Expanding the experimental data used to construct the local keratin stiffness data set is an excellent opportunity for future research to improve the accuracy of this method of prediction.

11.6 Modeling the Hoof Capsule

Using the link between local keratin properties and bulk wall behavior, an entire hoof capsule can be modeled and the behavior simulated using TD distributions from around the hoof perimeter. By leveraging the process presented in Chapter 8 the stiffness of a specific horse's entire hoof capsule can be predicted based on field data obtained from hoof trimming (cast offs produced during shoeing preparations), and any farrier can gain a deeper knowledge of how that animal should be shoed. A CAD model of the equine digit was constructed and used to simulate a handful of scenarios: a barefoot uniform hoof, a uniform hoof with a keg shoe, and a barefoot hoof with multi-toned keratin. The hoof capsule was divided into three regions that could be customized with local stiffness properties derived from the TD distribution profile of the horse in question.

The simulated barefoot hoof experienced less drop in the arch and frog region than the shoed hoof due to the lack of constriction from the keg shoe. The barefoot hoof also

saw less deformation in the dorsal wall and a more uniform displacement through the thickness. A general reduction of stress was seen in the simulated barefoot hoof, especially the lack of stress risers on the loading perimeter from the absence of nails. The keg shoe and nails caused localized areas of higher stress in the walls. This approach to modeling the hoof appears to be an accessible method with the ability to customize this model to match the specific hoof wall properties of monotoned and multitoned keratin as predicted by the TD distribution. A custom multitoned hoof capsule was modeled and simulated in the barefoot condition, and the stresses in the hoof capsule can be seen to clearly change depending on the region of pigmentation.

Opportunities for future research lay in expanding the range of modeled shoe scenarios with intent to generate an accessible database. This database would be organizable by general capsule shape/aspects, TD ranges, skeletal alignment, and shoe/attachment type. Such a database should include shoe/support recommendations that include the expanded design space provided by additive manufacturing technology.

11.7 Designing into 3D: Quadruped Orthotics and Clinical Trials

The end goal of this research is to leverage the equine keratin material properties and their correlation to hoof TD, hydration state (biological and environmental), temperature (biological and environmental), and activity (related to strain rate) in order to design custom horseshoes and/or orthotics that accommodate animal- and hoof-specific conditions. A farrier could analyze hoof trimmings to obtain an approximate TD distribution profile of the hoof capsule. The TD distribution profile paired with the local environment temperature and humidity can be used to reasonably predict the stiffness of the hoof capsule wall. From there, a standard horseshoe geometry can be modeled and

functionally graded to match the changing stiffness of the hoof capsule perimeter. If the hoof has conformation issues or injury, this process can be leveraged for a more detailed and powerful solution. The hoof capsule wall geometry can either be obtained via a three-dimensional exterior scan, an x-ray, manual measurements, or a combination of all three, and a CAD model can be constructed. An orthotic can then be designed to assist in correcting and healing a myriad of hoof issues, including but not limited to correcting skeletal alignment, keratin capsule growth/reshaping, promoting specific heel expansions/frog engagement, and improving the digital cushion.

REFERENCES

[1] "The Horse Industry by the Numbers," January 2017. [Online]. Available: https://www.ridewithequo.com/blog/the-horse-industry-by-the-numbers.

[2] G. Al-Ghamd, "Most Common Diseases Impacting Horse Health in the Major Regions of Saudi Arabia," *J. Anim. Vet. Adv.,* vol. 7(d), pp. 581-583, 2008.

[3] B. C. B. A. e. a. Broster CE, "The Range and Prevalence of Pathological Abnormalities Associated with Lameness in Working Horses from Developing Countries," *Equine Vet. J.,* vol. 5, no. 41, pp. 474-481, 2009.

[4] O. B. D. C. M. Balch, "Balancing the Normal Foot: Hoof Preparation, Shoe Fit and Shoe Modification in the Performance Horse," *Equine Vet. Educ.,* vol. 9, no. 3, pp. 143-154, 1997.

[5] W. S. J. Moyer, "Hoof Balance and Lameness: Commentary," vol. 6, p. 2, 1996.

[6] M. R. L. T. J. M. C. M. C. Peterson, *Racing Surfaces: Current Progress and Future Challenges to Optimize Consistency and Performance of Track Surfaces for Fewer Horse Injuries.,* Orono, Maine: Racing Surfaces Testing Laboratory, 2012.

[7] M. A.-R. M. Butcher, "Fetlock Joint Kinematics Differ with Age in Thoroughbred Racehorses," *Journal of Biomechanics,* vol. 35, pp. 563-571, 2002.

[8] O. S. M. I. Pleasant RS, "Farriery for Hoof Wall Defects.," *Vet. Clin. Equine. ,* no. 28, pp. 393-406, 2012.

[9] H. B. D. L. N. e. a. Schryver, "Locomotion in the Horse: Kinematics and External and Internal Forces in the Normal Equine Digit in the Walk and Trot," *Am. J. Vet. Res.,* vol. 39, pp. 1728-1733, 1978.

[10] C. K. R. Hill, "Shoeing For Soundness," in *Horseowners Guide to Lameness*, Philadelphia, Lea & Febiger, 1996, p. 377.

[11] J. G. J. Bertram, "Fracture Toughness Design in Horse Hoof Keratin," *J. Exp. Biol.,* vol. 125, pp. 29-47, 1986.

[12] T. K. K. a. W. A. Witte, "Determination of peak vertical ground reaction force from duty factor in the horse (Equus caballus)," *J. Exp. Biol. ,* no. 207, p. 3639-3648, 2004.

[13] B. A. B. J. Thomason JJ, "Surface Strain on the Equine Hoof Wall In Vivo: Implications for the Material Design and Functional Morphology of the Wall.," *J. exp. Biol. ,* no. 166, pp. 145-168, 1992.

[14] G. J. Kasapi MA, " Design Complexity and Fracture Control in the Equine Hoof Wall.," *J. exp. Biol. ,* no. 200, pp. 1639-1659, 1997.

[15] S. JE., "Anatomy of the Normal Equine Foot, Including Microscopic Features of the Laminar Region.," *J Am Vet Med Assoc. ,* no. 151, pp. 1588-1598, 1967.

[16] J. G. J. Bertram, "Functional Design of Horse Hoof Keratin: The Modulation of Mechanical Properties Through Hydration Effects," *J. Exp. Biol.,* no. 130, pp. 121-136, 1987.

[17] M. G. J. Kasapi, "Strain-Rate-Dependent Mechanical Properties of the Equine Hoof Wall," *J. Exp. Biol.,* vol. 199, pp. 1133-1146, 1996.

[18] J. C. D. M. R. C. D. Reilly, "Tubule Density in Equine Hoof Horn," *Biomimetics ,* vol. 4, no. 1, pp. 23-36, 1996.

[19] W. Banks, Applied Veterinary Histology, St. Louis: The Mosby Yearbook, 1993, p. 311–317.

[20] M. G. J. Kasapi, "Micromechanics of the Equine Hoof Wall: Optimizing Crack Control and Material Stiffness Through Modulation of the Properties of Keratin," *J. Exp. Biol.,* vol. 202, pp. 377-391, 1999.

[21] Y. N. Y. W. e. a. Huang W, "A Natural Energy Absorbent Polymer Composite: The Equine Hoof Wall.," *Acta Biomaterialia,* no. 90, pp. 267-277, 2019.

[22] A. J. Lungwitz A, A Textbook of Horseshoeing. 11th ed., London: J.B. Lippincott Co, 1913, p. 216.

[23] B. R. M. W. Lancaster LS, "Equine Hoof Wall Tubule Density and Morphology.," *J. Vet. Med. Sci. ,* vol. 6, no. 75, pp. 773-778. , 2013.

[24] N. R., " Iiber den Bau der Jufrohrchen und seine Bedeutung fur den Mechanismus des P'ferdehufes.," *Morph. Jahrbuch,* no. 82, pp. 119-160, 1938.

[25] N. R., "Untersuchungen über den Bau des Pferdehufes mit Besonderer Berücksichtigung des Hufmechanismus und von Huthankheiten.," *Dtsch. Tierarzfl. Wschl.,* no. 46, pp. 449-552, 1939.

[26] W. H., "Zur makroskopischen und mickroskopischen Morphologie der Rinderklaue mit einem Vergleich der Architektur von KlaJen-und Hufrohrchen.," *Zentralblarr Vererinarmedizin. ,* no. 11, pp. 163-200, 1964.

[27] P. C., "Anatomy and Physiology of the Inner Hoof Wall.," *Clinical Techniques in Equine Practice,* vol. 3, no. 1, p. DOI: 10.1053/j.ctep.2004.07.001, 2004.

[28] J. M. C. T. J. J. J. Douglas, "The Modulus of Elasticity of Equine Hoof Wall: Implications for the Mechanical Function of the Hoof," *J. Exp. Biol.,* vol. 199, pp. 1829-1836, 1996.

[29] M. Cabrera, *Structural Material Investigation of Horse Hoof.,* University of Scovde, 2013.

[30] R. M. T. Fraser, "Molecular Structure and Mechanical Properties of Keratins," in *Mechanical Properties of Biological Materials*, 1979.

[31] L. DH., *The Structure and Function of the Equine Hoof Wall.,* University of Sascatchewan, 1980.

[32] C. S. C. B. K. Hinterhofer, "Elastic Modulus of Equine Hoof Horn, Tested in Wall Samples, Sole Samples, and Frog Samples at Varying Levels of Moisture," *Berl. Munch. Tierarztl. Wochenschr.,* vol. 111, pp. 217-221, 1998.

[33] L. B. D. B. S. Landeau, "Mechanical Properties of Equine Hooves," *Am. J. Vet. Res.,* vol. 44, pp. 100-102, 1983.

[34] D. Z. G. Leach, "Mechanical Properties of Equine Hoof Wall," *Am. J. Vet. Res.,* vol. 44, pp. 2190-2194, 1983.

[35] N. R., "Iiber den Bau der Jufrohrchen und seine Bedeutung fur den Mechanismus des P'ferdehufes.," *Morph. Jahrbuch,* vol. 82, pp. 119-160, 1938.

[36] W. H., "Zur makroskopischen und mickroskopischen Morphologie der Rinderklaue mit einem Vergleich der Architektur von KlaJen-und Hufrohrchen.," *Zentralblarr Vererinarmedizin. ,* vol. 11, pp. 163-200, 1964.

[37] M. Craig, "How Moisture Affects the Hoof.," [Online]. Available: www.holistichorse.com/hoof-care/how-moisture-affects-the-hoof/. [Accessed August 2020.].

[38] M. Ryder, "Structure of Rhinoceros Horn," *Nature,* vol. 193, pp. 1199-1201, 1962.

[39] K. E., "Feet in the Heat—Healthy Horse Hooves in Hot, Dry Weather," 8 August 2019. [Online]. Available: https://equimed.com/news/health/feet-in-the-heat-healthy-horse-hooves-in-hot-dry-weather.

[40] M. Austin, "Light Vs. Dark: The Hoof Debate Rages On," *American Farriers Journal,* 2002.

[41] D. Butler, The Principles of Horseshoeing II, Laporte, CO: Doug Butler Publisher, 1985.

[42] C. Averill, "Black Wing Tips," *The Condor,* vol. 25, no. 2, pp. 57-59, 1923.

[43] G. S. F. Barrowclough, "Feather Pigmentation and Abrasion: Test of a Hypothesis," *The Auk,* vol. 97, no. 4, pp. 881-883, 1980.

[44] C. F. L. Guerra-Correa, "Albinism in the Gray Gull, Larus Modestus, In Northern Chile," *Le Gerfaut,* vol. 77, pp. 275-279, 1987.

[45] R. Bonser, "Malanin and the Abrasion Resistance of Feathers," *The Condor,* vol. 97, no. 2, pp. 590-591.

[46] R. W. M. Bonser, "Indentation Hardness of the Bill Keratin of the European Starling," *The Condor,* vol. 3, no. 95, pp. 736-738, 1993.

[47] G. F. K. B. B. M. S. I. J. a. E. B. J. Goldstein, "Bacterial Degradation fo Black and White Feathers," *The Auk,* vol. 121, no. 3, pp. 656-659, 2004.

[48] S. H. R. K. M. Kuckova, "Chapter 6: MALDI-MS Applied to the Analysis of Protein Paint Binders," in *Organic Mass Spectrometry in Art and Archaeology*, Chichester, John Wiley & Sons, 2009.

[49] W. Edwards, "Why Not Period Glue?," *Journal of the Society of American Period Furniture Makers,* 2001.

[50] Brauns, "Über Kitt und Leim, nach Haslett und Hackley," *Polytech. Cent.,* vol. 9, no. 6, pp. 89-91, 1858.

[51] L. Barham, From Hand to Handle: The First Industrial Revolution, Oxford University Press, 2013.

[52] J. Blinkhorn, "Examining the Origins of Hafting in South Asia," *J. Paleolithic Archaeol.,* vol. 2, no. 4, pp. 466-481, 2019.

[53] M. e. a. Wilson, "Modern Thermoplastic (Hot Glue) Versus Organic-Based Adhesives and Haft Bond Failure Rate in Experimental Prehistoric Ballistics," *International Journal of Adhesion & Adhesives,* vol. 104, pp. 1-7, 2021.

[54] A. Lucas, Ancient Egyptian Materials and Industries, Edward Arnold Publishers Ltd., 1934, p. 447.

[55] W. B. W. Hull, "Animal Glue: A Staff-Industry Collaborative Report," *Industrial Engineering Chemistry,* vol. 44, no. 10, pp. 2275-2284, 1952.

[56] R. Bogue, The Chemistry and Technology of Gelatin and Glue, New York: McGraw-Hill Book Co., Inc., 1922, p. 5.

[57] "History of the Horseshoe," American Equus, [Online]. Available: https://americanequus.com/history-of-horeshoes/. [Accessed 9 January 2022].

[58] J. Dollar, A Handbook of Horse-shoeing., New York: William R. Jenkins, 1898, p. 185.

[59] W. Russell, Scientific Horseshoeing for Leveling and Balancing the Action and Gait of Horses and Remedying and Curing the Different Diseases of the Foot, Cincinnati, OH, 1903, p. 117.

[60] O. W. K. B. D. M. S. Balch, "Hoof Balance and Lameness: Improper Toe Length, Hoof Angle, and Mediolateral Balance.," *Compend. Contin. Educ. Pract. Vet.,* vol. 17, no. 10, pp. 1275-1283, 1995a.

[61] O. W. K. B. D. a. M. S. Balch, "Hoof Balance and Lameness: Foot Bruising and Limb Contact," *Compend. Contin. Educ. Pract. Vet.,* vol. 17, no. 12, pp. 1503-1509, 1995b.

[62] C. R. R. G. B. e. a. Kobluk, "The Effect of Conformation and Shoeing: A Cohort Study of 95 Thoroughbred Horses.," *Proc. Am. Ass. Equine Practnrs.,* vol. 35, pp. 259-274, 1989.

[63] O. W. K. B. D. Balch, "Factors Involved in the Balancing of Equine Hooves," *J. Am. Vet. Med. Assoc.,* vol. 198, pp. 1980-1989, 1991.

[64] C. Colles, "Interpreting Radiographs. 1. The Foot.," *Equine Vet. J.,* vol. 15, pp. 297-303, 1983.

[65] C. Pollitt, Color Atlas of the Horse's Foot, London: Mosby-Wolfe, 1995, pp. 58-59.

[66] O. C. H. L. J. Balch, "Effects of Increasing Hoof Length on Limb Kinematics of Trotting Horses," *Proc. Am. Ass. Equine Practnrs.,* vol. 40, p. 43, 1994.

[67] F. M. D. M. E. G. J. Lockner, "In Vivo and In Vitro Measurement of Tendon Strain in the Horse," *Am. J. Vet. Res.,* vol. 41, pp. 1929-1937, 1980.

[68] D. V. D. B. A. J. M. e. a. Riemersma, "Influence of Shoeing On Ground Reaction Forces and Tendon Strains in the Forelimbs of Ponies," *Equine Vet. J.,* vol. 28, no. 2, pp. 126-133, 1996.

[69] P. N. D. B. D. Stephens, "Application of a Hall-Effect Transducer for Measurement of Tendon Strain in Horses," *Am. J. Vet. Res.,* vol. 50, pp. 1089-1095, 1989.

[70] O. Balch, *The Effects of Changes in Hoof Angle, Mediolateral Balance and Toe Length On Kinetic and Temporal Parameters of Horses Walking, Trotting, and Cantering On a High-Speed Treadmill,* Pullman, WA: College of Veterinary Medicine, Washington State University, 1994.

[71] K. Navarra, "Understand Breakover and the Implications of Manipulating It," 8 January 2021. [Online]. Available:

https://www.americanfarriers.com/articles/12300-understand-breakover-and-the-implications-of-manipulating-it?v=preview. [Accessed January 2022].

[72] F. Lessiter, "Check Shoeing Rules and Regulations from 191 Horse Organizations," *Am. Farriers Assoc.,* vol. 22, no. 6, pp. 260-277, 1996.

[73] A. Lungwitz, "The Changes in the Form of the Horse's Hoof Under the Action of the Bodyweight," *J. Comp. Pathol. Therap.,* vol. 4, no. 3, pp. 191-211, 1891.

[74] W. A. J. Moyer, "Sheared Heels: Diagnosis and Treatment," *J. Am. Vet. Med. Assoc.,* vol. 166, pp. 53-55, 1975b.

[75] O. W. K. Balch, "Degenerative Joint Disease in the Fetlock Managed by Balanced Shoeing: A Case Report," *Equine Pract.,* vol. 7, pp. 35-40, 1985.

[76] W. Murray, The Perfect Horse: How to Know Him, How to Train Him, How to Breed Him, How to Shoe Him, How to Drive Him, Boston, ME: James R. Osgood & Co., 1873, pp. 246-247.

[77] C. Colles, "The Relationship of Frog Pressure to Heel Expansion," *Equine Vet. J.,* vol. 21, pp. 13-16, 1989.

[78] T. S. C. Turner, "Hoof Abnormalities and Their Relationship to Lameness," *Proc. Am. Ass. Equine Practnrs.,* vol. 34, pp. 293-297, 1988.

[79] R. Luikart, Standards for Judging Farriery, Lexington, Kentucky: American Farriers Association Publishing, 1993, pp. 10-13.

[80] J. H. M. Hickman, Hickman's Farriery, London: J.A. Allen and Co., 1988.

[81] R. Edwards, "Anvil Maganzine Interview with Doyal Teel," *Anvil Magazine,* no. 1, pp. 11-17, 1997.

[82] J. Cota, "Understand When to Use Direct and Indirect Glue-On Shoes," 12 May 2018. [Online]. Available: https://www.americanfarriers.com/articles/10174-understand-when-to-use-direct-and-indirect-glue-on-shoes?v=preview. [Accessed January 2022].

[83] "Glue on Horseshoes," Soundhorse Technologies, 2022. [Online]. Available: https://soundhorse.com. [Accessed January 2022].

[84] D. G. Hyams, *CurveExpert Professional 2.6.5 Documentation; Subsection: Working With Results: Details,* 2018.

[85] J. C. S. C. B. H. L. L. R. Reilly, "Tubule Denssity of the Stratum Medium of Horse Hoof," *Equine Vet. J. Suppl.,* no. 26, pp. 4-9, 1998.

[86] *ASTM Standard D638-14: Standard Test Method for Tensile Properties of Plastics,* West Conshohocken, PA: ASTM International.

[87] C. Hinterhofer, *Untersuchungen zum Kleben von Hornspalten mit besonderer Berucksichtigung der Versorgung von Hornspalten beim Pferd,* University of Veterinary Medicine, 1996.

[88] C. S. C. H. H. Hinterhofer, "Finite Element Analysis (FEA) as a Model to Predict Effects of Farriery on the Equine Hoof," *Equine Vet. J. Suppl.,* vol. 33, pp. 58-62, 2001.

[89] J. M. H. J. J. Thomason, "Analysis of Strain and Stress in the Equine Hoof Capsule Using Finite Element Methods: Comparison With Principal Strains Recorded In Vivo," *Equine Vet. J.,* vol. 7, no. 34, pp. 719-725, 2002.

[90] C. S. C. H. H. Hinterhofer, "The Effect of Flat Horseshoes, Raised Heels and Lowered Heels on the Biomechanics of the Equine Hoof Assessed by Finite Element Analysis (FEA)," *J. Vet. Med. A.,* vol. 47, pp. 73-82, 2000.

[91] M. O. L. V. J. K. P. W. K. T. Z. Jansova, "A Finite Element Model of an Equine Hoof," *Journal of Equine Veterinary Science,* vol. 35, pp. 60-69, 2015.

[92] M. H. G. B. D. F. J. M. H. M. L. Ratzlaff, "Locomotor Forces of Galloping Horses," *Equine Exercise Physiology,* pp. 574-586.

[93] G. Bjorck, "Studies on the Draught Forces of Horses: Development of a Method Using Strain Gauges for Measuring Between Hoof and Ground," *Acts Agric. Scand. Suppl.,* vol. 4, 1958.

[94] M. A. K. H. B. R. J. R. Quddus, "A Force and Motion Study of the Foreleg of a Standardbred Trotter," *J. Equine Me. Surg.,* vol. 2, pp. 233-242, 1978.

[95] J. R. Q. M. A. K. H. B. Rooney, "A Laboratory Investigation of the Function o the Stay Apparatus of the Equine Foreleg," *J. Equine Med. Surg.,* vol. 2, pp. 173-180, 1978.

[96] J. B. T. T. J. J. J. Douglas, "Stress/Strain Behaviour of the Equine Laminar Junction," *The Journal of Experimental Biology,* vol. 201, pp. 2287-2297, 1998.

[97] J. M. H. F. B. J. J. Thomason, "Mechanical Behavior and the Quantitative Morphology of the Equine Laminar Junction," *Anat. Rec.,* vol. 238A, pp. 366-379, 2005.

[98] D. S. H. Riemersma, "In Vitro Mechanical Properties of Equine Tendons in Relation to Cross-Sectional Area and Collagen Content," *Res. Vet. Sci.,* vol. 39, pp. 263-270, 1985.

[99] R. Pellman, *Struktur und Funktion des Hufbeintragers beim Pferd,* Berlin: Free University-Berlin, 1995.

[100] F. Henke, *Hufbeintrager und Hufmechanismus im Seiten-, Trachten-, und Echstrebenteil des Pferdehufes,* Berlin: Free University-Berlin, 1997.

[101] D. W. M. T. M. H. H. Hood, "Wolff's Law and the Equine Digit," in *Proceedings of the 11th Annual Meeting of the Assoc. of Equine Sports Med.*, 1992.

[102] E. Barrey, "Investigation on the Vertical Hoof Force Distributed in the Equine Forelimb with an Instrumented Horseboot," *Eq. Vet. J. Supplement,* vol. 9, pp. 35-38, 1990.

[103] J. B. U. M. D. Koller, "High-tech in the Middle Palaeolithic: Neandertal-Manufactured Pitch Identified," *Eur. J. Archaeol.,* vol. 4, pp. 385-397, 2001.